

University of Windsor

Scholarship at UWindor

Electronic Theses and Dissertations

Theses, Dissertations, and Major Papers

2008

The hydrolysis behaviour of magnides, aluminides and sodides and its application to production of nanoparticles

Huabin Wang
University of Windsor

Follow this and additional works at: <https://scholar.uwindsor.ca/etd>

Recommended Citation

Wang, Huabin, "The hydrolysis behaviour of magnides, aluminides and sodides and its application to production of nanoparticles" (2008). *Electronic Theses and Dissertations*. 8190.
<https://scholar.uwindsor.ca/etd/8190>

This online database contains the full-text of PhD dissertations and Masters' theses of University of Windsor students from 1954 forward. These documents are made available for personal study and research purposes only, in accordance with the Canadian Copyright Act and the Creative Commons license—CC BY-NC-ND (Attribution, Non-Commercial, No Derivative Works). Under this license, works must always be attributed to the copyright holder (original author), cannot be used for any commercial purposes, and may not be altered. Any other use would require the permission of the copyright holder. Students may inquire about withdrawing their dissertation and/or thesis from this database. For additional inquiries, please contact the repository administrator via email (scholarship@uwindsor.ca) or by telephone at 519-253-3000ext. 3208.

NOTE TO USERS

This reproduction is the best copy available.

UMI[®]

**THE HYDROLYSIS BEHAVIOUR OF MAGNIDES,
ALUMINIDES AND SODIDES AND ITS
APPLICATION TO PRODUCTION OF
NANOPARTICLES**

by

Huabin Wang

A Dissertation
Submitted to the Faculty of Graduate Studies
through Engineering Materials
in Partial Fulfillment of the Requirements for
the Degree of Doctor of Philosophy at the
University of Windsor

Windsor, Ontario, Canada

2008

© 2008 Huabin Wang



Library and
Archives Canada

Bibliothèque et
Archives Canada

Published Heritage
Branch

Direction du
Patrimoine de l'édition

395 Wellington Street
Ottawa ON K1A 0N4
Canada

395, rue Wellington
Ottawa ON K1A 0N4
Canada

Your file Votre référence
ISBN: 978-0-494-47103-6
Our file Notre référence
ISBN: 978-0-494-47103-6

NOTICE:

The author has granted a non-exclusive license allowing Library and Archives Canada to reproduce, publish, archive, preserve, conserve, communicate to the public by telecommunication or on the Internet, loan, distribute and sell theses worldwide, for commercial or non-commercial purposes, in microform, paper, electronic and/or any other formats.

The author retains copyright ownership and moral rights in this thesis. Neither the thesis nor substantial extracts from it may be printed or otherwise reproduced without the author's permission.

AVIS:

L'auteur a accordé une licence non exclusive permettant à la Bibliothèque et Archives Canada de reproduire, publier, archiver, sauvegarder, conserver, transmettre au public par télécommunication ou par l'Internet, prêter, distribuer et vendre des thèses partout dans le monde, à des fins commerciales ou autres, sur support microforme, papier, électronique et/ou autres formats.

L'auteur conserve la propriété du droit d'auteur et des droits moraux qui protègent cette thèse. Ni la thèse ni des extraits substantiels de celle-ci ne doivent être imprimés ou autrement reproduits sans son autorisation.

In compliance with the Canadian Privacy Act some supporting forms may have been removed from this thesis.

Conformément à la loi canadienne sur la protection de la vie privée, quelques formulaires secondaires ont été enlevés de cette thèse.

While these forms may be included in the document page count, their removal does not represent any loss of content from the thesis.

Bien que ces formulaires aient inclus dans la pagination, il n'y aura aucun contenu manquant.

■ ■ ■
Canada

AUTHOR'S DECLARATION OF ORIGINALITY

I hereby certify that I am the sole author of this dissertation and that no part of this dissertation has been published or submitted for publication.

I certify that, to the best of my knowledge, my dissertation does not infringe upon anyone's copyright nor violate any proprietary rights and that any ideas, techniques, quotations, or any other material from the work of other people included in my dissertation, published or otherwise, are fully acknowledged in accordance with the standard referencing practices. Furthermore, to the extent that I have included copyrighted material that surpasses the bounds of fair dealing within the meaning of the Canada Copyright Act, I certify that I have obtained a written permission from the copyright owner(s) to include such material(s) in my dissertation and have included copies of such copyright clearances to my appendix.

I declare that this is a true copy of my dissertation, including any final revisions, as approved by my dissertation committee and the Graduate Studies office, and that this dissertation has not been submitted for a higher degree to any other University of Institution.

ABSTRACT

The hydrolysis phenomenon of transition metal (including Si and Ge) magnides, aluminides and sodides has been investigated in this study, and has been successfully developed to produce both transition metal and semiconductor element nanoparticles.

Both in-situ synthesized Mg_2Ni and as-cast Mg_2Ni exhibited a close to zero discharge capacity due to hydrolysis of Mg_2Ni and Mg_2NiH_4 . The hydrolysis characteristics of Mg_2Ni and Mg_2NiH_4 suggest that they are not suitable for use as electrodes in rechargeable batteries.

The hydrolysis byproduct of transition metal and semiconductor element magnides, $Mg(OH)_2$, can be easily removed by a dilute acid. After removal of $Mg(OH)_2$ from the hydrolysis product of Mg_2Ni , Ni nanoparticles were obtained. Besides Ni nanoparticles, Cu, Au and Ag nanoparticles have been successfully prepared by this method. The hydrolysis byproduct of magnides, $Mg(OH)_2$, has a very small solubility in water, and thus the newly-formed $Mg(OH)_2$ precipitates from water in the vicinity of the Mg dissolution sites. The existence of the $Mg(OH)_2$ particles, and the low mobility of transition metal atoms at room temperature, give rise to the formation of very fine transition metal nanoparticles. Therefore, the particle size of these transition metal nanoparticles prepared by this method was not sensitive to the concentration of the initial materials in aqueous solution.

Al_3Ni spontaneously undergoes hydrolysis in water at room temperature, and forms $\text{Al}(\text{OH})_3$, Ni nanoparticles and hydrogen in distilled water at room temperature. Due to chemical characteristics of $\text{Al}(\text{OH})_3$ including its low acidity, chemically active transition metal nanoparticles, such as Fe, Co, and Ni, can not be produced by using dilute hydrochloric acid to remove $\text{Al}(\text{OH})_3$. However, chemically inert transition metal nanoparticles such as Au and Ag could be prepared by this method.

The transition metal-sodium intermetallic compounds, i.e. sodides, undergo severe hydrolysis in water at room temperature. The reaction byproduct, NaOH, has a high solubility and is easier to remove than $\text{Mg}(\text{OH})_2$, the hydrolysis byproduct of magnides. This method, therefore, offers a simpler method of preparing transition metal nanoparticles. The drawback of this method is the difficulty in controlling the reaction rate.

DEDICATION

To My Parents

And

My Wife

ACKNOWLEDGEMENTS

First and foremost, I would like to thank my advisor, Professor Derek O. Northwood for his excellent guidance, encouragement, and thoughtful support throughout my entire graduate career. I greatly appreciated the freedom he gave me to pursue my own ideas. I will benefit for my whole life from his encouraging words (Jan Zwicky's poem) "Those who think metaphorically are enabled to think truly because the shape of their thinking echoes the shape of the world.". I am also very grateful for many rewarding academic, research, professional, and career-related experiences that he has given to me. These experiences have truly enriched my graduate school experience and helped prepare me for my future career.

I would like to thank my parents, my wife and my little sweet-heart. I would not have started on this path, let alone thought of finishing it without your care, understanding and support.

I would like to especially thank Dr. Henry Hu, Dr. Xueyuan Nie and Dr. Holger Eichhorn for use of their various instruments and their critical insights.

I would especially like to thank my friends, Lihong Han, Xin Hu, Zheng Zhong, Yan Wang and Dr. Andrea Demenev for their assistance with experimentation and subsequent discussions.

Last, but not least, to all those who gave me help and were not mentioned by name above, believe me, I am grateful for all your support and I thank you.

TABLE OF CONTENTS

AUTHOR'S DECLARATION OF ORIGINALITY.....	iii
ABSTRACT.....	iv
DEDICATION.....	vi
ACKNOWLEDGEMENTS.....	vii
LIST OF TABLES.....	xiii
LIST OF FIGURES.....	xiv
SYMBOLS.....	xx

I. INTRODUCTION

1.1 Characteristics of nanoparticles.....	1
1.2 Properties of nanoparticles.....	1
1.3 Synthesis of transition metal and semiconductor nanoparticles.....	2
1.4 Focus of this study.....	3
1.4.1 Discovery of hydrolysis behavior of Mg ₂ Ni.....	3
1.4.2 Preparation of magnides, aluminides and sodides.....	4
1.4.3 Investigation of hydrolysis of magnides.....	5
1.4.4 Oxidation behaviour and mechanism of nanoparticles in an aqueous solution.....	5
1.4.5 Effect of hydrolysis temperature on Si and Ge nanoparticles.....	6
1.4.6 Investigation of hydrolysis of aluminides and sodides.....	6

II. REVIEW OF LITERATURE

2.1 Introduction.....	8
2.2 General aspects of nanoparticles.....	8
2.2.1 Surface atoms and structure.....	9
2.2.2 Electronic properties.....	11
2.3 Size-dependent properties.....	13
2.3.1 Catalysis.....	13

2.3.2	Optical properties of Au, Ag, Pt, Ge and Si nanoparticles.....	14
2.3.3	Magnetism of Fe, Co and Ni nanoparticles.....	17
2.3.4	Melting point.....	18
2.4	Applications of nanoparticles.....	19
2.4.1	Catalysts	19
2.4.1.1	Ni nanoparticles.....	20
2.4.1.2	Cu nanoparticles.....	21
2.4.1.3	Au nanoparticles.....	22
2.4.1.4	Photochemistry on metal nanoparticles.....	24
2.4.2	Magnetic Fluids	25
2.4.3	Memories.....	27
2.4.4	Displays.....	29
2.4.5	Sensors.....	32
2.4.6	Nano-inks.....	34
2.5	Preparation methods	38
2.5.1	Chemical methods	38
2.5.1.1	Chemical reduction.....	38
2.5.1.2	Micro-emulsion.....	42
2.5.1.3	Electrochemical methods.....	45
2.5.1.4	Rapid expansion of supercritical fluid solutions.....	45
2.5.1.5	Thermal decomposition.....	48
2.5.2	Physical methods.....	50
2.5.2.1	Thermal evaporation.....	50
2.5.2.2	Magnetron sputtering.....	51
2.5.2.3	Laser ablation.....	51
2.5.2.4	Sonication.....	53
2.6	Comparison of preparation methods.....	53
2.6	Summary.....	56

III. EXPERIMENTAL DETAILS

3.1	The initial materials.....	57
3.2	Material preparation.....	57
3.2.1	Ball-milling.....	57
3.2.2	<i>In-situ</i> reaction synthesis of Mg ₂ Ni.....	58
3.2.3	<i>In-situ</i> reaction synthesis of Mg ₂ NH ₄	58
3.2.4	Preparation of MgNi ₂ , Ni ₃ Al, Ni ₂ Al ₃ , Mg ₃ Au, Mg ₅₄ Ag ₁₇ , Mg ₂ Ge, Mg ₂ Si, Ag ₂ Na and PtNa	59
3.2.5	Synthesis of nanoparticles by a hydrolysis method.....	61
3.3	Materials characterization.....	61
3.3.1	Morphology and structure.....	61
3.3.2	Charge/discharge capacity of Mg ₂ Ni.....	63
3.3.3	Hydrogen absorption/desorption capacity of Mg ₂ Ni.....	64
3.3.4	The specific surface area.....	66
3.3.5	The particle size.....	66

IV. THE HYDROGEN STORAGE PROPERTIES OF Mg₂Ni AND DISCOVERY OF ITS HYDROLYSIS BEHAVIOR

4.1.	Introduction.....	68
4.2	<i>In-situ</i> synthesized Mg ₂ Ni.....	69
4.2.1	Preparation procedures.....	71
4.2.2	Characteristics of the <i>In-situ</i> synthesized product.....	71
4.2.3	Hydrogen storage property.....	74
4.2.4	Electrochemical properties.....	80
4.3	Electrochemical properties of as-cast Mg ₂ Ni.....	82
4.4	<i>In-situ</i> synthesized MgNiH ₄	83
4.4.1	Preparation of Mg ₂ NiH ₄	84
4.4.2	Electrochemical properties.....	85
4.5	Hydrolysis behavior of the as-cast Mg ₂ Ni	86
4.6	Hydrolysis behavior of the in-situ synthesized Mg ₂ NiH ₄	95

4.7 Summary.....	99
V. HYDROLYSIS BEHAVIOUR OF Ni MAGNIDES AND ITS APPLICATION TO THE SYNTHESIS OF Ni NANOPARTICLES	
5.1 Introduction.....	100
5.2 Synthesis of Ni nanoparticles by hydrolysis of Mg ₂ Ni.....	101
5.3 Hydrolysis of MgNi ₂	109
5.4 Synthesis of Ni nanoparticles by hydrolysis of MgNi ₂	114
5.5 Summary.....	119
VI: APPLICATIONS OF THE HYDROLYSIS BEHAVIOUR OF MAGNIDES IN SYNTHESIS OF NANOPARTICLES	
6.1 Introduction.....	122
6.2 Synthesis of Cu nanoparticles by hydrolysis of Mg ₂ Cu.....	122
6.3 Synthesis of Au nanoparticles by hydrolysis of Mg ₃ Au.....	131
6.4 Synthesis of Ag nanoparticles by hydrolysis of Mg-Ag intermetallics.....	137
6.5 Study on hydrolysis behavior of Mg ₂ Ge.....	144
6.6 Study on hydrolysis behavior of Mg ₂ Si	154
6.7 Summary.....	159
VII: STUDY ON THE HYDROLYSIS BEHAVIOUR OF ALUMINIDES AND SODIDES	
7.1 Introduction.....	160
7.2 Hydrolysis of Ni aluminides.....	160
7.2.1 Hydrolysis of Al ₃ Ni.....	161
7.2.2 Hydrolysis of Al ₃ Ni ₂	162
7.3 Hydrolysis of sodides.....	165
7.3.1 Hydrolysis of Ag ₂ Na.....	165
7.3.2 Hydrolysis of PtNa.....	171
7.4 Summary.....	176

VIII:DISCUSSION AND CONCLUSIONS.....	179
IX: RECOMMENDATIONS FOR FUTURE WORK.....	188
REFERENCES.....	190
PUBLICATIONS DERIVED FROM THIS DISSERTATION	214
VITA AUCTORIS.....	218

LIST OF TABLES

Chapter II

- | | | |
|-----|---|----|
| 2.1 | Potential applications of Ni, Cu, Ag, Au, Pt, Si and Ge nanoparticles | 37 |
| 2.2 | Comparison of the critical constants for commonly used fluids | 47 |
| 2.3 | Preparation methods, characteristics and application of Ni, Cu, Au, Ag, Pt, Si and Ge nanoparticles | 54 |

Chapter III

- | | | |
|-----|--|----|
| 3.1 | Chemical composition of the arc-melted Mg ₂ Ni and Mg ₂ Cu pellets | 57 |
| 3.2 | Synthesis of MgNi ₂ , Al ₃ Ni, Ni ₂ Al ₃ , Mg ₃ Au, Mg ₅₄ Ag ₁₇ , Mg ₂ Ge, Mg ₂ Si, Ag ₂ Na and PtNa | 60 |

Chapter VIII

- | | | |
|-----|--|-----|
| 8.1 | Comparison of nanoparticle synthesis by hydrolysis of magnides, aluminides and sodides | 183 |
|-----|--|-----|

LIST OF FIGURES

Chapter II

2.1	Formation of a band structure from (a) a molecular state, (b) a nanoparticle with broadened energy states, and (c) bulk materials	11
2.2	Formation of a zero-dimensional (0D) quantum dot by the formal reduction of dimensions, correlating with the continuing discretization of the energy states	12
2.3	Blue shift of the band-gap energy ΔE as a function of particle radius R	15
2.4	Nanocrystalline Si to emit red light by stimulating it with an argon-ion laser beam	16
2.5	Relation between the size of gold particles and their melting point	18
2.6	Statistics of the number of journal publications per year during the past decade in the area of catalysis with nanoparticles	19
2.7	Schematic illustrations of a magnetic fluid seal	26
2.8	A schematic diagram of a nanocrystal memory device with nanocrystals formed in a 2D layer. (a) Si nanocrystals, and (b) Metal nanoparticles	29
2.9	Emission from blue, green, and red colloidal crystals segregated according to magic sizes and emission of colloids of under excitation using a commercial low intensity UV source with an average wave length of 365nm	30
2.10	A monochromatic 32-by-64-pixel prototype quantum dot LED	31
2.11	A schematic illustration of Si nanocrystal laser	32
2.12	Preparation of “nanocrystal molecules” consisting of two or three DNA modified Au particles attached to a complementary DNA template	34
2.13	The fine patterns with a line width of 3 μ m printed on a substrate using nano-inks	35
2.14	Schematic illustration of the microemulsion process	43
2.15	Comparison between direct and inverse microemulsion	44

2.16 Schematic illustration of the RESS process	46
2.17 Phase diagram and critical constants for carbon dioxide and water	47
2.18 Schematic illustration of the laser ablation process	52

Chapter III

3.1 Scanning electron microscope (JEOL Model JSM-5800LV)	61
3.2 JEOL 2010 Transmission Electron Microscope with an Energy Dispersive X-ray Spectrometer (EDX)	61
3.3 The electrochemical measurement system (Soltron 1285) used in this study	64

Chapter IV

4.1 Mg-Ni binary phase diagram[180]	70
4.2 SEM images of the initial mixture, the ball-milled mixture and the in-situ reaction product	72
4.3 XRD pattern of the initial mixture with a 2:1 atomic ratio of Mg:Ni	73
4.4 XRD pattern of the in-situ synthesized Mg ₂ Ni	73
4.5 Hydrogen absorption/desorption curves of the in-situ synthesized Mg ₂ Ni at 280°C	76
4.6 Hydrogen absorption/desorption curves of the in-situ synthesized Mg ₂ Ni at 300°C	77
4.7 Possible hydrogen atom sites in the antifluorite metal lattice structure of Mg ₂ NiH ₄	78
4.8 The initial charge/discharge curves of the in-situ synthesized Mg ₂ Ni at galvanostatic conditions	81
4.9 The initial charge/discharge curves of the as-cast Mg ₂ Ni at galvanostatic conditions	83
4.10 XRD powder diffraction patterns for a) the as-cast Mg ₂ Ni alloy, b) the <i>in-situ</i> synthesized Mg ₂ NiH ₄	85

4.11 XRD powder diffraction patterns for a) the hydrolysis product of the as-cast Mg ₂ Ni particles in distilled water, b) the hydrolysis product of the as-cast Mg ₂ Ni particles in 6M KOH solution.	88
4.12 TEM images of the hydrolysis product of Mg ₂ Ni	92
4.13 HRTEM image of the hydrolysis product of Mg ₂ Ni (membranes)	93
4.14 EDS spectrum of the hydrolysis product of Mg ₂ Ni (membranes)	94
4.15 XRD powder diffraction patterns for a) the hydrolysis product of the synthetic Mg ₂ NiH ₄ particles in distilled water, b) the hydrolysis product of the synthetic Mg ₂ NiH ₄ particles in 6M KOH solution	96

Chapter V

5.1 XRD powder diffraction patterns for the Ni nanoparticles prepared by hydrolysis of Mg ₂ Ni	101
5.2 TEM images of the Ni nanoparticles produced by hydrolysis of Mg ₂ Ni	102
5.3 HRTEM image of individual Ni nanopartilces produced by hydrolysis of Mg ₂ Ni	104
5.4 HRTEM image of individual Ni nanopartilce produced by hydrolysis of Mg ₂ N (corresponding Inverse FFT image at the upper-right corner)	105
5.5 EDS spectrum of Ni nanoparticles produced by hydrolysis of Mg ₂ Ni	106
5.6 Particle size of the Ni nanoparticles produced by hydrolysis of Mg ₂ Ni	106
5.7 Nitrogen adsorption (□) and desorption (∇) curves of Ni nanoparticles	107
5.8 Powder XRD patterns for a) as-cast MgNi ₂ alloy, b) its hydrolysis product in distilled water for 120h, c) the final product (Ni nanoparticles)	109
5.9 TEM image of the hydrolysis product of MgNi ₂	112
5.10 High resolution TEM images of a) Mg(OH) ₂ , and b) Ni nanoparticles in the hydrolyzed product of MgNi ₂	113
5.11 EDS spectrum of the hydrolysis product of MgNi ₂ (membranes)	114
5.12 TEM images of the Ni nanoparticles prepared by the hydrolysis of MgNi ₂ , a) a cluster of Ni nanoparticles, b) discrete Ni nanoparticles	116

5.13	High resolution TEM image of individual Ni nanoparticles prepared by the hydrolysis of MgNi ₂	117
5.14	EDS spectrum of the cluster of Ni nanoparticles prepared by the hydrolysis of MgNi ₂	118
5.15	Particle size distribution of the Ni nanoparticles prepared by hydrolysis of MgNi ₂	119

Chapter VI

6.1	XRD powder diffraction patterns for a) ball-milled Mg ₂ Cu particles, b) hydrolysis product of the ball-milled Mg ₂ Cu particles, c) the final product (Cu nanoparticles)	125
6.2	TEM images of Cu nanoparticles produced by hydrolysis of Mg ₂ Cu	127
6.3	High-resolution TEM image of an individual Cu ₂ O nanoparticle produced by hydrolysis of Mg ₂ Cu	128
6.4	Particle size of the Cu nanoparticles produced by hydrolysis of Mg ₂ Cu	130
6.5	Nitrogen adsorption and desorption curves for the Cu nanoparticles produced by hydrolysis of Mg ₂ Cu	130
6.6	XRD Powder diffraction pattern of as-cast Mg ₃ Au pellets	133
6.7	XRD diffraction powder pattern of the Au nanoparticles produced by hydrolysis of Mg ₃ Au	133
6.8	TEM images for the Au nanopartilces produced by hydrolysis of Mg ₃ Au	134
6.9	High-resolution TEM image of individual Au nanoparticles produced by hydrolysis of Mg ₃ Au	135
6.10	Particle size of Au nanoparticles produced by hydrolysis of Mg ₃ Au	136
6.11	EDS spectrum for Au nanoparticles produced by hydrolysis of Mg ₃ Au	136
6.12	XRD powder diffraction pattern of as-cast Ag-Mg pellets	138
6.13	XRD powder diffraction pattern of Ag nanoparticles produced by hydrolysis of Mg-Ag intermetallics	139
6.14	TEM of Ag nanoparticles produced by hydrolysis of MgAg intermetallics	140

6.15 HRTEM image of individual Ag nanoparticles produced by hydrolysis of Mg-Ag intermetallics	141
6.16 Particle size distribution of Ag nanoparticles produced by hydrolysis of Mg-Ag intermetallics	143
6.17 EDS pattern of Ag nanoparticles produced by hydrolysis of MgAg intermetallics	143
6.18 XRD powder diffraction pattern of the ball-milled Mg ₂ Ge powders	144
6.19 XRD powder diffraction pattern of hydrolysis product of the ball-milled Mg ₂ Ge powders	145
6.20 XRD powder diffraction pattern of the Ge nanocrystals derived from hydrolysis and acid rinsing of Mg ₂ Ge at room temperature	147
6.21 TEM image for the newly formed Ge produced from hydrolysis of Mg ₂ Ge at room temperature	151
6.22 EDS spectrum for for the newly formed Ge produced from hydrolysis of Mg ₂ Ge at room temperature	152
6.23 XRD powder diffraction pattern f the product after hydrolyszing and acid rinsing at 80°C for 24h	154
6.24 XRD patterns for: a) the ball-milled Mg ₂ Si particles, b) the hydrolysis product of the ball-milled Mg ₂ Ni particles at room temperature, c) the final product hydrolyzed at room temperature, d) the final product hydrolyzed at 60°C, e) the final product hydrolyzed at 80°C	155
6.25 TEM images of the product of after hydrolyzing and acid rinsing at room temperature	158
6.26 The EDS spectrum for the membrane in Fig 6.25	158

Chapter VII

7.1 XRD powder diffraction patterns for a) as-cast Al ₃ Ni alloy, b) its hydrolysis product in distilled water for 120h	161
7.2 XRD powder diffraction patterns for a) as-cast Al ₃ Ni ₂ alloy, b) its hydrolysis product in distilled water for 720h	163
7.3 XRD powder diffraction pattern of the Ag ₂ Na pellets prepared at 600°C for 2 hours	166
7.4 XRD powder diffraction pattern of the Ag nanoparticles prepared by hydrolysis of Ag ₂ Na	167

7.5	Morphology of Ag nanoparticles prepared by hydrolysis of Ag ₂ Na intermetallics, a) TEM image, b)HRTEM image	169
7.6	Particle size distribution of the Ag nanoparticles prepared by hydrolysis of Ag ₂ Na	170
7.7	EDS pattern of the Ag nanoparticles prepared by hydrolysis of Ag ₂ Na	170
7.8	XRD powder diffraction pattern of the PtNa pellets prepared at 600°C for 2 hours	172
7.9	XRD powder diffraction pattern of the Pt nanoparticles prepared by hydrolysis of PtNa	173
7.10	Morphology of the Pt nanoparticles prepared by hydrolysis of PtNa, a) TEM image, b) HRTEM image	176
7.11	Particle size distribution of the Pt nanoparticles prepared by hydrolysis of PtNa	176
7.12	EDS pattern of the Pt nanoparticles prepared by hydrolysis of PtNa	176

Chapter VII

8.1	A comparison of particle size distribution of Au, Ag, Cu and Ni nanoparticles prepared by hydrolysis of Mg ₂ Ni, MgNi ₂ , Mg ₂ Cu, Mg ₄₅ Ag ₁₇ and Mg ₃ Au, respectively.	179
-----	---	-----

LIST OF ABBREVIATIONS, SYMBOLS, NOMENCLATURE

Ag	Silver
Al	Aluminum
Au	Gold
C	Carbon
Cl	Chlorine
Co	Cobalt
Cu	Copper
DC	Direct current
EDS	Energy dispersive spectroscopy
FCC	Face centered cubic
Fe	Iron
Ge	Germanium
H	Hydrogen
HCP	Hexagonally close-packed
K	Potassium
LCD	Liquid crystal display
LEDs	Light-emitting diodes
LTWGS	Low-temperature water-gas shift reaction
MOS	Metal oxide semiconductor
MOSFET	Metal oxide semiconductor field effect transistor
Na	Sodium
NC	Nano crystals
Ni	Nickel
O	Oxygen

Pd	Pladium
Pt	Platinum
PTFE	Polytetrafluoroethylene
SEM	Scanning electron microscope
SFCO ₂	Supercritical carbon dioxide
Si	Silicon
TEM	Transmission electron microscope
TCE	Trichloroethylene
Ti	Titanium
UV	Ultraviolet
WGS	Water-gas shift
XRD	X-ray diffraction

Symbols

A	Ampere
D	Dimension
E	Electric potential
ΔE	Band-gap energy
e-h	Electrohole
eV	Electron volt
g	Gas
ΔG	Gibbs free energy
ΔH	Enthalpy Change
<i>l</i>	Liquid
R	Gas constant
<i>s</i>	Solid
ΔS	Entropy
T	Temperature

Greek symbols

α Solid solution phase

β Hydrides

CHAPTER ONE: INTRODUCTION

1.1 Characteristics of nanoparticles

The transition from microparticles to nanoparticles can lead to a number of changes in physical properties due to an increase in the ratio of surface area to volume and the size of particles moving into the realm where the quantum effects predominate [1].

As a particle becomes extremely small, the physical and chemical properties of the particles may be dominated by the properties of the surface atoms. In addition, valence electrons in a crystalline solid occupy continuous energy bands. However, the valence electrons in very small particles (below 10-20nm) occupy discrete, but broadened electronic densities. The occupation, width and separation of these bands determine most of the fundamental electrical, optical and magnetic properties of the solid. Thus, transition metal nanoparticles exhibit many unique properties that are different from those of bulk metals when their particle sizes are as small as nanometer size (10^{-9} m) [2].

1.2 Properties of nanoparticles

As the particle size is reduced, more atoms are on the surface, which makes small nanoparticles, especially metallic ones, highly reactive catalysts. In general, the high surface area of nanoparticles is a critical factor in the performance of catalysts for gaseous reactions in the chemical industry [1].

Chapter I. Introduction

Transition metal nanoparticles, in particular, Au, Ag, and Pt, exhibit optical activity in the visible range of the spectrum. Si and Ge nanocrystals under the quantum confinement effect, exhibit photoluminescence.

The magnetic domains of the magnetic material nanoparticles may change from multiple to single due to the quantum effects. For example, it was reported that Ni nanoparticles exhibited a superparamagnetic behaviour above the blocking temperature [2].

1.3 Synthesis methods for transition metal or semiconductor nanoparticles

Various methods have been developed to synthesize transition metal or semiconductor nanoparticles. These methods essentially fall into two categories: chemical and physical methods. Among the chemical synthesis method, transition metal or semiconductor nanoparticles have been conventionally prepared by micro-emulsion, chemical reduction of metal-salts, thermal decomposition, electrochemical methods, and the rapid expansion of supercritical fluid solutions. Of these methods, chemical synthesis in solution is favoured for fabricating nanoparticles because it allows the tailored design of materials at the molecular level, and also because it offers a cost-effective method of producing nanoparticles in large quantities. In addition, colloidal chemistry offers a possible route for the synthesis of a uniform dispersion of fine metallic particles by stabilizing the particles in the presence of a surfactant.

Although these synthesis methods of nanoparticles are, in certain ways, reaching maturity, a scaling up synthesis method of these materials is still required.

Chapter I. Introduction

1.4 Focus of this study

1.4.1 Discovery of hydrolysis behaviour of Mg_2Ni

Rechargeable nickel metal hydride (NiMH) batteries have many advantages for use as power sources in electric and hybrid vehicles such as higher power densities and environmental friendliness. When compared with conventional AB_5 alloys, Mg_2Ni exhibits a good hydrogen storage capacity (3.6wt%) and lower specific gravity. The theoretical discharge capacity of Mg_2Ni is as high as 999mAh/g [3]. However, polycrystalline Mg_2Ni shows a very low electrochemical discharge capacity (less than 10mAh/g). It has been reported that the electrochemical discharge capacity can be improved through the use of nano-crystalline Mg_2Ni . A very high discharge capacity of 1082mAh/g (exceeding the theoretically calculated value) has even been reported [4]. Therefore, Mg_2Ni is thus expected to be amongst the next generation of electrode materials.

In general, the hydrogen storage capacity of the alloys prepared by the melting and casting method is higher than that of the materials synthesized by the mechanical alloying method. However, mechanical alloying can significantly improve both the activation and the reaction kinetics of hydrogen storage alloys. Contamination is a major drawback of mechanical alloying. No contamination is introduced by in-situ reaction synthesis (or combustion synthesis). Its products are porous, and have a high purity and large surface areas of “fresh” surface, which results in easy activation of the combustion synthesis product.

During an investigation into the charge/discharge capacity of the in-situ reaction synthesized Mg_2Ni , the Mg_2Ni exhibited a near zero charge/discharge capacity. The

Chapter I. Introduction

hydrolysis reactions of both in-situ reaction synthesized Mg_2Ni and Mg_2NiH_4 were examined in detail from the viewpoint of thermodynamics. The analysis results indicated that the hydrolysis reactions of both Mg_2Ni and Mg_2NiH_4 were spontaneous in both distilled water and a 6M KOH solution, and formed $Mg(OH)_2$, Ni and hydrogen. The XRD results showed that the width of the Ni diffraction peaks was fairly broad, which reflected the fact that the crystallite size of Ni was extremely small. In addition, the hydrolysis byproduct, $Mg(OH)_2$, can be easily removed by dilute acids. Hence, the hydrolysis of Mg_2Ni had the potential to be developed to produce Ni nanoparticles [5].

The initial materials used in this method could easily be produced by a conventional melting and casting method or a reaction-synthesis method. The hydrolysis processing of the metal and the magnesium intermetallic compounds and the removal of $Mg(OH)_2$ could potentially be carried out on a large scale. Therefore, compared with conventional preparation methods for Ni nanoparticles, the method has a great potential to economically produce Ni nanoparticles on a large scale [5].

1.4.2 Preparation of magnides, aluminides and sodides

Of all the magnides, aluminides and sodides used in this research only Mg_2Ni and Mg_2Cu are commercially available. Production of other magnides, aluminides and sodides was done in our laboratory. Due to differences in chemical characteristics (reactivity) of magnesium, aluminum and sodium, magnides and aluminides were fabricated under a protective atmosphere (a mixture gas of sulphur hexafluoride and 0.5% carbon dioxide) by a conventional melting and casting method, and the sodides were fabricated under a protective atmosphere of 0.5MPa argon by a reaction-synthesis method.

Chapter I. Introduction

1.4.3 Investigation of hydrolysis of magnides

Besides Mg_2Ni , MgNi_2 is also formed in the binary Mg-Ni system. The hydrolysis reaction of MgNi_2 was analyzed from a thermodynamics point of view. The analysis results also indicated that the hydrolysis reaction of MgNi_2 was spontaneous, which was then confirmed by actual hydrolysis experiments.

Hydrolysis of Mg_2Cu , Mg_3Au , Mg_2Cu , $\text{Mg}_{54}\text{Ag}_{17}$, MgAg , Mg_2Ge , and Mg_2Si were then investigated. The results showed that all these magnides exhibited hydrolysis behaviour. This suggested that hydrolysis is a common phenomenon. The corresponding transition metal and semiconductor element nanoparticles were produced by using this phenomenon. The size of the nanoparticles prepared by the hydrolysis method was around 10nm.

1.4.4 Oxidation behaviour of nanoparticles in an aqueous solution

The oxidation behaviour of their nanoparticles in water was investigated in detail. Due to the differences in chemical affinities of the transition metals to oxygen, transition metal nanoparticles exhibited different oxidation behaviour in an aqueous solution. For the relatively highly chemically active elements, such as Ni and Si, their nanoparticles were oxidized into the corresponding hydroxides by the dissolved oxygen in the solution during hydrolysis and removal of $\text{Mg}(\text{OH})_2$ by using dilute acid. For the relatively low chemically active elements, such as Cu and Ge, their nanoparticles were first oxidized into the corresponding hydroxides by the dissolved oxygen in the solution during hydrolysis and removal of $\text{Mg}(\text{OH})_2$ by using dilute acid, and then these hydroxides further dissociated into their oxides (Cu_2O for Cu nanoparticles, and GeO_2 for Ge

Chapter I. Introduction

nanoparticles). For the chemically inert elements, such as Au and Ag, their nanoparticles were not oxidized by the dissolved oxygen in the solution during hydrolysis, or during removal of $\text{Mg}(\text{OH})_2$ using a dilute acid.

1.4.5 Effect of hydrolysis temperatures on formation of Si and Ge nanoparticles

A general trend for the formation of crystalline Si and Ge is that the more covalent the element, the higher is its crystallization temperature. At low temperatures, amorphous phases become more common as the material becomes more covalent. Hence, the effects of the hydrolysis temperature on the formation of Si and Ge nanoparticles were investigated in detail.

1.4.6 Investigation of the hydrolysis of aluminides and sodides

There are many intermetallic compounds that have similar chemical characteristics to magnides, for example, aluminides and sodides. Therefore, an investigation of the hydrolysis of aluminides and sodides would help us better understand the hydrolysis behaviour of intermetallic compounds.

Among the Ni aluminides, Al_3Ni spontaneously underwent hydrolysis in water at room temperature, and formed $\text{Al}(\text{OH})_3$, Ni and hydrogen. Although from thermodynamic considerations, the negative standard free energy change for the hydrolysis reaction of Al_3Ni is much larger than that for Mg_2Ni , and from a crystal structure point of view, more Al atoms surround a Ni atom in Ni_3Al than Mg atoms surround a Ni atom in Mg_2Ni , the hydrolysis of Al_3Ni seemed to be much easier than that of Mg_2Ni . In addition, Al_3Ni_2 barely underwent a hydrolysis reaction under the same conditions. The hydrolysis of AlNi

Chapter I. Introduction

and AlNi_3 in the Ni-Al binary system would be much slower than for Al_3Ni_2 due to thermodynamic and kinetics factors including crystal structure. Due to the low acidity of $\text{Al}(\text{OH})_3$, using dilute hydrochloric acid to remove $\text{Al}(\text{OH})_3$ would lead to a fairly low PH value of solution. As a result, the chemically active transition metals such as Fe, Co, Ni, or even Cu nanoparticles will be difficult to produce by this method, in particular, when they are exposed to air.

The hydrolysis reactions of sodides were very fast, and were accompanied by small explosions or combustion due to the high chemical activity of sodium. A colloid containing the transition metal nanoparticles was formed almost instantaneously. The reaction byproduct, NaOH, had a high solubility and was easier to remove than $\text{Mg}(\text{OH})_2$, the hydrolysis byproduct of magnides. This method offers a simpler method for preparing transition metal nanoparticles. The drawback of this method is the difficulty in controlling the reaction rate.

**CHAPTER TWO: LITERATURE REVIEW:
CHARACTERISTICS, PROPERTIES, APPLICATIONS
AND PREPARATION OF TRANSITION METAL, Si AND
Ge NANOPARTICLES**

2.1 Introduction

This chapter describes general characteristics of nanoparticles, their physical properties, application and methods of preparation. Particular emphasis is given to transition metal and semiconductor nanoparticles (Si and Ge) in this dissertation due to their potential application as catalysts, memories and displays.

2.2 General aspects of nanoparticles

It is generally known that nanoparticles exhibit properties that are different from those of bulk metals when their particle sizes are as small as the nanometer size (10^{-9} m). The transition from microparticles to nanoparticles can lead to a number of changes in physical properties. Two of the major factors contributing to this change in physical properties are the increase in the ratio of surface area to volume, and the size of particles moving into the realm where the quantum effects predominate [1].

2.2.1 Surface atoms and structure

The first, very important property of nanoparticles is the large surface-to-volume ratio which makes them distinct from larger particles. If a 1cm cube of metal is broken into small cubes of 10nm edge length, the overall surface will increase 10^6 times, although the amount of matter remains the same. In general, nanoparticles have a specific surface area of 10^2 - 10^3 m²/g. From a purely geometrical consideration, in crystalline particles smaller than 10nm size, the amount of atoms at the surface becomes relevant as it is comparable to that of atoms in the interior of the particle. The ratio of surface atoms to volume atoms is inversely proportional to the size of the particle [1].

The surface is generally considered to take up a thickness of 3 atomic spacings. For a 10nm metallic particle, 10% of the atoms are surface atoms; and for a 1nm particle, more than half of them are surface atoms. Thus, the volume of this surface layer becomes significant in nanoparticles [1]. It is known that the composition, or the crystal structure, is modified at the free surface of a material. The composition or the crystal structure at the surface layer of nanoparticles could be different from those of the particle core. The clean surface of crystalline materials relaxes and reconstructs in order to minimize the total Gibbs energy, given the new chemical environment of the semi-infinite crystal.

In metallic nanoparticles, for example, the surface tends to smooth out the electronic charge distribution and the atoms on the surface layer respond by reconstruction. Most clean surfaces of metallic nanoparticles either contract or expand and in some cases they reconstruct. However, their construction is limited by the ability of the atom that hybridizes and adapts their bond lengths and angles to the new configuration. These are measurable effects in nanoparticles, as the "surface volume" is not negligible.

Chapter II: Literature review: Characteristics, properties, applications and preparation of transition metal, Si and Ge nanoparticles

Selected examples of these surface effects are the surface contraction in palladium nanoparticles and the crystal lattice distortion for other metal nanoparticles [2]. Nickel is a notable example; while the bulk crystal has the face centered cubic (FCC) structure, nanoparticles smaller than 4nm are hexagonal close-packed (HCP) [2].

While the atoms lying in the core volume of nanoparticles are surrounded by a specific number of atoms (which is called the coordination number), on the surface layer their coordination number is reduced. Thus, as a particle becomes extremely small, the physical properties of the particles may be dominated by the properties of the surface atoms.

The chemistry of the surface can also change owing to environmental conditions. Molecules can be adsorbed from the environment. It must be taken into account that nanoparticles are always exposed to some kind of atmosphere both during and after their production, and during their different applications. The adsorbed molecules may react with the surface atoms (chemisorption) to form a new phase [2].

The large surface area also results in some interactions between the different components in nanocomposites, leading to special properties such as increased strength and/or increased chemical/heat resistance. Pure metal nanoparticles can be induced to merge into a solid without melting (a process called sintering) at lower temperatures than larger particles, leading to improved and “easier-to-create” coatings, particularly in electronics applications such as capacitors [2].

Chapter II: Literature review: Characteristics, properties, applications and preparation of transition metal, Si and Ge nanoparticles

2.2.2 Electronic properties

For individual atoms and molecules, the electronic density of state is discrete, resulting in intrinsically sharp spectral line widths (see Fig.2.1a) [2]. In a crystalline solid, valence electrons occupy continuous energy bands and the occupation, width and separation of these bands determines most of the fundamental electrical, optical and magnetic properties of the solid (see Fig.2.1c). The electronic structure of a nanocluster or a nanocrystal might fall somewhere between these two extremes. The increasing presence of the surface tends to perturb the periodicity of the "infinite" lattice of a regular crystal. The electronic configurations in tiny particles (below 10-20nm) are similar to those of the particle-in-a-box, exhibiting discrete, but broadened electronic densities (see Fig.2.1b).

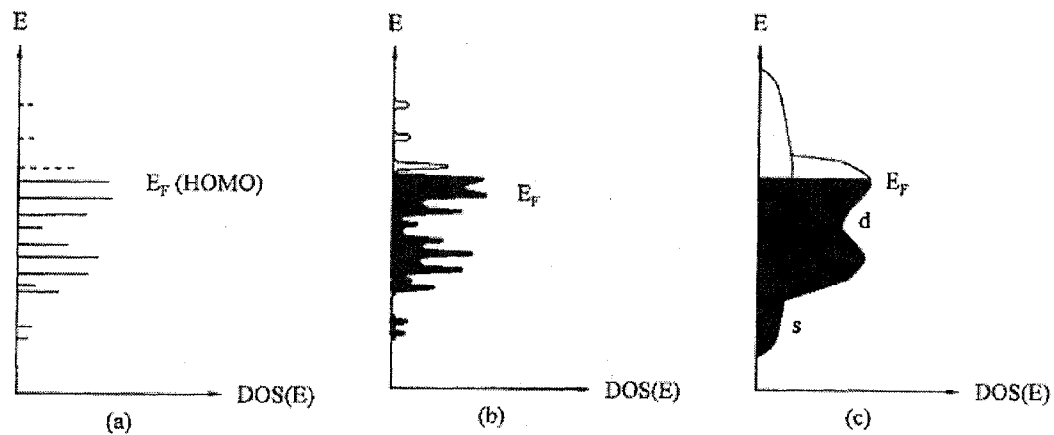


Fig. 2.1 Formation of a band structure from (a) a molecular state, (b) a nanoparticle with broadened energy states, and (c) bulk materials (HOMO: Highest Occupied Molecular orbital; DOS: the electronic density of states) [2].

If a piece of metal is reduced by making it thinner and thinner until the electrons can only move in two instead of three dimensions, a two dimensional (2D) quantum confinement

Chapter II: Literature review: Characteristics, properties, applications and preparation of transition metal, Si and Ge nanoparticles

will be obtained, which is called a quantum well. Further reduction in dimensionality will generate a quantum wire (1D). Reducing dimensions will finally end in a quantum dot (0D). The energy states in the bulk, a quantum well, a quantum wire and a quantum dot are shown in Fig. 2.2 [4].

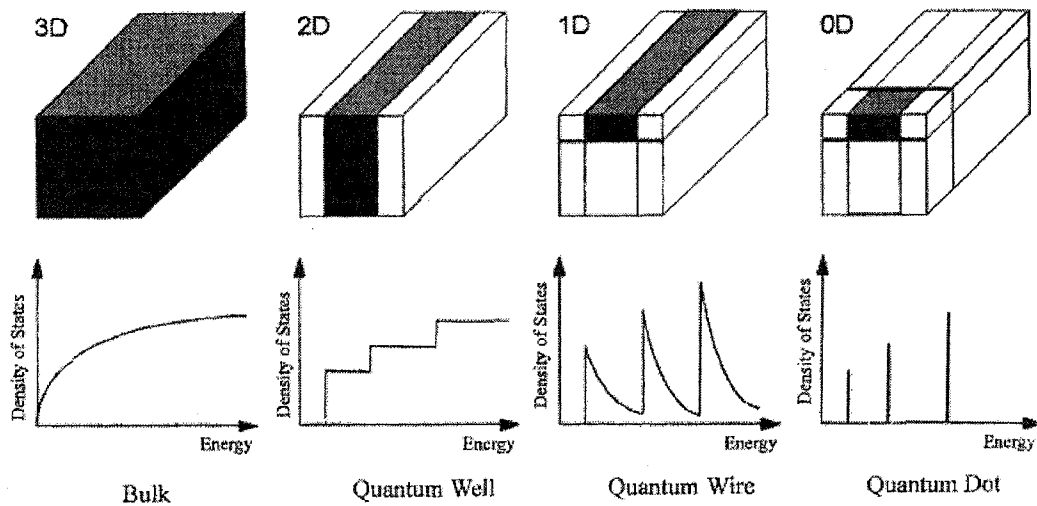


Fig. 2.2 Formation of a zero-dimensional (0D) quantum dot by the formal reduction of dimensions, correlating with the continuing discretization of the energy states [4].

In the case of metals, the electrical properties are determined by the electron mean free path, which typically ranges from 5 to 50nm for most metals. If the crystal becomes comparable in size to the electron mean free path, the electrons are then also scattered at the surface, which increases the electronic resistance of the nanoparticles. One of the most important consequences of the size confinement is therefore the extremely small capacitance of isolated nanoclusters and nanocrystals. This can give rise to an appreciable charging energy when a single electron is transferred to the cluster. The very small capacitance strongly affects its electronic structure, giving rise to single-electron charging

Chapter II: Literature review: Characteristics, properties, applications and preparation of transition metal, Si and Ge nanoparticles

effects. For these reasons metallic nanoparticles and nanowires are promising unit elements in building nanoscopic circuits with tunnelling junctions involving jumps of single electrons.

Electronic devices based on nanoparticles (e.g. metal and semiconductor nanoparticles) will not function analogously to their macroscopic counterparts. Thus, a conventional MOSFET (metal oxide semiconductor field effect transistor) will no longer be able to control the flow of electrons as its size reaches the sub-50nm regime. At this dimensions, electron transport in n- and p- doped contacts is affected by the quantum mechanical probability that electrons will simply tunnel through the interface. These tunnelling processes will begin to dominate in the nanometer size regime, causing errors in electronic data storage and manipulation [2].

2.3 Size-dependent properties

2.3.1 Catalysis

With an increase in the ratio of surface area to volume, the behaviour of atoms on the surface of a particle will gradually dominate those in the interior of the particle. This affects both the properties of the particle in isolation, and its interaction with other materials [1].

The high surface area of nanoparticles is a critical factor in the performance of catalysts for gaseous reactions in the chemical industry and structures such as electrodes, since the efficiency of a particular reaction is proportional to the area of the available surface. In a catalytic activity, a material is able to speed up a particular chemical reaction without changing itself and its properties. As the particle size is reduced, more atoms are on the surface and this makes small nanoparticles, especially metallic ones, highly reactive

Chapter II: Literature review: Characteristics, properties, applications and preparation of transition metal, Si and Ge nanoparticles

catalysts, as the surface atoms are the active centers for catalytic elementary processes that can be used for chemical synthesis, reducing pollutants from domestic environment and car exhaust systems [1].

For particles smaller than the electron mean free path, the electronic band structure may significantly change with particle size and materials such as gold, which are usually chemically quite inert, become catalytically active [5]. It has been found that gold nanoparticles, supported on a silicate substrate, catalyze the production of propylene oxide with a high selectivity of more than 90%. Since the only byproduct of this reaction is water, application of gold nanoparticle catalysts is expected to be a clean process for partial oxidation. The selective oxidation processes that are used to make compounds contained in agrochemicals, pharmaceuticals and other chemical products can be accomplished more cleanly and more efficiently with nanoparticle catalysts [5].

2.3.2 Optical properties of Au, Ag, Pt, Ge and Si nanoparticles

The modified electronic configuration of a confined crystal has a great effect on the optical transitions between different energy levels. Furthermore, the scattering of light from tiny particles is affected by the modified electron cloud which influences the dielectric function of the material [6].

Transition metal nanoparticles e.g., Au, Ag, and Pt, are optically active in the visible range of the spectrum. A colloidal solution of noble-metal nanoclusters has an intense color. When the crystal size becomes smaller than the wavelength of the visible light, these metal nanoparticles partially transmit the light. A strong optical absorption in the visible region arises from the surface plasmon excitation in response to the external electromagnetic field. This results in changes of the color of the suspension. A decrease

Chapter II: Literature review: Characteristics, properties, applications and preparation of transition metal, Si and Ge nanoparticles

of the nanocluster size gives rise to a significant increase in the surface plasmon resonance band width, and results in a shift in the resonance position as known as a red-shift. For example, the smaller Au nanoparticles exhibit a broad surface plasma absorption between the green and yellow wave lengths, and allow only red light to be transmitted. As a result, the smaller Au nanoparticles show a red color [4].

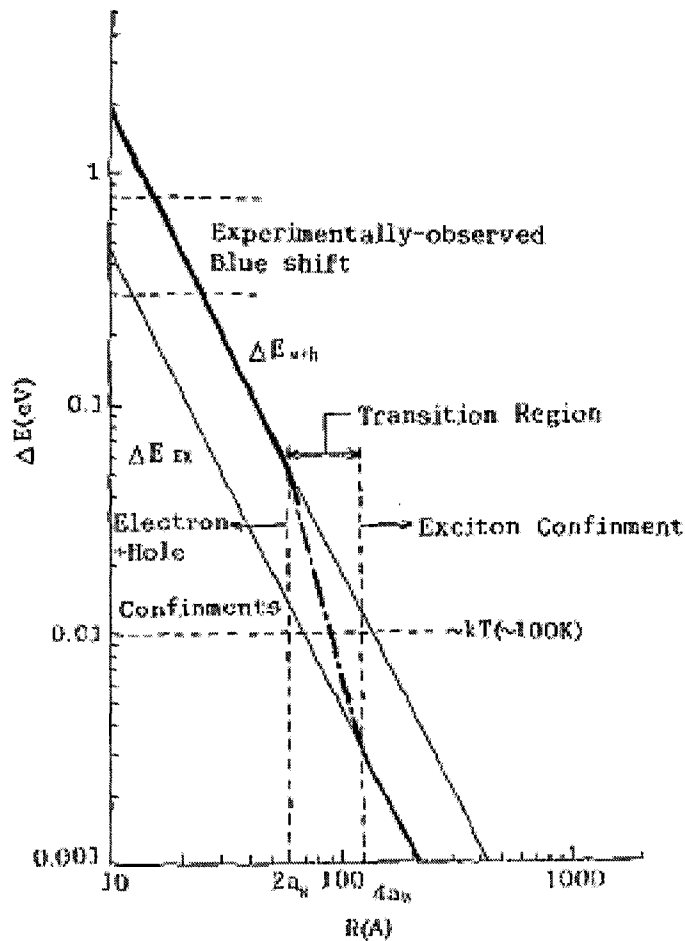


Fig.2.3 Blue shift of the band-gap energy ΔE as a function of particle radius R [6].

Where, the E_{e+h} is the independent confinements of the electrons and holes; E_{EX} is the exciton confinement.

Chapter II: Literature review: Characteristics, properties, applications and preparation of transition metal, Si and Ge nanoparticles

Bulk Si and Ge are indirect bandgap semiconductors and poor emitters of light. However, surface effects, as well as quantum confinement effects are considerably enhanced in Si and Ge nanocrystals, which control the photoluminescence. A quantum mechanical treatment shows that the eigen-state of particles confined to a small potential well become discrete and move up from the bottom of the well, which result in the increase in apparent bandgap energy of the semiconductor (blue shift of the bandgap) [6-11]. If the Radius of the quantum well R is greater than the exciton Bohr radius a_B , the exciton as quasi-particles are confined to the well; if a_B is larger than R , the excitons are no more stable in the well [6].

The extent of the blue shift as function of particle radius for Si is illustrated in Fig.2.3 [6]. It is found that the transition from exciton confinement occurs at a radius of around 100 Å. Visible light emission from Si particles should only occur in particles with a radius less than 20 Å. The particle size in this range is already at the dividing criterion between ultrafine particles and clusters.



Fig.2.4 Nanocrystalline Si to emit red light by stimulating it with an argon-ion laser beam (green light) [8].

Chapter II: Literature review: Characteristics, properties, applications and preparation of transition metal, Si and Ge nanoparticles

The photoluminescence from Si nanocrystals (see Fig.2.4) was first discovered by Canham [8]. Silicon nanocrystals emit light from near IR to visible to ultraviolet due to the quantum confinement effect as the size of silicon decrease exciton Bohr radius (4.9 nm). This also allows for an increase in internal quantum efficiency from 10–20% to 60%.

2.3.3 Magnetism of Fe, Co and Ni nanoparticles

The magnetic properties of nanoparticles are different from those of bulk materials. The magnetic properties of transition metals such as Fe and Co differ significantly from the bulk and depend strongly on the particle size [12]. The experimental results on small magnetic clusters in the gas phase have shown that the total magnetic moment depends on the size of the clusters, in particular, it is a function of the number of atoms. Both orbital and spin moments on the surface of tiny magnetic nanoparticles are strongly enhanced. The spin moment then decreases to the bulk value as the size of the particle exceeds a few nanometers. This is a consequence of the fact that a high number of atoms with lower coordination number sit on the surface and therefore exhibit uncompensated distributions of magnetic moments (spins). This effect is very strong only for tiny clusters of less than 1000 atoms, but in some case it is still present for larger particles.

As the particle diameter of such magnetic materials as iron and nickel approaches the nano range, their magnetic domains are changed from multiple to single due to the quantum effects, and their magnetic properties also change. It is highly desirable to use particles that are magnetically separated from each other, and where the particle size is such that each individual particle can be considered as an elementary magnet [12]. Ni nanoparticles exhibit a superparamagnetic behaviour above the blocking temperature

[13,14]. The coercivity of the Ni nanowires increases with decreasing wire diameter due to the tendency toward single domain nature [15,16].

2.3.4 Melting point

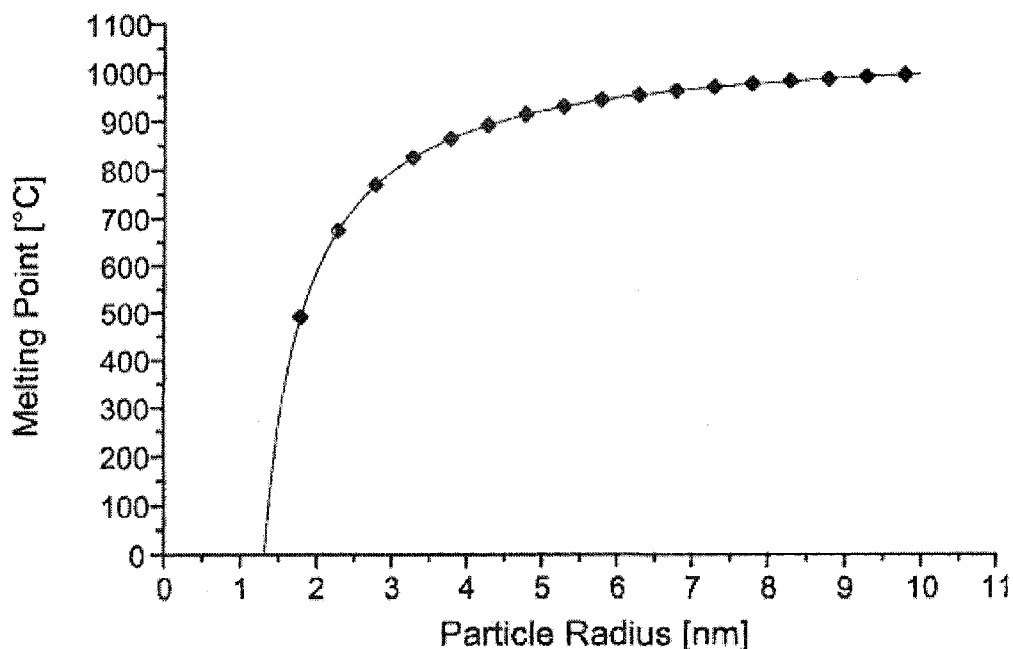


Fig.2.5 Relation between the size of gold particles and their melting point [17].

The majority of metals have a hexagonal or a cubic close-packed structure with a coordination number of 12. The surface atoms only have a coordination number of 9 or smaller. It is typical for bulk materials that the surface atoms form a negligible part of the total number of atoms. A spherical particle of 10nm in diameter has around 10% of surface atoms, so that the surface atoms cannot be neglected for the smaller particles. These surface atoms with a coordination number of 9 or smaller are more easily rearranged than those atoms in the center of particles. In addition, the decrease in the

Chapter II: Literature review: Characteristics, properties, applications and preparation of transition metal, Si and Ge nanoparticles

average coordination number of surface atoms leads to a weaker cohesive energy. As a consequence, the melting temperature is reduced. According to the calculation by the method of Rosenberger, there is a dramatic decrease of melting point for particles smaller than 3-4nm (see Fig.2.5) [17].

2.4 Applications of nanoparticles

2.4.1 Catalysts

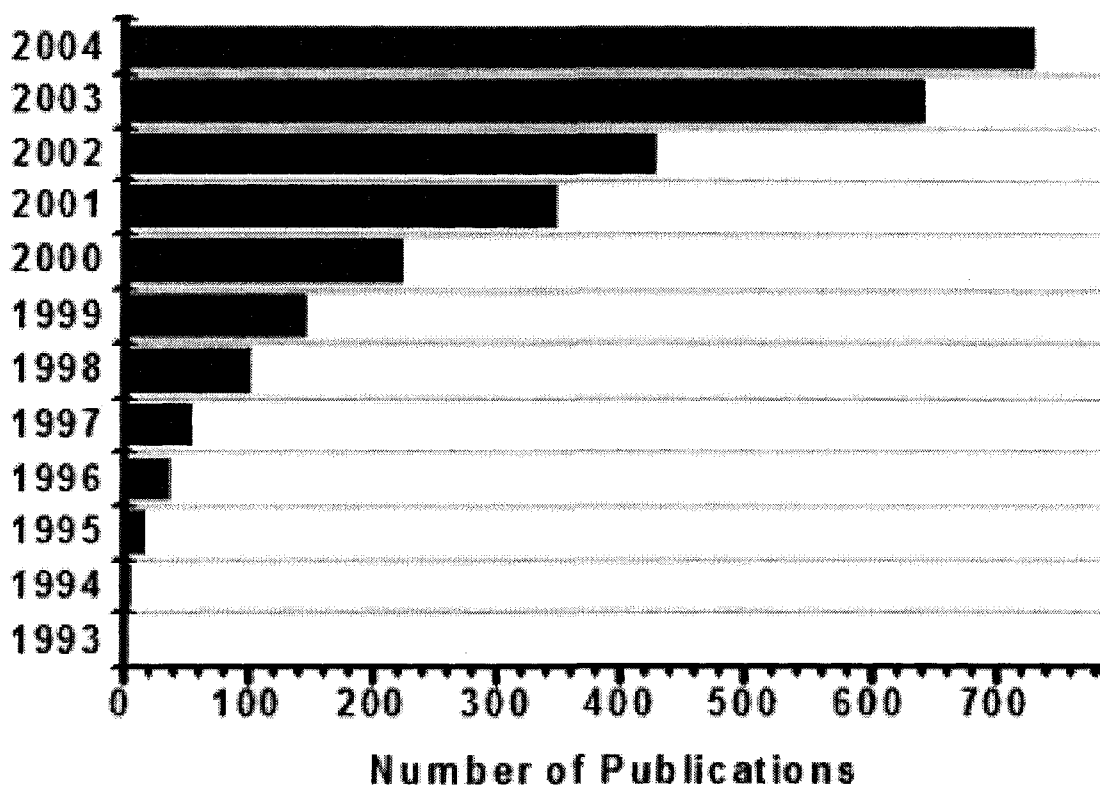


Fig.2.6 Statistics of the number of journal publications per year during the past decade in the area of catalysis with nanoparticles [18].

Chapter II: Literature review: Characteristics, properties, applications and preparation of transition metal, Si and Ge nanoparticles

Since nano-metals have a large surface-to-volume ratio compared to bulk materials, they are attractive to use as catalysts in fuel cells and organic chemical synthesis. The field of nanocatalysis (the use of nanoparticles to catalyze reactions) has undergone an explosive growth during the past decade. The number of journal publications that have been published in the area of catalysis with nanoparticles for each year in the past decade are listed in Fig.2.6 [18], which shows that catalysis with nanoparticles is a growing field of research.

2.4.1.1 Ni nanoparticles

Nano-nickel has very high catalytic activity, and is physically and chemically robust. There is a large potential market for nano-nickel in the chemical processing industry. Nickel catalysts, in general, are active for the hydrogenolysis of carbonyl and carbon-carbon bonds [19].

Ni nanoparticles have been used as Raney catalysts for unsaturated vegetable oils to margarine and other food products for more than 80 years [1]. The main constituents of these vegetable oils are glycerol ester of various un-saturated fatty acids, especially C₁₆ and C₁₈ acids. The main process requirement is the hydrogenation of some olefinic bonds, not all, together with some isomerization and olefinic bond migration along the carbon chain. Batch processes at 150–200°C with 10–70 bar hydrogen are widely used. The necessary selectivity is achieved by high surface area (50–100m²g⁻¹) nickel catalysts (unsupported or on a silica support) and appropriate process control.

Methane as the major component of natural gas is being widely used as an energy source and in the production of fine chemicals. Ni metal is considered as an excellent catalyst for

Chapter II: Literature review: Characteristics, properties, applications and preparation of transition metal, Si and Ge nanoparticles

CH₄ dissociation [20]. The dissociation of CH₄ can be further used to prepare highly pure hydrogen, carbon nanotubes and carbon fibers with special properties [20].

Several companies are experimenting with the material in fuel-cell catalytic membranes, using particle sizes of 10–15nm diameter. Because nickel atoms are about a third of a nanometre across, these near-spherical particles are about 30atoms across and contain about 3500 atoms — a remarkably low number. This provides very high catalytic activity, and is sufficient for most applications. Nano-nickel could replace a significant portion of the platinum catalyst market, and sales were expected to be \$500m–\$1bn in five years [21-24].

Ni nanoparticles with a high surface area can also be used as catalysts for ketone and aldehyde reduction [25], ethylene cracking [26], steam reforming of methanol [27], hydrothermal gasification of organic compounds [28], emission control in diesel vehicles [29], and for the thermal decomposition of ammonium perchlorate (AP) in composite propellants [30].

2.4.1.2 Cu nanoparticles

The water-gas shift (WGS) process at high temperatures (Reaction 2-1) is used for the conversion of carbon monoxide to hydrogen in ammonia synthesis plants.



The process is usually followed by a second stage of low-temperature water-gas shift reaction (LTWGS). The LTWGS process is typically operated at 200–230°C. The catalyst for the second, low-temperature stage (LTWGS) is nanosize copper, usually supported by copper/zinc oxide/alumina substrate [1].

Chapter II: Literature review: Characteristics, properties, applications and preparation of transition metal, Si and Ge nanoparticles

Nano-copper catalysts are highly effective catalysts for methanol synthesis [31-33]. The methanol synthesis reaction is written as follows



Nano-copper catalysts are also being used as a catalyst for the synthesis of dimethyl carbonate ((CH₃O)₂CO) [34]. Dimethyl carbonate is an important chemical in the current chemical industry because it can substitute for highly toxic compounds such as phosgene and dimethyl sulfate in many reactions. The by-product when dimethyl carbonate is used is methanol or carbon dioxide, which is easily separated from the product and leads to less pollution.



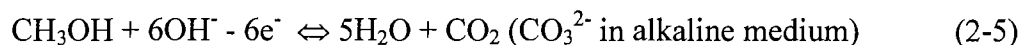
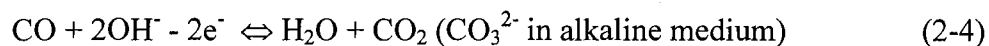
Cu nanoparticles have been also widely used as catalysts for the synthesis of symmetrical and unsymmetrical biaryls and polyaryls [35] and for the higher alcohol synthesis from syngas [36].

2.4.1.3 Au nanoparticles

Gold, one of the most stable metals, is typically chemically inert including a resistance to oxidation. However, Au nanoparticles, in particular supported on very active oxides such as Co₃O₄, Fe₂O₃, and TiO₂, exhibit a significant catalysis for various reactions [37-39]. The gold clusters impregnated by Mn, Fe, Co, Ni, Cu, or Cu hydroxides have been found to have a catalytic activity in CO oxidation at sub ambient temperatures (below 0°C and even at -70°C) [40-42]. It has been suggested that a synergistic mechanism occurs at the Au nanoparticles/metal oxide interface, with the oxide support being part of the catalytic process. Adsorption of CO would proceed on the Au nanoparticles on a site adjacent to a

Chapter II: Literature review: Characteristics, properties, applications and preparation of transition metal, Si and Ge nanoparticles

metal oxide site occupied by an adsorbed O₂ molecule. The reaction would involve an intermediate carbonate-like species decomposing to CO₂ upon desorption from the surface. Alkanethiolate-Au nanoparticles, precipitated onto a glassy carbon electrode by cross-linking the Au nanoparticles with 9-nonanedithiol and leading to a 3D network thin film, exhibited pronounced catalysis in the electro-oxidation of CO [43] and CH₃OH [44-46].



Gold nanoparticles are one of the most effective catalysts yet identified for remediation of one of the nation's most pervasive and troublesome groundwater pollutants, trichloroethylene (TCE). TCE, which is commonly used as a solvent to degrease metals and electronic parts, is one of the most common and poisonous organic pollutants in groundwater. It is found at 60 percent of the contaminated waste sites on the US Superfund National Priorities List, is considered one of the most hazardous chemicals at these sites because of its prevalence and its toxicity [47]. Human exposure to TCE has been linked to liver damage, impaired pregnancies and cancer. The catalyst containing Au and Pd converts TCE directly into non-toxic ethane. By contrast, breaking down TCE with more common catalysts, like iron, produces intermediate chemicals, such as vinyl chloride, that is more toxic than TCE [47-48].

Au nanoparticles under high dispersion are highly active catalysts for NO reduction [49], water-gas shift reaction [50], and CO₂ hydrogenation [51].

Besides Ni, Cu, Au nanoparticles, Ag nanoparticles can also be used as catalysts for oxidation of benzyl alcohol [52], and oxidation of methane [53]. In addition, Pt

Chapter II: Literature review: Characteristics, properties, applications and preparation of transition metal, Si and Ge nanoparticles

nanoparticles can be used as catalysts for formation of water at room temperature [54], and in fuel cell [55,56].

2.4.1.4 Photochemistry on metal nanoparticles

It is well known that a well-defined Fermi edge develops in transition metal or semiconductor nanoparticles containing several thousands of atoms, which separates occupied and unoccupied electronic states (see Section 2.1.2). Thus, the electrons below the Fermi level of a metal nanoparticle can be excited by absorption of photons and form electron-hole (e-h) pairs. A transient thermal e-h distribution develops rapidly by electron-electron scattering. A quasithermal distribution describable by a distinct electron temperature is reached, which is much higher than the lattice temperature. Then, the resultant thermal hot electron distribution cools down further by electron-phonon interactions. The dynamics depends on the excitation density. The dynamics of the hot electrons photo-generated in the metal nanoparticles, play a crucial role in determining the dynamics of chemical reactions on their surfaces if these hot electrons trigger the chemical processes in the adsorbents [57,58].

In addition, metal nanoparticles strongly exhibit the size- and shape-dependent collective electronic excitation called Mie plasmon, which leads to strong field enhancement around the particles. As a result, a large increase of absorption is generated in all photo-induced effects [58].

To induce photochemistry, *i.e.*, to convert electronic excitation energy into energy of nuclear motion, an optical excitation has to bring the molecule concerned to a potential-energy curve with large slope in the Franck-Condon region, so that the atoms can be accelerated along it. The simplest process usually considered is desorption of an

Chapter II: Literature review: Characteristics, properties, applications and preparation of transition metal, Si and Ge nanoparticles

adsorbate or a fragment of it; in a photochemical reaction this may be the starting step.

On metal and semiconductor surfaces electronically excited adsorbents are deexcited very rapidly, which strongly modifies the desorption probability compared to dissociation of a similar free molecule. The bond to be broken can be that between the adsorbate and the substrate or an internal bond of the adsorbed molecule; neutral or charged molecular and atomic fragments can then leave the surface, and fragments can also stay adsorbed [53].

Methane physisorbed on Pt (111), Pd (111), and Cu (111) surfaces is readily dissociated into methyl and hydrogen by irradiation with a 193 nm (6.42eV) Ar laser. On Cu (111), methane photo dissociation leads to ethylene formation. These observations are surprising because light absorption in gaseous methane does not occur at wave lengths above 145nm (8.55eV). The peculiarity of the methane/transition-metal systems consists of the fact that methane on these surfaces is excited by a direct electronic transition localized within the adsorbate-substrate complex [59, 60].

The excited state responsible for dissociation to CH_3+H is formed from mixing of an antibonding Rydberg state of methane, localized 10eV above the HOMO of gas phase methane, and unoccupied states of the metal. The excitation energy depends strongly on the cluster size because electron redistribution over the metal cluster plays an important role in stabilizing this charge transfer state [61, 62].

2.4.2 Magnetic Fluids

Magnetic fluids, or ferrofluids, are stable suspensions of colloidal ferromagnetic particles (e.g. magnetite) in suitable, non-magnetic carrier liquids. The materials used are Fe, Co, Ni, and Fe_3O_4 with particle sizes of around 10nm. The colloidal particles are covered with surfactants in order to prevent agglomeration due to attractive Van der Waals forces. Due

Chapter II: Literature review: Characteristics, properties, applications and preparation of transition metal, Si and Ge nanoparticles

to their small size, the colloidal particles can be considered as ferromagnetic monodomain particles [63]. Since the colloidal particles contain several 1.000 atomic magnetic moments, the magnetic fluids, are often referred to as superparamagnets. Ni nanoparticles exhibited a superparamagnetic behaviour above the blocking temperature as mentioned in Section 2.2.3.

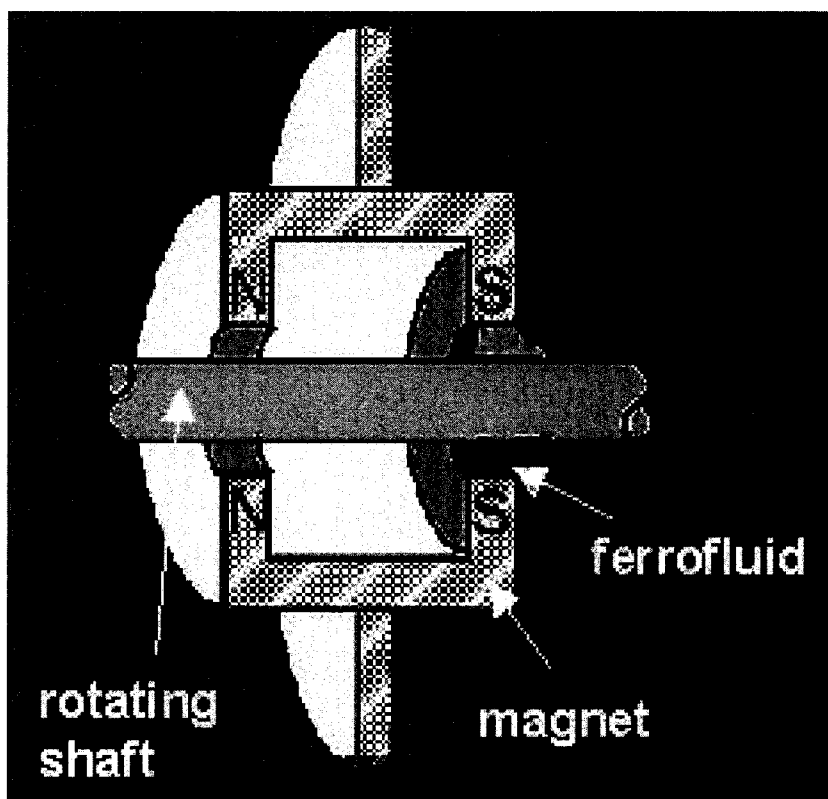


Fig.2.7 Schematic diagram of a magnetic fluid seal [63].

Conventional ferrofluid applications use DC magnetic fields from permanent magnets for use as a liquid O-ring in rotary (see Fig.2.7) and exclusion seals; almost every computer disk drive uses a magnetic fluid rotary seal for contaminant exclusion and the semiconductor industry use silicon crystal growing furnaces that employ ferrofluid rotary

Chapter II: Literature review: Characteristics, properties, applications and preparation of transition metal, Si and Ge nanoparticles

shaft seals. In addition, magnetic fluid can be used as dampers in stepper motors and shock absorbers, and for heat transfer in loud speakers [63].

2.4.3 Memories

A flash cell in memories is a floating gate metal oxide semiconductor (MOS) transistor where charge from the channel can be injected or extracted. This requires isolation of the floating gate by thin dielectrics that allow the charge to travel in and out the floating gate through suitable polarization of the MOS device electrodes. The dielectric that isolates the floating gate from the channel is usually SiO_2 . It has a thickness of 7 – 10nm and it is called a tunnel oxide since Fowler–Nordheim tunnelling occurs through it. However, further scaling of the memory is limited by the device structure because of storage node capacitive coupling and tunnelling oxide scaling limitation [64, 65].

A conventional MOSFET (metal oxide semiconductor field effect transistor) will no longer be able to control the flow of the electrons as its size reaches the sub-50nm regime. The quantum mechanical probability will gradually dominate in the nanometer size regime and cause errors in electronic data storage and manipulation as mentioned in Section 2.1.2.

As an alternative of the conductive floating gate node, the conventional polysilicon floating gate is replaced by a dense array of silicon nanocrystals embedded in the gate oxide as shown in Fig.2.8a, where, CO represents the control oxide (oxide between nanocrystal layer and gate), and TO represents the tunnelling oxide (oxide between nanocrystal layer and channel). Because of the discontinuous nature of the floating gate these approaches allow for thinner tunnel oxide and consequently more aggressive scaling of the flash memory. The resistance of metal nanoparticles caused by scattering at their

Chapter II: Literature review: Characteristics, properties, applications and preparation of transition metal, Si and Ge nanoparticles

surface and the extremely small capacitance of isolated nanoclusters or nanocrystals due to the size confinement can give rise to an appreciable charging energy when a single electron is transferred to the cluster [66].

In nanocrystal memories, a localized single leakage path due to a defect in the tunnelling oxide can only discharge one nanocrystal or a small number of nanocrystals thus allowing for the use of thinner insulators. Performance benefits expected from this change in the floating gate structure include improved retention times and improved radiation hardness due to decreased sensitivity to localized oxide leakage paths as well as improved prospects for CMOS integration due to reduce device aspect ratios [67-70].

Ge has a higher electron affinity than Si. Thus, the minimum of the conduction band of Ge nanocrystals is lower than the minimum of the conduction band of the Si channel of the MOS memory device. This allows for the same programming voltages but for better retention characteristics for Ge nanocrystals since the back tunnelling probability from the NC to the channel is considerably reduced. Therefore, Ge nanocrystals are more attractive than Si nanocrystals [71].

In principle, the memories built upon metal nanoparticles (see Fig.2.8b) should present advantages over silicon nanocrystal memories. The higher electron affinity of metals as compared with Si allows for engineering the potential well of the storage nodes in order to create an asymmetric barrier between the Si channel and the storage nodes. This form of the barrier makes the write operation easier creating a higher energy barrier to the other direction for the electron that favours retention characteristics [71].

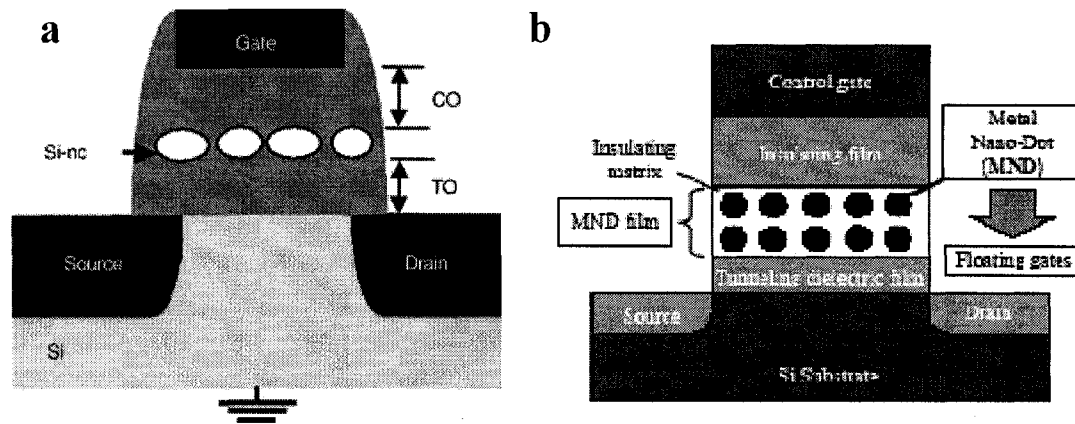


Fig.2.8 A schematic diagram of a nanocrystal memory device with nanocrystals formed in a 2D layer. (a) Si nanocrystals [66], and (b) Metal nanoparticles [71].

2.4.4 Displays

In general, silicon is an inefficient light emitter, but the nanocrystalline silicon particles emit high intensity visible light. Depending on the size of the nanocrystalline particles, the nanocrystalline silicon particles emit different light colors such as red, green, or blue by the electron confinement. Fig.2.9 shows emission from blue, green, and red colloidal crystals in top row according to magic sizes of 1.0, 1.67, and 2.9nm diameters when these crystals are illuminated by light from a mercury lamp. The background is due to a weak bright field. The colloids of the magic family 1.0, 1.67, 2.15, and 2.9nm in diameter from right to left in bottom row exhibit different colours under excitation using a commercial low intensity UV source with an average wave length of 365nm [72]

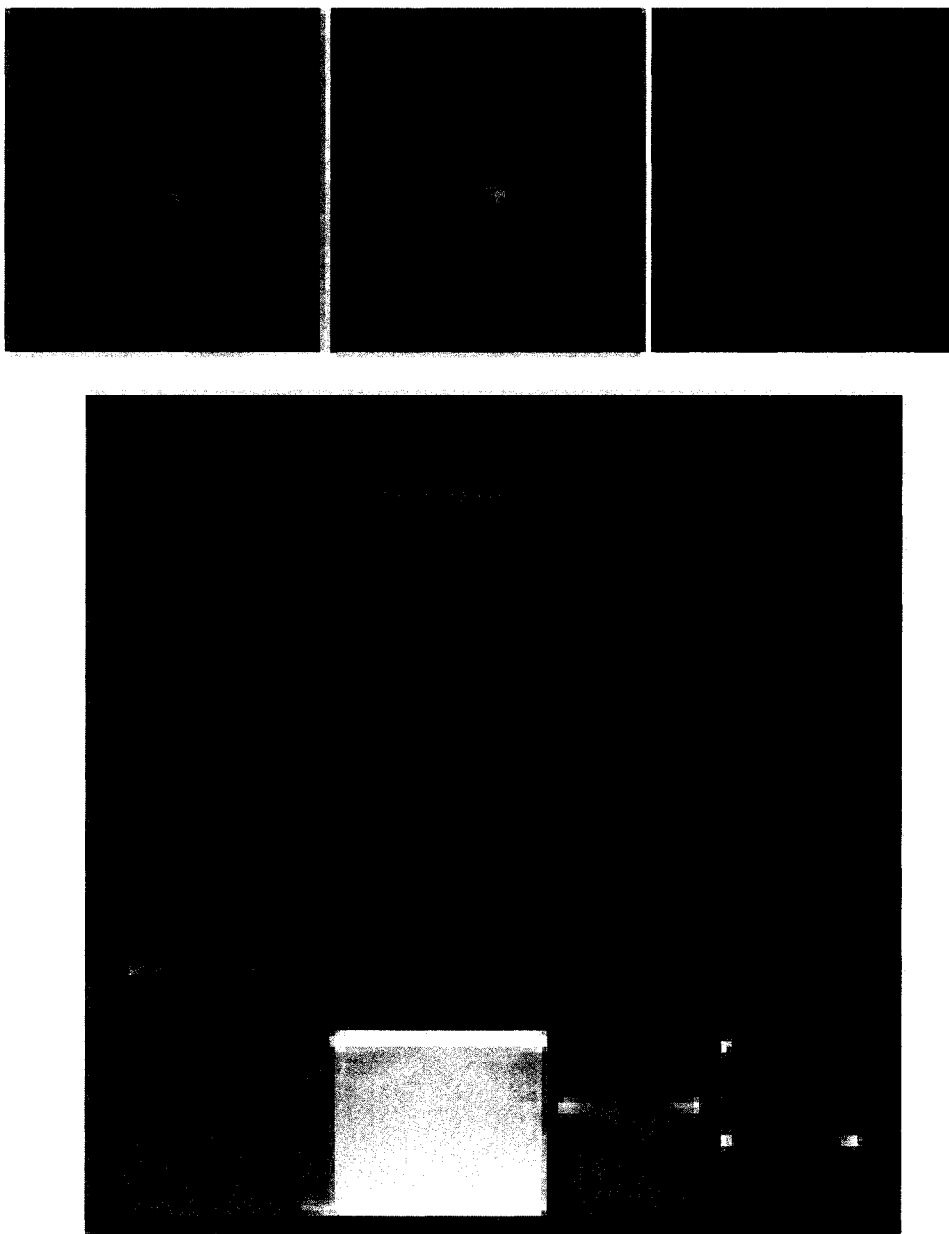


Fig.2.9 Emission from blue, green, and red colloidal crystals segregated according to magic sizes of 1.0, 1.67, and 2.9nm diameters (Top row) and emission of colloids of four members of the magic family 1.0, 1.67, 2.15, and 2.9nm in diameter under excitation using a commercial low intensity UV source with an average wave length of 365nm (Bottom, right to left) [72].

Chapter II: Literature review: Characteristics, properties, applications and preparation of transition metal, Si and Ge nanoparticles

Electrically driven emission of light from semiconductors is the basis of tiny light-emitting diodes (see Fig.2.10) and lasers (see Fig.2.11). Traditional semiconductor LEDs are formed from p-type and n-type semiconductors, which donate positively charged 'holes' and negatively charged electrons, respectively, when a voltage is applied across the structure. Recombination of an electron and hole, within the semiconductor, produces a photon and leads to the emission of light. If the efficiency of light emission is high enough and the whole structure is placed between two highly reflective mirrors, the LED can be turned into a miniature laser. Pavesi, *et al* [72], have demonstrated good optical emission from a layer of silicon nanocrystals stimulated by pulses of ultraviolet light (not electrons). Now the challenge is to electrically stimulate these nanocrystals into producing LED or a beam of laser light [73].

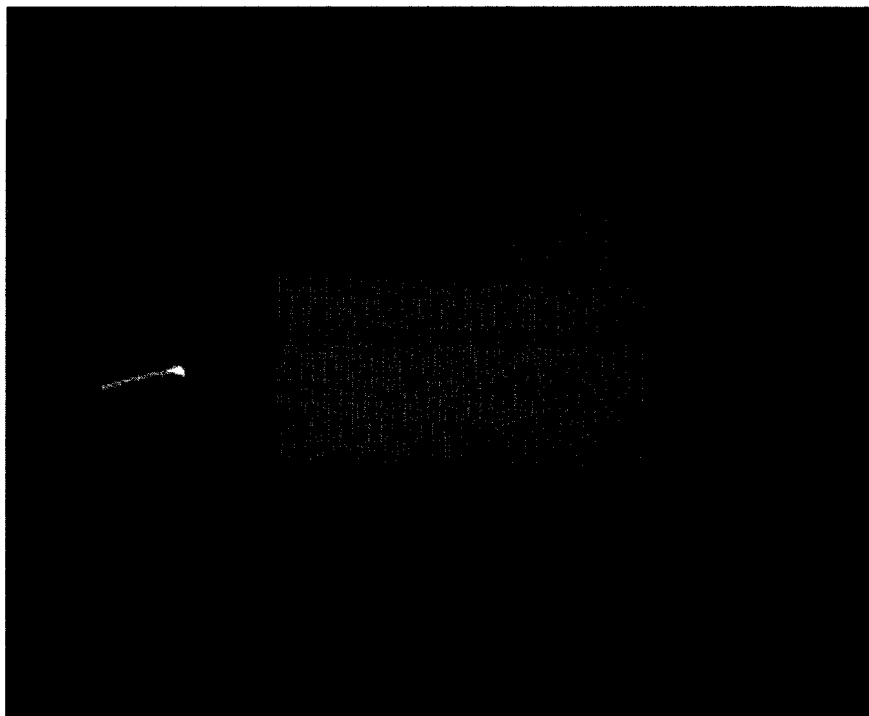


Fig.2.10 A monochromatic 32-by-64-pixel prototype quantum dot LED [74].

Chapter II: Literature review: Characteristics, properties, applications and preparation of transition metal, Si and Ge nanoparticles

In addition, the “light bulbs” built by Si nanocrystals, are expected to last 100 times longer than current incandescent light bulbs, and be 10 times more efficient.

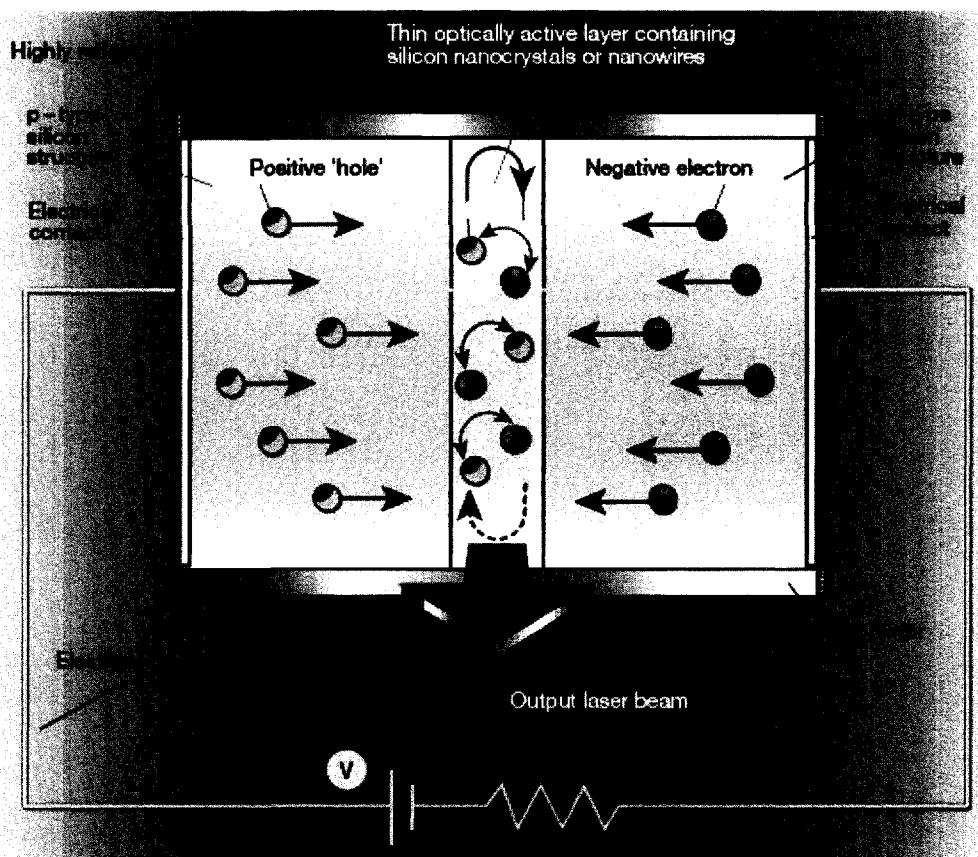


Fig.2.11 A schematic illustration of Si nanocrystal laser [8].

2.4.5 Sensors

A variety of biosensors for detection, diagnosis and monitoring diseases, drug discovery, proteomics, and environment pollutants are being developed. A biosensor derives from the coupling of a ligand-receptor binding reaction to a signal transducer, which could be developed by these methods including optical, radioactive, electrochemical, piezoelectric, micromechanical, and mass spectrometric [75].

Chapter II: Literature review: Characteristics, properties, applications and preparation of transition metal, Si and Ge nanoparticles

Metal nanoparticles have excellent conductivity and catalytic properties, which make them suitable for acting as “electronic wires” to enhance the electron transfer between redox centers in proteins and electrode surfaces, and as catalysts to increase electrochemical reactions. Many kinds of transition metal nanoparticles and their oxide nanoparticles have been widely used in electro-chemical sensors and biosensors [75-77].

Among the nanoparticles, gold nanoparticles are probably the most frequently used. Conjugates of Au nanoparticles-oligonucleotides have been applied to biosensors for the programmability of DNA base-pairing to organize nanocrystals in space and the multiple ways of providing a signature for the detection of precise DNA sequences, which have many potential applications in the fields of biosensors, disease diagnosis, and gene expression [78]. The principle is shown in Fig.2.12

Biosensors for immunoassays in human serum using Au nanoparticles have been developed, in which the recognition of proteins for diagnostics is based on the interaction between Au nanoparticles-antibody conjugates and their antigens. This classic type of immunoassay allows the evaluation of Au nanoparticle tags in a standard mode of antigen detection [79-81].

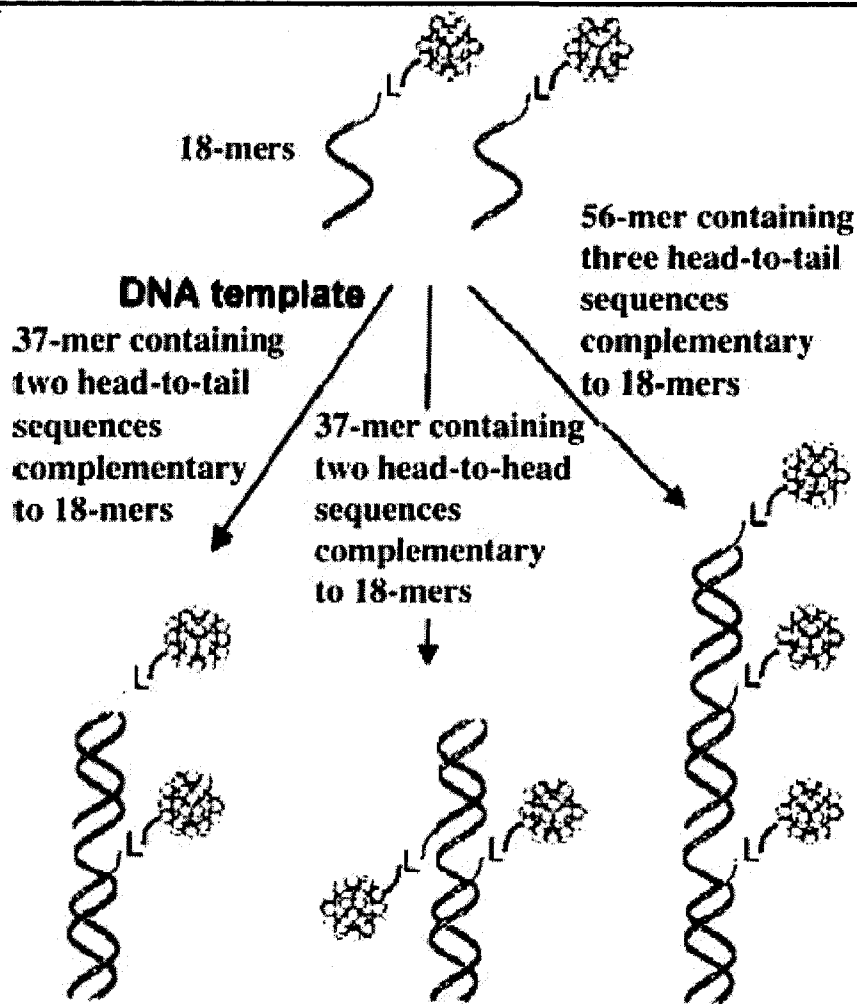


Fig.2.12 Preparation of "nanocrystal molecules" consisting of two or three DNA modified Au particles attached to a complementary DNA template, using phosphine-stabilized 1.40nm Au nanoparticles modified with a single thiol-capped oligonucleotide and two different DNA template lengths and sequences [78].

2.5.6 Nano-inks

The conventional method for forming fine patterns of 10 μ m or less line widths involved vacuum sputtering or evaporation and photolithographic etching. Use of these techniques allows the formation of uniform thin films and accurate fine-line patterns, but also

Chapter II: Literature review: Characteristics, properties, applications and preparation of transition metal, Si and Ge nanoparticles

requires use of expensive vacuum deposition equipment. However, with the development of large-size flat panel displays including LCDs in recent years, there is a growing need for the development of an alternative low-cost technology that does not make use of the vacuum evaporation/sputtering process. Hence, nano-metal inks have been developed to meet the need. In general, nano-metal inks contain metal (Ag, Cu and Ni) nanoparticles whose diameters are 30 nm or less [82-84].

Ultra fine wiring patterns with a few microns width are directly printed on a given substrate and are then fired at high temperatures. The technology is considered a crucial factor in the development of surface mounting technology, and will lead to further miniaturization of electronic devices, whose development and manufacturing demands will be sharply increased. Fig.2.13 shows three examples of the fine pattern having a line width of 3 μ m formed on a substrate.

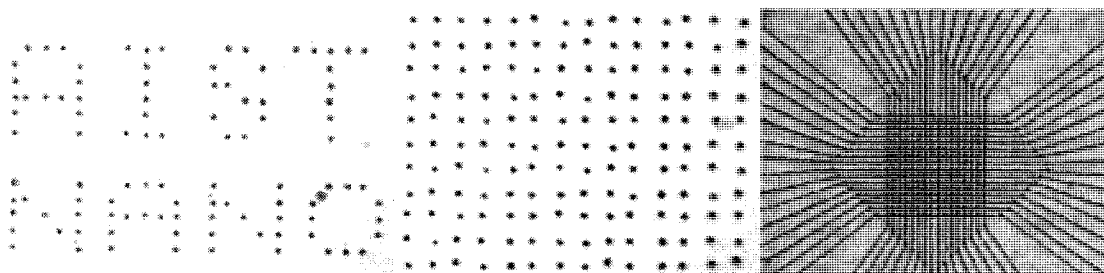


Fig.2.13 The fine patterns with a line width of 3 μ m printed on a substrate using nano-inks (a). An example of fine characters using sub- μ m dots. (dot pitch 3 μ m); (b). An example of fine lattice pattern using sub- μ m dots. (dot pitch 3 μ m); and (c), Fine circuit of conducting polymer. (line width 3 μ m, 10 μ m pitches at lattice area) [82].

Chapter II: Literature review: Characteristics, properties, applications and preparation of transition metal, Si and Ge nanoparticles

There are some applications of nanoparticles in other fields. For example, Ni nanoparticles have some potential applications in magnetic drug delivery [85,86], magnetic and fluorescent tags in biology [87], hypothermic cancer therapy [88], and contrast agents in magnetic resonance imaging [89, 90]. Ag nanoparticles have been widely used as antibacterial and anti-fungal agents [91]. Pt nanoparticles can be applied in medical diagnosis and therapy [92].

The potential applications of Ni, Cu, Ag, Au, Pt, Si and Ge nanoparticles, which has been synthesized in work for this dissertation, are summarized in Table 2.1.

Chapter II: Literature review: Characteristics, properties, applications and preparation of transition metal, Si and Ge nanoparticles

Table 2.1 Potential applications of Ni, Cu, Ag, Au, Pt, Si and Ge nanoparticles.

	Applications
Ni	Catalysts for: oil hydrogenation [1], dissociation of CH ₄ [20], ketone and aldehyde reduction [25], ethylene cracking [26], steam reforming of methanol [27], hydrothermal gasification of organic compounds [28], emission control in diesel vehicles [29], for the thermal decomposition of ammonium perchlorate (AP) in the composite propellants [30]. synthesis of the carbon nanofibers and nanotubes [21-24]; Magnetic fluids for seal, dampers in stepper motors and shock absorbers, and heat transfer in loud speakers [58]; Nano-inks [82-83]; magnetic drug delivery [85,86]; magnetic and fluorescent tags in biology [87]; hypothermic cancer therapy [88]; contrast agents in magnetic resonance imaging [89,90].
Cu	Catalysts for: water-gas shift (WGS) reaction [1], methanol synthesis [31-33], synthesis of dimethyl carbonate((CH ₃ O) ₂ CO) [34], symmetrical and unsymmetrical biaryls and polyaryls [35] and the higher alcohol synthesis from syngas [36], photochemical dissociation of methane [61]; hypothermic cancer therapy [88]; and nano metallic ink [83].
Au	Catalysts for oxidation of CO, H ₂ , alkanes, alkenes and CH ₃ OH [42-46], degradation of trichloroethylene [47-48], NO reduction [49], water-gas shift reaction [50], CO ₂ hydrogenation [51]; biosensors [75-77]; disease diagnosis [78]; and gene expression [79-81].
Ag	Catalysts for oxidation of benzyl alcohol [52], oxidation of methane [53]; nano metallic ink [79]; antibacterial and anti-fungal agents [91];
Pt	Catalysts for formation of water at room temperature [54]; fuel cell [55,56], photochemical dissociation of methane [59,60]; medical diagnosis and therapy [92].
Si	Memories [66-70]; Displays [74], lasers [8]
Ge	Memories [71]; lasers [8]

Chapter II: Literature review: Characteristics, properties, applications and preparation of transition metal, Si and Ge nanoparticles

2.5 Preparation methods

A variety of methods have been developed to synthesize transition metal or semiconductor nanoparticles. These methods essentially fall into two categories: chemical and physical methods.

2.5.1 Chemical methods

Among the chemical synthesis methods, transition metal or semiconductor nanoparticles have been conventionally prepared by chemical reduction of metal-salts [93-111], micro-emulsion [112-121], thermal decomposition [122-136], electrochemical methods [137-139], and rapid expansion of supercritical fluid solutions [140-142]. Of these methods, chemical synthesis in solution is favoured for fabricating nanoparticles because it allows the tailored design of materials at the molecular level, and also because it offers a cost-effective method of producing nanoparticles in large quantities. In addition, colloidal chemistry offers a possible route for the synthesis of a uniform dispersion of fine metallic particles by stabilizing the particles in the presence of a surfactant.

2.5.1.1 Conventional chemical reduction method

The chemical reduction of transition metal salts in solution is the most common and simplest method of generating colloidal transition metal nanocatalysts. Common reducing agents used are ethylene glycol alcohols, mainly ethanol and methanol [93, 94]. Ag nanowires have been prepared by the reduction of AgNO_3 with ethylene glycol [93]. In this reduction method, the alcohol acts both as a solvent and reducing agent and the reduction of the transition metal salt takes place when the solution is refluxed. The use of alcohols as a reducing agent results in a fast reduction of the precursor transition metal

Chapter II: Literature review: Characteristics, properties, applications and preparation of transition metal, Si and Ge nanoparticles

salt with colloid formation occurring quickly. In this reduction process, the precursor transition metal salts are reduced to form the transition metal nanoparticles, while the alcohols are oxidized to form the corresponding carbonyl compound. There have been many studies conducted on how the size of the transition metal colloids is dependent on the structure and quantity of alcohol used to reduce the precursor transition metal salt. It has also been shown that in the case of the formation of platinum, palladium, and rhodium nanoparticles in colloidal solution that the higher the boiling point of the alcohol used as the reducing agent, the smaller the size of the nanoparticles formed.

Sodium borohydride reduction is another common method of preparing transition metal and semiconductor nanoparticles. This method of reduction is generally fast with colloid formation occurring quickly after the addition of sodium borohydride. Sodium borohydride reduction has been used to synthesize Ni [94], Cu [95] Ag [96,97], and Au [98]. The as-produced Cu nanoparticles prepared by using NaBH_4 are 1-2nm in diameter and spherical in shape [95]. Thiol-derivatised cubic Ag nanoparticles were prepared by adding an AgNO_3 solution containing a trace amount of alkanethiol into a solution of NaBH_4 and sodium oleate [96]. Gold nanowires with an aspect ratios of up to 200 can be obtained through seeding by 4nm gold nanoparticles, then modifying by CATB [99]. A number of structural architectures, from rod-, rectangle-, hexagon-, cube-, triangle-, and star-like outlines to branched Au nanoparticles have been achieved in the presence of CATB. The formation of various shapes is likely the outcome of the interplay between the faceting tendency of the stabilizing agent and the growth kinetics [100]

Some other reducing agents such as hydrazine, NaH_2PO_2 and sodium citrate have been used to synthesize metal nanoparticles in a solution that involved the chemical reduction of the precursor transition metal salt. Hydrazine has been used to synthesize Ni

Chapter II: Literature review: Characteristics, properties, applications and preparation of transition metal, Si and Ge nanoparticles

[101,102], Ag [103], and Pt/Ag [104]. The Ni nanoparticles prepared by using hydrazine had a mean size of 12 nm, and exhibited superparamagnetic properties [101,102]. Hexagonal silver nanoparticles have been obtained by the reduction of Ag_2SO_4 with $\text{N}_2\text{H}_4\cdot\text{H}_2\text{O}$ [103]. Sodium citrate has been used to synthesize Ag [104]. $\text{NaH}_2\text{PO}_2\cdot\text{H}_2\text{O}$ has been used to synthesize Ni nanobelts [105], and hollow Ni nanospheres [106]. In addition, Au, Ag, Pd and Pt nanoparticles have been synthesized by the reduction of their salts with potassium bitartrate ($\text{KHC}_4\text{H}_4\text{O}_6$) [107], glucose [108] and even Neem leaf broth [109] as the reductant.

Hydrogen gas [110] and carbon nanotubes [111] have also been used as reducing agents for the preparation of transition metal nanocatalysts. The hydrogen reduction method involves bubbling hydrogen gas into a solution containing the transition metal salt and colloidal nanoparticles are formed through a slow reduction process. Tetrahedral, cubic and truncated octahedral shaped platinum nanoparticles have all been formed by the hydrogen reduction method. Tetrahedral shaped nanoparticles, which are composed of (111) facets, are especially attractive for use as catalysts due to the large fraction of surface atoms that are present in the edges and corners [110]. Au, Pd, Pt, Ag and Cu nanoparticles and fibres were successfully synthesized by simple solid-state reaction between carbon nanotubes and their salts. However, such nanoparticles are rarely formed on other carbon substrates such as graphite or active carbon using the same synthesis process [111].

Synthesis of transition metal nanoparticles through chemical reduction can be enhanced by heating [112], radiolysis [113,114] and sonication [115,116].

Chapter II: Literature review: Characteristics, properties, applications and preparation of transition metal, Si and Ge nanoparticles

Chemical reduction synthesis of transition metal nanoparticles enhanced by heating is a simple and economical method. Platinum, palladium, silver and copper nanoparticles with a narrow size distribution have been synthesized by using the thermal reduction method [112]. The thermally derived copper show the presence of irregularly shaped particles (200-250nm) having sharp edges and facets [115].

The photochemical reduction method of synthesizing colloidal transition metal nanoparticles can be conducted in two ways: reduction of precursor transition metal salt by radiolytically produced reducing agents, or degradation of an organometallic complex by radiolysis. The radiolysis source could be x-ray, γ -ray, laser and ultraviolet light. Radiolysis of transition metal salts in aqueous solution produces solvated electrons that result from radiolysis, which reacts with molecules in solution to form new radicals that are able to reduce the transition metal salts.

It has been reported that the use of UV-visible radiation results in smaller and better dispersed transition metal nanoparticles [105]. Au, Ag nanoparticles or nanorods have been produced by irradiating an aqueous AgNO_3 solution with ultraviolet light in the presence of poly-(vinylalcohol) [105,113,114].

The radiolysis method permits continuous control of the concentration of the nanoparticles formed without the addition of reducing agents to the system.

Sonochemical reduction is another method of synthesizing colloidal transition metal nanoparticles. Sonication is an acoustic cavitation phenomenon that involves the formation, growth, and explosion of bubbles in liquid media. The sonochemical reduction method of precursor transition metal salts involves generation of the active species, reduction of the transition metal, and growth of the colloid in a sonicated liquid medium.

Chapter II: Literature review: Characteristics, properties, applications and preparation of transition metal, Si and Ge nanoparticles

These steps occur in different compartments: in the gas phase in the cavitation bubbles where high temperature and pressure allow water pyrolysis to form H and OH radicals; at the interface between the cavitation bubbles and the solution, and finally in the solution. The sonochemical reduction method has been applied for the generation of colloidal copper, platinum, palladium, gold, and silver nanoparticles [115,116]. The sonochemically derived copper powders show the presence of copper oxide (Cu_2O) contamination, and the porous aggregates (50-70nm) that contained an irregular network of small nanoparticles [115]. In the case of transition metal salts, the reduction process mainly takes place at the bubble/solution interface and in solution and does not take place in the gas phase due to the low vapour pressure of the precursor transition metal salts [116].

2.5.1.2 Micro-emulsion

Microemulsions are specially formulated heterophase systems in which stable nano droplets of one phase are well dispersed in a second, continuous phase (see Fig.2.14). Each of the nano droplets can be regarded as a nanoscopic, individual batch reactor, in which a whole variety of reactions and processes resulting in transition metal or semiconductor nanoparticles can be performed [117,118].

To create a stable emulsion of very small droplets, the droplets must be stabilized against molecular diffusion degradation (Ostwald ripening) and against coalescence by collisions. Stabilization of emulsions against coalescence can be obtained by the addition of appropriate surfactants, which provide either electrostatic or steric stabilization to the droplets.

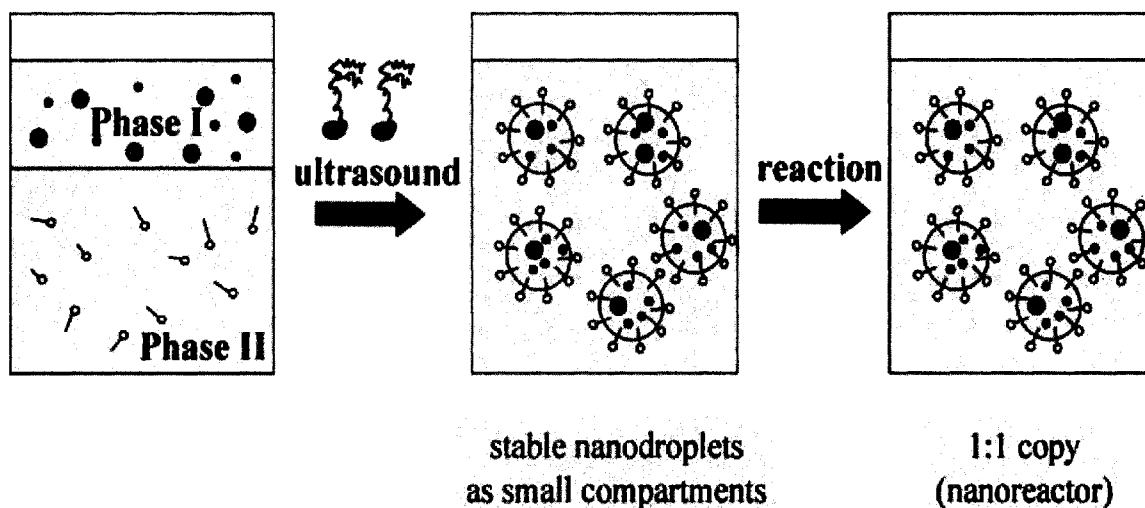


Fig. 2.14 Schematic illustration of the microemulsion process [118].

In direct (oil-in-water) microemulsions, the droplet size is determined by the amount of oil and water, oil density, oil solubility, and amount of surfactant. The droplets rapidly approach a pseudosteady state throughout the sonication process, because of constant fusion and fission processes. Au/Ag and Pt/Ag bimetallic nanoparticles have been synthesized in microemulsions of water/Aerosol OT/isooctane by the co-reduction of HAuCl_4 (or H_2PtCl_6) and AgNO_3 with hydrazine [119,120]

In inverse microemulsions, the osmotic pressure is built up by an agent that is insoluble in the continuous oily phase, a so-called lipophobe. Ionic compounds, *e.g.*, simple salts, show a low solubility in organic solvents and can be used as lipophobes in water-in-oil microemulsions. Fig.2.15 shows the differences between direct microemulsion and inverse microemulsion. Monodisperse nickel nanoparticles around 3.7nm have been prepared by inverse microemulsions through reduction of $\text{Ni}(\text{acac})_2$ (acac: acetyl-acetone)

Chapter II: Literature review: Characteristics, properties, applications and preparation of transition metal, Si and Ge nanoparticles

with sodium tetrahydridoborate in a mono-surfactant system, in which hexadecylamine (HDA) serves as stabilizer and solvent. The Ni nanoparticles have a mean size of 3.7nm, and show the characteristic of a superparamagnet with a blocking temperature of 12K [121]. Metastable Co nanorods and superlattices of Co nanocrystals have been obtained in a binary passivating ligand system. In these studies, oleic acid, alkylphosphine (oxide) or oleylamine was used as the stabilizer. Besides these ligands, long chain alkylamines can also be introduced to passivate the surface of nanoparticles [122,123]. Ge nanocubes have been prepared by a low-temperature inverse microemulsion using the surfactant heptaethylene glycol monododecyl ether as a capping agent [124]. Cylindrical copper metallic particles have been obtained when the synthesis is performed in cylindrical reverse micelles [125].

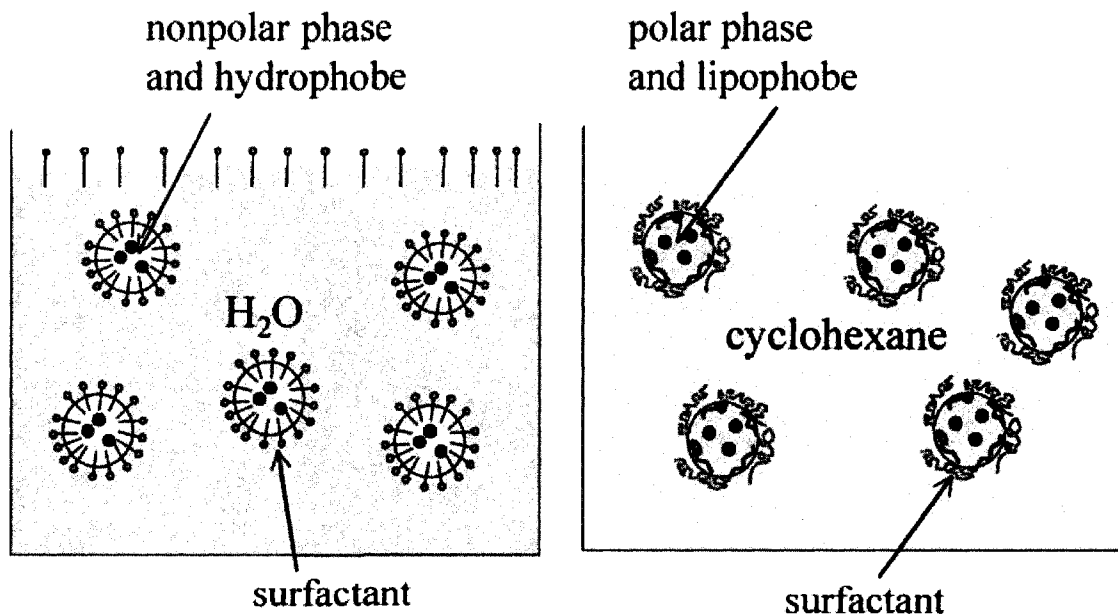


Fig.2.15 Comparison between direct (left) and inverse (right) microemulsion [127].

Chapter II: Literature review: Characteristics, properties, applications and preparation of transition metal, Si and Ge nanoparticles

CO₂ also can be used in the continuous phase for the formulation of inverse microemulsions [126]. The size of the Cu nanoparticles prepared in SF CO₂ was in the range 5-15 nm [126]. One of the problems of using water-in-oil microemulsions for nanoparticle synthesis is the separation and removal of solvent from products. Silver and copper nanoparticles have been also synthesized in sodium bis(2-ethylhexyl) sulfosuccinate (AOT) reverse micelles in compressed propane and supercritical ethane solutions [127].

2.5.1.3 Electrochemical method

An electrochemical method for preparing size-controlled transition metal nanoparticles in colloidal solution has been developed [128-130]. It is based on the dissolution of a metallic anode in an aprotic solvent, which consists of the electrolyte and the stabilizer. The precursor transition metal ions are reduced at the cathode to yield the colloidal transition metal nanoparticles. This method has been successfully used to synthesize nickel [128], copper [129] and cobalt nanoparticles [130]. The Cu nanoparticles prepared by direct electrochemical reduction from CuO nanoparticles had a size of around 100nm [129].

An advantage to this method of synthesizing transition metal nanoparticles is that the particle size can be controlled by the current density. When the current density is increased, smaller transition metal nanoparticles are produced.

2.5.1.4 Rapid expansion of supercritical fluid solutions

Supercritical fluids possess properties that are intermediate between liquids and gases. The rapid expansion of supercritical fluid solution (RESS) technique (see Fig.2.16) has

Chapter II: Literature review: Characteristics, properties, applications and preparation of transition metal, Si and Ge nanoparticles

been used in the production of polymer particles and fibres of narrow size distributions. In a classical rapid expansion into vacuum or air, the supercritical fluid solution is transferred rapidly to subcritical pressures. The “solution droplets” from the rapid expansion through a nozzle are extremely unstable, resulting in rapid solute precipitation. Because of the high velocity of the expanding supercritical fluid solution, the microscopic conditions at the end of the expansion nozzle are little affected by the receiving medium, air or liquid. Nanoscopic metal ion solute droplets produced in the RESS process may be chemically reduced in the receiving liquid solution to form Ni nanoparticles [131,132] and Ag [104, 133]. Ag nanoparticles with spherical or triangular shape, and nanowires have been produced without the use of surfactants [133].

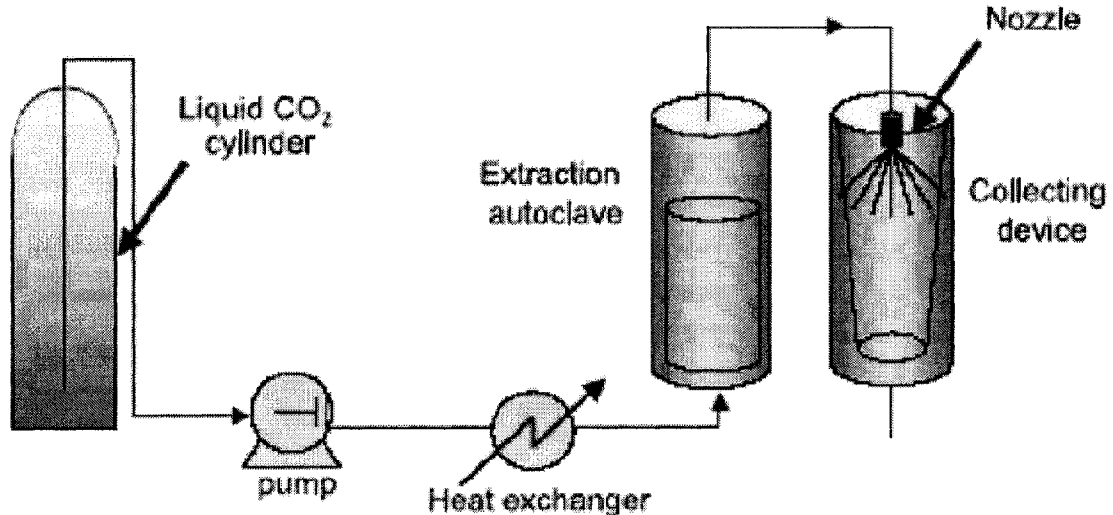


Fig.2.16 Schematic illustration of the RESS process [131]

H₂O, CO₂, CH₄, and Ar have been utilized as a media to prepare nanoparticles [134].

Chapter II: Literature review: Characteristics, properties, applications and preparation of transition metal, Si and Ge nanoparticles

Supercritical carbon dioxide (SFCO₂) has been extensively studied as a solvent for chemical synthesis. SFCO₂ offers several advantages over conventional organic solvents including (i) being one of the most environmentally friendly and low-cost solvents available, (ii) rapid separation of dissolved solute from the solvent by reduction of pressure, (iii) providing high diffusivity and thus accelerated reaction rates, (iv) enable solvent strength through manipulation of the density and thus providing some control of the solubility of solutes. The phase diagram and critical constants for the most commonly-used water and carbon dioxide are shown in Fig.2.17 [135].

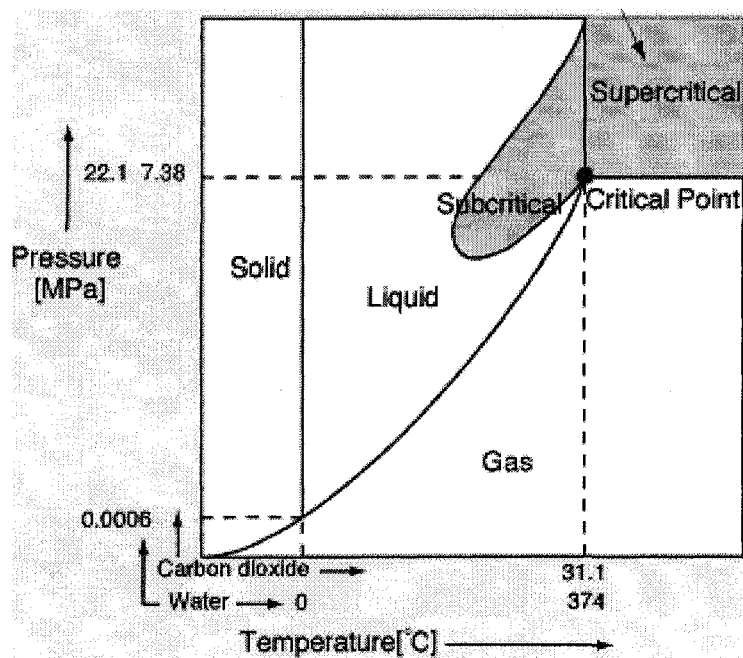


Fig.2.17 Phase diagram and critical constants for carbon dioxide and water [135].

The limiting property of super critical CO₂ is that this medium is only capable of dissolving nonpolar organic-based solutes. However, the addition of small amounts of a co-solvent such as acetone has been shown to significantly improve the solubility of

Chapter II: Literature review: Characteristics, properties, applications and preparation of transition metal, Si and Ge nanoparticles

relatively polar solutes. Recently, solubility of ionic compounds such as aqueous metal salts has been enhanced through inverse micelle formation using fluorinated surfactants. [136].

The disadvantages are that production costs are high and the equipment that is used is also fairly large due to the high pressure and the cost of pumping. In addition, the RESS method can cause aggregation of the particles during expansion, resulting in a wider size distribution.

2.5.1.5 Thermal decomposition

Many transition metal and semiconductor nanoparticles with different shapes have been synthesized by thermal decomposition of transition metal salts or the decomposition of the precursor organometallic salt. For thermal decomposition, a transition metal carbonyl has often been used as a precursor to generate the nanoparticles since it leads to particles displaying a clean and controllable surface and, in some cases, an adjustable size and shape [137-140]. However, the carbonyl is strongly toxic and relatively expensive. Therefore alternatives such as olefinic complexes [141], and transition metal acetate tetrahydrate salts [142] have been used. Olefinic complexes have been used as a source of metal atoms. Hydrogenation of the olefinic ligands into the corresponding, coordinatively inert alkanes yielded nanoparticles with non-contaminated surfaces [141].

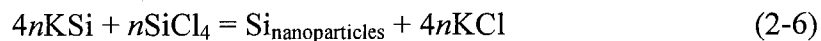
It is well known that covalent bonding is a dominant bonding in the semiconductor elements such as Si and Ge. A general trend for the formation of crystalline nuclei of semiconductor elements is that the more covalent the element, the higher is its crystallization temperature. Thus, amorphous phases would become more common as the material becomes more covalent when they are prepared at low temperatures. Hence, both

Chapter II: Literature review: Characteristics, properties, applications and preparation of transition metal, Si and Ge nanoparticles

high temperature and high pressure are generally required to obtain Si and Ge nanocrystals by a solution method. However, solution synthesis at those high temperatures pose a serious challenge since most organic solvents, including pentane and longer alkyl chains, are unstable.

For semiconductor Si and Ge nanocrystals, the most successful method is the gas-phase decomposition aided with heating [143], laser [144-146], microwave [147] and plasma [148].

CO₂-laser-induced decomposition of SiH₄ in a gas flow reactor has been shown to be very useful for the synthesis of large quantities of silicon nanoparticles [145,146]. In a typical reaction set-up, SiH₄ in an inert gas is exposed to focused radiation from a pulsed CO₂ laser in the reaction chamber resulting in the dissociation of the silane molecules by resonant laser absorption. The growth of the so-formed silicon nuclei is abruptly stopped as soon as they leave the hot chamber, and they are subsequently extracted from an adjacent high-vacuum chamber through a conical nozzle. The resulting nanoparticles have sizes that can be tuned in the 3–20nm range by varying the silane concentration and flow rate. Monodisperse, single crystal silicon nanoparticles have been achieved by using a SiH₄/H₂ mixture in a high density plasma [148]. Ge nanocrystals have been synthesized by thermal decomposition of diphenylgermane (DPG) and tetraethylgermane (TEG) at 400-550°C and 20.7MPa in a continuous flow reactor, which modified by Octanol [149]. Besides the gas-decomposition, a thermal co-decomposition of KSi and SiCl₄ (or KGe and GeCl₄) in a suitable solvent has been developed to synthesize Si and Ge nanocrystals [150,151]. The reaction for synthesis of Si nanocrystals can be written as follows:



Chapter II: Literature review: Characteristics, properties, applications and preparation of transition metal, Si and Ge nanoparticles

The synthesis of silicon and germanium nanoparticles from reactions involving alkyl semiconductor halides or metal silicides/germanides in solution to find mild conditions, higher yields, and better surface manipulation, which are necessary requirements for the production of nanoparticles on a large scale.

The wet chemical methods offer a simple method of producing nanoparticles and allow the tailored design of materials at the molecular level. However, subsequent washing, filtering, and drying processes lead to significant agglomeration of the final powder. Major advantages of gas thermal decomposition are that: it does not require a drying process; it is easy to obtain crystalline powders of the desired phase without calcination and grain growth; the possibility of scaling up the device for higher production rates; and the applicability of measurement techniques for an online determination of particle sizes. However, thermal decomposition presents difficulties in modifying the shape and size and manipulating the surface of nanoparticles. In addition, the surface of as-prepared nanoparticles is sometimes contaminated by the byproduct of thermal decomposition.

2.5.2 Physical methods

Physical methods comprising thermal evaporation, magnetron sputtering, laser ablation and sonication have been successfully developed to prepare transition metal, Si and Ge nanoparticles.

2.5.2.1 Thermal evaporation

The thermal evaporation method involves the evaporation of relatively volatile transition metals at reduced pressure and a subsequent co-condensation of these transition metals at a low temperature with or without the vapors of organic salts [11, 152]. Approximately

Chapter II: Literature review: Characteristics, properties, applications and preparation of transition metal, Si and Ge nanoparticles

1nm size gold nanoparticles have been obtained by a thermal evaporation method (at a processing condition of 133Pa at 1124°C) [152]. The colloidal Au nanoparticles were stable for several months, but a limitation of this method is that there is no precise control of the size of the nanoparticles. This is a major limitation in terms of applications in catalysis since control of size of the nanoparticles is necessary to conduct reproducible catalytic reactions. Silicon nanoparticles with diameters ranging from 3 to 50 nm were prepared by thermal evaporation of Si chips [11]. The Si nanocrystals showed visible light emissions from 5000 Å to 9000 Å, with peak intensity at 8000-8200 Å [11]. Cu nano-rods have been prepared by thermal vapour deposition in vacuum [153].

2.5.2.2 Magnetron sputtering

Magnetron sputtering offers greater freedom with many of the processing variables, which then allows one to control the resulting nanoparticle microstructures including size, shape and phase, and then determines the characteristics of the end product. Transition metals *e.g.* Co [154], and semiconductors *e.g.* Si nanoparticles [155,156], have been achieved by this method. A broad luminescence band in the red region was observed from Si-doped SiO₂ thin films deposited by co-sputtering of Si and SiO₂ on p-type Si (100) substrates, annealed in an Ar and O₂ atmosphere [155]. The cost for producing nanoparticles using this method is relatively high.

2.5.2.3 Laser ablation

In the laser ablation technique, the nanoparticles are generated by irradiation of a solid target of by a focused laser beam in a reactor chamber under inert atmosphere where

Chapter II: Literature review: Characteristics, properties, applications and preparation of transition metal, Si and Ge nanoparticles

temperature, pressure, and residence time can be accurately controlled, followed by deposition on a hard, cold substrate.

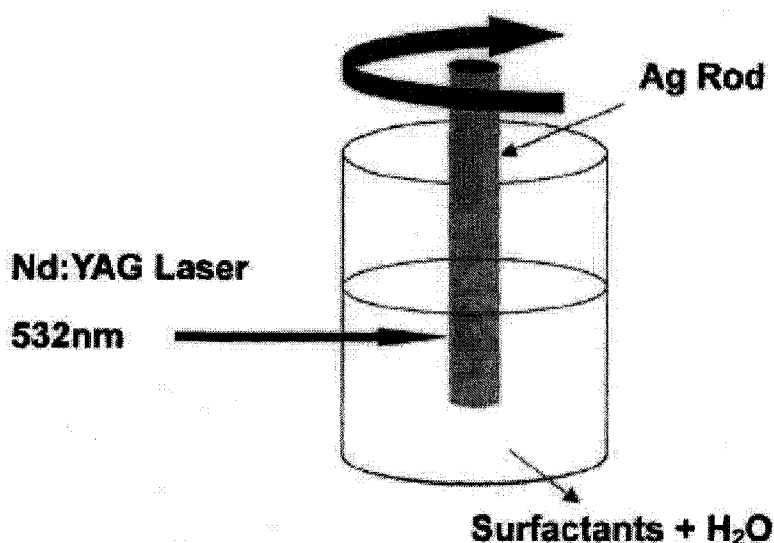


Fig. 2.18 Schematic illustration of the laser ablation process [157].

The laser ablation method has been further developed in a liquid solution, which was introduced by Fojtik *et al* [157], as a novel method of metal nanoparticle preparation. With pulsed laser beam irradiation, chemically pure element nanoparticles are formed by continuously ablating a bulk target immersed in a solution as shown in Fig.2.18. The fabrication rate and morphology of the nanoparticles are dependent upon laser wave length, pulse energy, absorption of laser energy by the liquid environment and ablation time. Co [158, 159], Ag [160-162], Si [163] and Ge [164] nanoparticles have been produced by the laser ablation method. Well monodispersed Ag colloids could be prepared using the laser ablation technique with the aid of surfactants [161]. The Si

Chapter II: Literature review: Characteristics, properties, applications and preparation of transition metal, Si and Ge nanoparticles

nanoparticles prepared by a laser ablation method exhibited bright photoluminescence in the visible wavelength range [163].

The nanoparticles formed in this way usually suffer from inhomogeneous particle sizes and aggregation. It has been clearly shown that the interaction between the pulsed laser and metal particles leads to severe particle aggregation and a broad size distribution via the melting/fragmentation processes [162].

2.5.2.4 Sonication

Ultrasonic synthesis involves the electrochemical etching of a silicon wafer to form porous silicon that can be dispersed in a variety of solvents by suspension in an ultrasonic cleaning bath for a determined period of time [72,165]. Si nanocrystals in diameters of 1.0, 1.67, 2.15, 2.9 and 3.7nm have been obtained [72]. They exhibited ultra bright blue, green, yellow and red luminescence (see Fig.2.9).

The main advantages of this method are its product with high degree of crystallinity, low particle surface contamination due to employing high-purity semiconductor-grade substrates. However, the obtained nanocrystals present irregular shapes and sizes (from a few nanometers to several micrometers).

2.6 Comparison of preparation methods.

The methods commonly used for preparation of Ni, Cu, Au, Ag, Pt, Si and Ge nanoparticles (that will be synthesized and discussed in this dissertation), characteristics of the corresponding resultant nanoparticles, and applications of these nanoparticles are summarized in Table 2.3.

Chapter II: Literature review: Characteristics, properties, applications and preparation of transition metal, Si and Ge nanoparticles

Table 2.3 Preparation methods, characteristics and application of Ni, Cu, Au, Ag, Pt, Si and Ge nanoparticles.

Preparation method		Types	Characteristics of nanoparticles	Notes	Advantages and disadvantages
Chemical methods	Chemical reduction	Ni	12nm, Superparamagnetic	NiCl ₂ and N ₂ H ₅ OH [101,102]	A: Simple process D: Difficult to control size
			Hollow nano-sphere	Ni dodecylsulfate and NaH ₂ PO ₄ [106]	
		Cu	Spherical in shape, 1-2nm	Cu(NO ₃) ₂ and NaBH ₄ [95]	
			Irregular shapes, 200-250nm	Enhanced by heating [115]	
			Porous aggregates, 50-70nm	Enhanced by ultrasound [115]	
		Ag	Nanowires	AgNO ₃ with ethylene glycol [93]	
			Cubic Ag nanoparticles	Modified by alkanethiol [96]	
			Hexagonals, 67.3nm	Ag ₂ SO ₄ and N ₂ H ₄ ·H ₂ O [103]	
		Au	Nano rods with aspect ratios of up to 200	Modified by CATB [99]	
	Cubic, triangle, hexagonal, branched, or rod-like		Modified by CATB [100]		
	Pt	Tetrahedral, cubic and truncated octahedral	Reduced by hydrogen [100]		
	Microemulsion	Ni	3.7nm, Superparamagnetic	Ni diacetylacetone and NaBH ₄ [121]	A: Easy to obtain particles of narrow size distribution D: Contamination
		Cu	Nano rods	Reverse micelles [125]	
	Electrochemical method	Cu	About 100nm	Reduction from CuO [129]	A: Simple process D: Large particle size
	Rapid expansion of supercritical fluid solutions	Ni	About 6 nm	NiCl ₂ in ethanol [131]	A: Easy to obtain particles of narrow size distributions D: High cost and aggregation
Cu		5-15nm	NaCH ₃ CN in SF CO ₂ [126]		
Ag		Triangle, 2–20 nm	In supercritical water [133]		

Chapter II: Literature review: Characteristics, properties, applications and preparation of transition metal, Si and Ge nanoparticles

Table 2.3 Preparation methods, characteristics and application of Ni, Cu, Au, Ag, Pt, Si and Ge nanoparticles (Continued).

Preparation method		Metal	Characteristics of nanoparticles	Notes	Advantages (A) and disadvantages (D)
Chemical method	Thermal decomposition	Ni	Nano rods	Ni(COD) ₂ as precursor, modified by HAD [141]	A: Easy to obtain crystalline powders D: Difficult to control shape, size and surface contamination.
			Branched nanoparticles	Ni carbonyl [137]	
		Si	6nm crystalline	Decomposition of silane, aided by microwave [147]	
			monodisperse, single crystal nanoparticles.	Decomposition of silane, aided by plasma [148]	
			4-5nm, crystalline	Co-decomposition [150]	
Ge	5nm crystalline	decomposition of DPG and TEG [149]			
Physical method	Thermal evaporation	Au	1nm	133Pa at 1124°C [152]	A: Simple process D: Difficult in size control and high cost
		Cu	Nano-rods and nanowires	In vacuum [153]	
		Si	3 to 50 nm	light emissions from 5000 Å to 9000 Å [11]	
	Magnetron sputtering	Au		Broad luminescence band in the red region [155]	A: Simple process. D: High cost.
	Laser ablation	Ag	Monodispersed Ag colloids	Modified by SDS and CTAB [161]	A: Simple process. D: Inhomogeneous particle sizes
		Si	Exhibit photoluminescence [163]		
	Sonication	Si	1.0, 1.67, 2.15, 2.9 and 3.7nm	Exhibited ultra bright blue, green, yellow and red luminescence [72]	A: high crystallinity and low contamination D: Irregular shapes and sizes

Chapter II: Literature review: Characteristics, properties, applications and preparation of transition metal, Si and Ge nanoparticles

2.5 Summary

Nanoparticles, which exhibit some unique properties that are different from those of bulk metals when their particle sizes are as small as the nanometer size, have various applications in catalysts, displays, memories, nanoinks, and biomedicines. Although a variety of preparation methods have been developed to synthesize transition metal or semiconductor nanoparticles, and some synthesis methods for nanoparticles among them are, in certain ways, reaching maturity, an economically-feasible synthesis method for these materials that can be scaled up, is still required.

CHAPTER THREE: EXPERIMENTAL DETAILS

3.1 The initial materials for production of magnides, aluminides and sodides

Magnesium powders (M-0160, ACP Chemicals Inc., Montreal, QC, Canada), -100mesh 99wt% pure nickel powders (M-1358, ACP Chemicals Inc., Montreal, QC, Canada), aluminium powder (EMD Chemical Inc, Gibbstown, NJ, USA), -325 mesh 99.99wt% pure gold and silver powders(Sigma Aldrich Inc. St. Louis, MO, USA), 99.9wt% pure platinum powders with particle sizes ranging from 0.15 micron to 0.45 micron, Ge and Si, and 99.95wt% pure sodium cubes in mineral oil were used to produce magnides, aluminides, and sodides.

In addition, Mg_2Ni and Mg_2Cu pellets (MPD Technology Corporation, Wyckoff, USA) were also used as initial materials in this study. The chemical compositions of Mg_2Ni and Mg_2Cu pellets are listed in Table 3.1.

Table 3.1 Chemical composition of the arc-melted Mg_2Ni and Mg_2Cu pellets (wt%).

Elements	Mg	Ni (Cu)	O	N	C
$Mg_{2.35}Ni$	49.3	50.6	0.042	0.018	0.023
$Mg_{2.08}Cu$	44.2	55.4	0.020	0.047	0.009

3.2 Material preparation

3.2.1 Ball-milling

The initial material mixtures were ball-milled under an atmosphere of argon in a laboratory high-energy ball mill Spex 8000 (Spex Industries, Inc, Edison, NJ, USA). For

the purpose of mixing, a 1:1 weight ratio of ball to the initial material and 1 hour milling were used. For reducing the particle size, a 2:1 weight ratio of ball to the initial material and 2 hour milling were used. The Spex 8000 mill was equipped with two fans for cooling. The milling vial is made of tungsten carbide and is 6.35cm in diameter and 7.62cm long. The milling balls are made from 440C martensitic stainless steel and are 1.27 cm in diameter. The vial is clamped and shaken at a speed of 1200rpm in a complex motion, which combines back-and-forth swings with short lateral movements. To minimize any oxygen intake, the Spex 8000 mill was put in a plastic glove bag, which was filled with a 99.9wt% pure argon.

3.2.2 *In-situ* reaction synthesis of Mg₂Ni

10 grams of a Mg and Ni particle mixture with a 2:1 atomic ratio, which were ball-milled for two hours, were loosely laid in a graphite boat, and then were put into a stainless tube furnace. The chamber of the furnace was purged by an argon flow for 5 min. The sample was heated up to 690°C at a rate of 10°C/min and held for 2 hours, and then cooled down to room temperature in furnace.

3.2.3 *In-situ* reaction synthesis of Mg₂NiH₄

10 grams of Mg and Ni particle mixture with a 2:1 atomic ratio, which were ball-milled for two hours, were loosely laid in a graphite boat, and then were put into a stainless tube furnace. The chamber of the furnace was purged by an argon flow for 5 min. The sample was heated up to 690°C at a rate of 10°C/min and held for 2 hours, then, was cooled down to 350°C in furnace. Subsequently, the argon in the chamber was replaced by

hydrogen. The Mg_2Ni formed at high temperatures was hydrogenated for 2h at 350°C under a hydrogen pressure of 0.5MPa. It was then cooled down to room temperature in the furnace under a 0.5MPa hydrogen pressure. The hydrogen remaining in the chamber after preparation of M_2NiH_4 was burned off using a propane torch.

3.2.4 Synthesis of MgNi_2 , Al_3Ni , Ni_2Al_3 , Mg_3Au , $\text{Mg}_{54}\text{Ag}_{17}$, Mg_2Ge , Mg_2Si , Ag_2Na and PtNa

The parameter selection principles for synthesis of MgNi_2 , Al_3Ni , Ni_2Al_3 , Mg_3Au , $\text{Mg}_{54}\text{Ag}_{17}$, Mg_2Ge , Mg_2Si , Ag_2Na and PtNa are 1) making sure that there is a total transformation of all transition metal, Si and Ge powders into the corresponding compounds; 2) avoiding oxidation of transition metal, Si and Ge powders; and 3) producing as many types of compounds as possible in one batch.

Commercially available Mg, Al, Ni, Si, Ge, Au and Ag powders (see Section 3.1) were used to synthesize MgNi_2 , Al_3Ni , Ni_2Al_3 , Mg_3Au , $\text{Mg}_{54}\text{Ag}_{17}$, Mg_2Ge and Mg_2Si by a conventional melting and casting method according to the compositions given in Table 3.2.

These initial mixtures were ball-milled for 1 hour under an atmosphere of argon in a laboratory Spex 8000 mill. Then, these mixtures were melted at 900°C for 2 hours in graphite crucibles and then cooled down to room temperature. To protect the melt from excessive oxidation or possible burning, a protective gas (Sulfur Hexafluoride, SF_6 0.5% + Carbon Dioxide CO_2) was used during both melting and casting. The temperature of the molten liquid metal was measured by a digital thermometer (Omega HH509).

Chapter III Experimental details

The mixtures of Ag or Pt powders and small Na pellets with a weight ratio of 1:4 were placed into crucibles in a tube furnace. The chamber of the furnace was first purged with argon. The mixtures were then heated up to 700°C at a speed of 10°C/min, and held at 700°C for 2 hours under a protective atmosphere of 0.5MPa argon and cooled down to room temperature in the furnace.

Table 3.2 Synthesis of MgNi₂, Al₃Ni, Ni₂Al₃, Mg₃Au, Mg₅₄Ag₁₇, Mg₂Ge, Mg₂Si, Ag₂Na and PtNa.

	Stoichiometric composition	Composition of pellets	Synthesis method	Phase composition in products
MgNi ₂	82.8wt% Ni, 17.2wt% Mg	80wt% Ni, 20wt% Mg	Melting and casting (900°C for 2 hours, protected by a gas mixture of SF ₆ and CO ₂)	Mg ₂ Ni and MgNi ₂
Al ₃ Ni	42 wt% Ni, 58 wt% Al	30wt% Ni, 70 wt% Al		Al ₃ Ni + Al
Ni ₂ Al ₃	58 wt% Ni, 42 wt% Al	70 wt% Ni, 30wt% Al		Al ₃ Ni, Ni ₂ Al ₃ and Ni
Mg ₃ Au	73 wt% Au, 27 wt% Mg	60wt% Au, 40wt% Mg		Mg ₃ Au + Mg
Mg ₅₄ Ag ₁₇	57 wt% Ag, 43 wt% Mg	50wt% Ag, 50wt% Mg		Mg ₅₄ Ag ₁₇ +MgAg+MgO
Mg ₂ Ge	60wt% Ge, 40 wt% Mg	40wt% Ge, 60 wt% Mg		Mg ₂ Ge +Mg
Mg ₂ Si	36.6wt% Si, 63.4wt%Mg	20wt% Si, 80wt% Mg		Mg ₂ Si + Mg
Ag ₂ Na	90.2wt% Ag, 9.8wt% Na	20wt% Ag, 80wt% Na	In-situ synthesis (700°C for 2 hours, under 0.5MPa Ar)	Ag ₂ Na+Na+NaOH
PtNa	89.6wt% Pt, 10.4wt% Na	20wt% Pt, 80wt% Na		PtNa+Na ₂ PtH ₆ + NaOH

3.2.5 Synthesis of nanoparticles by a hydrolysis method

The intermetallic pellets were ball-milled under an argon atmosphere for 2 hours in a laboratory high energy ball mill SPEX8000 at a speed of 1200rpm. Either 1 gram of the ball-milled noble metal intermetallic particles were immersed in 200ml of distilled water and stirred for 48h, or 10 grams of the ball-milled transition metal intermetallic particles were immersed in 500ml of distilled water and stirred for 120h. Then, the hydrolysis product, $Mg(OH)_2$, was carefully removed by adding 0.5M hydrochloric acid. The product was rinsed three times using distilled water, followed by three times using ethanol. The sample was divided into two samples. Sample one was used for TEM and particle size analysis (no drying process). Sample two was used for XRD analysis. The ethanol in Sample two was evaporated using a Rotavapor at 60°C.

3.3 Materials characterization

3.3.1 Morphology and structure

Scanning electron microscopy (SEM) using a JEOL JSM-5800LV microscope (see Fig.3.1) was used to observe the morphology of raw material particles and reaction-synthesized Mg_2Ni and Mg_2NiH_4 , and roughly measure the average particle sizes of the reaction product. The Mg_2NiH_4 specimen was coated with a layer of gold to increase its conductivity. The accelerating voltage used was 15kV, while SEM image data were recorded on the floppy discs and the images were printed on the 11x14 cm sheet photograph papers.



Fig. 3.1 Scanning electron microscope (JEOL Model JSM-5800LV).



Fig. 3.2 JEOL 2010 Transmission Electron Microscope with an Energy Dispersive X-ray Spectrometer (EDX).

TEM investigations were undertaken in McMaster University with a JEOL 2010 transmission electron microscope (TEM) equipped with an energy dispersive X-ray spectrometer (EDX) at an operating voltage of 200 keV, as shown in Fig. 3.2. Selected area electron diffraction (SAED) patterns and energy dispersive spectroscopy (EDS) spectra were usually used to identify the various phases.

The phase composition was mostly investigated with the help of John Robinson using a Phillips X-ray diffractometer (Mahwah, NJ, USA) with a proportional counter detection head. Graphite monochromated $\text{CuK}\alpha$ radiation, at a voltage of 40kV and a current of 20mA, was utilized as the diffracting medium. The structures of the Ag, Au and Pt final product sealed in a glass capillary were analyzed by a Siemens D-500 powder diffractometer in Department of Chemistry and Biochemistry, University of Windsor since the amounts of these noble metal nanoparticles were not enough to meet the needs of the Phillips X-ray diffractometer.

3.3.2 Charge/discharge capacity of Mg_2Ni

The ball-milled Mg_2Ni powders were first sieved to a mean size of about 40 microns using a 325 mesh sieve. The fine Mg_2Ni particles were mixed with a -325 mesh Ni particles in a 2:1 weight ratio. A polytetrafluoroethylene (PTFE) dispersion (4wt%) was added into the mixture as a binder. The powder mixture of 0.6g was pressed into a porous Ni sponge with a diameter of 10.0mm in a mould at a pressure of 500MPa for 2 mins. The cylinders were used as the negative electrode in the experimental cells. A sintered $\text{Ni}(\text{OH})_2/\text{NiOOH}$ sheets with a dimension of 1.5 cm \times 4 cm were used as a positive electrode.

The electrochemical cell comprised of three compartments. The negative electrode (working electrode) was placed in the central compartments, and two positive electrode sheets were placed on either side. The electrolyte was 6M KOH aqueous solution. A Hg/HgO/6M KOH electrode was used as a reference electrode.

The charge/discharge behaviour of the experimental cell was conducted using a Solartron 1285 Potentiostat (see Fig.3.3) with CorrWare for Windows. The constant charge and discharge currents were 20mA/g and 2mA/g, respectively. The discharge process was ended until the potential of the negative electrode reached -0.5V with respect to the Hg/HgO/6MKOH electrode.

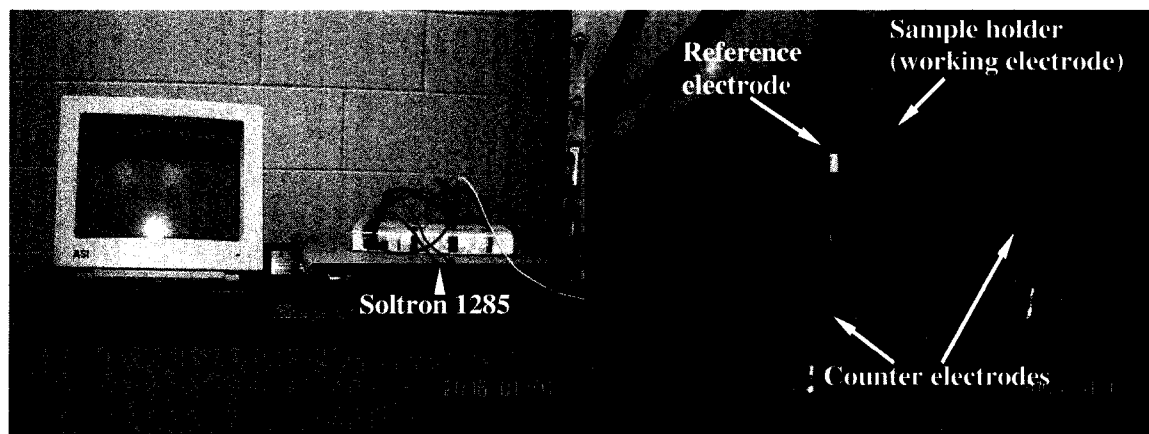


Fig.3.3 The electrochemical measurement system (Solartron 1285) used in this study.

3.3.3 Hydrogen absorption/desorption capacity of Mg₂Ni

The hydrogen adsorption/desorption isotherms were measured by a computer controlled commercial 'Gas Reaction Controller' manufactured by the Advanced Materials Corporation of Pittsburgh, PA. Highly purified hydrogen (99.9995% purity) was used as

Chapter III Experimental details

the adsorbent. Typically the mass required for the hydrogen sorption measurement is 500-1000 mg. The size of the sample chamber is 2.5 cc. Lightly packed powder materials were used for all measurements. Before all measurements the materials, were degassed at 200°C under high vacuum for at least one day in order to remove any physisorbed water or volatile impurities.

The temperature of the gas reservoir was measured by two AD590 IC thermometers that are calibrated against a standard mercury thermometer within $\pm 0.1^\circ\text{C}$ at room temperature. The sample temperature was measured with type K thermocouple by converting voltage reading to temperature according to ITS-90 (The International Temperature Scale of 1990). The limits of error are $\pm 2^\circ\text{C}$ or 0.75 % above 0°C and $\pm 2^\circ\text{C}$ or 2 % below 0°C . The pressure of both the gas reservoir and the sample chamber were measured by a Heise model HP0 pressure transducer, which has a fullscale range of 1500 psi (about 100 atm). The accuracy of this transducer is rated to be 0.05 % of the full scale including non-linearity, drift, and hysteresis by the manufacturer. The GRC operates by admitting an appropriate amount of gas to the reservoir and determines its molar amount from its pressure and temperature. The system then manipulates the valves between the reservoir and the reaction chamber and transfers a desired amount of the gas from the reservoir to the gas reaction chamber. After equilibrium is attained, the system re-calculates the number of hydrogen molecules. The system employs a modified Benedict-Webb-Rubin equation of state in calculating the amount of absorbed hydrogen from the pressure, temperature, and volume. The apparatus gradually increases the hydrogen pressure to the maximum specified value, while summing the absorbed hydrogen. The amount of hydrogen released from the sample is then determined by

pumping out the gas reservoir and gradually bleeding hydrogen from the sample chamber into the gas reservoir. This experiment was carried out with the help of Dr Xin Hu in Department of Chemistry and Biochemistry, University of Windsor.

3.3.4 The specific surface area of nanoparticles

The specific surface area of nanoparticles was measured by a BET method. Nitrogen adsorption and desorption data were collected on a Micromeritics ASAP 2010 apparatus. Before the sorption analysis, the sample was subjected to the degassing vacuum system under ultra high vacuum (10^{-9} bar) at a temperature of 120°C overnight. The sample was backfilled with nitrogen and transferred to the analysis system. The sample was then again degassed under ultrahigh vacuum (10^{-9} bar) until analysis. Sorption analysis was carried out at liquid nitrogen temperature (77 K). Helium was used for the free space determination, after sorption analysis, both at ambient temperature and at 77 K. Apparent surface areas were calculated from N₂ adsorption data by multi-point BET analysis. This experiment was carried out with the help of Dr Xin Hu in Department of Chemistry and Biochemistry, University of Windsor.

3.3.5 The particle size of nanoparticles

The size distribution of the nanoparticles (no drying) was determined using a Zetasizer 3000HS instrument. This experiment was carried out with the help of Ms Yanyan Lou in Instrumental Analysis and Research Center, Shanghai University, P.R.China. The suspended nanoparticles were first taken titration with 0.1M NaCl and 0.25M NaOH

Chapter III Experimental details

solution. The pH value was obtained when the maximum zeta potential has reached. Then, the size distribution of nanoparticles was measured at that pH value.

CHAPTER FOUR: THE HYDROGEN STORAGE PROPERTIES OF Mg_2Ni AND THE DISCOVERY OF ITS HYDROLYSIS BEHAVIOR

4.1. Introduction

Rechargeable nickel metal hydride (NiMH) batteries have many advantages for use as power sources in electric and hybrid vehicles such as higher power densities and environmental friendliness [166,167]. When compared with conventional AB_5 alloys, Mg_2Ni exhibits a good hydrogen storage capacity (3.6wt%) and lower specific gravity. The theoretical discharge capacity of Mg_2Ni is as high as 999mAh/g. Mg_2Ni is thus expected to be amongst the next generation of electrode materials. However, polycrystalline Mg_2Ni shows a very low electrochemical discharge capacity (less than 10mAh/g) [168]. It has been reported that the electrochemical discharge capacity can be improved through the use of nano-crystalline Mg_2Ni [168-174]. A very high discharge capacity of 1082mAh/g (exceeding the theoretically calculated value of Mg_2Ni) has even been reported [170]: the supporting evidence for this high discharge capacity was not, however, provided in the paper.

In general, the hydrogen storage capacity of the alloys prepared by a melting and casting method is higher than that of materials synthesized by a mechanical alloying method. However, mechanical alloying can significantly improve activation and reaction kinetics of hydrogen storage alloys. Contamination is a drawback in mechanical alloying [175].

Chapter IV: The hydrogen storage properties of Mg_2Ni and the discovery of its hydrolysis behavior

No contamination is introduced by in-situ reaction synthesis (or combustion synthesis). The reaction synthesis products are porous, and have high purity and large surface areas of “fresh” surface, which result in easy activation of the combustion synthesis product. During synthesis of Mg_2NiH_4 , an intermediate product (Mg_2Ni) with easy activation is formed first, which makes the hydriding reaction to Mg_2NiH_4 much easier. The maximum hydrogen storage capacity obtained with the combustion synthesis product in the primary cycle without any activation has been reported as 3.4-3.6wt.%, which is close to the theoretical value of 3.6wt.% [175-179]. This contrasts with the 10 or more hydriding /dehydriding cycles required to produce Mg_2NiH_4 using conventional ingot material, due to its surface oxidation or adsorbed gas [179].

In this chapter, the hydrogen storage capacity and the charge/discharge capacity results for both in-situ synthesized Mg_2Ni and as-cast Mg_2Ni will be reported. Both types of Mg_2Ni exhibited a near zero charge/discharge capacity. Further investigation has shown that Mg_2Ni spontaneously hydrolyzed in both distilled water and 6M KOH solution, and formed $Mg(OH)_2$, Ni and hydrogen. The hydrolysis characteristics of both Mg_2Ni and Mg_2NiH_4 suggest that they are not suitable for use as electrodes in rechargeable batteries. The hydrolysis of Mg_2Ni or Mg_2NiH_4 , however, provides a new and relatively simple method for the production of nickel nanoparticles

4.2 *In-situ* synthesized Mg_2Ni

The Mg-Ni binary phase diagram contains the intermediate compounds Mg_2Ni and $MgNi_2$ which are primarily metallicly bonded and have fixed compositions and definite stoichiometries (see Fig.4.1). Mg_2Ni has a hexagonal structure, and is said to be an

Chapter IV: The hydrogen storage properties of Mg_2Ni and the discovery of its hydrolysis behavior

incongruently melting compound since, upon heating, it undergoes peritectic decomposition into liquid and MgNi_2 at 760°C . MgNi_2 is a congruently melting compound since it maintains its composition right up to the melting point. Based on the Mg-Ni binary phase diagram, the in-situ reaction temperature for this study was set at 690°C in order to achieve high conversion and avoid generating a large amount of liquid eutectic.

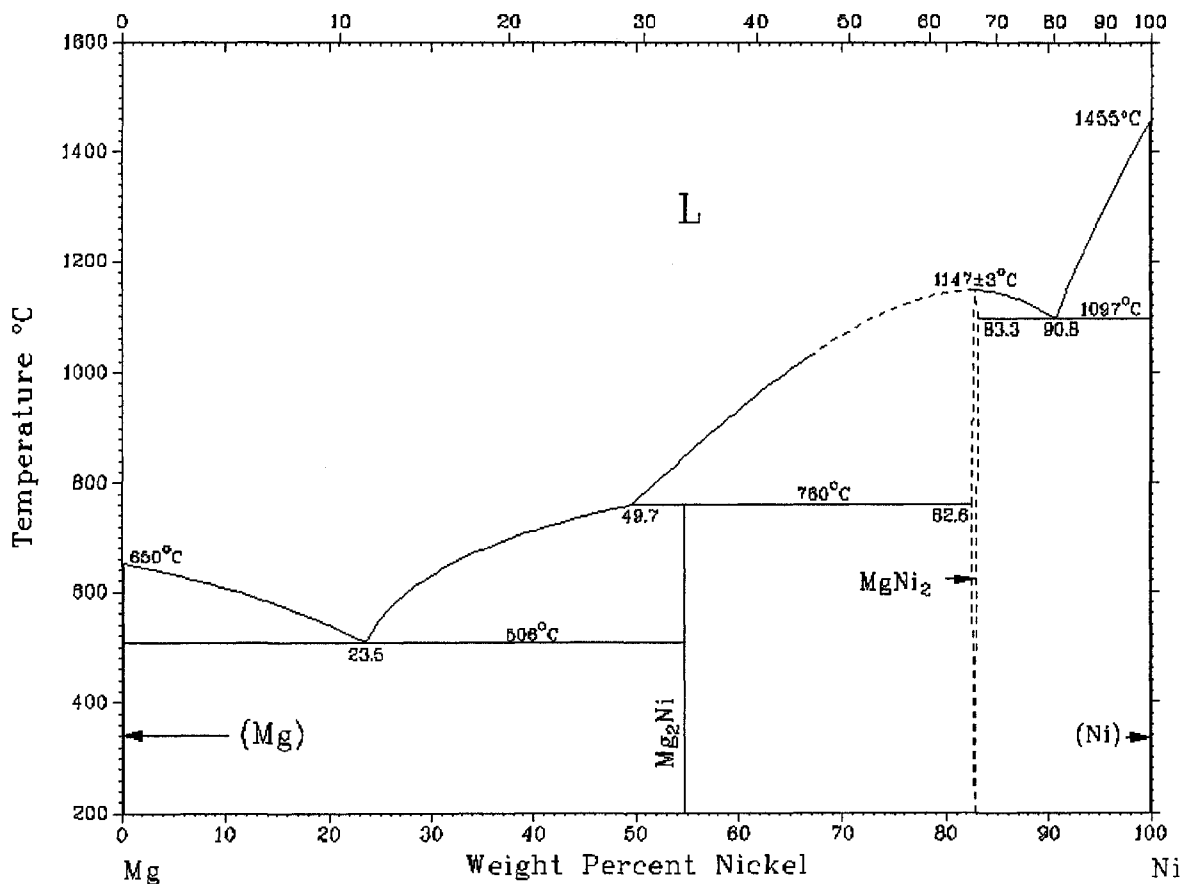


Fig. 4.1 Mg-Ni binary phase diagram [180].

4.2.1 Preparation procedures for *In-situ* synthesized Mg₂Ni

Magnesium powders and 100mesh 99wt% pure nickel powders were used to *in-situ* reaction-synthesize Mg₂Ni compound. A 20g mixture of Mg and Ni powders with a stoichiometric ratio (2:1) of Mg₂Ni was first ball-milled under the protection of 1.1 atmosphere of argon for 1h. The ball-milled mixture of 20 grams was loosely laid in a graphite boat, and then was put into a stainless steel tube furnace. The furnace chamber was purged by an argon flow for 5 min. The argon pressure in furnace chamber was then maintained at a pressure of two atmospheres. The sample was heated up to 690°C at a rate of 10°C/min and held for 2 hours, and then cooled down to room temperature in furnace.

4.2.2 Characteristics of the *In-situ* synthesized product

The morphology of the Mg and Ni powders in the initial materials is shown in Figs 4.2a and 4.2b. The larger spheres with a rough surface are the Mg powders. The smaller spheres with a smooth surface are the Ni powders. The morphology of the ball-milled mixture of Mg and Ni with an atomic ratio of 2 to 1 is shown in Figs 4.2c and 4.2d. The ball-milled powders were coarse due to cold-welding. Since some liquid eutectic was formed above the eutectic transformation temperature, the *in-situ* synthesized Mg₂Ni was very coarse, but not as coarse as in the ingot.

Chapter IV: The hydrogen storage properties of Mg_2Ni and the discovery of its hydrolysis behavior

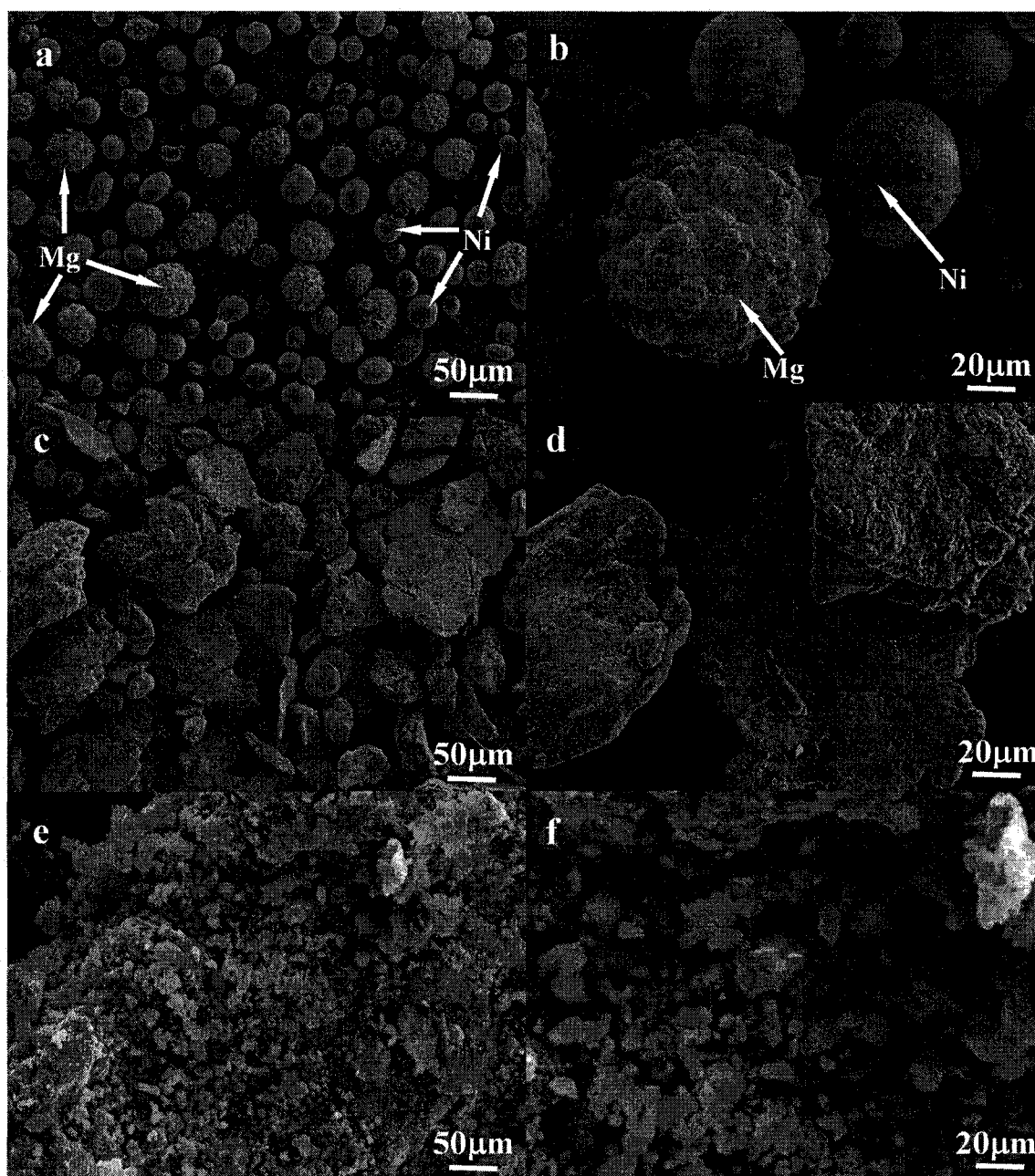


Fig.4.2 SEM images of the initial mixture ((a) low magnification and (b) high magnification); the ball-milled mixture ((c) low magnification and (d) high magnification) and the *in-situ* reaction product ((e) low magnification and (f) high magnification).

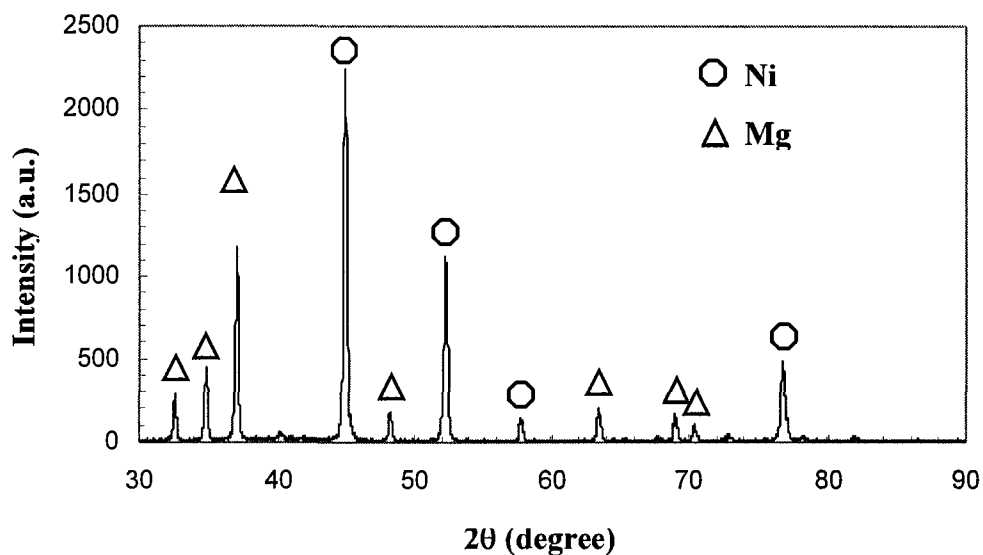


Fig. 4.3 XRD pattern of the initial mixture with a 2:1 atomic ratio of Mg:Ni.

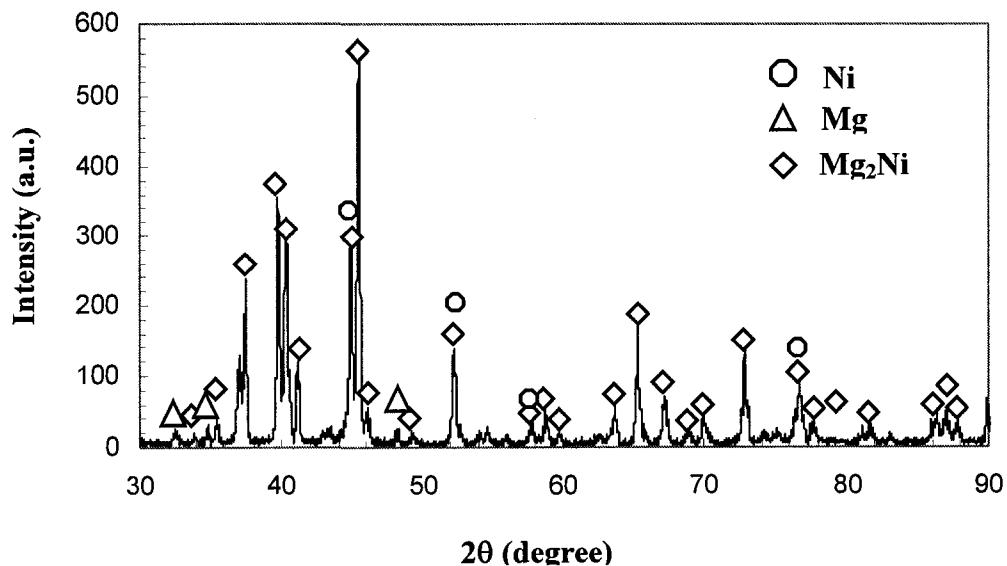


Fig. 4.4 XRD pattern of the in-situ synthesized Mg_2Ni .

By comparison with the XRD diffraction pattern of the mixture of the initial materials (Fig.4.3), it was noted that besides some lower intensity Mg or Ni peaks, strong Mg_2Ni

diffraction peaks (JCPDS file No 65-9715) were present in the XRD pattern of the in-situ synthesized Mg₂Ni as shown in Fig.4.4. This indicates that the Mg and Ni in the initial mixture were mostly converted into the Mg₂Ni compound.

4.2.3 Hydrogen storage properties

The hydrogen absorption/desorption curves of the in-situ synthesized Mg₂Ni at 280°C is shown in Fig. 4.5. At 280°C, the *in-situ* synthesized Mg₂Ni particles began to absorb hydrogen when the hydrogen pressure reached 2.38atms. At the beginning of hydrogen absorption, the hydrogen absorption pressure slightly dropped from 2.38atms to 2.16atms (AB). With increasing amount of the absorbed hydrogen, the hydrogen absorption pressure began to slightly increase up to 2.84atms (AC). At this time, the hydrogen concentration in the *in-situ* synthesized Mg₂Ni particles reached 1.05wt%. After that point, the relationship of the hydrogen absorption pressure versus the hydrogen concentration in Mg₂Ni was parabolic from 2.84atms to the preset highest pressure (10atms)(CD). The corresponding hydrogen concentration was 1.63wt%. Then, the hydrogen pressure began to decrease. At the beginning, while the hydrogen pressure abruptly dropped from 10atms to 2.80atms, the hydrogen concentration in the *in-situ* synthesized Mg₂Ni particles slightly increased from 1.63wt% to 1.65wt% (DE). After this point, the *in-situ* synthesized Mg₂Ni particles started hydrogen desorption. When the hydrogen desorption pressure dropped slightly from 1.65atms to 1.40atms (EI), the hydrogen concentration dramatically decreased from 1.65wt% to 0.24wt%. At the beginning of hydrogen desorption, there is a stage (GH) that the hydrogen desorption pressure increased from 1.60atms to 1.80atms. At the point where the hydrogen

Chapter IV: The hydrogen storage properties of Mg₂Ni and the discovery of its hydrolysis behavior

desorption pressure was 1.40atms, and the hydrogen concentration was 0.24wt%, the hydrogen desorption rate became slower. The hydrogen desorption pressure abruptly dropped from 1.40atms to zero pressure, while the hydrogen concentration decreased slightly from 0.24wt% to 0.1wt%.

When the temperature of the hydrogen absorption/desorption test was increased to 300°C, the hydrogen absorption/desorption curves of the in-situ synthesized Mg₂Ni were as shown in Fig. 4.6, which was similar to Fig. 4.5.. The *in-situ* synthesized Mg₂Ni particles began to absorb hydrogen at a hydrogen pressure of 3.7atms. The absorption plateau pressure ranged from 3.7atms to 4.04atm (AB). The corresponding hydrogen concentration increased from 0.01wt% to 1.27wt%. After the plateau region, the hydrogen absorption pressure parabolically increased from 4.04atms to 10atms (BC). The corresponding hydrogen concentration increased from 1.27wt% to 1.96wt%. When the hydrogen pressure abruptly dropped from 10atms to 4.19atms, the hydrogen concentration in the *in-situ* synthesized Mg₂Ni particles slightly increased from 1.96wt% to 1.99wt% (CD). The hydrogen desorption plateau pressure decreased slightly from 2.60atm to 2.23atms (EH). The corresponding hydrogen concentration, however, significantly decreased from 1.96 wt% to 0.22wt%. At the beginning of hydrogen desorption, there is also a stage (EF) that the hydrogen desorption pressure increased from 2.60atms to 2.65atms.

It well known that hexagonal Mg₂Ni as a solid solution (α -phase) is able to absorb only a small amount of hydrogen (up to 0.3wt%), i.e. Mg₂NiH_{0.3} [175,176]. At this time, the hydrogen concentration in the Mg₂Ni is pressure dependent and can be described as follows [177]:

Chapter IV: The hydrogen storage properties of Mg_2Ni and the discovery of its hydrolysis behavior

$$C_H = kP^{1/2} \quad (4-1)$$

Where, C_H is the hydrogen content in the α -phase, k is a temperature dependent constant, and P is the hydrogen pressure.

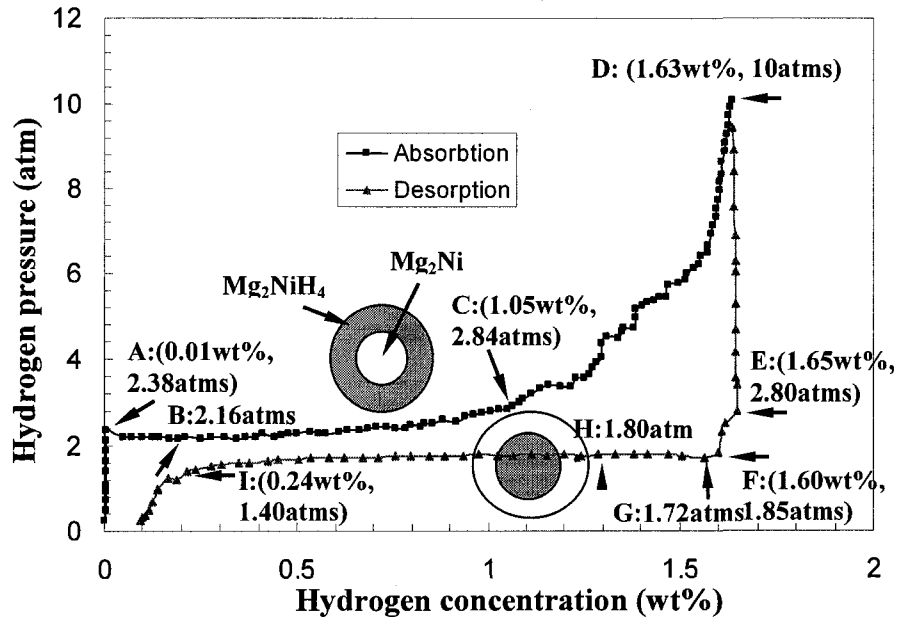


Fig 4.5 Hydrogen absorption/desorption curves of the in-situ synthesized Mg_2Ni at $280^\circ C$.

As the hydrogen concentration exceeds the saturated concentration in Mg_2Ni as a solid solution, nucleation and growth of the Mg_2NiH_4 (β phase) will begin. While the two phases (α and β phase) coexist, theoretically, the conversion of the saturated solid solution to hydride should take place at a constant pressure according to Gibbs phase rule, which shows a flat plateau in a PCT curve. The (mean) absorption plateau pressures at $280^\circ C$ and $300^\circ C$ were about 2.61atms and 3.87atms, respectively. The temperature dependent pressure is the equilibrium dissociation pressure of the hydride. The plateau or equilibrium pressure strongly depends on temperature and is related to the changes of enthalpy and entropy, respectively.

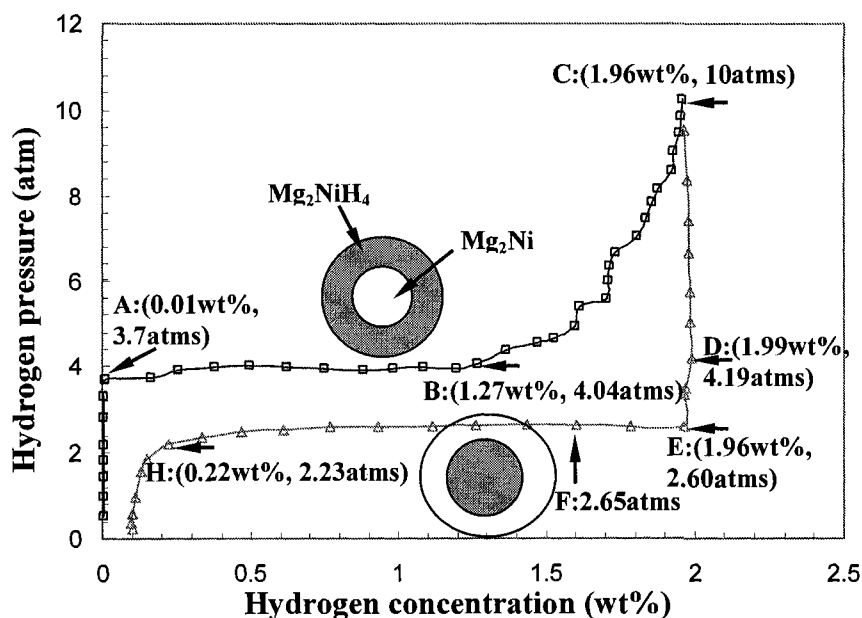


Fig 4.6 Hydrogen absorption/desorption curves of the in-situ synthesized Mg_2Ni at $300^\circ C$.

The relationship can be given by the van't Hoff equation:

$$\ln(P_{H_2}/P_{H_2^0}) = -\Delta H/RT + \Delta S/R \quad (4-2)$$

where, ΔS and ΔH represent the entropy and enthalpy change, respectively, R is the gas constant and T is temperature. According to Equation 4-2, an increase of temperature will lead to an increase in the absorption /desorption pressure as can be seen in Figs 4.5 and 4.6.

However, Mg_2Ni like most practical hydriding metals does not show perfectly flat plateau and zero hysteresis due to the limitation of kinetics.

As Mg_2Ni transforms to Mg_2NiH_4 due to hydrogen absorption, it undergoes a structural rearrangement with an accompanying 32% increase in volume. Mg_2NiH_4 has a antifluorite structure, built up of an tetrahedral $[NiH_4]$ complex surrounded by a cube of

Chapter IV: The hydrogen storage properties of Mg_2Ni and the discovery of its hydrolysis behavior

magnesium ions at temperatures above $237^\circ C$ [181]. For the cubic phase, there are still several basic uncertainties with respect to the location of hydrogen in the lattice. The position occupied by the hydrogen atoms in the metal lattice influence the static, dynamic electronic and magnetic properties of metal-hydrogen systems. Possible hydrogen atom sites in the antifluorite metal lattice structure of Mg_2NiH_4 are shown in Fig.4.7.

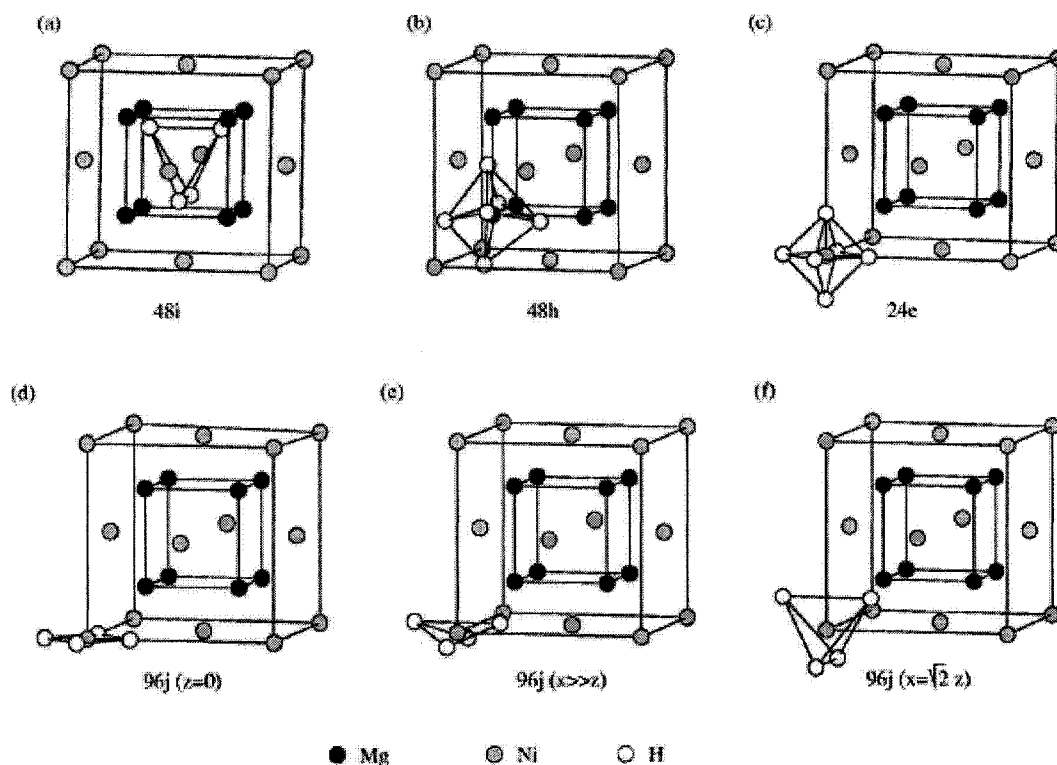


Fig.4.7 Possible hydrogen atom sites in the antifluorite metal lattice structure of Mg_2NiH_4 , these sites are indicated in terms of Wyckoff notation [182].

Therefore, as the Mg_2Ni particles absorbed hydrogen and formed Mg_2NiH_4 at $280^\circ C$ or $300^\circ C$, a layer of cubic Mg_2NiH_4 would be formed as shown schematically in Figs 4.5

Chapter IV: The hydrogen storage properties of Mg_2Ni and the discovery of its hydrolysis behavior

and 4.6 (The dark and blank area denote Mg_2NiH_4 and Mg_2Ni , respectively). The growth of the Mg_2NiH_4 layer depended on hydrogen diffusion through the layer during hydrogenation. However, compressive stress was induced in the Mg_2NiH_4 layer due to the volume expansion that resulted from the phase transformation, which increased the activation energy for the diffusion of hydrogen atoms in this layer. As a result, the absorption plateau was sloped.

On the contrary, a layer of Mg_2Ni was formed in the hydrogenated particle during dehydrogenation. The transformation of Mg_2NiH_4 to Mg_2Ni gave rise to a decrease of 32% in volume. A tension stress was induced in the Mg_2Ni layer, which would aid the diffusion of hydrogen atoms from the inner hydride to the particle surface. Therefore, the desorption pressure plateau was relatively flat.

It has been reported that Mg_2Ni only exhibits rapid absorption/desorption kinetics above 350°C [182]. Below this temperature, it has sluggish kinetics for hydrogen absorption/desorption that are mainly controlled by diffusion. Moreover, the PCT test depends on the absorption rate to adjust an increase or a decrease of the hydrogen pressure. The hydrogen concentration increased from 1.63wt% to 1.65wt% (DE in Fig.4.5) at 280°C or from 1.96wt% to 1.99wt% (CD in Fig.4.6) at 300°C while the hydrogen pressure abruptly dropped from 10atms. At the beginning of the reduction in hydrogen pressure, hydrogen still diffuses from the surface to the center, where it could still be Mg_2Ni . Therefore, the Mg_2Ni particles didn't reach their maximum hydrogen storage capacity (3.6wt%) at 280°C and 300°C. Below 350°C, increasing the temperature will improve the absorption/desorption kinetics of Mg_2Ni . This is the reason that the maximum hydrogen concentration reached in the experiment at 300°C was higher than that in the experiment at

Chapter IV: The hydrogen storage properties of Mg₂Ni and the discovery of its hydrolysis behavior

280°C. Due to equipment limitations (mainly built for low temperature measurements), the experiments at 350°C could not be performed.

In addition, there was pressure drop at the beginning of hydrogenation (AB in Fig.4.5), and pressure increases at the beginning of dehydrogenation (GH in Fig.4.5 and EF in Fig.4.6), which suggests that the absorption/desorption of Mg₂Ni requires an activation. This is another reason that the in-situ synthesized Mg₂Ni cannot achieve the maximum hydrogen absorption capacity (3.6wt%) on the first hydrogen absorption/desorption cycle at 280°C or 300°C. It has been reported that Mg₂Ni must be activated by over ten hydriding/dehydriding cycles under 7MPa hydrogen pressure at 400°C for practical application [179].

4.2.4 Electrochemical properties

When a PTFE dispersion was added as a binder to the ball-milled Mg₂Ni particles for preparing the electrode samples, heat release from these samples was observed. Our first thought was that the heat could be coming from the reaction between any remaining Mg in the *in-situ* synthesized Mg₂Ni and water in the PTFE dispersion. Therefore, additional drops of the PTFE dispersion were needed, or else the mixture was too “dry” to prepare the electrodes, which suggested that water was consumed by some chemical reactions (this will be discussed in Section 4.5).

Charge/discharge curves are the basis for the measurement of specific discharge capacity. During the charging process, a cathodic current was applied to break down the water in 6M KOH aqueous solution, and atomic state hydrogen was absorbed by Mg₂Ni. At the

Chapter IV: The hydrogen storage properties of Mg_2Ni and the discovery of its hydrolysis behavior

initial stage of charging, the equilibrium potential rapidly shifted in the cathodic direction as the hydrogen content in the electrode increased.

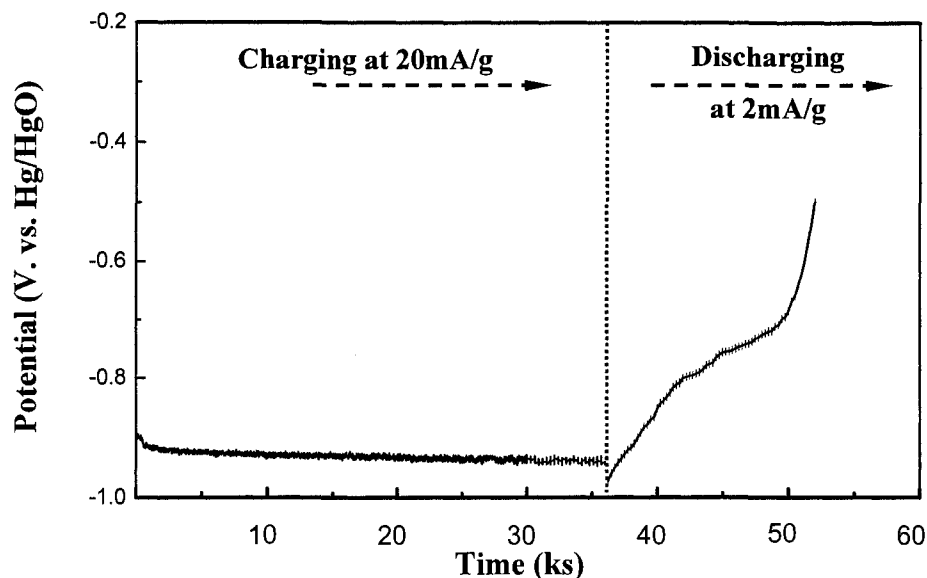


Fig.4.8 The initial charge/discharge curves of the in-situ synthesized Mg_2Ni at galvanostatic conditions at room temperature.

With further increase of the hydrogen content in Mg_2Ni , the equilibrium potential reached a plateau, which theoretically means that the hydrogen content reached a saturated level in the solid solution (hydrogen occupies the interstitial sites in the lattice). In practice, the hydrogen absorption process is affected by many factors including the surface condition of the Mg_2Ni particles, the particle size, and the temperature. A positive current was imposed on the charged Mg_2Ni electrodes to release the absorbed hydrogen.

In this study, the negative electrode was charged under a constant current density of $20mA/g$ for two hours. The discharge process was conducted using a current density of

Chapter IV: The hydrogen storage properties of Mg_2Ni and the discovery of its hydrolysis behavior

2mA/g until the potential of the negative electrode reached -0.5V vs. to the Hg/HgO/6MKOH electrode.

Fig.4.8 presents the initial (1st cycle) charge/discharge curves for the ball-milled Mg_2Ni particles. The equilibrium potential reached a plateau within 200 seconds. The discharge capacity of the in-situ synthesized Mg_2Ni was fairly low, less than 5mAh/g, which agrees with the results of Cui et al [168], who reported a discharge capacity of 8mAh/g measured at a discharge current of 2mA/g after the electrode was charged at a 20mA/g at room temperature.

4.3 Electrochemical properties of as-cast Mg_2Ni

To further investigate the electrochemical properties of Mg_2Ni , the as-cast Mg_2Ni powder was used to prepare the electrodes. When the PTFE dispersion was added as a binder to the as-cast Mg_2Ni particles for preparing the electrode samples, heat release from these samples was observed as the case for the ball-milled, in-situ synthesized Mg_2Ni particles. The initial charge/discharge curves for the ball-milled, as-cast Mg_2Ni powder electrodes are shown in Fig.4.9. In comparison with the in-situ synthesized Mg_2Ni electrode, the as-cast Mg_2Ni electrode took a much longer time to reach the equilibrium potential (about 2000 seconds). The discharge capacity of the as-cast Mg_2Ni electrode was also fairly low, being only about 6mAh/g.

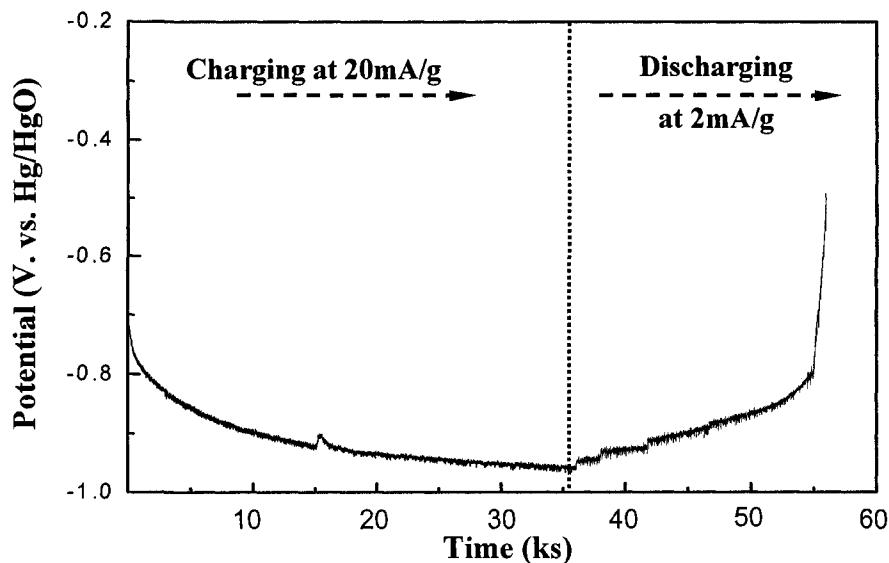


Fig.4.9 The initial charge/discharge curves of the as-cast Mg_2Ni at galvanostatic conditions.

4.4 *In-situ* synthesized $MgNiH_4$

The low temperature (LT) $MgNiH_4$ is a monoclinic antiferite structure, and exists in two modifications, LT_1 without microtwinning and LT_2 with microtwinning [181]. The LT_1 modification is formed by hydriding the alloy well below $235^\circ C$, never allowing the reorientation motion of hydrogen. The LT_2 modification is pressure sensitive and readily transforms into LT_1 when subjected to isostatic pressure [181]. The x-ray powder diffraction patterns of the two LT modifications are very similar. The main difference is that the LT_2 yields some extra peaks due to the micro-twinning. The micro-twinning could increase in the LT lattice if there is no excess of magnesium in the compound. There is a distinct color difference between the two modifications. The LT_2 modification is orange to rust color, while the LT_1 modification is brownish grey.

4.4.1 Preparation of Mg_2NiH_4

The as-cast Mg_2Ni pellets were ball-milled under an argon atmosphere for 2 hours in a laboratory high energy ball mill (SPEX8000). Mg_2NiH_4 particles were synthesized by hydrogenating the ball-milled Mg_2Ni particles under a hydrogen atmosphere of 6atm at 350°C for 2 hours in a tube furnace, then cooling down to room temperature in furnace. The synthesized Mg_2NiH_4 particles were rust brown in colour, which is the distinct color of the LT_2 modification.

There was 10wt% surplus Mg in the initial as-cast Mg_2Ni pellets. Therefore, besides the Mg_2Ni peaks, some small Mg diffraction peaks were observed in the XRD pattern for the ball-milled particles (see Fig.4.10a). Some weak MgH_2 diffraction peaks ((JCPDS file No. 12-0697) were observed in the XRD pattern for the synthesized Mg_2NiH_4 particles, together with strong Mg_2NiH_4 diffraction peaks (JCPDS file No. 38-0792), but no Mg_2Ni peaks as shown in Fig.4.10b. These results suggest that after hydrogenation under a hydrogen atmosphere of 6atm at 350°C for 2 hours in a tube furnace, the ball-milled Mg_2Ni and the surplus Mg particles had transformed into LT_2 Mg_2NiH_4 and MgH_2 , respectively.

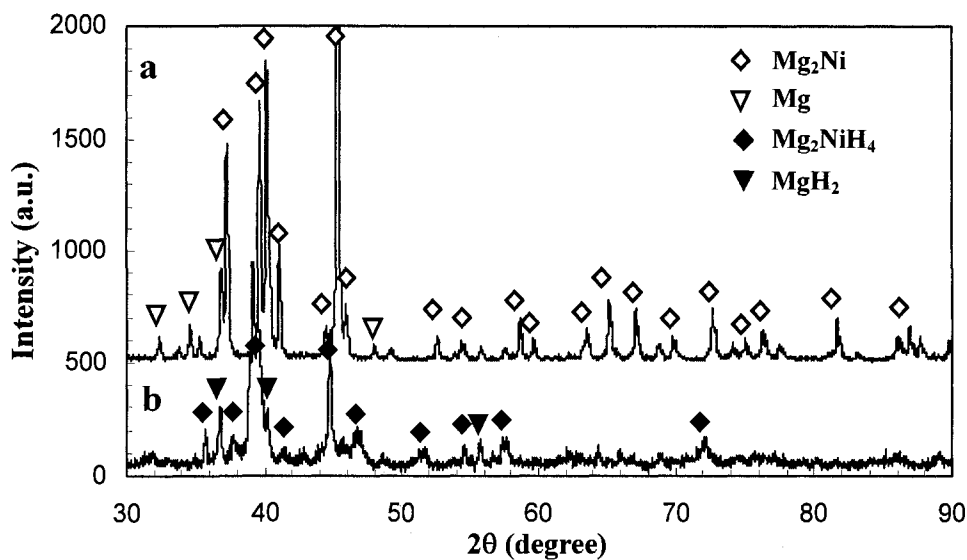


Fig.4.10 XRD powder diffraction patterns for a) the as-cast Mg_2Ni alloy, b) the *in-situ* synthesized Mg_2NiH_4 .

4.4.2 Electrochemical properties of Mg_2NiH_4

When a PTFE dispersion was added as a binder to the ball-milled synthesized Mg_2NiH_4 particles for preparing the electrode samples, both heat release and gas bubbles were observed. More drops of PTFE were needed for preparing the electrodes.

The Mg_2NiH_4 electrodes exhibited a near zero discharge capacity. Thus, the *in-situ* synthesized Mg_2Ni electrode, the as-cast Mg_2Ni electrode, and the synthesized Mg_2NiH_4 electrode all exhibited a near zero charge/discharge capacity. We believed that there was possibly a dynamic limitation, *eg.* hydrogen diffusion in the compound lattice at room temperature, that was the reason for the near zero charge/discharge capacities.

In order to further investigate the discharge capacity of Mg_2NiH_4 , the *in-situ* synthesized Mg_2NiH_4 was then directly pressed into an electrode without any binder in order to avoid

Chapter IV: The hydrogen storage properties of Mg₂Ni and the discovery of its hydrolysis behavior

the above phenomena. This Mg₂NiH₄ electrode was unable to maintain its shape in a 6M KOH solution and broke into many pieces with the generation of numerous gas bubbles. In some instances, the Mg₂NiH₄ electrode caught fire when the sample contacted the surface of the alkaline solution.

4.5 Hydrolysis behavior of as-cast Mg₂Ni

A rapid degradation of Mg₂Ni alloys in alkaline solutions during the charge-discharge process has been observed by a number of researchers [171-174]. The degradation has generally been attributed to the corrosion of Mg₂Ni alloy in the highly corrosive electrolyte. Kuji *et al* [174], observed the hydrolysis phenomenon of Mg₂Ni in both distilled water and a KOH solution. They assumed that Mg₂Ni alloys were easily hydrogenated by simply immersing the alloys in 6M KOH solution or in distilled water. In fact, the increase in hydrogen concentration in their samples resulted from the hydrolyzed Mg(OH)₂ since it was not removed from their samples.

In this study arc-melted Mg₂Ni was used to investigate the hydrolysis behaviour of Mg₂Ni and Mg₂NiH₄. The thermodynamics and mechanisms of the hydrolysis of Mg₂Ni and Mg₂NiH₄ are discussed in detail.

While the ball-milled as-cast Mg₂Ni particles were immersed in 500ml of 6M KOH solution or distilled water, there was initially a rapid release of hydrogen bubbles. Then, the release rate of hydrogen bubbles gradually slowed down. The pH value of the solution, determined using pH papers, rapidly reached a value of 10~11 in the samples immersed in water, and thereafter retained that level.

Chapter IV: The hydrogen storage properties of Mg₂Ni and the discovery of its hydrolysis behavior

After the ball-milled Mg₂Ni was immersed in 500ml of distilled water or 6M KOH for 120h, the solid product was filtered out, and then dried in a Rotavapor at 60°C (no rinse cycle). Brucite (Mg(OH)₂), and Ni peaks were observed in the XRD pattern for the hydrolysis product of the ball-milled Mg₂Ni in distilled water (see Fig.4.11a). Thus, Mg₂Ni had hydrolyzed into Mg(OH)₂ and Ni after being immersed in distilled water for 120h. The width of the Ni peaks was fairly broad, which reflects the fact that the crystallite size of Ni was extremely small.

Besides Brucite, some weak Mg₂Ni peaks were observed in the XRD pattern for the hydrolysis product of the ball-milled Mg₂Ni in the 6M KOH solution (see Fig.4.11b). The amount of Mg(OH)₂, reflected by the peak intensities in Fig.4.11b, is much more than that resulting from the hydrolysis of the surplus Mg. Although, no significant Ni peaks can be identified in Fig.4.11b, a paramagnetism test showed that there were some Ni particles in the hydrolysis product.

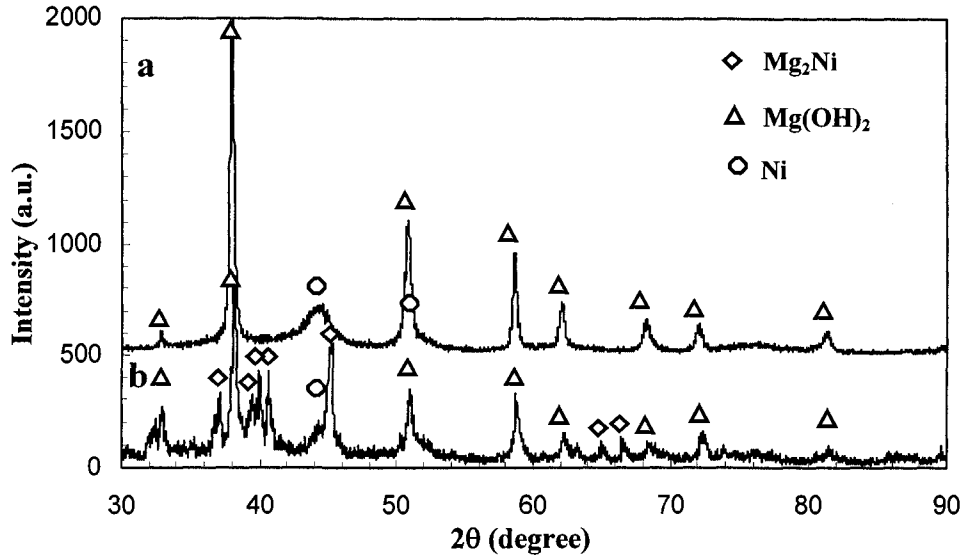
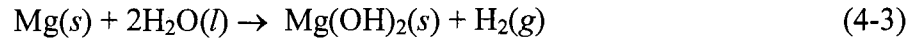


Fig.4.11 XRD powder diffraction patterns for the hydrolysis product of the as-cast Mg₂Ni particles a) in distilled water, b) in 6M KOH solution.

Mg can react with water and form Mg(OH)₂ thereby releasing hydrogen gas. The reaction can be written as follows:



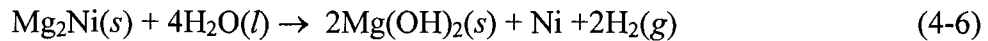
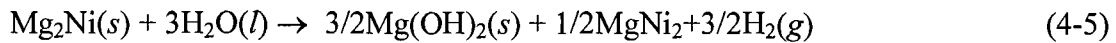
where, *s*, *l*, and *g* in brackets denote the solid, liquid and gas state, respectively. The standard free energy change for Mg(OH)₂ and H₂O are -833.7KJ/mol and -237.14KJ/mol, respectively [184]. The standard free energy change, ΔG_1° , of Reaction (4-3) is about -359.42KJ/mol. The free energy change ΔG_1 of Reaction 4-3 is given as

$$\Delta G_{4-3} = -359.42 \text{ KJ/mol} + RT \ln \frac{\alpha_{\text{Mg}(\text{OH})_2} P_{\text{H}_2}}{\alpha_{\text{Mg}} \alpha_{\text{H}_2\text{O}}^2} \quad (4-4)$$

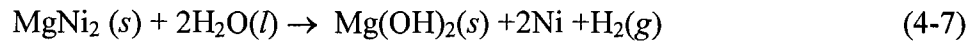
where, α is activity, and P is partial pressure.

Under the conditions of hydrolysis (abundant water and a limited amount of Mg₂Ni), two possible reactions for the hydrolysis of Mg₂Ni are as follows:

Chapter IV: The hydrogen storage properties of Mg₂Ni and the discovery of its hydrolysis behavior



Reaction (4-5) can be thought as an intermediate step of Reaction (4-6) if the further hydrolysis of MgNi₂ can take place. This reaction is given as follows:



The standard free energy change for Mg₂Ni and MgNi₂ are -51.9KJ/mol and -61.1KJ/mol, respectively [185]. The free energy changes ΔG₄₋₅, ΔG₄₋₆ and ΔG₄₋₇, are given as follows:

$$\Delta G_{4-5} = -517.78 \text{KJ/mol} + RT \ln \frac{\alpha_{\text{Mg}(\text{OH})_2}^{3/2} \alpha_{\text{MgNi}_2}^{1/2} P_{\text{H}_2}^{3/2}}{\alpha_{\text{Mg}_2\text{Ni}} \alpha_{\text{H}_2\text{O}}^3} \quad (4-8)$$

$$\Delta G_{4-6} = -666.94 \text{KJ/mol} + RT \ln \frac{\alpha_{\text{Mg}(\text{OH})_2}^2 \alpha_{\text{Ni}} P_{\text{H}_2}^2}{\alpha_{\text{Mg}_2\text{Ni}} \alpha_{\text{H}_2\text{O}}^4} \quad (4-9)$$

$$\Delta G_{4-7} = -298.32 \text{KJ/mol} + RT \ln \frac{\alpha_{\text{Mg}(\text{OH})_2} \alpha_{\text{Ni}} P_{\text{H}_2}}{\alpha_{\text{MgNi}_2} \alpha_{\text{H}_2\text{O}}^2} \quad (4-10)$$

The hydrolysis conditions in this study are room temperature and one atmosphere pressure. Therefore, the free energy changes for the reactions can be approximately considered as the standard free energy changes, if the activities are neglected. The negative standard free energy changes for Reactions 4-3, 4-4, 4-5 and 4-6 indicate that these reactions are spontaneous. The chemical affinities for Reactions 4-5, 4-6 and 4-7 are in the following order:

$$\Delta G_{4-6} < \Delta G_{4-5} < \Delta G_{4-7} \quad (4-11)$$

Therefore, Reaction 4-6 is more favourable than Reaction 4-5. In addition, if there is an intermediate Reaction 4-5, MgNi₂ should not start to hydrolyze until the hydrolysis is complete for all Mg₂Ni since Mg₂Ni is more active than MgNi₂. Both Mg₂Ni and Ni, but

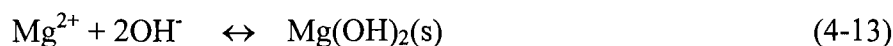
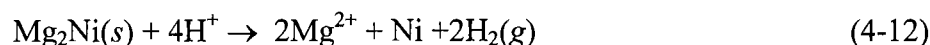
Chapter IV: The hydrogen storage properties of Mg₂Ni and the discovery of its hydrolysis behavior

not MgNi₂, were found in the hydrolysis product. Thus, Mg₂Ni probably directly hydrolyzed into Ni.

When the ball-milled Mg₂Ni particles were immersed in the distilled water, a small amount of the surplus Mg and a larger amount of Mg₂Ni gave rise to many small cells with small cathodes and large anodes. Thus, Reaction 4-3 is enhanced, and the hydrolysis reaction for Mg₂Ni was inhibited until all the Mg was consumed. At that stage, the hydrolysis of Mg₂Ni would begin.

There is not a large difference in the thermodynamics for hydrolysis between the ball-milled Mg₂Ni particles in water and in the 6M KOH solution. However, the activities of Mg(OH)₂ and H₂O are significantly affected.

Reaction 4-6 can be written as two ionic reactions:



The solubility of product constants of Mg(OH)₂ is 5.6×10^{-12} . The OH⁻ concentration is estimated as 2.237×10^{-4} . The corresponding pH value is 10.4, which agrees with the pH value (10 ~11) of the solution in the samples immersed in distilled water. Kuji *et al.*, reported that the pH value is 11.2 [174]. The pH value of the 6M KOH solution is higher than 14. Hence, the concentration of the H⁺ ions in the samples immersed in the 6M KOH solution is much lower than that of the samples immersed in water. Therefore, the hydrolysis rate of Mg₂Ni in the 6M KOH solution is much slower than that in water. In other words, if the pH value of the solution is reduced (adding some acid), the hydrolysis rate of Mg₂Ni will be greatly increased.

Chapter IV: The hydrogen storage properties of Mg_2Ni and the discovery of its hydrolysis behavior

The morphology of the hydrolyzed product of Mg_2Ni is shown in Figs.4.12. There are many spread membranes and needle-like rods shown in Fig.4.12a. These needle-like rods are rolled-up membranes (see Fig.4.12b). High-resolution TEM image of the membranes (see Fig.4-13) shows that there are many small crystallites in these membranes. The spacing of the lattice fringes for these crystallites ranges from 0.208nm to 0.248nm. The spacings of the (101) planes in $Mg(OH)_2$ and the (111) planes in Ni are 0.2367nm and 0.2035nm, respectively. Therefore, those crystallites with a lattice fringe spacing close to 0.208nm are from the (111) planes of the Ni nanoparticles and the crystallites with a lattice fringe spacing to 0.248nm are from the (111) planes of crystalline $Mg(OH)_2$. The EDS spectrum (see Fig.4.14) shows that these membranes contained a large amount of Mg and O and a small amount of Ni. In addition, these membranes should contain some hydrogen that cannot be detected by EDS. EDS examination always caused a hole in the membranes due to burning off, which suggests that the membranes contained something that can dissociate on bombardment by the electron beam.

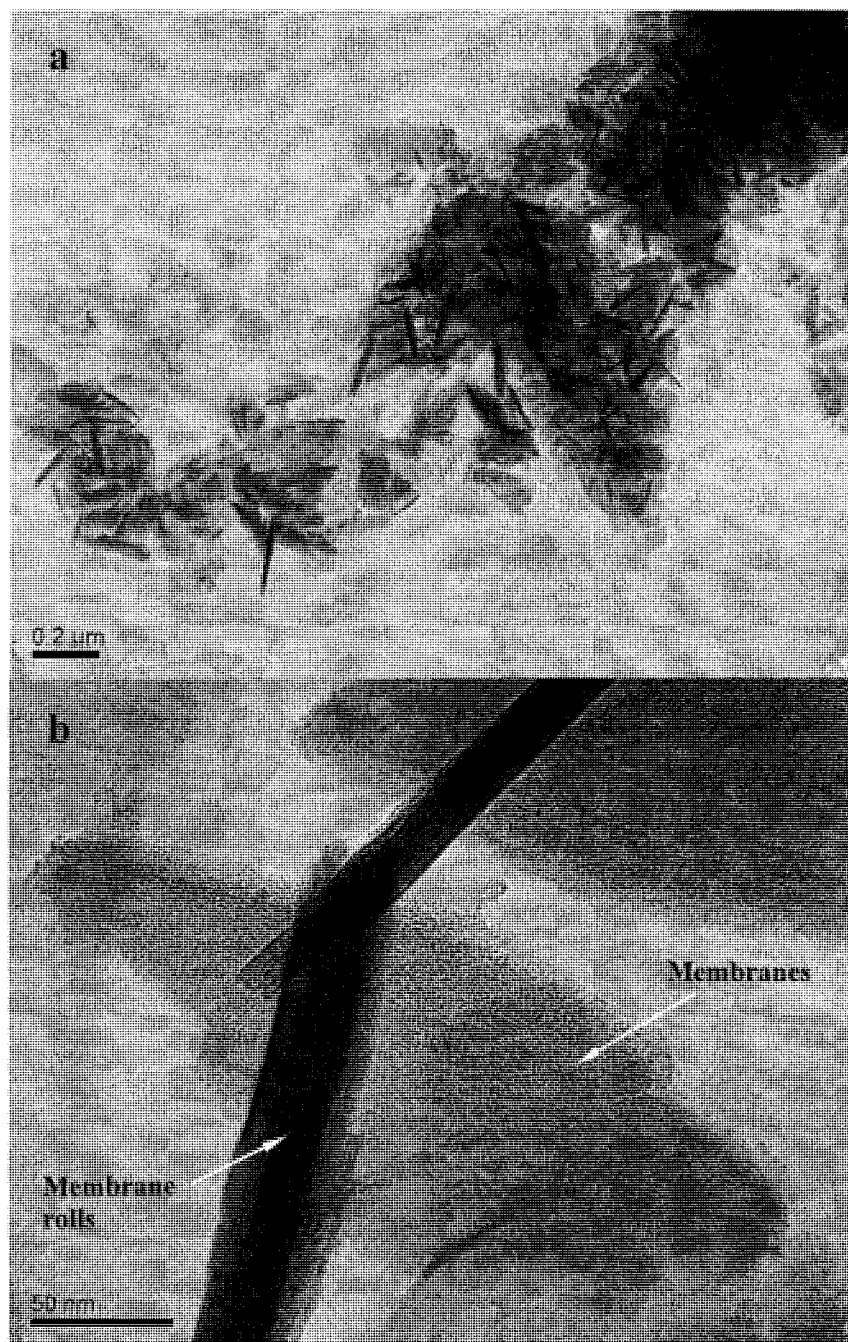


Fig.4.12 TEM images of the hydrolysis product of Mg_2Ni , a) Low magnification, b) High magnification.

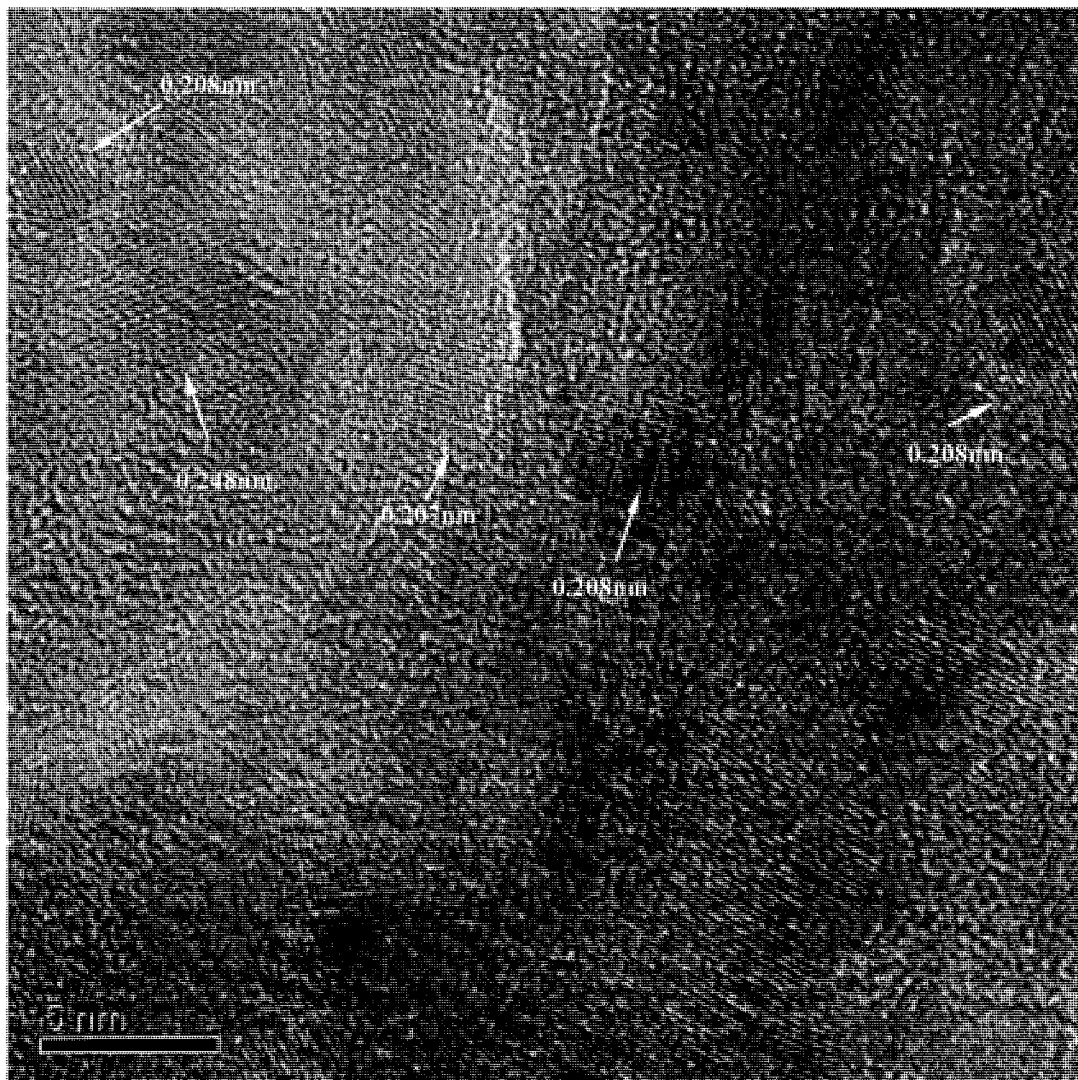


Fig.4.13 HRTEM image of the hydrolysis product of Mg_2Ni (membranes).

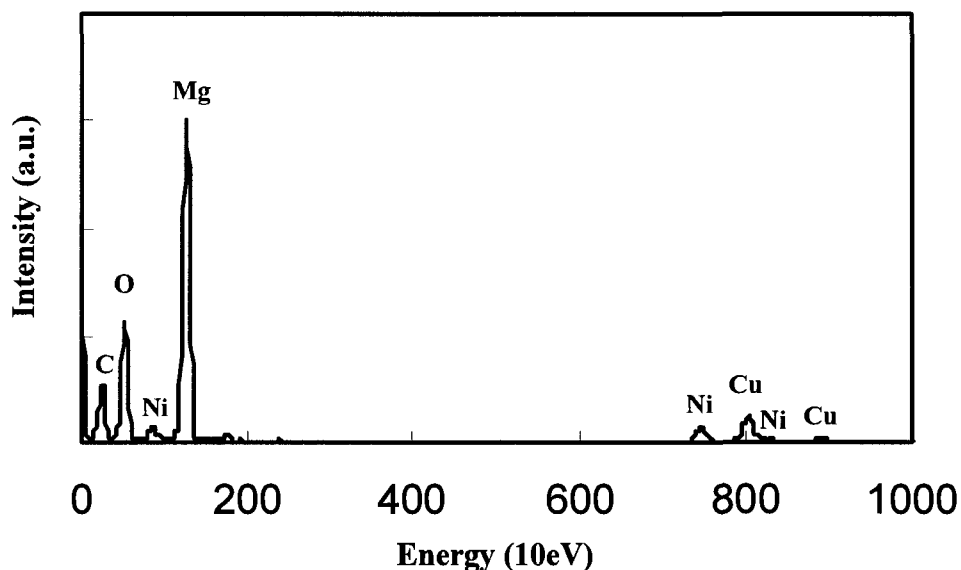


Fig.4.14 EDS spectrum of the hydrolysis product of Mg_2Ni (membranes).

Mg is more active than Mg_2Ni . Thus, Mg_2Ni will be protected from reaction with water by hydrolysis of Mg when the ball-milled Mg_2Ni particles were immersed in distilled water. Therefore, the hydrolysis reaction for Mg_2Ni was not initiated until all the Mg was consumed.

Mg_2Ni has a hexagonal structure with $a = 0.519nm$ and $c=1.322nm$ [186]. The structure is built up by square antiprisms of magnesium that are centered by Ni atoms. The antiprisms are connected via the square faces to columns [186]. Each Ni atom is surrounded by two Ni atoms at a distance of $0.26nm$ and eight Mg atoms at a distance of $0.27nm$. Each Mg atom is surrounded by four Ni atoms at a distance of $0.27nm$ and eleven Mg atoms at a distance from 0.295 to $0.33nm$ [186]. Thus, the larger magnesium atoms form a

Chapter IV: The hydrogen storage properties of Mg_2Ni and the discovery of its hydrolysis behavior

continuous skeleton, in the voids of which are situated the smaller Ni atoms. Therefore, Mg atoms in the Mg_2Ni compound are still very active.

When Mg_2Ni comes into contact with water, Mg atoms on the surface of Mg_2Ni particles will react with the OH^- ions in water, and form $Mg(OH)_2$. At the same time, the Ni atoms were released from the Mg_2Ni . The Ni atoms have a very weak affinity to the excess H^+ ions resulting from the consumption of the OH^- ions. However, the Ni atoms combine together to form Ni nanoparticles under the action of surface energy, and the H^+ ions combine together to generate hydrogen gas.

The solubility of $Mg(OH)_2$ in water is very small. The newly-formed $Mg(OH)_2$ has to precipitate from water in the vicinity of the Mg dissolution sites. The existence of the $Mg(OH)_2$ particles, and the low mobility of Ni atoms at room temperature, give rise to the formation of very fine Ni nanoparticles (see Fig.4.13). Therefore, the particle size of Ni nanoparticles prepared by this method was not sensitive to the concentration of Mg_2Ni in aqueous solution.

The byproduct of Mg_2Ni hydrolysis, $Mg(OH)_2$, can be easily removed by a dilute acid. After the $Mg(OH)_2$ in the hydrolysis product of Mg_2Ni in distilled water was carefully removed using dilute hydrochloric acid, Ni nanoparticles in the hydrolysis product were left. The hydrolysis of Mg_2Ni could thus provide a new and relatively simple method for the production of nickel nanoparticles. This will be discussed in more detail in Chapter 5.

4.6 Hydrolysis behavior of the in-situ synthesized Mg_2NiH_4

While the synthesized Mg_2NiH_4 powders were immersed in 500ml of 6M KOH solution or distilled water, the hydrogen release from the Mg_2NiH_4 samples was much more severe

Chapter IV: The hydrogen storage properties of Mg_2Ni and the discovery of its hydrolysis behavior

than for the Mg_2Ni samples. Sometimes, the Mg_2NiH_4 samples would catch fire due to the severe hydrolysis reaction. The release rate of hydrogen bubbles then gradually slowed down. After the synthesized Mg_2NiH_4 particles were immersed in 500ml of distilled water or 6M KOH for 120h, the solid particles were filtered out, and then dried in a Rotavapor at 60°C (no rinse cycle).

Only Brucite, Ni and few Mg_2NiH_4 peaks were found in the XRD pattern for the hydrolysis product of the synthesized Mg_2NiH_4 in distilled water (see Fig.4.15a). No Mg_2Ni peaks were detected, which shows that Mg_2NiH_4 had hydrolyzed into $Mg(OH)_2$ and Ni after being immersed in distilled water for 120h.

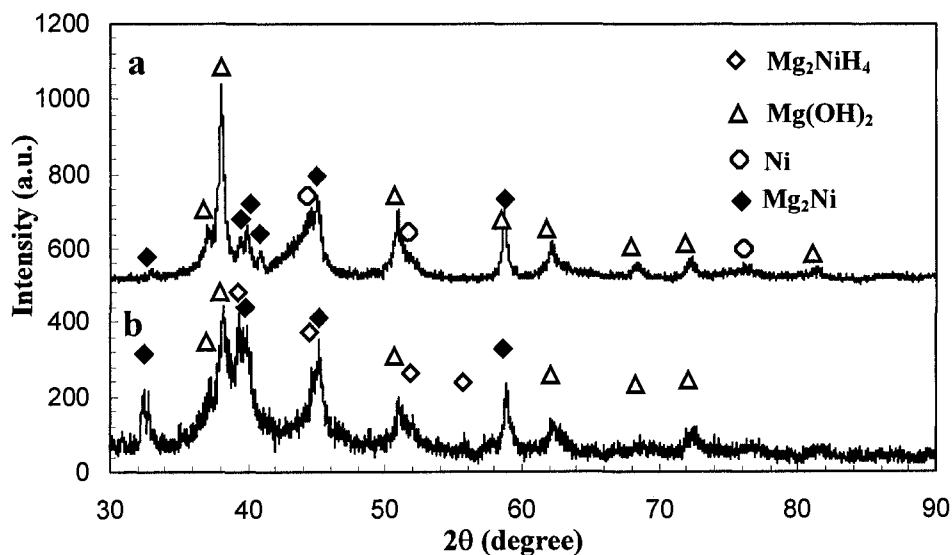


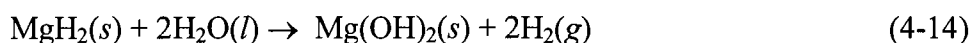
Fig.4.15 XRD powder diffraction patterns for a) the hydrolysis product of the synthetic Mg_2NiH_4 particles in distilled water, b) the hydrolysis product of the synthetic Mg_2NiH_4 particles in 6M KOH solution.

Chapter IV: The hydrogen storage properties of Mg₂Ni and the discovery of its hydrolysis behavior

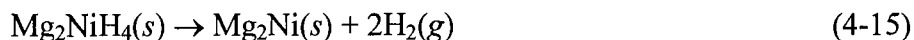
Mg(OH)₂, Mg₂Ni, and Mg₂NiH₄ peaks were observed in the XRD pattern for the hydrolysis product of Mg₂NiH₄ in the 6M KOH solution (see Fig.4.15b). As was the case for the Mg₂Ni sample in the alkaline solution, no significant Ni peaks were observed in the XRD pattern, Fig.4.15b. However, Ni particles were detected in the hydrolysis product using the paramagnetism test.

This may be explained as follows: The hydrolysis products (Mg(OH)₂ and Ni particles) are extremely fine. Hence, their diffraction peaks are of low intensity, and are broad. The amount of Mg(OH)₂ is relatively higher than Ni because of the surplus Mg in the initial material. Some of the Ni peaks also overlap with peaks from Mg(OH)₂ and Mg₂Ni.

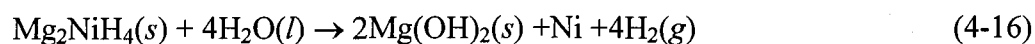
MgH₂ and Mg₂NiH₄ in the hydrogenated samples can react with water and form Mg(OH)₂, and release hydrogen gas. The reaction can be written as follows:



The XRD patterns for the hydrolysis product of Mg₂NiH₄ in water and the alkaline solution suggest that Mg₂NiH₄ first dissociated into Mg₂Ni and hydrogen. The dehydrogenation of Mg₂NiH₄ can be written as:



The Mg₂Ni will further hydrolyze into Mg(OH)₂ and Ni in water or an alkaline solution (Reaction 4-6). The overall reaction for the Mg₂NiH₄ hydrolysis is:



The standard free energy change for MgH₂ and Mg₂NiH₄ are -35.9KJ/mol, -64.4KJ/mol, respectively [187]. The free energy changes ΔG_{4-14} , ΔG_{4-15} and ΔG_{4-16} for Reactions 4-14, 4-15 and 4-16 are given as:

Chapter IV: The hydrogen storage properties of Mg₂Ni and the discovery of its hydrolysis behavior

$$\Delta G_{4-14} = -323.52 \text{ KJ / mol} + RT \ln \frac{\alpha_{Mg(OH)_2} P_{H_2}^2}{\alpha_{MgH_2} \alpha_{H_2O}^2} \quad (4-17)$$

$$\Delta G_{4-15} = 12.5 \text{ KJ / mol} + RT \ln \frac{\alpha_{Mg_2Ni} P_{H_2}^2}{\alpha_{Mg_2NiH_4}} \quad (4-18)$$

$$\Delta G_{4-16} = -654.44 \text{ KJ / mol} + RT \ln \frac{\alpha_{Mg(OH)_2}^2 \alpha_{Ni} P_{H_2}^4}{\alpha_{Mg_2NiH_4} \alpha_{H_2O}^4} \quad (4-19)$$

From a thermodynamics point of view, the hydrolysis of Mg is easier than MgH₂ since $\Delta G_{4-3} < \Delta G_{4-15}$. However, it was observed that the hydrolysis of MgH₂ is more severe than for Mg regardless of whether it is in water or in an alkaline solution. Possible reasons for this behaviour are as follows: There is a volume expansion of 32% accompanying the transition from hcp Mg to rutile MgH₂. Hence, the chemical bonds in MgH₂ are greatly weakened. In addition, MgH₂ is an ionic compound, which is relatively easily affected by the ionic water molecules.

Mg₂NiH₄ has a monoclinic antiferroite structure, built of an irregular tetrahedral [NiH₄] complex surrounded by a distorted cube of magnesium ions [169]. H atoms prefer to be located in the neighbourhood of the Ni atoms and are covalently bonded with Ni forming a complex of nominal composition NiH₄. The NiH₄ is ionically bonded to magnesium [188]. The ionic characteristic of Mg₂NiH₄ may be the reason for the release of hydrogen on immersion in water.

The hydrolysis characteristics of Mg₂Ni and Mg₂NiH₄ in water and in alkaline solutions may be the reason for the rapid degradation and a poor cycle life of Mg₂Ni in alkaline solution. Hence, Mg₂Ni is not suitable for use as electrodes in rechargeable batteries. In addition, their electrochemical discharge capacities cannot be improved through

Chapter IV: The hydrogen storage properties of Mg_2Ni and the discovery of its hydrolysis behavior

generating nano-crystalline Mg_2Ni since reducing the Mg_2Ni particle size will accelerate the hydrolysis rate.

4.6 Summary

The main conclusions from this study are as follows:

1. The in-situ synthesized Mg_2Ni particles did not reach their maximum hydrogen storage capacity (3.6wt%) on the first hydrogenation cycle at 280°C and 300°C due to the limitations of the hydrogen diffusion kinetics.
2. Both the in-situ synthesized Mg_2Ni and the as-cast Mg_2Ni exhibited a near zero charge/discharge capacity.
3. When Mg_2Ni is immersed in water or in an alkaline solution, it will spontaneously react with water to form $Mg(OH)_2$, Ni and hydrogen.
4. When Mg_2NiH_4 is immersed in water or in an alkaline solution, it will spontaneously first dissociate into Mg_2Ni and hydrogen. The Mg_2Ni will then further hydrolyze into $Mg(OH)_2$ and Ni.
5. Reducing the pH value of the solution (adding an acid) will accelerate the hydrolysis of Mg_2Ni and Mg_2NiH_4 .
6. The hydrolysis characteristics of Mg_2Ni and Mg_2NiH_4 suggest that they are not suitable for use as electrodes in rechargeable batteries.

CHAPTER FIVE: HYDROLYSIS BEHAVIOUR OF Ni MAGNIDES AND ITS APPLICATION TO THE SYNTHESIS OF Ni NANOPARTICLES

5.1 Introduction

As has been discussed in Chapter 4, High-resolution TEM images show that there were many nanocrystallites in the hydrolysis product of Mg_2Ni . Besides amorphous $Mg(OH)_2$, some of these nanocrystallites were Ni. If the hydrolysis byproduct of Mg_2Ni , $Mg(OH)_2$, is carefully removed by a dilute acid, Ni nanoparticles are left. Therefore, the hydrolysis of Mg_2Ni can be utilized to produce Ni nanoparticles. The characteristics of the Ni nanoparticles prepared by a hydrolysis method are reported in detail in this chapter.

Besides Mg_2Ni , there is another intermetallic compound, $MgNi_2$, in the binary Mg-Ni system. $MgNi_2$ has a hexagonal C36 structure. The stacking of the Mg dimers is ABACABAC. Although, $MgNi_2$, a Ni-rich phase, does not have a continuous Mg skeleton like Mg_2Ni , Mg atoms form a series of continuous layers in the $MgNi_2$ structure[189]. This kind of lattice structure may be helpful for the hydrolysis of $MgNi_2$. It was thus thought that an investigation of the hydrolysis of $MgNi_2$ would help us further understand whether hydrolysis is a common phenomenon for magnides.

5.2 Synthesis of Ni nanoparticles by hydrolysis of Mg_2Ni

The $Mg(OH)_2$ in the hydrolysis product of Mg_2Ni in distilled water for 120h was carefully removed using dilute hydrochloric acid. After the soluble $MgCl_2$ was rinsed away, three characteristic peaks in the XRD pattern for the final solid product were indexed as the face-centered cubic (FCC) structure of Ni, in accordance with the reported XRD data (JCPDS file No. 65-2865) as shown in Fig.5.1. Some very small theophrastite ($Ni(OH)_2$, JCPDS file No. 14-0117) peaks were identified (see Fig.5.1), which suggests that the final product consisted of Ni and a small amount of $Ni(OH)_2$.

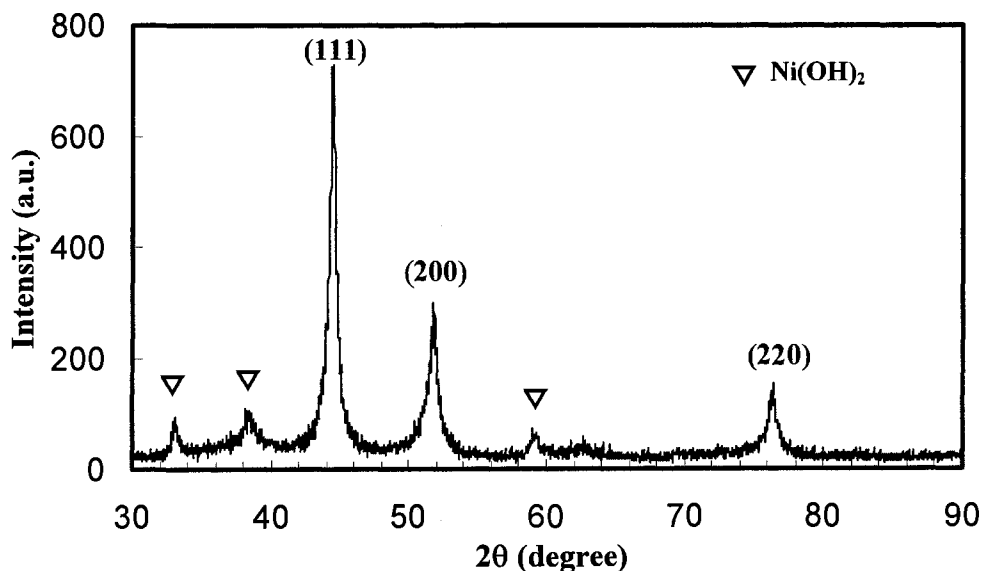


Fig.5.1 XRD powder diffraction patterns for Ni nanoparticles produced by hydrolysis of Mg_2Ni .

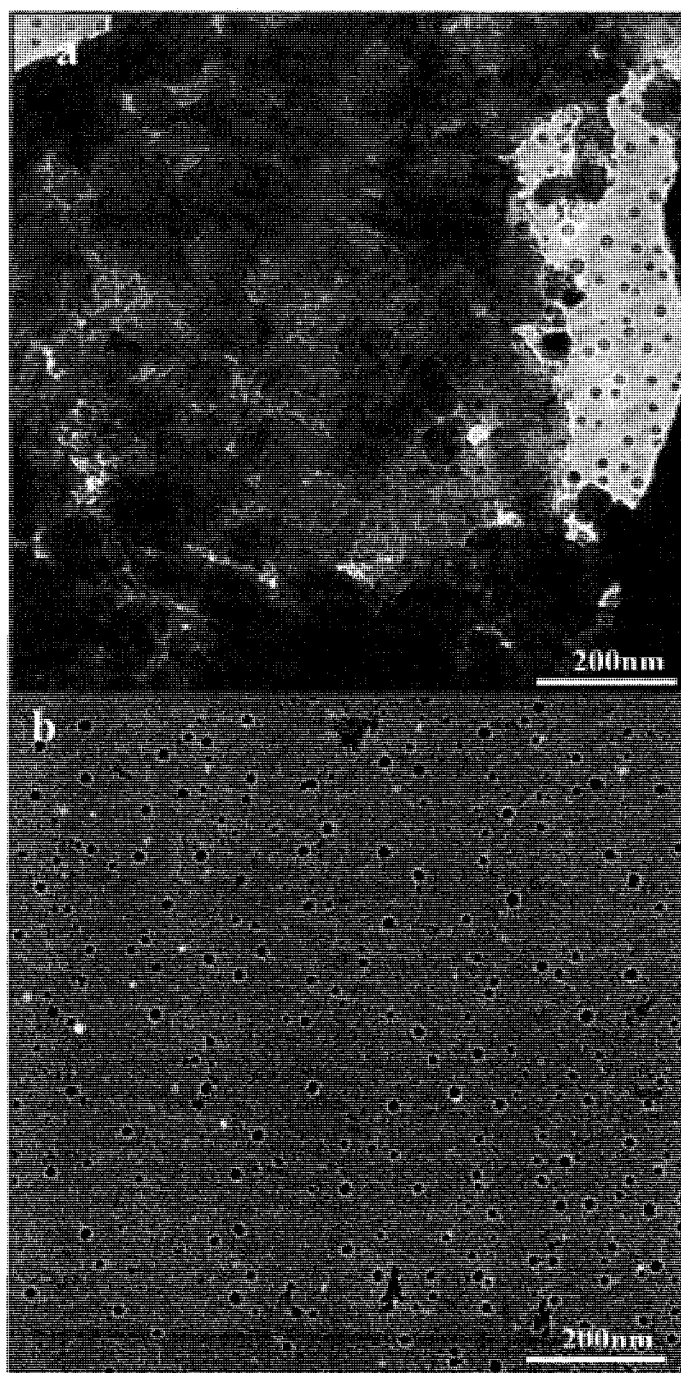


Fig.5.2 TEM images of Ni nanoparticles, a) a cluster of Ni nanoparticles, b) discrete Ni nanoparticles.

Chapter V. Hydrolysis behaviour of Ni magnides and its application to the synthesis of Ni nanoparticles

Since no surfactant was used in these experiments, and the Ni particles resulting from the hydrolysis of Mg_2Ni were very small, the Ni particles generally agglomerated together after they were stored in solution for several days (see Fig.5.2a). However, some discrete Ni particles could occasionally be observed (see Fig.5.2b). These discrete Ni particles are close to spherical in shape and have a size of about 10 nm. Fig.5.3 shows that these nanoparticles are Ni nanoparticles because the spacing of the lattice fringes was about 0.208nm (the spacing of the (111) planes). The spacing of the lattice fringes for the particles in Fig.5.4 was 0.174nm, which is close to 0.176nm, the spacing of the (200) planes in Ni. Five small facets can be observed in the Inverse Fast Fourier Transform image at the upper-right corner of Fig.5.4, which suggests that some Ni nanoparticles were polyhedrons.

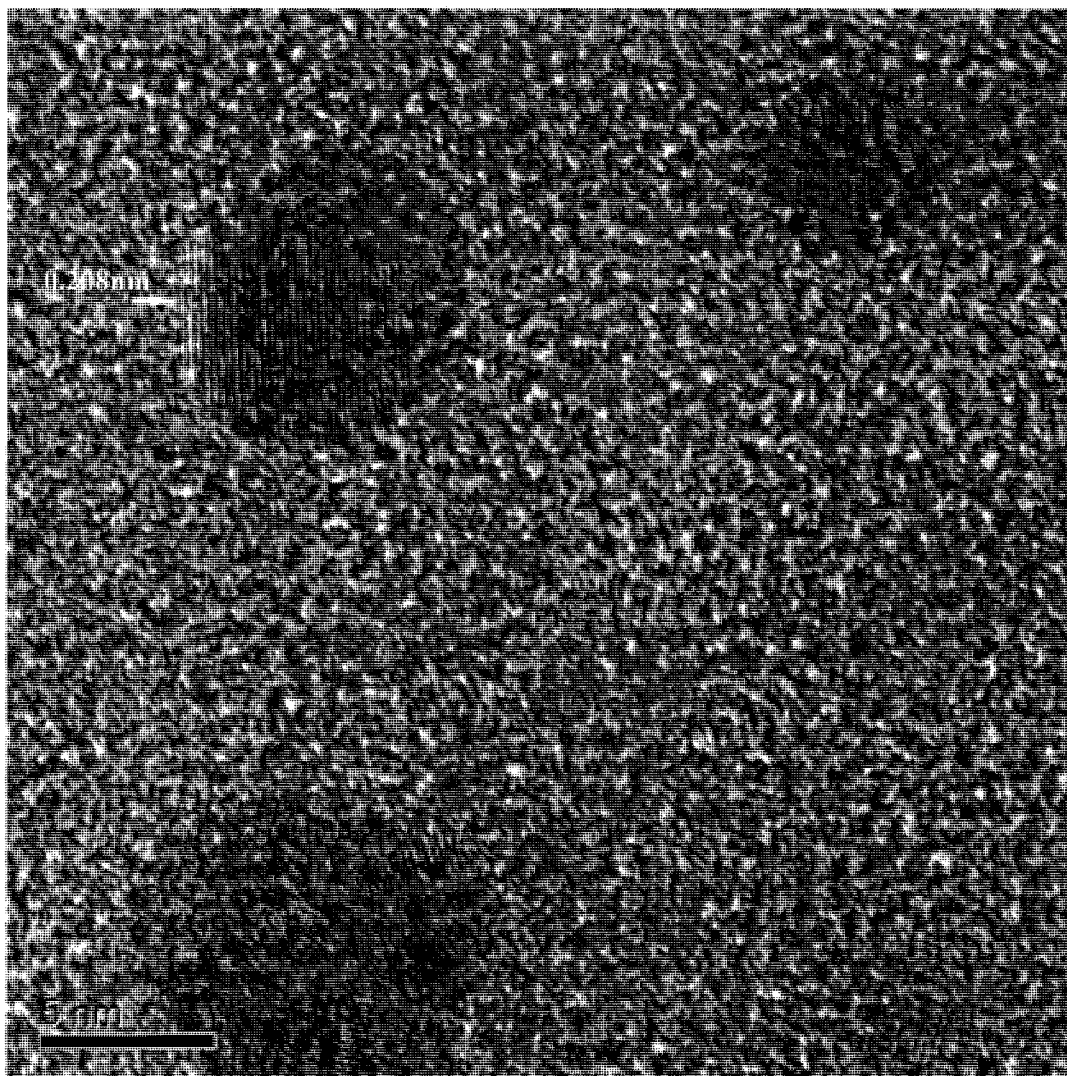


Fig.5.3 HRTEM image of individual Ni nanoparticles.

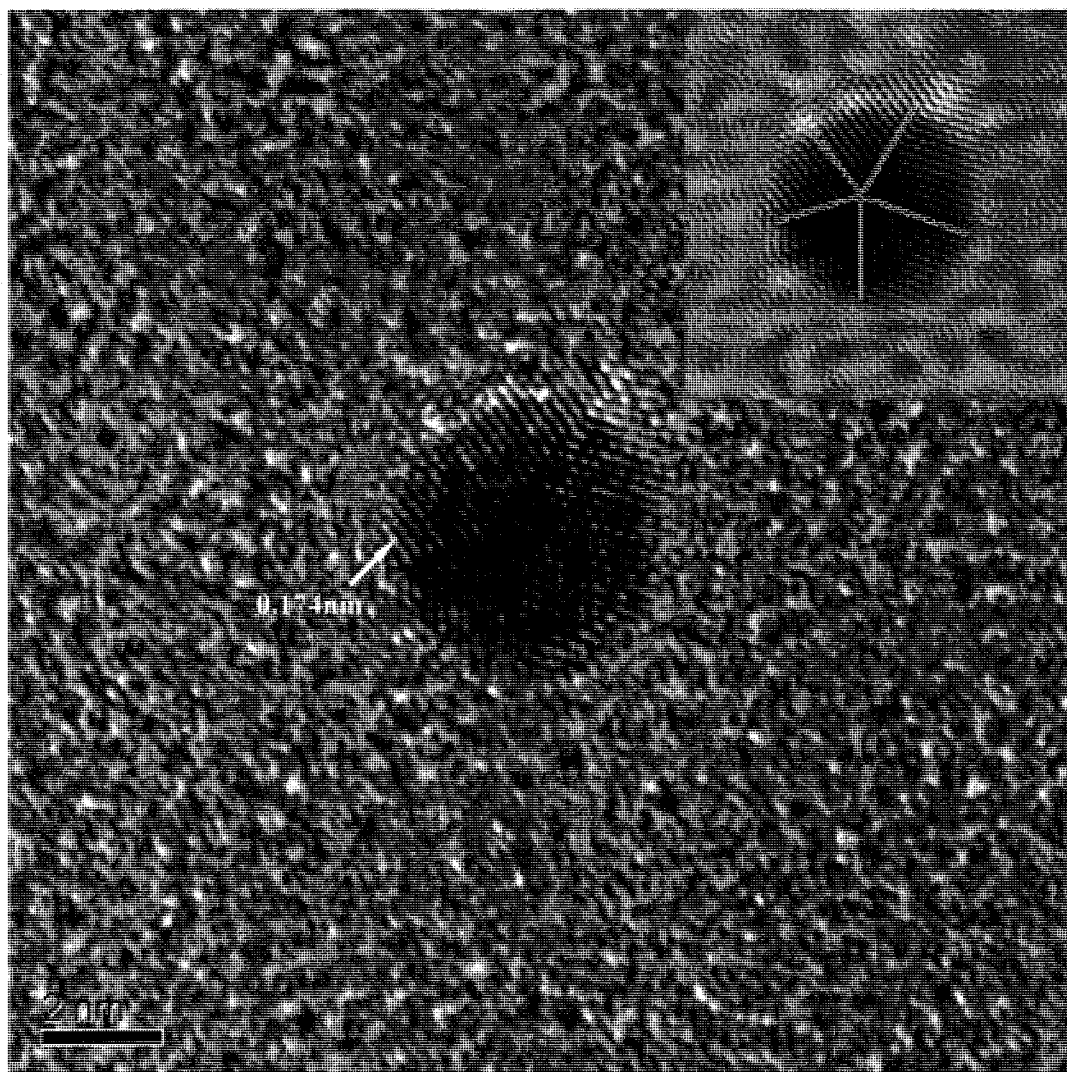


Fig. 5.4 HRTEM image of individual Ni nanoparticle (corresponding Inverse Fast Fourier Transform image at the upper-right corner).

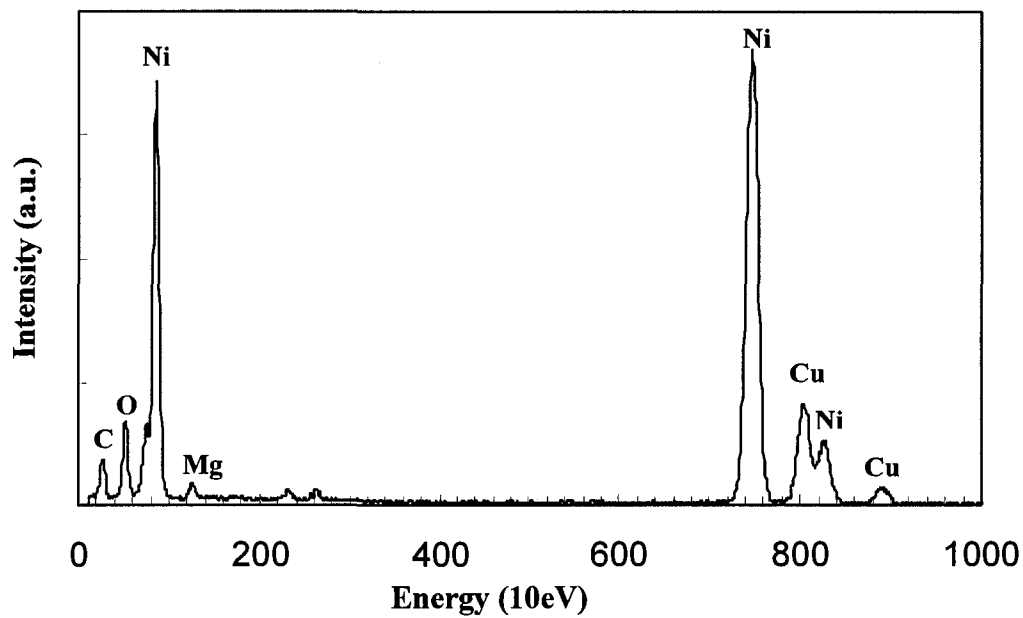


Fig.5.5 EDS spectrum of Ni nanoparticles produced by hydrolysis of Mg_2Ni .

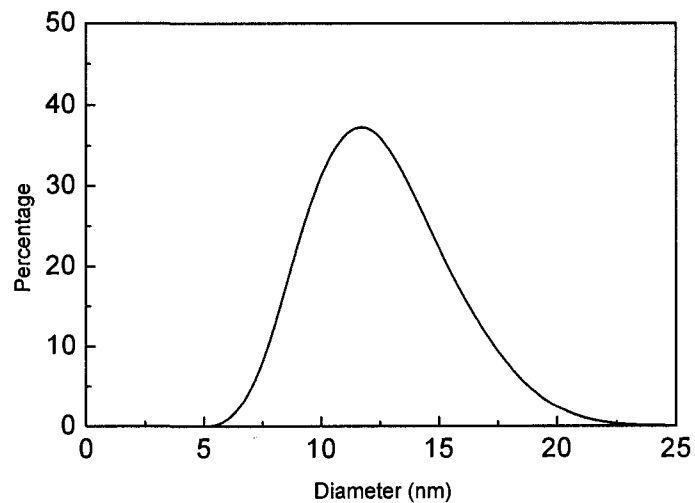


Fig.5.6 Particle size distribution of Ni nanoparticles produced by hydrolysis of Mg_2Ni .

Chapter V. Hydrolysis behaviour of Ni magnides and its application to the synthesis of Ni nanoparticles

The result of EDS analysis(see Fig.5.5) shows that some Mg and oxygen impurities are present in the Ni nanoparticles. Some of these impurities came from any remaining $Mg(OH)_2$, and some oxygen impurities could come from $Ni(OH)_2$.

Fig.5.6 shows that the size of the Ni particles ranged from several nanometers to around 20nm with a mean size of 11.7nm.

Fig. 5.7 shows the nitrogen adsorption and desorption curves for the Ni particles. Calculations based on the curves suggest that the specific surface area of the Ni particles is $43.99m^2/g$. The theoretical mean diameter is about 15.3nm on the basis of the specific surface area if the Ni nanoparticles were assumed to be a spherical with the same diameter, which is slightly higher than the mean diameter (11.7nm) measured by a Zetasizer 3000HS instrument (no drying). The difference could result from the drying process.

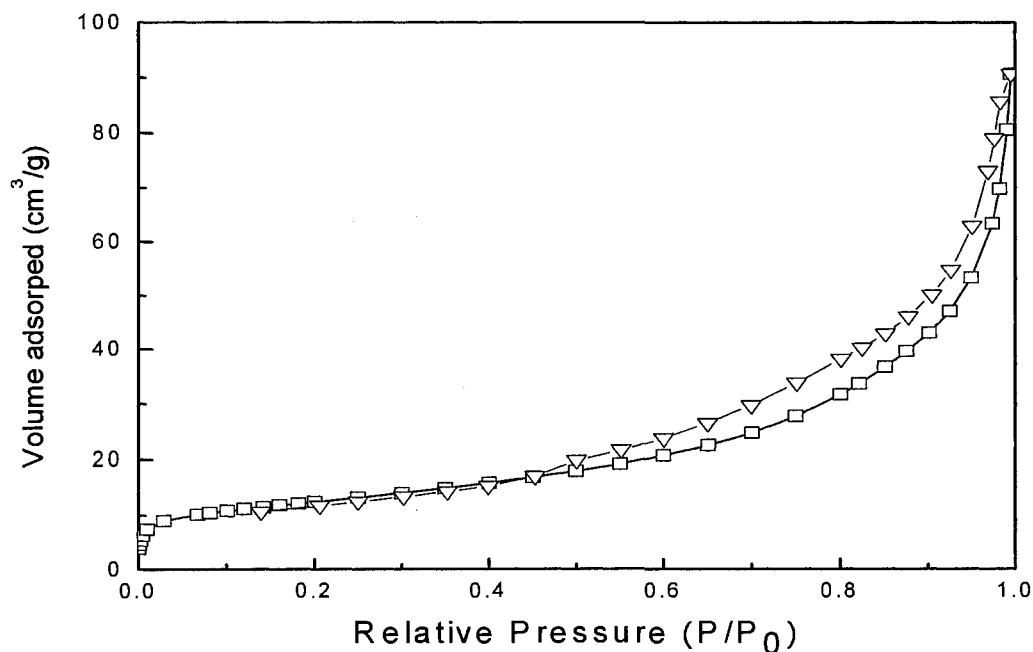


Fig.5.7 Nitrogen adsorption (□) and desorption (▽) curves of Ni nanoparticles at 77.2 K.

The high chemical affinity of the magnesium atoms in the Mg_2Ni compound to oxygen leads to the selective oxidation of magnesium and protects the newly formed Ni nanoparticles from oxidation. Hence, before the Mg_2Ni particles are totally consumed by hydrolysis, the Ni nanoparticles will not oxidize and will have an opportunity to grow in size. After all the Mg_2Ni particles are consumed, the protection of Ni nanoparticles from oxidation will be lost. The Ni nanoparticles could then be oxidized by the dissolved oxygen in the solution during hydrolysis and removal of $Mg(OH)_2$ by using dilute acid. The oxidation reaction is as follows:



Chapter V. Hydrolysis behaviour of Ni magnides and its application to the synthesis of Ni nanoparticles

Ni(OH)_2 is a weak alkali. A decrease in the acidity of the solution would reduce the oxidation rate of the Ni nanoparticles.

It is generally thought that Ni(OH)_2 is formed on the surfaces of Ni nanoparticles because of the oxidation of Ni nanoparticles in the solution. Only very small Ni crystallites were observed in the hydrolysis product. This means that Ni nanoparticles could be growing in size during removal of Mg(OH)_2 .

The formation of a layer of Ni hydroxide on the surface of the Ni nanoparticles might give rise to a growth arrest of the Ni nanoparticles. Hence, the Ni nanoparticle size is determined by the temperature and the concentration of both Mg_2Ni and oxygen.

The oxidation of any Ni nanoparticles prepared by the hydrolysis method requires dissolved oxygen. If there is no dissolved oxygen in solution, Reaction 5-1 can not take place. Therefore, if all preparation procedures were carried out in a near-zero oxygen environment, Ni nanoparticles with low oxygen content could be synthesized by this method.

5.3 Hydrolysis of MgNi_2

Mg and Ni powders with a 1:3 weight ratio were blended for 1 hour under an argon atmosphere. The mixture was melted at 900°C for 2 hours in a mild steel crucible under a protective gas (Sulfur Hexafluoride SF_6 0.5% + Carbon Dioxide CO_2).

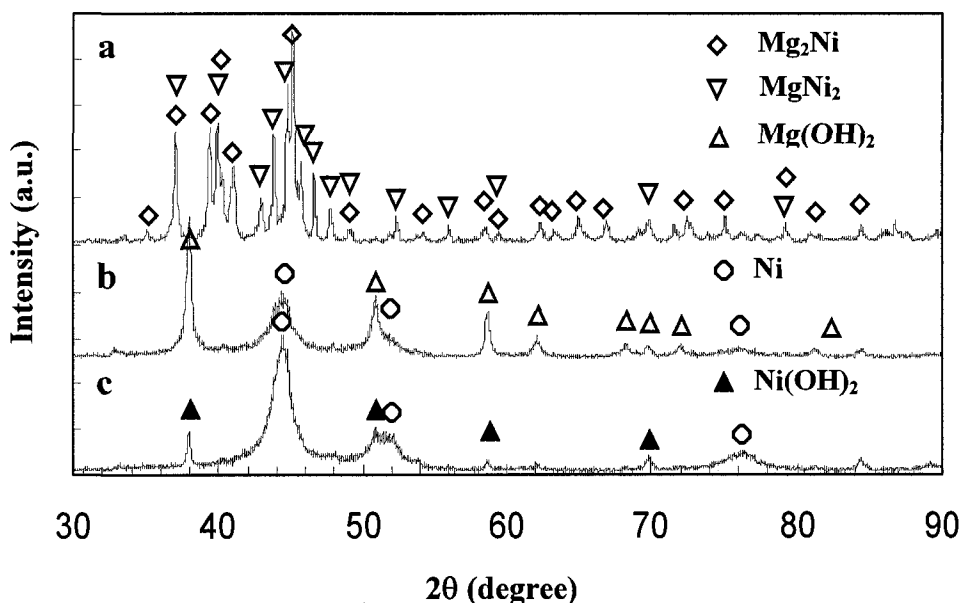


Fig.5.8 Powder XRD patterns for a) the as-cast MgNi₂ alloy, b) its hydrolysis product in distilled water for 120h, c) Ni nanoparticles.

In order to avoid formation of the Ni solid solution phase due to the segregation of Ni, and the loss of magnesium (evaporation and oxidation) at high temperatures during preparation, a composition of 75wt% Ni and 25wt%Mg was selected in this study. As a result, the as-cast MgNi₂ alloys consist of both Mg₂Ni and MgNi₂ compounds (see Fig.5.8a). No Ni diffraction peaks were observed in Fig.8a, which shows that all Ni powders in the initial materials were totally converted into Mg₂Ni or MgNi₂ during melting and casting.

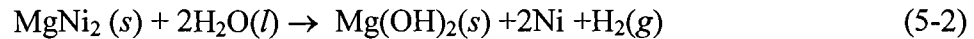
The as-cast MgNi₂ ingot was ball-milled for 2 hour under an argon atmosphere. 10 grams of the ball-milled as-cast MgNi₂ powders was used for the hydrolysis experiment. Once the ball-milled MgNi₂ powders were immersed in 500ml distilled water, many fine hydrogen bubbles were immediately released. The hydrolysis of MgNi₂ was similar to

Chapter V. Hydrolysis behaviour of Ni magnides and its application to the synthesis of Ni nanoparticles

that of Mg₂Ni, but milder. The PH value for the solution is also about 10 to 11 because the solubility of product constants of Mg(OH)₂ is 5.6×10^{-12} .

The XRD results (see Fig.5.8b) suggest that the hydrolysis product of the ball-milled MgNi₂ particles consisted of Mg(OH)₂ and Ni. In other words, both Mg₂Ni and MgNi₂ were hydrolyzed into Mg(OH)₂ and Ni at room temperature. The broad Ni diffraction peaks suggest that the crystallite size of Ni nanoparticles prepared by hydrolysis of MgNi₂ was fairly small. No MgNi₂ diffraction peaks were observed in Fig.5.8b, which shows that the hydrolysis of MgNi₂ was complete after being immersed into distilled water and stirred for 120h.

A possible reaction for the hydrolysis of MgNi₂ is given as follows:



The standard formation enthalpies and the standard entropies for Mg(OH)₂, H₂O, and MgNi₂ are -924.7KJ/mol and 63.24J/°C•mol, -285.53 KJ/mol and 69.95J/°C•mol[184, 185], and are -56.47 KJ/mol and 88.68 J/°C•mol, respectively. The standard entropies for Ni and H₂ are 29.85J/°C•mol and 130.68 J/°C•mol, respectively. The free energy change ΔG_1 for Reaction 5-2 is as follows:

$$\Delta G_{5-2} = -304.65 \text{ KJ/mol} + RT \ln \frac{\alpha_{\text{Mg(OH)}_2} \alpha_{\text{Ni}}^2 P_{\text{H}_2}}{\alpha_{\text{MgNi}_2} \alpha_{\text{H}_2\text{O}}^2} \quad (5-3)$$

From a thermodynamics viewpoint, the hydrolysis reaction of MgNi₂ is spontaneous.

The morphology of the hydrolysis product of MgNi₂ is shown in Fig.5.9. There are many membranes and needle-like rods in the hydrolysis product. In fact, these needle-like rods are rolled-up membranes. The morphology of the hydrolysis product of MgNi₂ was very similar to that of Mg₂Ni.

Chapter V. Hydrolysis behaviour of Ni magnides and its application to the synthesis of Ni nanoparticles

High-resolution TEM images of the membranes (see Figs.5.10a and 5.10b) shows that there are many small crystallites in these membranes. The spacing of the lattice fringes for these crystallites in the rim of the membranes (see Fig.5.10a) ranged from 0.228nm to 0.247nm, which is close to 0.2367nm, the spacings of the (101) planes in $\text{Mg}(\text{OH})_2$. Sometimes, irregular crystallites can be observed in the membranes as shown in Fig.5.10b. The spacing of the lattice fringes for these crystallites was about 0.208nm, which close to 0.2035nm, the (111) plane spacing in Ni. Therefore, those crystallites with a lattice fringe spacing close to 0.208nm were from the (111) planes of the Ni nanoparticles and the crystallites with a lattice fringe spacing ranged from 0.228nm to 0.247nm were from the (101) planes of crystalline $\text{Mg}(\text{OH})_2$.

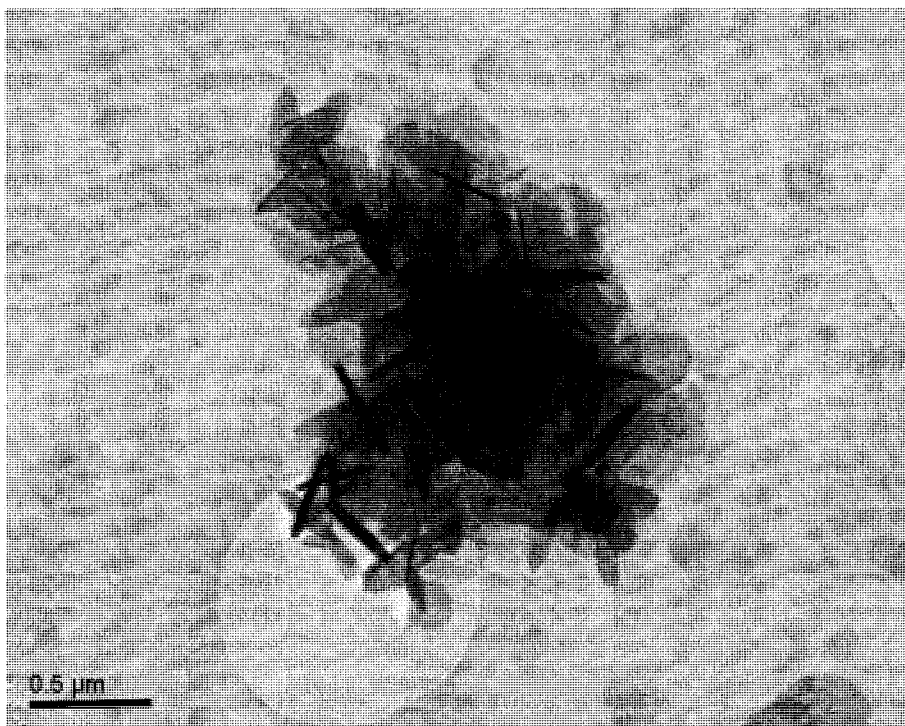


Fig.5.9 TEM image of the hydrolysis product of MgNi_2 .

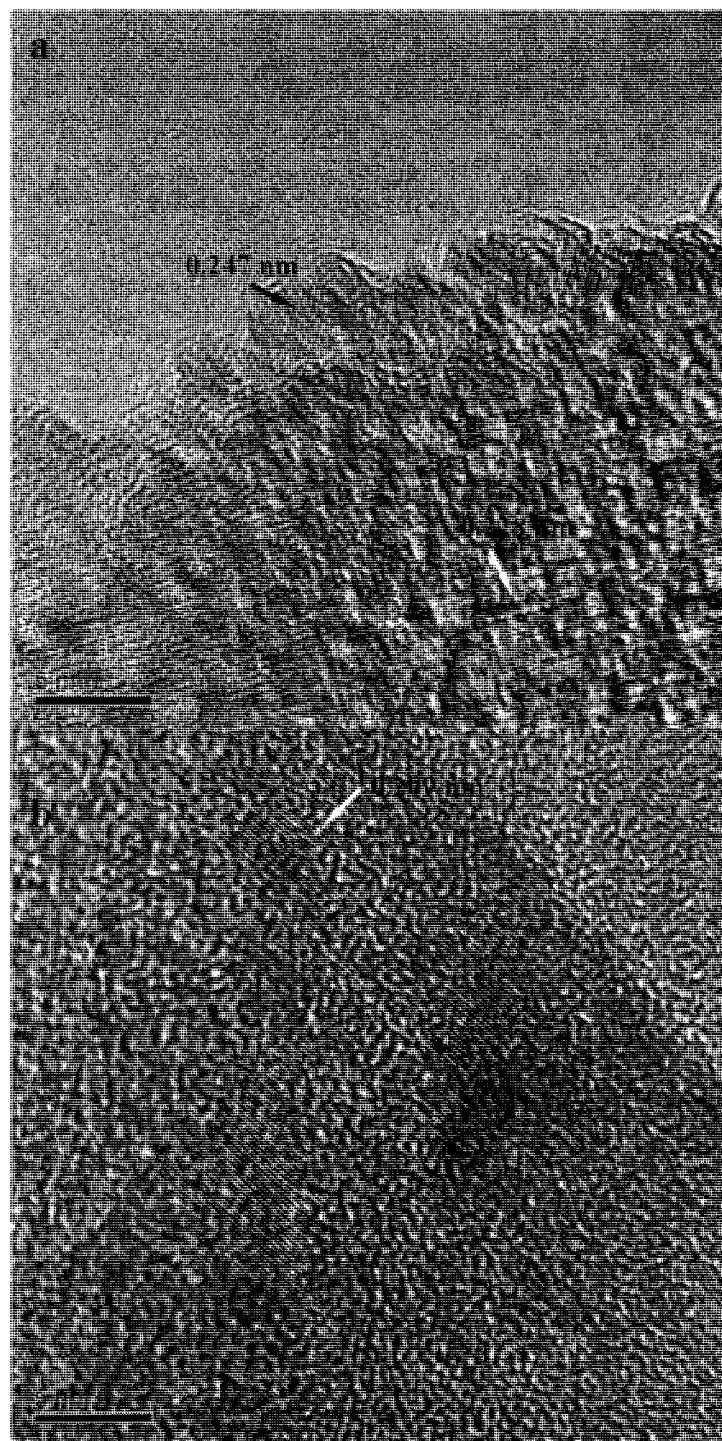


Fig.5.10 High resolution TEM image of (a) $\text{Mg}(\text{OH})_2$, and b) Ni nanoparticles in the hydrolysis product of MgNi_2 .

The EDS spectrum of the hydrolysis product (see Fig.5.11) shows that these membranes contained Mg and O and Ni. In addition, these membranes should contain some hydrogen that cannot be detected by EDS due to the limitation of test technology.

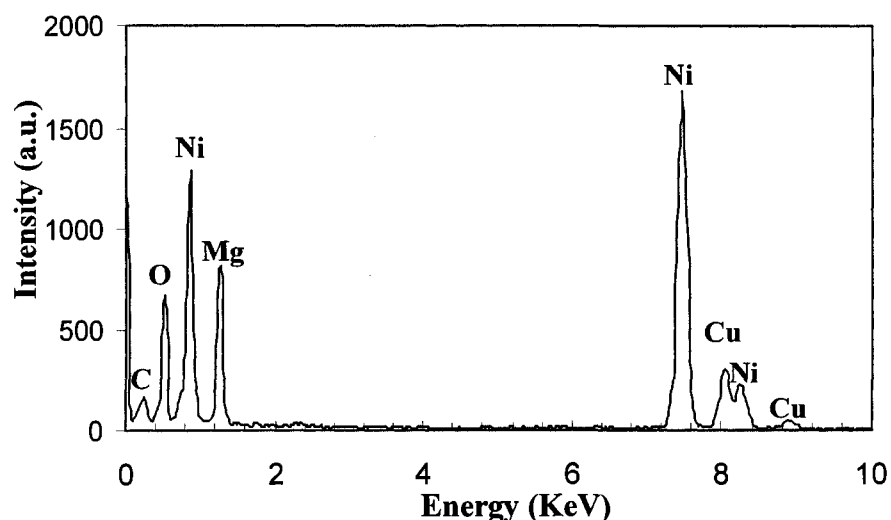


Fig.5.11 EDS spectrum of the hydrolysis product of $MgNi_2$ (membranes).

5.4 Synthesis of Ni nanoparticles by hydrolysis of $MgNi_2$

After the ball-milled $MgNi_2$ powders were immersed in distilled water and stirred for 48h, 0.5M hydrochloric acid was very slowly added in the solution till the pH value of the solution remained stable at 5-6. As a result, the by-product ($Mg(OH)_2$) was totally dissolved and formed soluble $MgCl_2$. Subsequently, the $MgCl_2$ was rinsed out using distilled water, followed by ethanol.

The XRD results show that Ni and a small amount of $Ni(OH)_2$ were present in the final product (see Fig.5.8c). The crystalline nature of the Ni nanoparticles was confirmed from these Ni peaks in the XRD pattern in Fig.5.8c.

Chapter V. Hydrolysis behaviour of Ni magnides and its application to the synthesis of Ni nanoparticles

The oxidation behavior of Ni nanoparticles prepared by hydrolysis of MgNi_2 was very similar to that produced by Mg_2Ni . The newly formed Ni nanoparticles in an aqueous solution would readily react with the dissolved oxygen to form Ni(OH)_2 after the hydrolysis of MgNi_2 was totally complete. Any oxidation of the Ni nanoparticles requires the presence of dissolved oxygen. Therefore, Ni nanoparticles with a low oxygen content can be produced by this method in a near-zero oxygen environment.

The morphology of Ni nanoparticles after removal of Mg(OH)_2 were close to spherical in shape with a size of about 10nm (see Figs 5.12a and 5.12b). High-resolution TEM image (see Fig.5.13) confirm that these nanoparticles were Ni nanoparticles because the spacing of the lattice fringes was about 0.208nm. The spherical shape of the Ni nanoparticles was significantly different from the irregular Ni nanoparticles in the hydrolysis product (Fig.5.10). The results suggest that the Ni atoms on the surface of the Ni nanoparticles had undergone rearrangement during removal of Mg(OH)_2 .

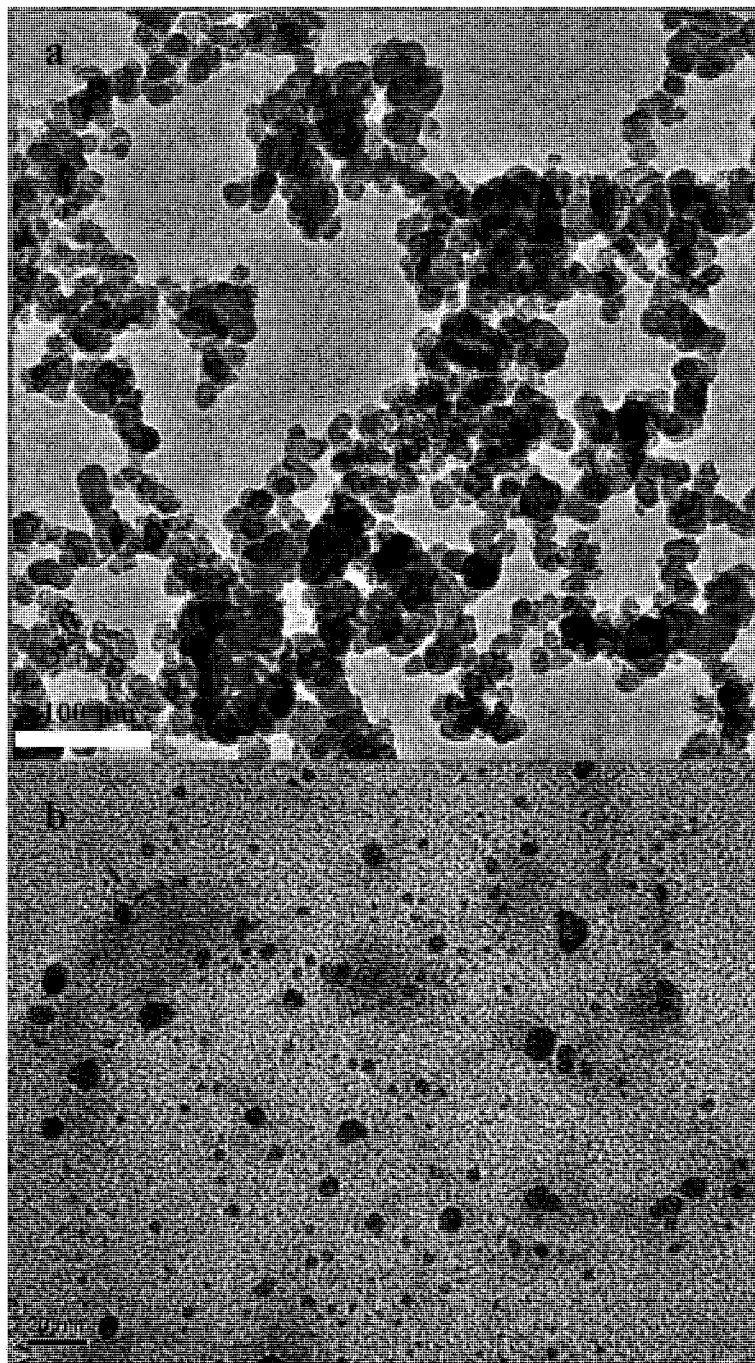


Fig.5.12 TEM images of the Ni nanoparticles prepared by hydrolysis of MgNi_2 , a) a cluster of Ni nanoparticles, b) discrete Ni nanoparticles.

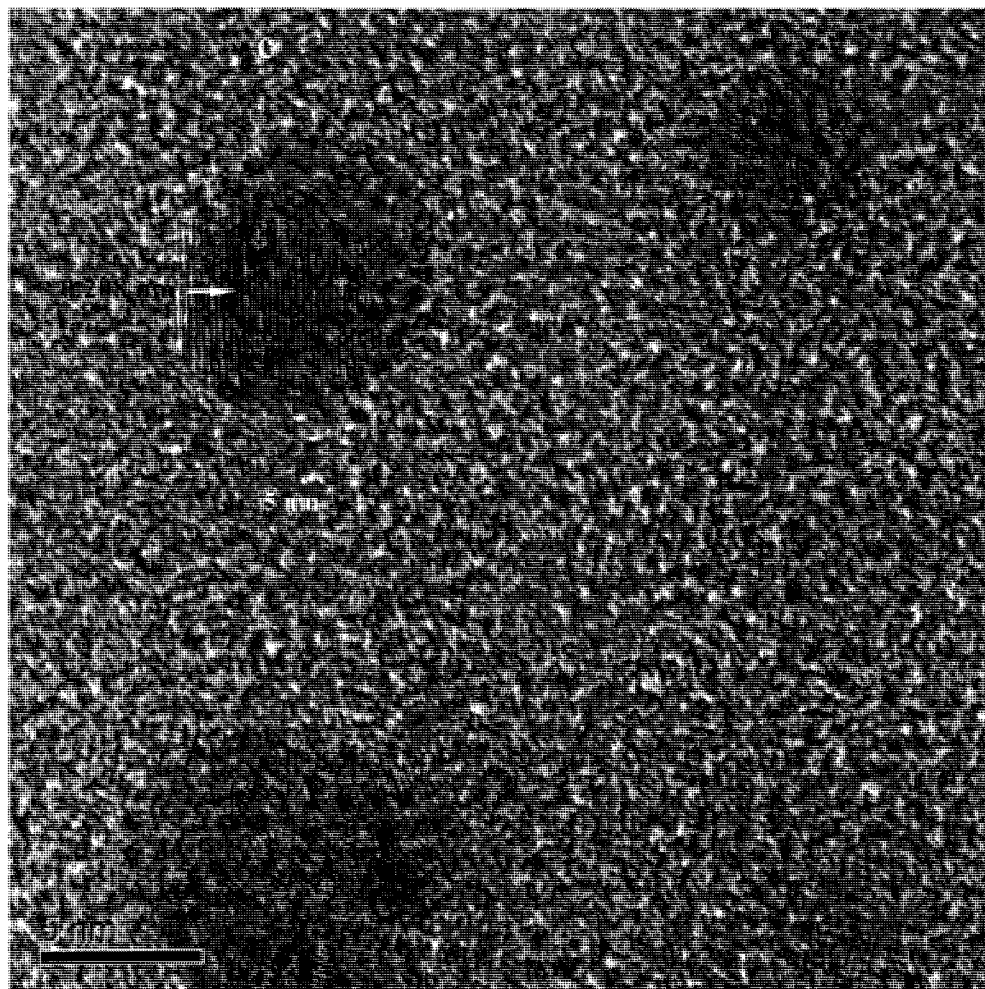


Fig.5.13 High resolution TEM image of individual Ni nanoparticles prepared by hydrolysis of $MgNi_2$.

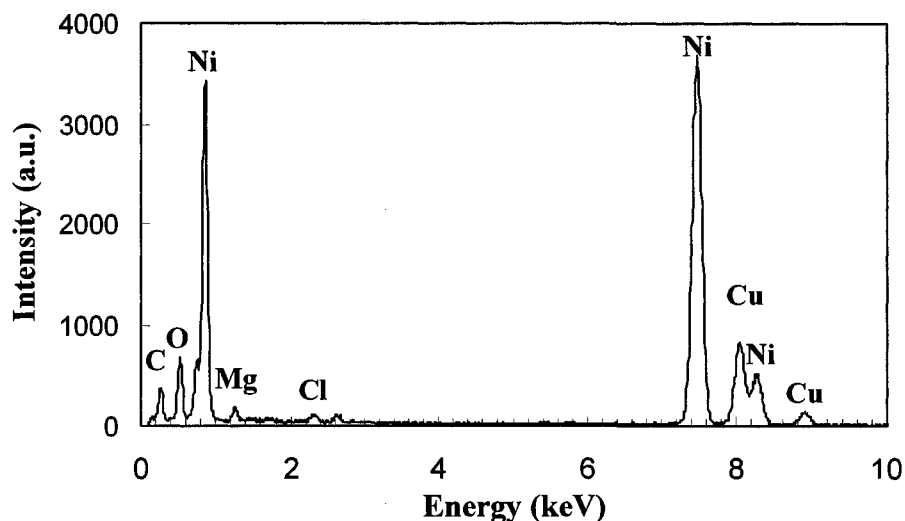


Fig.5.14 EDS spectrum of the cluster of Ni nanoparticles prepared by hydrolysis of MgNi_2

A large amount of Ni, a small amount of O, and traces of Mg and Cl were detected by EDS in the cluster of Ni nanoparticles (see Fig.5.14). The Mg and Cl probably came from the remnants of the dissolved product of Mg(OH)_2 after rinsing in dilute acid.

The size of the Ni nanoparticles ranged from 8.3nm to 22.2nm with a mean diameter of 16.1nm as shown in Fig.5.15, which was slightly coarser than the Ni nanoparticles derived from the hydrolysis of Mg_2Ni . It is generally thought that the newly-formed Mg(OH)_2 has to precipitate from water in the vicinity of the Mg dissolution sites due to small solubility of Mg(OH)_2 in water. Therefore, the existence of the Mg(OH)_2 particles will assist the formation of very fine Ni nanoparticles. The concentration of Mg(OH)_2 particles in the hydrolysis product of MgNi_2 is less than that in the hydrolysis product of

Chapter V. Hydrolysis behaviour of Ni magnides and its application to the synthesis of Ni nanoparticles

Mg_2Ni . Thus, the Ni nanoparticles have more opportunity to grow during hydrolysis of $MgNi_2$.

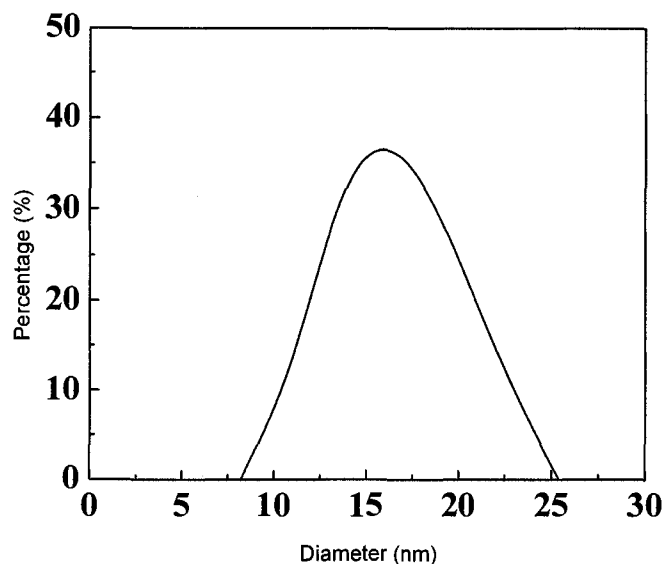


Fig.5.15 Particle size distribution of the Ni nanoparticles prepared by hydrolysis of $MgNi_2$

The initial materials used in this hydrolysis method can be readily fabricated using a melting-casting method on a large scale. The hydrolysis processing of the metal and magnesium intermetallics, and the removal of $Mg(OH)_2$, can also be scaled up. Therefore, compared with conventional preparation methods for Ni particles, this method has a greater potential for economical production of Ni nanoparticles on a large scale.

Compared with using Mg_2Ni , using the hydrolysis behavior of $MgNi_2$ to produce Ni nanoparticles offers a higher efficiency, saves raw materials (esp. Mg) and reduces the pollution resulting from the dissolution of the hydrolysis byproduct ($Mg(OH)_2$) by using an acid.

5.5 Summary

The main conclusions from this chapter are summarized as follows:

1. MgNi_2 spontaneously undergoes hydrolysis in water at room temperature, to form Mg(OH)_2 , Ni and hydrogen as is the case for the hydrolysis of Mg_2Ni . Therefore, Ni nanoparticles can be produced by hydrolysis of either MgNi_2 or Mg_2Ni .
2. The Ni nanoparticles prepared by hydrolysis of both Mg_2Ni and MgNi_2 were spherical in shape (or polyhedrons). The size of the Ni nanoparticles prepared by hydrolysis of MgNi_2 ranged from 8.3nm to 22.2nm with a mean diameter of 16.1nm, which was slightly coarser than the Ni nanoparticles derived from the hydrolysis of Mg_2Ni , which had a mean size of around 10 nm. The size difference could be related to the fact that the concentration of Mg(OH)_2 in the hydrolysis product of MgNi_2 is less than that in the hydrolysis product of Mg_2Ni . Hence, the Ni nanoparticles prepared by hydrolysis of Mg_2Ni have more opportunities to grow during hydrolysis of MgNi_2 .
3. Compared with conventional preparation methods for Ni nanoparticles, the hydrolysis of either Mg_2Ni or MgNi_2 has the potential to inexpensively produce Ni nanoparticles on a large scale.
4. Before the Mg_2Ni or MgNi_2 particles are totally hydrolyzed, the Ni nanoparticles are protected from oxidation due to the higher chemical affinity of the magnesium atoms in both Mg_2Ni and MgNi_2 to oxygen.
5. After the Mg_2Ni or MgNi_2 particles are consumed, the newly formed Ni nanoparticles will be readily oxidized into Ni(OH)_2 by the dissolved oxygen in solution during hydrolysis and the removal of Mg(OH)_2 using a dilute acid.

Chapter V. Hydrolysis behaviour of Ni magnides and its application to the synthesis of Ni nanoparticles

6. If all preparation procedures were conducted in a near-zero oxygen environment, Ni nanoparticles with low oxygen content could be synthesized by hydrolysis of both Mg_2Ni and MgNi_2 .
7. Compared with using Mg_2Ni , using the hydrolysis of MgNi_2 to produce Ni nanoparticles offers a higher output efficiency, saves raw materials and reduces the pollution resulting from the dissolution of the hydrolysis byproduct ($\text{Mg}(\text{OH})_2$) by using an acid.

CHAPTER SIX: APPLICATION OF THE HYDROLYSIS BEHAVIOUR OF MAGNIDES IN THE SYNTHESIS OF NANOPARTICLES

6.1 Introduction

In Chapter Five, it was described how both the Mg-rich compound (Mg_2Ni) and the Ni-rich compound ($MgNi_2$) in the Mg-Ni binary system, spontaneously undergo hydrolysis in water at room temperature. There were many similar transition metal (or semiconductor element) – magnesium intermetallic compounds that could have possibly exhibited a hydrolysis behavior. In this Chapter, the hydrolysis behavior of Mg-Cu, Mg-Ag, Mg-Au, Mg-Ge, and Mg-Si intermetallic compounds will be described in detail. Cu, Au, Ag, Si and Ge nanoparticles were produced by hydrolysis of their magnides.

6.2 Synthesis of Cu nanoparticles by hydrolysis of Mg_2Cu

Arc-melted Mg_2Cu pellets were used in this study. The chemical analysis of the arc-melted Mg_2Cu pellets (nominal formula: $Mg_{2.08}Cu$) is given in Table 3-1. There was surplus Mg in the initial Mg_2Cu pellets. The pellets were ball-milled for 2 hours in a laboratory high energy ball mill SPEX8000. No significant Mg diffraction peaks were observed in the XRD pattern for the ball-milled Mg_2Cu (see Fig.6.1a).

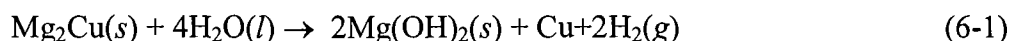
Then, 10 grams of the ball-milled Mg_2Cu particles were immersed in 500ml of distilled

Chapter VI. Application of the hydrolysis behaviour of magnides in the synthesis of nanoparticles

water and stirred for 48h. Initially, there was a rapid release of hydrogen bubbles. The release rate of hydrogen bubbles then gradually slowed down. The pH value of the solution, determined using pH papers, rapidly reached a value of 10 to 11 in the samples immersed in water, and thereafter remained at that level. The hydrolysis behavior for Mg₂Cu was thus almost identical to that of Mg₂Ni.

Brucite (Mg(OH)₂) and some Mg₂Cu diffraction peaks (JCPDS file No.65-1116) were observed in the XRD pattern for the hydrolysis product of the ball-milled Mg₂Cu in distilled water (see Fig.6.1b). Thus, part of the Mg₂Cu had hydrolyzed into Mg(OH)₂ and Cu after being immersed in distilled water for 48h. Small diffraction peaks from Cu could be seen in the XRD pattern: Fig.6.1b.

A reaction for the hydrolysis of Mg₂Cu is as follows:



The standard formation enthalpies and entropies for Mg(OH)₂, H₂O and Mg₂Cu are -924.7KJ/mol and -149.1J/°C•mol, -285.53 KJ/mol and 69.95J/°C•mol, and -29.1KJ/mol and 92.32 J/°C•mol, respectively[185]. The standard entropies for Cu and H₂ are 33.16J/°C•mol and 130.68 J/°C•mol, respectively. The free energy change of the hydrolysis reaction (6-1) is given as follows:

$$\Delta G_{6-1} = -566.51\text{KJ} / \text{mol} + RT \ln \frac{\alpha_{\text{Mg}(\text{OH})_2}^2 \alpha_{\text{Cu}} P_{\text{H}_2}^2}{\alpha_{\text{Mg}_2\text{Cu}} \alpha_{\text{H}_2\text{O}}^4} \quad (6-2)$$

The hydrolysis conditions in this study were room temperature, one atmosphere pressure, abundant water and a limited amount of Mg₂Cu. The effects of the activities can, therefore, be neglected. The free energy change for Reaction 6-1 can be approximated as -566.51KJ/mol.

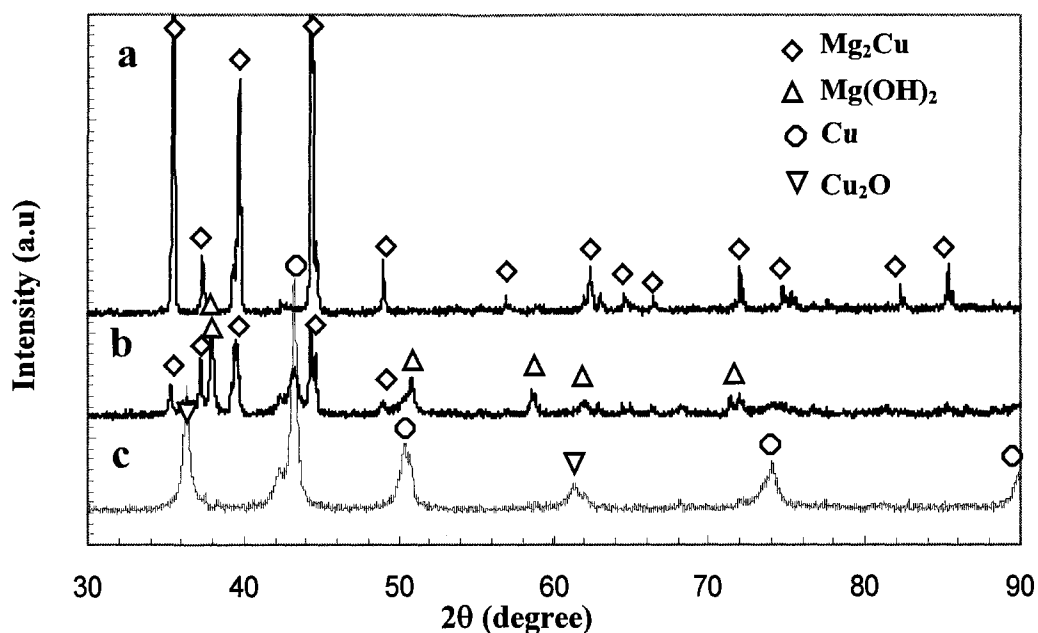


Fig.6.1 XRD powder diffraction patterns for a) ball-milled Mg₂Cu particles, b) hydrolysis product of the ball-milled Mg₂Cu particles, c) the final product (Cu nanoparticles).

Thus, the thermodynamic analysis results suggest that Mg₂Cu could spontaneously hydrolyze into Mg(OH)₂, Cu and hydrogen similar to the hydrolysis of Mg₂Ni. Our XRD results confirm the existence of a hydrolysis reaction for Mg₂Cu.

The hydrolysis process of Mg₂Cu should be similar to the case of Mg₂Ni. First, the surplus Mg in the Mg₂Cu alloy reacts with water at room temperature, forms Mg(OH)₂ and releases hydrogen before Mg₂Cu starts to hydrolyze.

Mg₂Cu has an orthorhombic structure (C15) with $a = 0.5273\text{nm}$, $b=0.905\text{nm}$ and $c=1.829\text{nm}$. Each Cu atom is surrounded by two Cu atoms and eight Mg atoms. Each Mg

Chapter VI. Application of the hydrolysis behaviour of magnides in the synthesis of nanoparticles

atom is surrounded by four Cu atoms and eleven Mg atoms[189]. A continuous skeleton of the larger magnesium atoms is formed in the Mg_2Cu structure. Thus, Mg atoms in the Mg_2Cu compound are still very active. Therefore, Mg atoms have a larger affinity to the OH^- ions in water.

When the Mg_2Cu particles contact water, Mg atoms on the surface of the Mg_2Cu particles will combine with the OH^- ions and form $Mg(OH)_2$. At the same time, Cu atoms in Mg_2Cu will be released. However, the Cu atoms have a very weak affinity to the excess H^+ ions resulting from the OH^- ions being consumed by the combination of Mg atoms and OH^- ions. Thus, the Cu atoms and H^+ ions prefer to combine with like-species to form Cu particles and hydrogen gas, respectively.

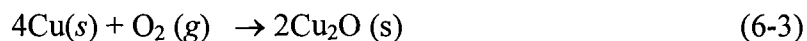
However, when dilute hydrochloric acid was carefully added into the solution, the hydrolysis of the ball-milled Mg_2Cu particles was accelerated, and some fine hydrogen bubbles were released. Additional dilute hydrochloric acid was slowly added into the solution until the pH value of the solution reached 5-6. After the resulting $MgCl_2$ was rinsed out, the XRD diffraction pattern, Fig.6.1c, shows that the final product consisted of Cu and Cuprite (Cu_2O , JCPDS file No.05-0667). The widths of both Cu and Cu_2O peaks were fairly broad, which reflects that the crystallite sizes of both Cu and Cu_2O were extremely small.

Selective oxidation of magnesium in the Mg_2Cu compound will give rise to protection of the newly formed Cu nanoparticles from oxidation during the hydrolysis of Mg_2Cu , as is the case for Ni nanoparticles and Mg_2Ni . Hence, until the Mg_2Cu particles were totally consumed by hydrolysis, the Cu nanoparticles will not be attacked by the dissolved oxygen in solution. Once the hydrolysis of Mg_2Cu is complete, the oxidation of the Cu

Chapter VI. Application of the hydrolysis behaviour of magnides in the synthesis of nanoparticles

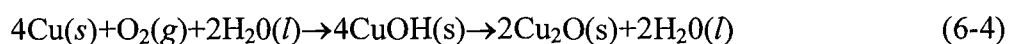
nanoparticles will readily take place due to the affinity of Cu to oxygen.

Only Cu₂O, but no Cu hydroxides, was found in the final product based on the XRD results. The oxidation reaction of Cu nanoparticles in an aqueous solution seems to be as follows:



In general, the oxidation product of Ni nanoparticles in water is their hydroxides. The above oxidation reaction of Cu nanoparticles in water is different from that of Ni nanoparticles.

However, the oxidation rate of Cu nanoparticles was sensitive to the pH value of the solution. The lower the pH value, the higher the oxidation rate, which is in agreement with the oxidation behavior of Ni nanoparticles. In addition, some yellow particles were observed on the surface of the deposited particles after removal of Mg(OH)₂. CuOH is yellow, and unstable, in particular at higher temperatures. Therefore, the oxidation reaction of Cu nanoparticles in an aqueous solution should be as follows:



The oxidation of Cu nanoparticles prepared by this hydrolysis method requires the presence of dissolved oxygen. Theoretically, if all preparation procedures were carried out under a near-zero oxygen environment (under nitrogen or argon protection), Reaction 6-4 would not take place. In other words, Cu nanoparticles with low oxygen contamination could be produced by this method.

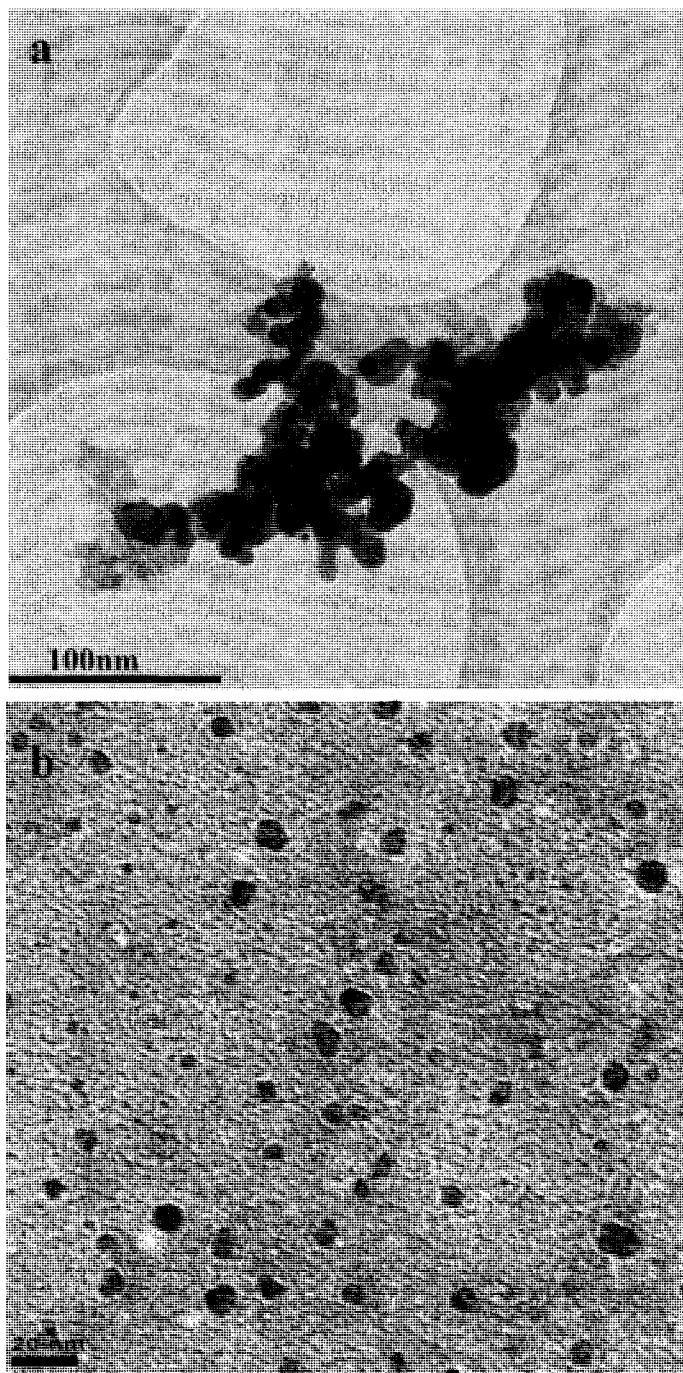


Fig.6.2 TEM images of Cu nanoparticles produced by hydrolysis of Mg_2Cu , a) a cluster of Cu nanoparticles, b) discrete Cu nanoparticles.

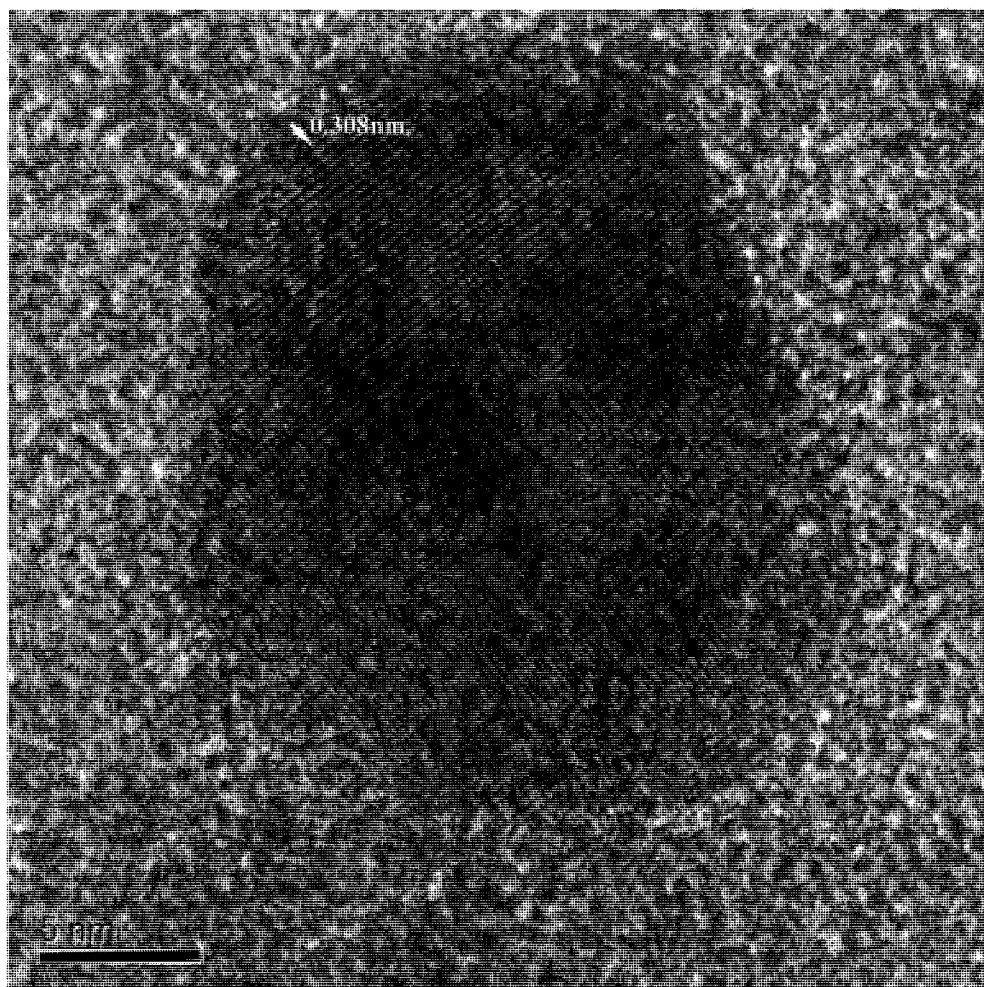


Fig.6.3 High-resolution TEM image of an individual Cu_2O nanoparticle.

Chapter VI. Application of the hydrolysis behaviour of magnides in the synthesis of nanoparticles

No surfactant was used in these experiments. The Cu nanoparticles were generally agglomerated together (see Fig.6.2a) due to the surface energy. Some discrete Cu nanoparticles were occasionally observed (see Fig.6.2b). These discrete Cu nanoparticles were close to spherical in shape and had a size of about 10 nm.

The high-resolution TEM images for individual particles indicated that the spacing for the lattice fringes in Fig.6.3 was about 0.308nm, which is close to 0.302nm (the spacing of the (110) planes in Cu_2O).

The result of particle size analysis shows that the particle size of Cu nanoparticles ranged from 7.7nm to 24.2nm and was about 12.3nm (see Fig. 6.4). The specific surface area of Cu nanoparticles, as determined by a nitrogen adsorption and desorption method (see Fig.6.5), was about $38\text{m}^2/\text{g}$. The theoretical mean diameter of Cu nanoparticles is about 17.7nm on basis of the specific surface area if the Cu nanoparticles were assumed to be spherical. The differences in the mean size of the Cu nanoparticles determined by the two methods may have come from the agglomeration of Cu nanoparticles during evaporation processing.

Chapter VI. Application of the hydrolysis behaviour of magnides in the synthesis of nanoparticles

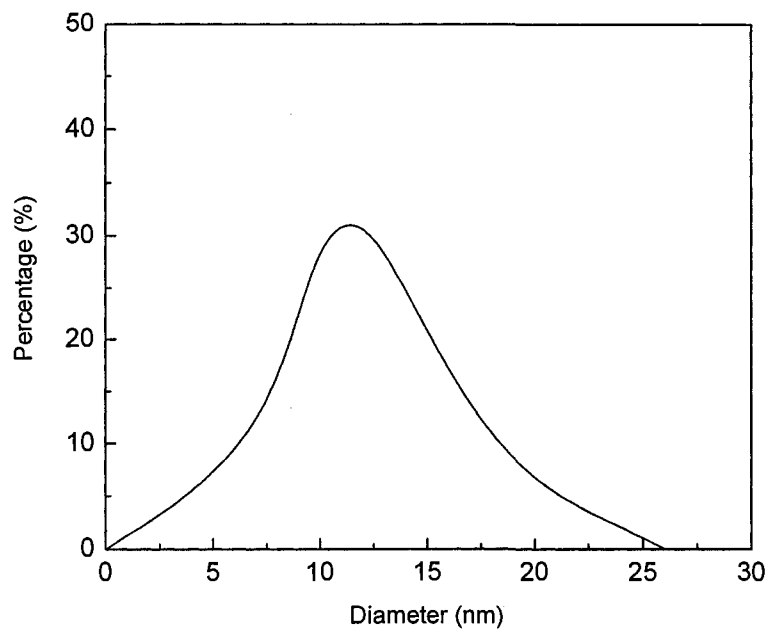


Fig. 6.4 Particle size distribution of Cu nanoparticles produced by hydrolysis of Mg_2Cu .

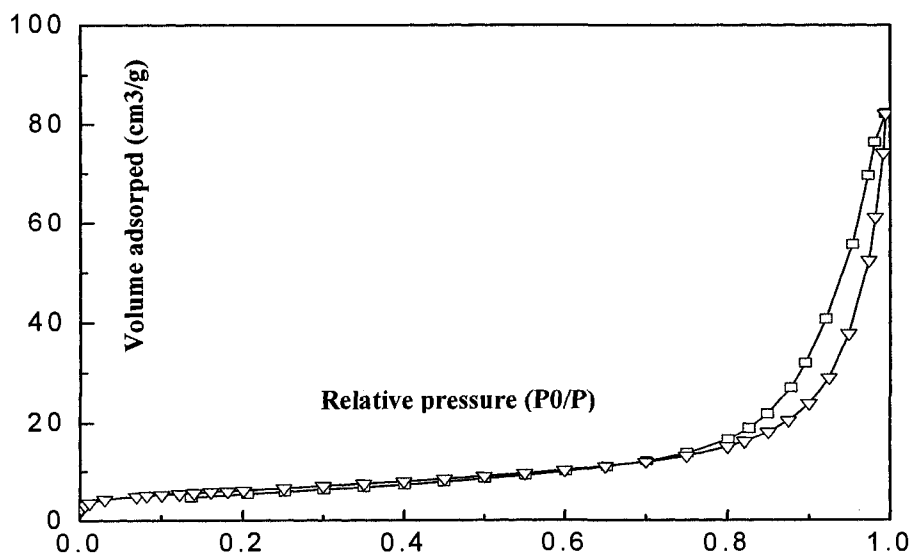


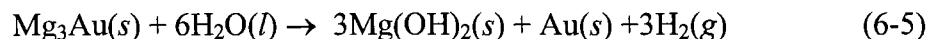
Fig.6.5 Nitrogen adsorption (∇) and desorption curves(□) for Cu nanoparticles at 77.2 K.

6.3 Synthesis of Au nanoparticles by hydrolysis of Mg₃Au

Mg₃Au alloy was prepared by a conventional melting and casting method using commercially available Mg and gold powders from Aldrich. Surplus Mg was added in order to improve the castability of the Mg₃Au alloy. The weight ratio of Mg to Au was 2:3.

Mg₃Au (JCPDS file No. 65-0732) and Mg diffraction peaks were observed in the XRD patterns for the ball-milled Mg₃Au powders (see Fig.6.6). No Au peaks were observed, which shows that all the gold particles in the initial materials were totally converted to Mg₃Au after the conventional melting and casting process.

1 gram of ball-milled Mg₃Au powders was immersed in 200ml of distilled water, with the immediate release of many fine hydrogen bubbles. The pH value of the solution, determined using pH strips, rapidly reached values of 10~11. The phenomenon was the same as previously observed for the hydrolysis of Mg₂Ni and Mg₂Cu. The above results suggest that Mg₃Au should spontaneously undergo a hydrolysis in water. A possible reaction for the hydrolysis of Mg₃Au is as follows:



After the ball-milled Mg₃Au powders were immersed in 200ml of distilled water and stirred for 48h, Mg(OH)₂, which is derived from the hydrolysis, was carefully dissolved by adding 0.5M hydrochloric acid. The soluble product, MgCl₂, was rinsed out using distilled water and 99% pure ethanol. Due to the chemical inertness of Au, gold nanoparticles will not be dissolved by the dilute hydrochloric acid, and will not be

Chapter VI. Application of the hydrolysis behaviour of magnides in the synthesis of nanoparticles

oxidized by the dissolved oxygen in solution, which was the cases for the Ni or Cu nanoparticles. Therefore, the XRD results show that the final product consisted only of Au particles (see Fig.6.7). The crystalline nature of the Au nanoparticles was confirmed from the XRD diffraction patterns.

Since no surfactant was used in this study, most of the Au nanoparticles were agglomerated because of the high surface energy (see Fig.6.8a). Discrete Au nanoparticles were sometimes observed (see Fig.6.8b). The high-resolution TEM image for individual nanoparticles (see Fig.6.9) shows that the spacings for the lattice fringes of two indicated nanoparticles are 0.231nm and 0.235nm, respectively. This is close to the interplanar spacing for the (111) planes of Au (0.2355nm). In addition, the fringes for individual particles indicate that some of the small Au nanoparticles are single crystals. The Au nanoparticles were predominantly spherical in shape and had a size of about 10 nm, which agrees with the results of the particle size analysis (see Fig.6.10). The size of the Au nanoparticles ranged from 6.1nm to 15.3nm with an average size of about 8.4nm. The EDS spectrum shows that the Au nanoparticles have around 1.5wt% Rb impurities (see Fig.6.11). The most probable source of the Rb impurities was from the initial Au powders. Except for Au, Rb, C and Cu, no other elements were observed in the EDS spectrum. The absence of characteristic peaks from elemental oxygen and nitrogen indicates that these Au nanoparticles were pure and free of oxides. In addition, the amount of Rb is not high enough to form the Au-richest intermetallic compound (Au_5Rb) between Au and Rb. The solubility of Rb in Au is negligible. Hence, Rb might segregate within the Au nanoparticles.

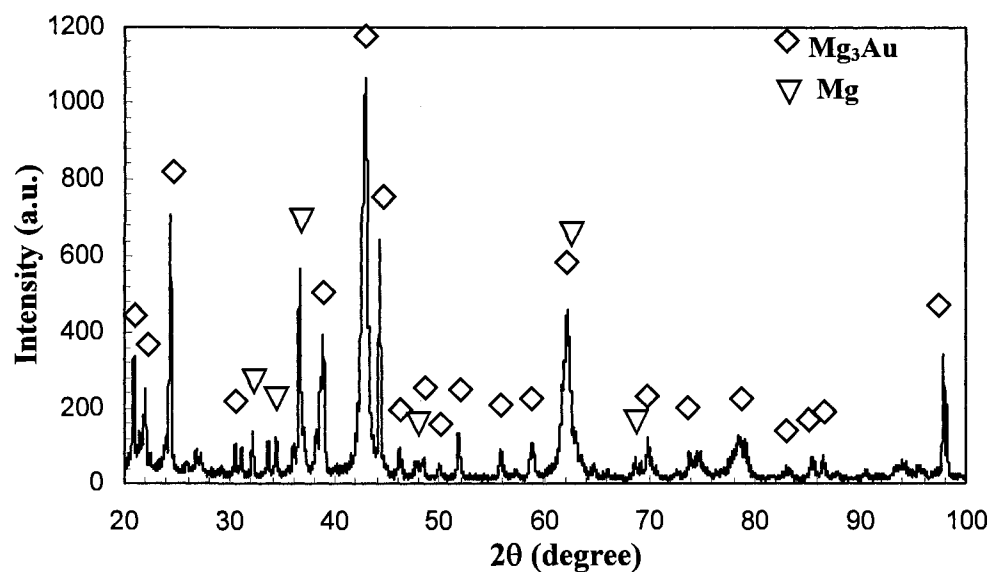


Fig.6.6 XRD powder diffraction pattern of as-cast Mg_3Au pellets showing excess Mg.

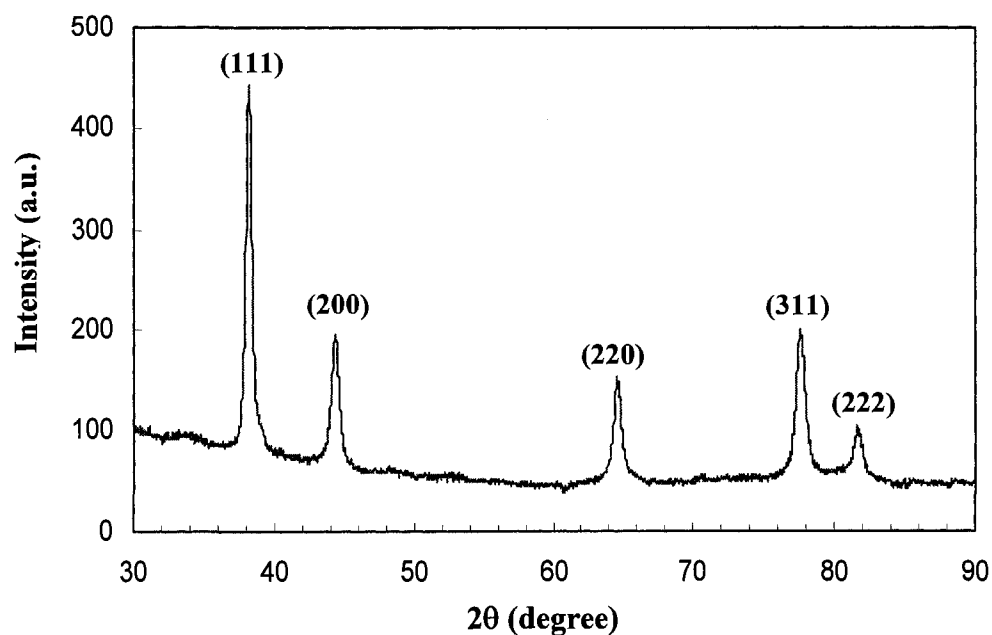


Fig.6.7 XRD powder diffraction pattern of the Au nanoparticles produced by hydrolysis of Mg_3Au .

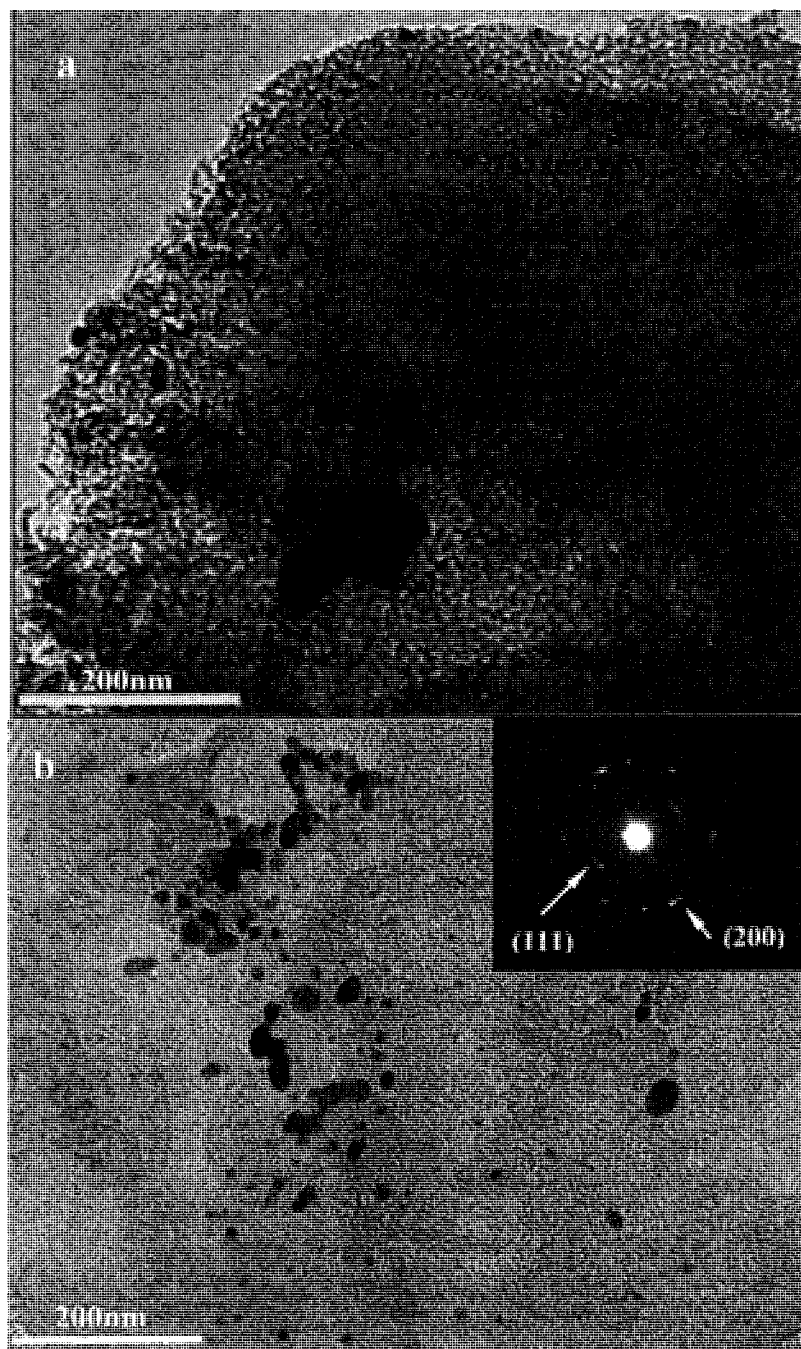


Fig.6.8 TEM images for Au nanoparticles produced by hydrolysis of Mg_3Au , a) a cluster of Au nanoparticles, b) discrete Au nanoparticles.

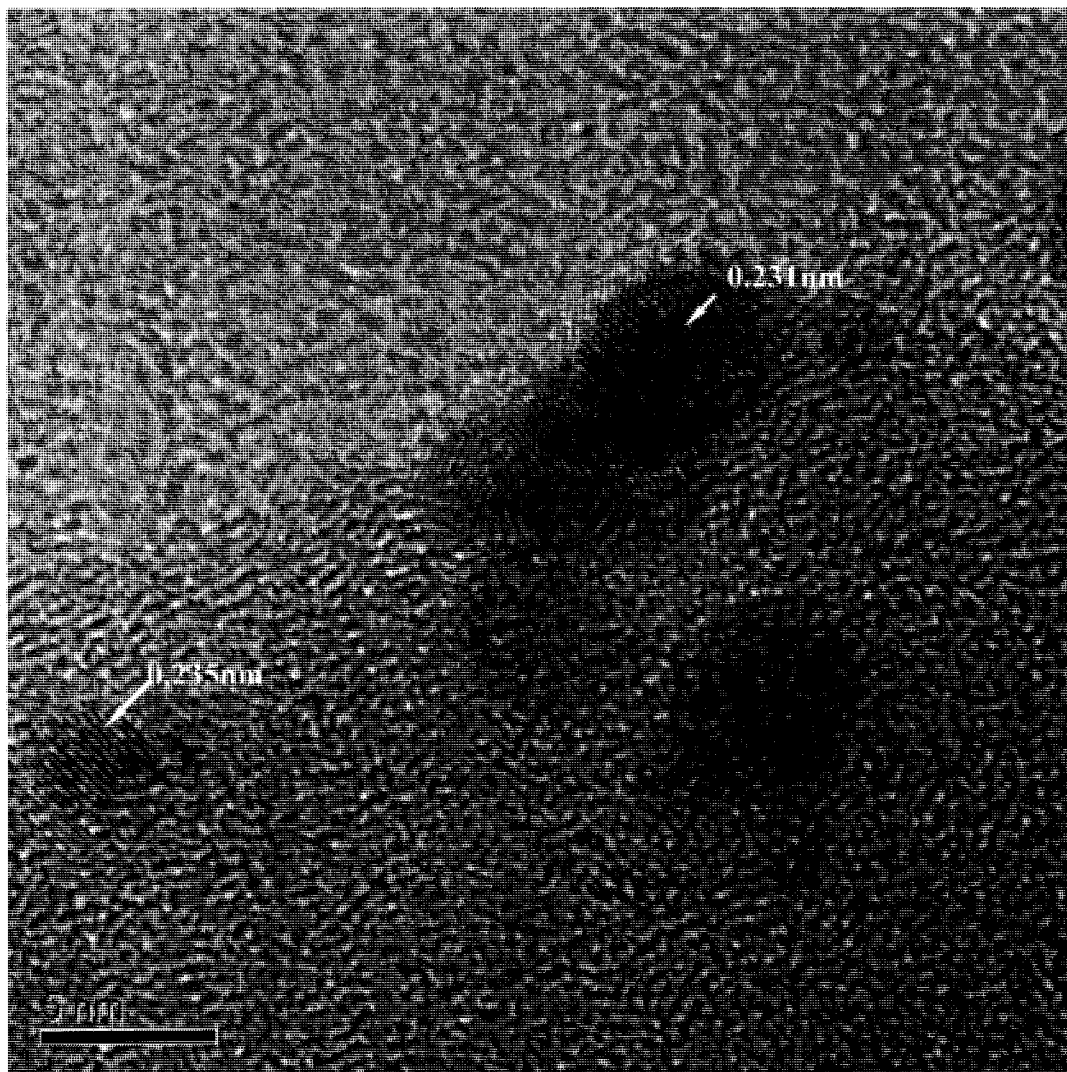


Fig.6.9 High-resolution TEM image of individual Au nanoparticles produced by hydrolysis of Mg_3Au .

Chapter VI. Application of the hydrolysis behaviour of magnides in the synthesis of nanoparticles

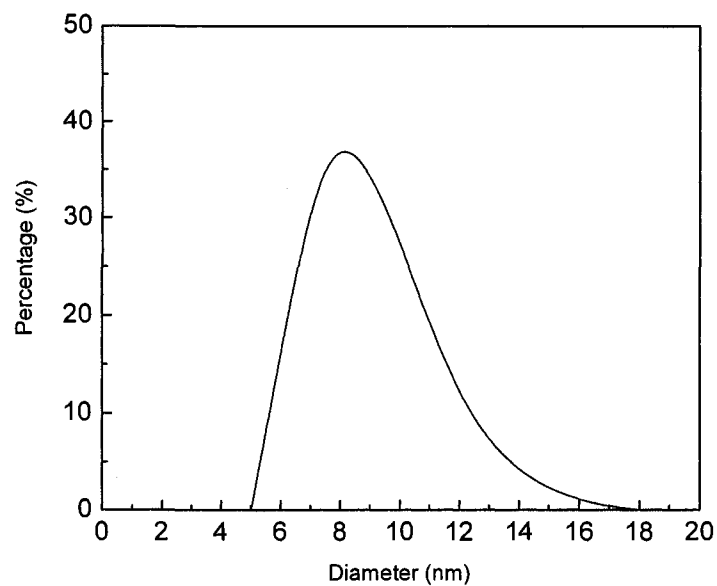


Fig.6.10 Particle size distribution of Au nanoparticles produced by hydrolysis of Mg_3Au .

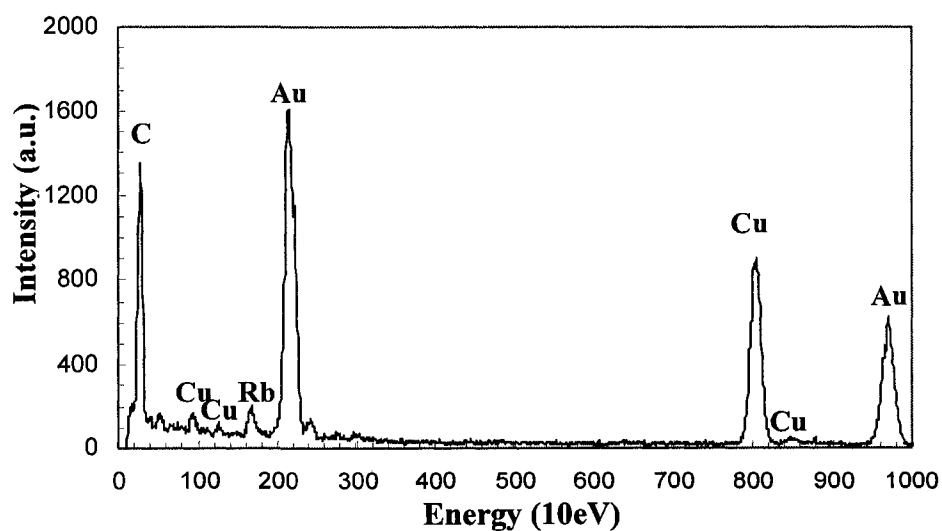


Fig.6.11 EDS spectrum for Au nanoparticles produced by hydrolysis of Mg_3Au (C and Cu peaks resulted from Cu grid).

6.4 Synthesis of Ag nanoparticles by hydrolysis of Mg-Ag intermetallics

The Mg-Ag intermetallic cast ingots were prepared by a conventional melting and casting method using commercially available Mg and silver particles. The weight ratio of Mg to Ag was 1:1. The Mg-Ag intermetallic ingots were broken into small pellets, and then ball-milled under an argon atmosphere for 2 hours in a laboratory high energy ball mill SPEX8000

1 gram of the ball-milled particles were immersed in 200ml of distilled water and stirred for 48h. $Mg_{54}Ag_{17}$ (JCPDS file No.65-8314), MgAg (JCPDS file No.29-0871) and periclase (MgO, JCPDS file No.45-0946) diffraction peaks were observed in the XRD pattern of the as-cast Ag-Mg pellets (see Fig.6.12). No Ag diffraction peaks were seen in the XRD pattern, indicating that all the silver in the initial material has been totally converted into Mg-Ag intermetallics after melting and casting. In addition, although a small amount of surplus Mg was added to the initial materials, no Mg diffraction peaks were observed in the XRD pattern. The XRD results suggest that part of the Mg was oxidized during the melting and casting, leading to the formation of MgO. Due to the oxidation of some Mg, some MgAg phase was formed, which should not have been present based on the composition of the initial materials.

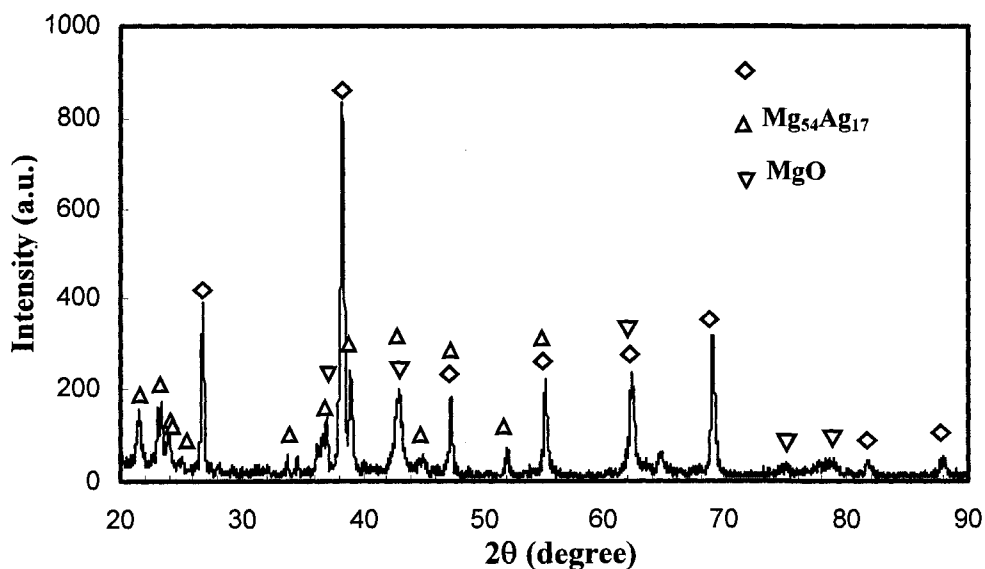
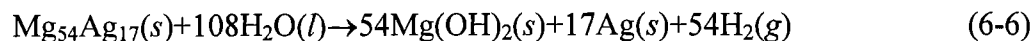


Fig.6.12 XRD powder diffraction pattern of as-cast Ag-Mg pellets.

As 1 gram of the ball-milled particles was immersed in 200ml of distilled water, many fine hydrogen bubbles were immediately released. The pH value of the solution, determined using pH papers, rapidly reached 10 to 11. This behavior was the same as for the hydrolysis of Mg_2Ni , Mg_2Cu and Mg_3Au . The results suggest that both $Mg_{54}Ag_{17}$ and $MgAg$ could spontaneously undergo hydrolysis in water. Possible reactions for the hydrolysis of $Mg_{54}Ag_{17}$ and $MgAg$ are as follows:



Since the solubility of $Mg(OH)_2$ in water is very small, the newly formed $Mg(OH)_2$ precipitates from the water at a site close to where Mg dissolved. It is thought that the formation of $Mg(OH)_2$ particles, and the low mobility of Ag atoms at room temperature,

Chapter VI. Application of the hydrolysis behaviour of magnides in the synthesis of nanoparticles

assist in the formation of very fine Ag nanoparticles. Adding a dilute acid to reduce the pH value of the solution during the hydrolysis should accelerate the hydrolysis rate of both $Mg_{54}Ag_{17}$ and MgAg.

The XRD pattern showed that the final product consisted only of Ag particles (see Fig.6.13). The crystalline nature of the Ag nanoparticles can be seen from the XRD diffraction peaks. No silver oxide diffraction peaks were observed in the XRD pattern. This result indicates that Ag is inert in an aqueous solution, which is different from the behavior we have seen with Ni and Cu. Ni and Cu nanoparticles in an aqueous solution exposed to air were first oxidized to their hydroxides, but CuOH further dissociated into Cu_2O .

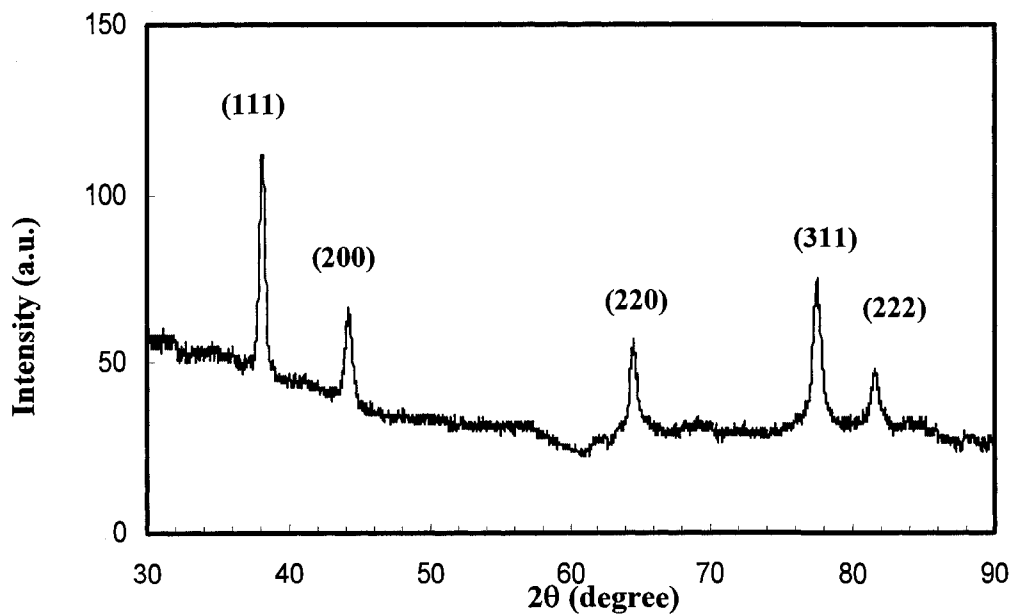


Fig.6.13 XRD powder diffraction pattern of Ag nanoparticles produced by hydrolysis of $Mg_{54}Ag_{17}$ and MgAg.

Chapter VI. Application of the hydrolysis behaviour of magnides in the synthesis of nanoparticles

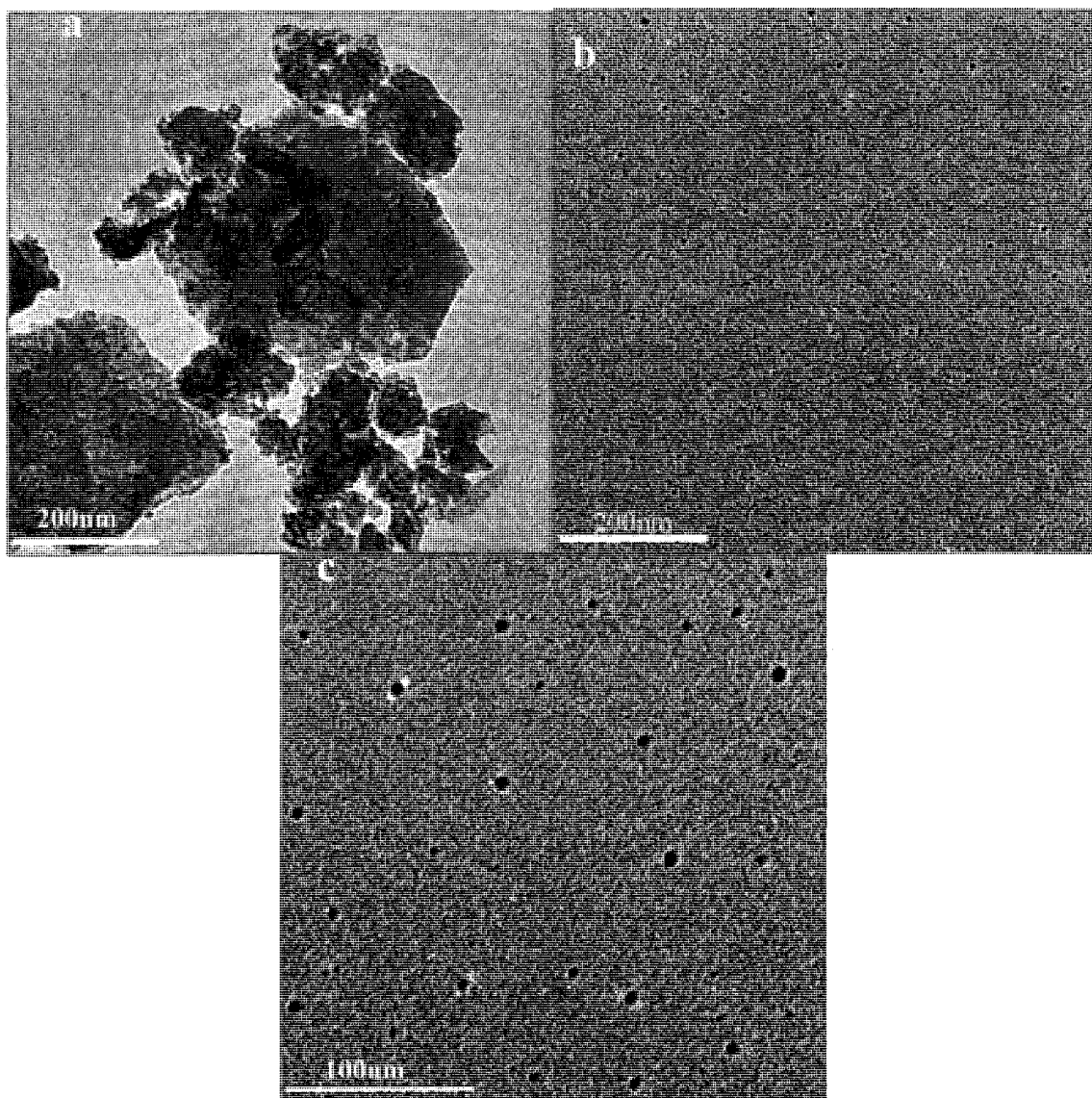


Fig.6.14 TEM images of Ag nanoparticles produced by hydrolysis of $Mg_{54}Ag_{17}$ and MgAg, a) a cluster of Ag nanoparticles, b) and c) discrete Ag nanoparticles, respectively.

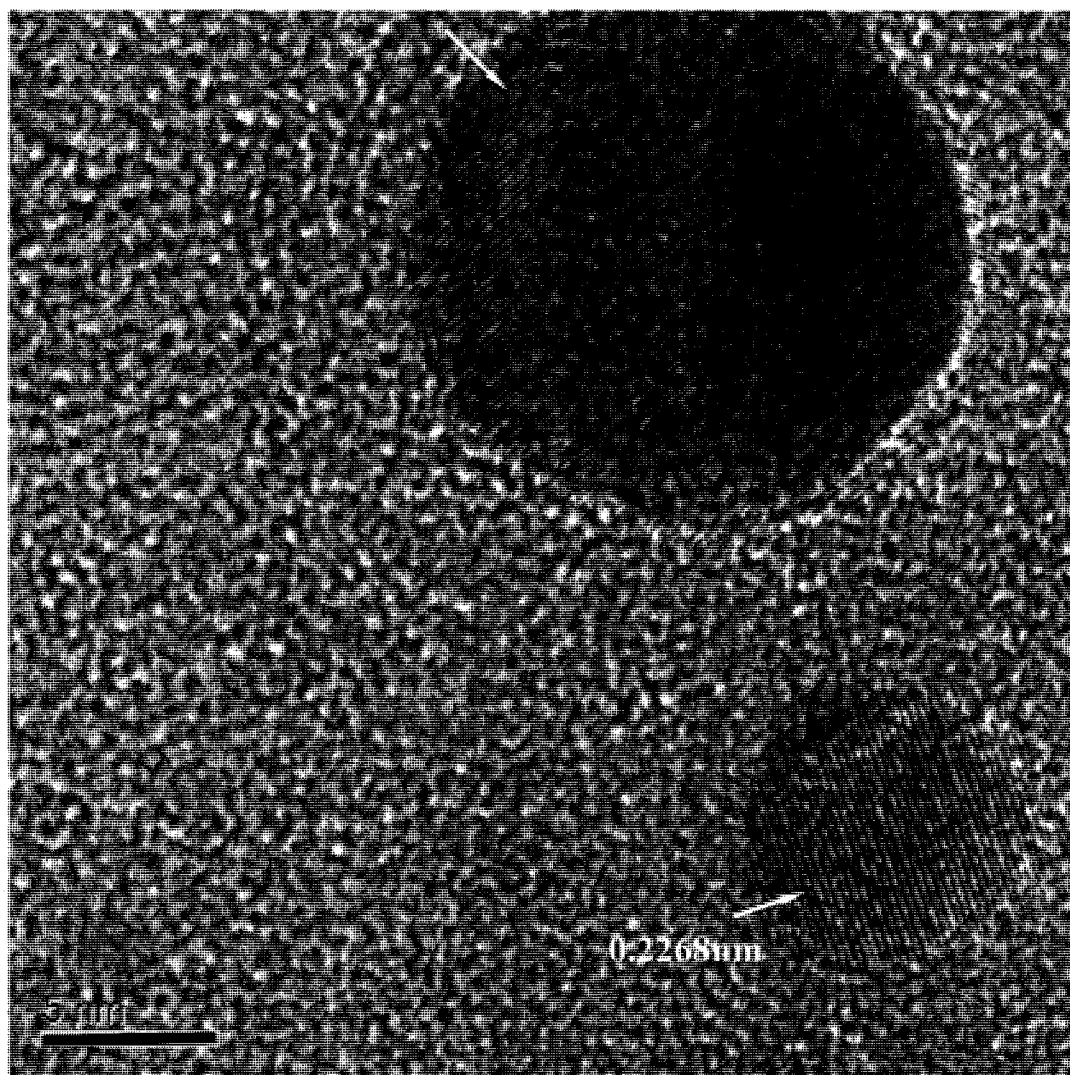


Fig.6.15 HRTEM image of individual Ag nanoparticles produced by hydrolysis of $Mg_{54}Ag_{17}$ and MgAg.

Since no surfactant was used in this study, most of the Ag nanoparticles in the as prepared condition aggregated due to surface energy considerations as shown in Fig.6.14a. Discrete Ag nanoparticles were occasionally observed (see Figs.6.14b and

Chapter VI. Application of the hydrolysis behaviour of magnides in the synthesis of nanoparticles

6.14c). High-resolution TEM images (e.g. Fig.6.15) for the individual Ag nanoparticles indicates that they are highly crystalline and are single crystals. The interplanar spacings for the two nanoparticles shown in Fig.6.18 are 0.2355nm (smaller particle) and 0.2268nm (larger particle), respectively, which are close to the (111) planar spacing of Ag (0.2359nm). No obvious oxide layers were observed on the surface of the Ag nanoparticles.

These discrete silver nanoparticles were close to spherical in shape with a size of about 10nm, which agrees with the results of particle size analysis by Zetasizer 3000HS where it was found that the size of the Ag nanoparticles ranged from 5.4nm to 21.5nm with an average size of 8.4nm (see Fig.6.16). The chemical composition of the Ag nanoparticles as determined by EDS show no significant amounts of oxygen and Mg (see Fig.6.17), which further confirms that the Ag nanoparticles are resistant to oxidation from the dissolved oxygen in aqueous solution.

Chapter VI. Application of the hydrolysis behaviour of magnides in the synthesis of nanoparticles

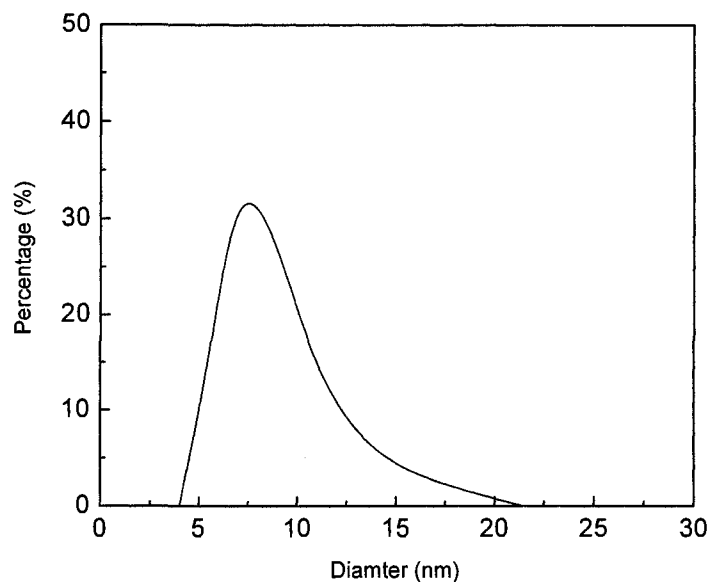


Fig.6.16 Particle size distribution of Ag nanoparticles produced by hydrolysis of $Mg_{54}Ag_{17}$ and $MgAg$.

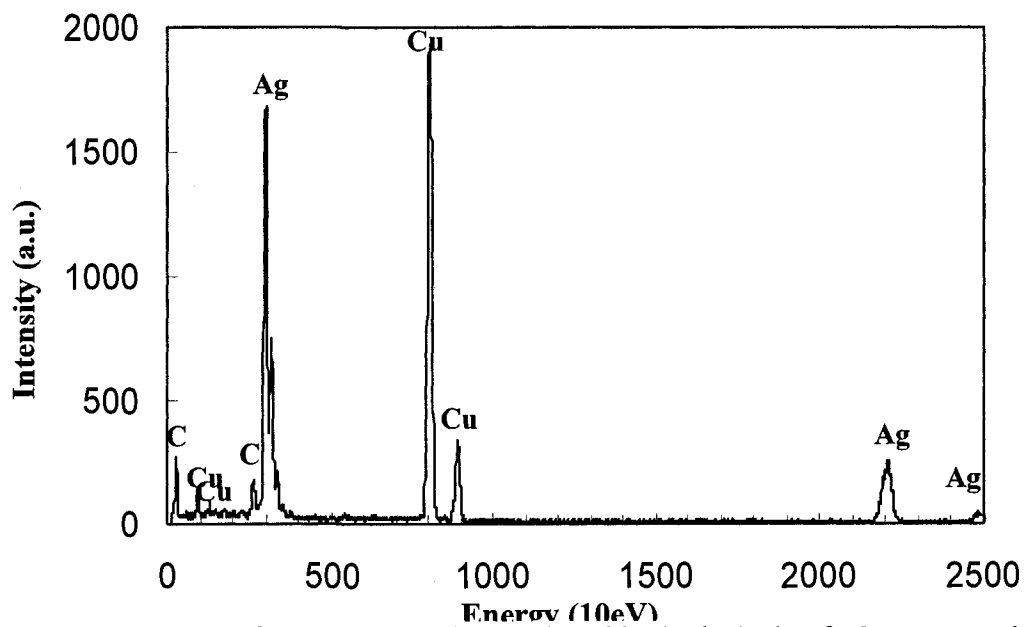


Fig.6.17 EDS pattern of Ag nanoparticles produced by hydrolysis of $Mg_{54}Ag_{17}$ and $MgAg$.

6.5. Study on hydrolysis behavior of Mg_2Ge

Mg_2Ge was synthesized by a conventional melting and casting method. Some surplus Mg was added in order to improve the castability of the Mg_2Ge alloy. The weight ratio of Mg to Ge was 3:2. 10 gram of the ball-milled Mg_2Ge particles were immersed into 500ml of distilled water and stirred for 48h at room temperature or 80°C. Then, the hydrolyzed product, $Mg(OH)_2$, was carefully removed from the hydrolysis product by adding 0.5M hydrochloric acid. The sample was rinsed three times using distilled water, then three times using 99% pure ethanol.

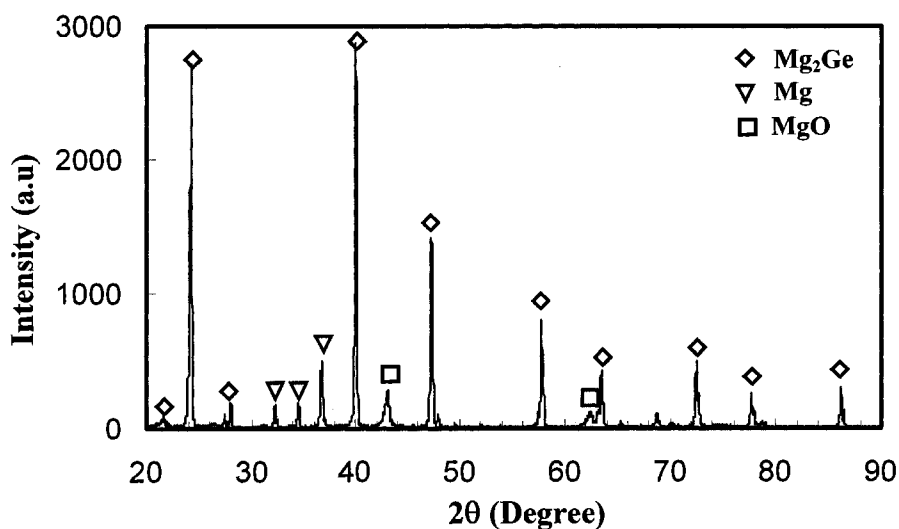


Fig.6.18 XRD powder diffraction pattern of the Mg_2Ge ingots.

Besides surplus Mg and periclase (MgO , JCPDS file No.45-0946)) diffraction peaks, Mg_2Ge diffraction peaks (JCPDS file No.65-2990) were observed in the XRD pattern for the ball-milled Mg_2Ge powders (see Fig.6.18). No Ge diffraction peaks were observed in Fig.18, which shows that all Ge powders in the initial materials were totally converted

Chapter VI. Application of the hydrolysis behaviour of magnides in the synthesis of nanoparticles

into Mg_2Ge during conventional melting and casting. Since part of the surplus Mg was oxidized to periclase during the melting and casting, MgO was found in the Mg_2Ge pellets.

When 1 gram of the ball-milled powders was immersed in 200ml distilled water, many fine hydrogen bubbles were immediately released. The pH value of the solution, determined by pH papers, rapidly reached about 10 to 11, which is in agreement with the 10.4 pH value for a saturated $Mg(OH)_2$ solution based on the solubility of product constants of $Mg(OH)_2$, which is 5.6×10^{-12} .

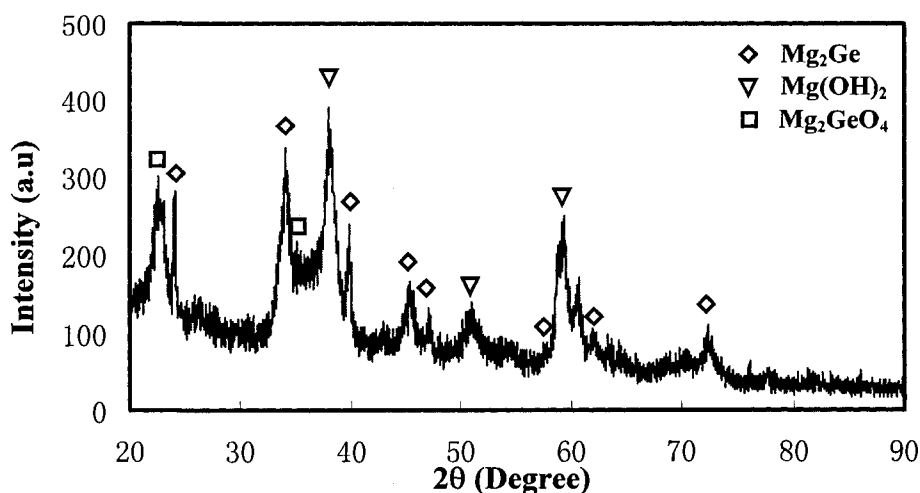


Fig.19 XRD powder diffraction pattern of hydrolysis product of the ball-milled Mg_2Ge powders.

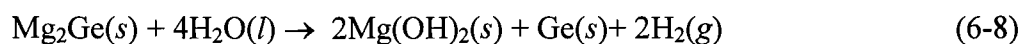
The XRD diffraction pattern of hydrolysis product of the ball-milled Mg_2Ge particles, Fig. 6.19, shows that there are Mg_2Ge (JCPDS file No.34-0669), $Mg(OH)_2$ and Mg_2GeO_4 (JCPDS file No.11-0013). In addition, there is strong diffraction of an unknown

Chapter VI. Application of the hydrolysis behaviour of magnides in the synthesis of nanoparticles

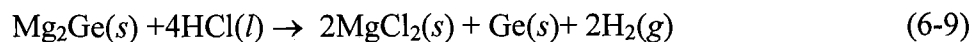
amorphous phase in Fig.6.19, which has not been observed in the diffraction patterns for the hydrolysis product of transition metal magnides (see Figs.4.11a, 5.8b and 6.1b).

A hydrolysis reaction is assumed to have take place because of the presence of Mg_2GeO_4 in the product. A large amount of Mg_2Ge in the hydrolysis product suggests that the hydrolysis of Mg_2Ge is very sluggish. The unknown amorphous phase was assumed to be newly-formed amorphous Ge particles.

A possible reaction for the hydrolysis of Mg_2Ge is thus as follows:



This reaction spontaneously takes place at room temperature under one atmosphere, but proceeds fairly sluggishly. After the ball-milled Mg_2Ge powders were immersed in 200ml distilled water and stirred for 48 hours, 0.5M hydrochloric acid was slowly added in the solution. A release of many fine hydrogen bubbles were observed, which means that the hydrolysis of Mg_2Ge was not completed within 48h. As the pH value of the solution was reduced by adding the hydrochloric acid, the hydrolysis rate of Mg_2Ge was significantly accelerated. The “hydrolysis” reaction of Mg_2Ge then changes into an acid dissolution reaction as follows:



Dilute hydrochloric acid was slowly added into the solution until the pH value of the solution remained stable at 4. As a result, the remained Mg_2Ge and the by-product ($Mg(OH)_2$) were totally dissolved and formed $MgCl_2$. Subsequently, $MgCl_2$ was rinsed out using distilled water, followed by ethanol. The Ge diffraction peaks (JCPDS file No. 65-0333) and some small germania (GeO_2) diffraction peaks (JCPDS file No.36-1463)

Chapter VI. Application of the hydrolysis behaviour of magnides in the synthesis of nanoparticles

were observed in the XRD pattern for the final product as shown in Fig.6.20. The Ge diffraction peaks suggest that it is crystalline, but has a poor crystallinity since the lattice fringes in the high-resolution TEM images of the individual Ge nanoparticles were very weak (see Fig.6.21)

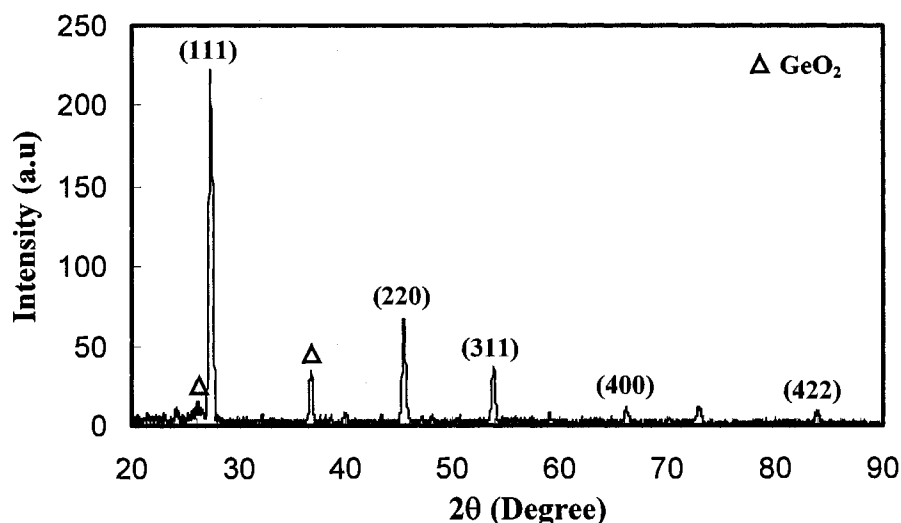


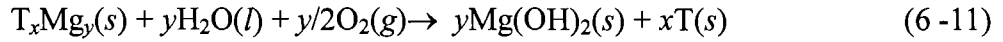
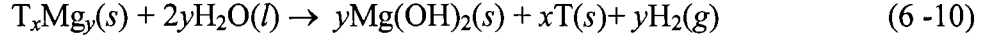
Fig.6.20 XRD powder diffraction pattern of the Ge nanocrystals derived from hydrolysis and acid rinsing of Mg_2Ge at room temperature.

It was worth noting that the Ge was amorphous in the hydrolysis product, but was crystalline in the final product after acid rinsing. The difference could be caused by the evaporation process of the solution at 60°C.

In general, the newly formed transition metal nanoparticles can be protected from oxidation before hydrolysis of transition metal magnides was complete. However, in this case, the existence of both Mg_2Ge and Mg_2GeO_4 in the hydrolysis product suggests that there is no such protection during hydrolysis of Mg_2Ge .

Chapter VI. Application of the hydrolysis behaviour of magnides in the synthesis of nanoparticles

The overall hydrolysis reaction of magnides and the protection reaction of the newly-formed nanoparticles from oxidation can be written as follows;



Where, T is transition metal, Ge or Si.

These reactions occur at room temperature under one atmosphere pressure. Therefore, the free energy changes for the reactions can be approximately considered as the standard free energy changes, if the activities are neglected. Therefore, the free energy changes ΔG_{6-10} and ΔG_{6-11} are given as follows:

$$\Delta G_{6-10} = y\Delta G^\circ_{Mg(OH)_2} + x\Delta G^\circ_T + y\Delta G^\circ_{H_2} - \Delta G^\circ_{T_xMg_y} - 2y\Delta G^\circ_{H_2O} \quad (6-12)$$

$$\Delta G_{6-11} = y\Delta G^\circ_{Mg(OH)_2} + x\Delta G^\circ_T - \Delta G^\circ_{T_xMg_y} - y\Delta G^\circ_{H_2O} - y/2\Delta G^\circ_{O_2} \quad (6-13)$$

The difference in the standard free energy changes between Reaction 6-11 and Reaction 6-10 is:

$$\Delta G_{6-14} = \Delta G_{6-11} - \Delta G_{6-10} = y(\Delta G^\circ_{H_2O} - 1/2\Delta G^\circ_{O_2} - \Delta G^\circ_{H_2}) \quad (6-14)$$

Therefore, ΔG_{6-14} is approximately equivalent to y times the standard free energy change for water formation. Hence, ΔG_{6-14} is negative at room temperature under one atmosphere pressure. In other words, Reaction 6-11 is more favorable than Reaction 6-10.

However, due to very small solubility and slow dissolution rate of oxygen in water (the controlling step of Reaction 6-11) and the high decomposition rate of transition metal magnides in water, the hydrolysis reaction of transition metal magnides still dominates the decomposition of these magnides in water.

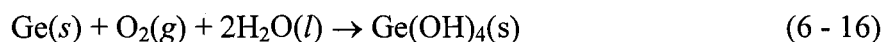
Chapter VI. Application of the hydrolysis behaviour of magnides in the synthesis of nanoparticles

In the case of Mg_2Ge , its sluggish decomposition means that Reaction 6-11 is comparable with, or even dominant over, Reaction 6-10. Thus, the newly formed Ge particles could be readily attacked by the dissolved oxygen in the solution.

Only germania, and no Ge hydroxides, was found in the final product. Hence, the oxidation reaction of Ge nanocrystals seems to be as follows:

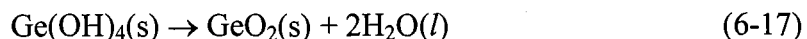


The pH value of the aqueous solution of Ge nanoparticles, determined by pH paper, was around 5, which suggests the existence of $Ge(OH)_4$. The reaction can be written as follows:



$Ge(OH)_4$ is a weak alkali. $Mg(OH)_2$, the byproduct in Reactions 6-10 and 6-11, is a weak acid. $Ge(OH)_4$ will react with $Mg(OH)_2$, and form Mg_2GeO_4 . As a result, Mg_2GeO_4 was found in the hydrolysis product of Mg_2Ge .

In addition, $Ge(OH)_4$ is an unstable intermediate product, and would dissociate into germania and water during the evaporation of ethanol. The dissociation reaction of $Ge(OH)_4$ can be written as follows:



When Mg_2Ge was rinsed by a dilute acid, Reaction 6-9 dominated the overall process, and Reactions 6-10 and 6-11 were negligible. Thus, oxidation of the newly formed Ge could be minimized.

The as-prepared Ge nanoparticles were generally aggregated together as shown in Fig.6.21. The chemical composition of the Ge nanoparticles determined by EDS shows

Chapter VI. Application of the hydrolysis behaviour of magnides in the synthesis of nanoparticles

that only oxygen and Ge, no Mg was detected (see Fig.6.22). The results indicate Mg(OH)_2 or MgCl_2 was totally removed from the final product. No discrete Ge nanoparticles were observed unlike transition metal nanoparticles prepared by the hydrolysis method. Therefore, the aggregation of the Ge nanoparticles cannot be totally attributed to high surface energy, and may be related with the intrinsic chemical characteristics of Ge(OH)_4 . The unstable Ge(OH)_4 has a strong tendency to undergo self condensation reactions to give compounds containing the Ge-O-Ge linkage. Thus, there is a chemical affinity among the unstable Ge(OH)_4 layers on different Ge nanocrystals, which may be the reason that the as-prepared Ge nanoparticles were always aggregated together.

A general trend for the formation of crystalline nuclei of semiconductor elements, *eg.* Ge and Si, is that the more covalent the element, the higher is its crystallization temperature[190]. At low temperatures, amorphous phases become more common as the material becomes more covalent. Hence, it has been reported that both high temperature and high pressure are generally required to obtain Ge and Si nanocrystals by a solution method[191].

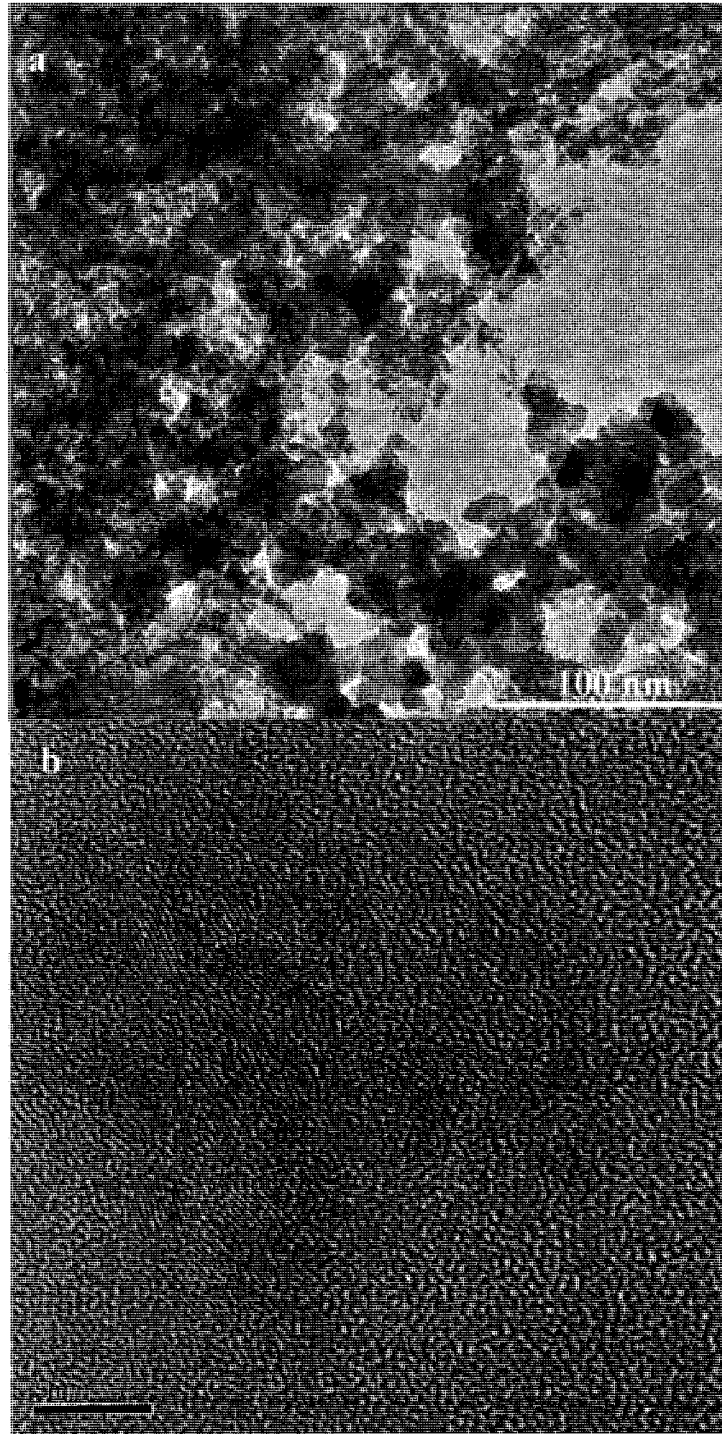


Fig.6.21 The newly formed Ge produced from hydrolysis of Mg_2Ge at room temperature, a) TEM image, b) HRTEM.

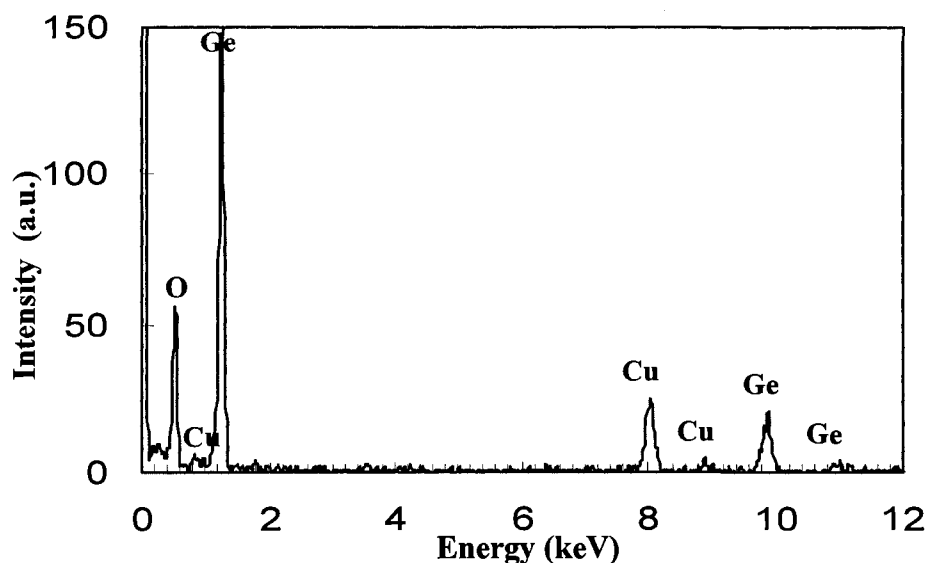


Fig. 6.22 EDS spectrum for the newly formed Ge produced from hydrolysis of Mg_2Ge at room temperature.

Thus, to improve the crystallinity of the newly formed Ge derived from the hydrolysis of Mg_2Ge , the hydrolysis temperature should be increased. To test this hypothesis, ball-milled Mg_2Ge particles were hydrolyzed at $80^\circ C$ for 24h and then cooled down to room temperature. 0.5M hydrochloric acid was carefully and slowly added to the solution to remove the $Mg(OH)_2$ from the hydrolysis product. Initially, many fine hydrogen bubbles were released. The result suggests that the hydrolysis of Mg_2Ge was not complete after 24 hours. When the pH value of the solution reached 4, the addition of the dilute acid was stopped. The final product was rinsed three times using distilled water, then three times using 99% pure ethanol.

Chapter VI. Application of the hydrolysis behaviour of magnides in the synthesis of nanoparticles

The XRD powder diffraction pattern, Fig. 6.23, shows that the final product derived from hydrolysis of Mg_2Ge at 80°C for 24h consisted of Ge ((JCPDS file No. 65-0333) and $\text{Mg}_3\text{Ge}_2\text{O}_5(\text{OH})_4$ (JCPDS file No.11-0250). Compared with the result for hydrolysis at room temperature, a new product, $\text{Mg}_3\text{Ge}_2\text{O}_5(\text{OH})_4$, was found in the final product hydrolyzed at 80°C . The result suggests that hydrolysis at high temperatures promoted Reaction 6-11 rather than Reaction 6-10. As a result, more $\text{Ge}(\text{OH})_4$ was generated compared with hydrolysis at room temperature. $\text{Ge}(\text{OH})_4$ reacted with $\text{Mg}(\text{OH})_2$ and formed $\text{Mg}_3\text{Ge}_2\text{O}_5(\text{OH})_4$. The reaction can be written as follow:



Compared with $\text{Mg}(\text{OH})_2$, $\text{Mg}_3\text{Ge}_2\text{O}_5(\text{OH})_4$ was relatively difficult to remove by adding a dilute acid till the pH value reached a value of 4. As a result, $\text{Mg}_3\text{Ge}_2\text{O}_5(\text{OH})_4$ was always found in the hydrolysis product of Mg_2Ge at high temperatures, i.e. 80°C .

If Mg_2Ge underwent hydrolysis at higher temperatures under a zero oxygen environment, Reactions 6-11, 6-17 and 6-18 would not take place, and Ge nanocrystals could probably be produced.

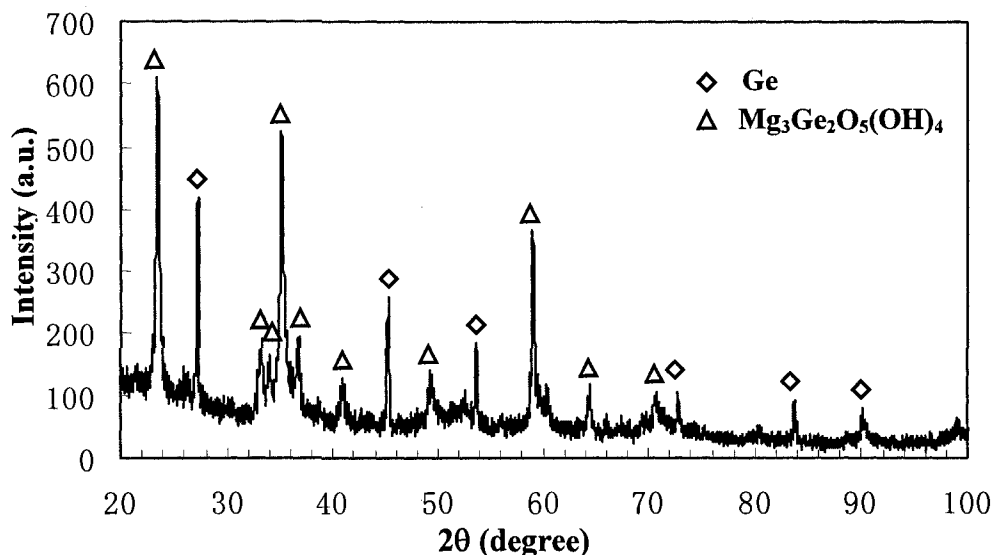


Fig.6.23 XRD powder diffraction pattern of the product after hydrolyzing and acid rinsing at 80°C for 24h.

6.6. Study on hydrolysis behavior of Mg₂Si

Mg₂Si was synthesized by a conventional melting and casting method. Some surplus Mg was added in order to improve the castability of the Mg₂Si alloy. The weight ratio of Mg to Si is 3:1. 10 gram of the ball-milled Mg₂Si particles were immersed into 500ml of distilled water and stirred for 48h at room temperature, 60°C or 80°C. Then, the hydrolyzed product, Mg(OH)₂, was carefully removed from the hydrolysis product by adding 0.5M hydrochloric acid. The sample was rinsed three times using distilled water, then three times using 99% pure ethanol.

Due to a small amount of surplus Mg in the initial materials, Mg and Periclase (MgO) diffraction peaks were observed in the XRD pattern for the ball-milled Mg₂Si particles (see Fig.6.24a). In addition, the Mg₂Si diffraction peaks ((JCPDS file No. 65-9365), but

Chapter VI. Application of the hydrolysis behaviour of magnides in the synthesis of nanoparticles

no Si peaks, were observed, which shows that all the Si particles in the initial materials totally converted into Mg_2Si after melting and casting. Some of the surplus Mg was oxidized during the melting and casting, which gave rise of the formation of MgO .

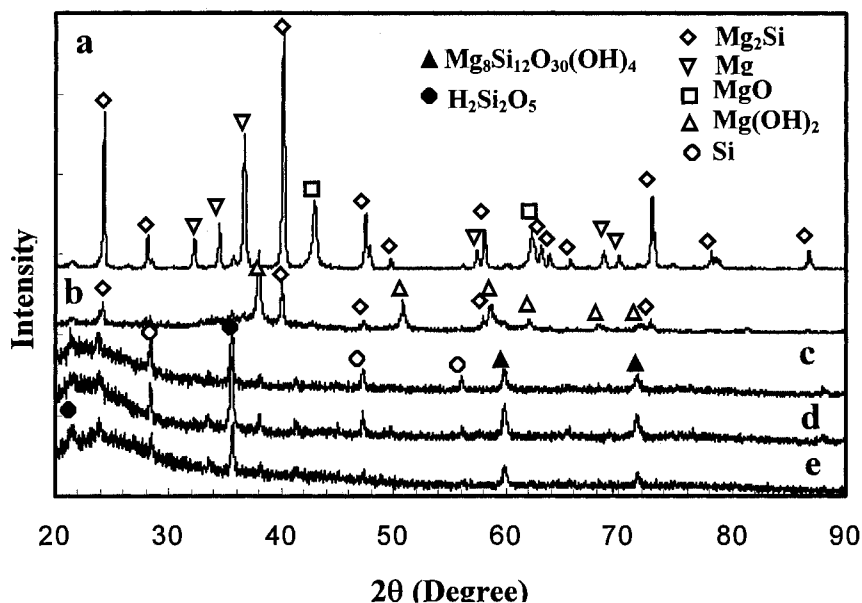


Fig.6.24 XRD patterns for: a) the ball-milled Mg_2Si particles, b) the hydrolysis product of the ball-milled Mg_2Ni particles at room temperature, c) the solid product after acid rinsing at room temperature, d) the solid product after hydrolyzing for and acid rinsing at 60°C, e) the solid product after hydrolyzing and acid rinsing at 80°C.

As the ball-milled particles of 10gram were immersed in 500ml of distilled water at room temperature, many fine hydrogen bubbles were immediately released. The pH value of the solution, determined using pH papers, soon reached about 10~11, which agrees with the pH value for a saturated $\text{Mg}(\text{OH})_2$ solution.

Chapter VI. Application of the hydrolysis behaviour of magnides in the synthesis of nanoparticles

After the ball-milled Mg_2Si particles were immersed into 500ml of distilled water and stirred for 48h at room temperature, Mg_2Si , and $Mg(OH)_2$ peaks were found in the XRD pattern for the hydrolyzed product (see Fig.6.24b). Diffraction from the amorphous phase is much weaker than that observed for the hydrolysis product of Mg_2Ge . This result indicates that the hydrolysis rate of Mg_2Si was much slower than that of transition metal magnides and Mg_2Ge .

After the Mg_2Si powders were immersed in water for 48h, 0.5M hydrochloric acid was very slowly added to the solution, and the hydrolysis of the ball-milled Mg_2Si particles was accelerated. Many fine hydrogen bubbles were continuously released, which shows that the hydrolysis of Mg_2Si can be promoted by increasing the pH value of the solution.

More dilute hydrochloric acid was slowly added to the solution till the pH value of the solution remained stable at 4-5, and hydrogen bubbles were no longer released. This indicated that decomposition of the remaining Mg_2Si , and the removal of $Mg(OH)_2$ by the acid, were complete.

After $MgCl_2$ was rinsed out using distilled water and ethanol, Si (JCPDS file No.25-1402), $H_2Si_2O_5$ (JCPDS file No. 27-0606) and $Mg_8Si_{12}O_{30}(OH)_4$ (JCPDS file No.26-1227) were found in the final product (see Fig.6.24c). It was worth noticing that there is a strong amorphous phase background, especially at the low diffraction angles. However, some weak Si diffraction peaks were observed, which reflects the fact that there are some Si crystals in the hydrolyzed product of Mg_2Si . The results suggest that the Si derived from decomposition of Mg_2Si consisted of a large amount of amorphous Si phase and a small amount of Si crystals.

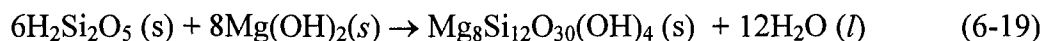
Chapter VI. Application of the hydrolysis behaviour of magnides in the synthesis of nanoparticles

During decomposition of Mg_2Si by adding an acid, the newly formed Si will readily react with the dissolved oxygen in solution due to the strong affinity of Si to oxygen.

The oxidation reaction of the Si nanoparticles can be written as follows:



$\text{H}_2\text{Si}_2\text{O}_5$ is called silicic acid (a weak acid with a pH value between 4 and 5). Therefore, the new formed $\text{H}_2\text{Si}_2\text{O}_5$ will further react with $\text{Mg}(\text{OH})_2$ (a weak alkali) and form some magnesium silicate hydroxide. The reaction can be written as follows:



Therefore, $\text{Mg}_8\text{Si}_{12}\text{O}_{30}(\text{OH})_4$ was always found in the product.

As was the case for Ge, the as-prepared Si nanoparticles always formed aggregates as shown in Fig.6.25. The aggregation of the Si nanoparticles may be related to the intrinsic chemical characteristics of the silicon hydroxides. The silicon hydroxides ($\text{Si}(\text{OH})_4$) have a strong tendency to undergo self condensation reactions to form $\text{H}_2\text{Si}_2\text{O}_5$. Thus, there is a chemical affinity between the unstable hydroxide layers on different Si nanoparticles, which may be the reason that the as-prepared Si nanoparticles always formed aggregates. The EDS analysis result (see Fig.6.26) indicates that Si, O and a small amount of Mg were presented in the final product. This result is in accord with the XRD analysis results.

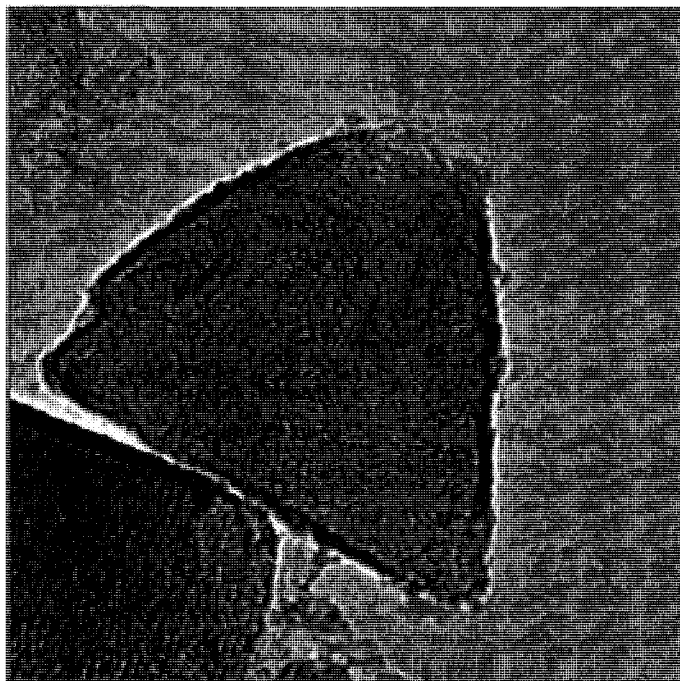


Fig.6.25 TEM image of the product after hydrolysis and acid rinsing at room temperature.

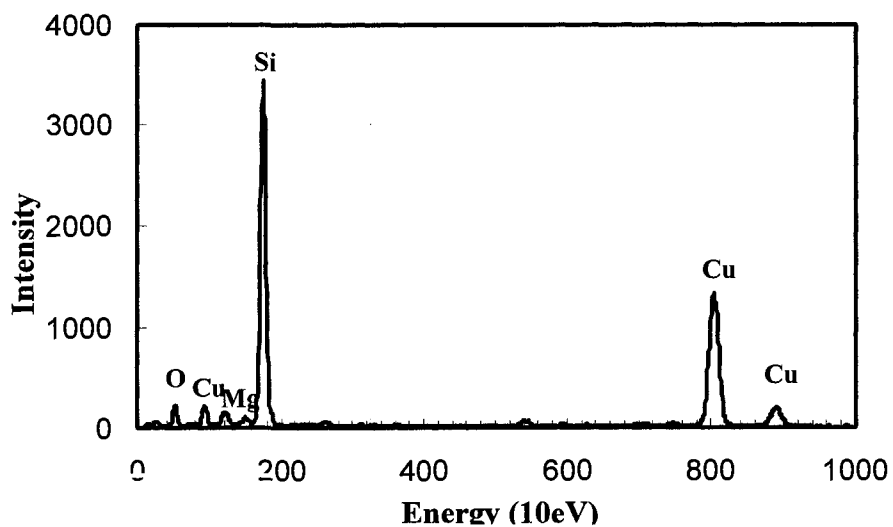


Fig.6.26 The EDS spectrum for the membrane in Fig 6.25.

Chapter VI. Application of the hydrolysis behaviour of magnides in the synthesis of nanoparticles

The XRD analysis results (see Figs.6.24c, d and e) show that the final product of hydrolysis at room temperature, 60°C and 80°C. consisted of both amorphous and crystalline Si, and $\text{Mg}_8\text{Si}_{12}\text{O}_{30}(\text{OH})_4$. There is no significant difference among the final product of the three samples hydrolyzed at room temperature, 60°C and 80°C. The hydrolysis at such low temperatures could not significantly produce the crystalline Si nanoparticles.

6.7 Summary

The main conclusions from this section of the work are as follows:

1. Besides Ni nanoparticles, other transition metal nanoparticles (Cu, Ag and Au) have been successfully synthesized by hydrolysis of their magnides. These nanoparticles were all close to spherical in shape and had a mean size of around 10nm.
2. Au and Ag nanoparticles prepared by this method are resistant to oxidation from the dissolved oxygen in an aqueous solution. The oxidation rate of Cu nanoparticles was sensitive to the pH value of the solution: The lower the pH value, the higher the oxidation rate. Cu nanoparticles in an aqueous solution were first oxidized into CuOH by the dissolved oxygen, which then quickly dissociated into Cu_2O .
3. The hydrolysis of Mg_2Ge was sluggish at room temperature under one atmosphere, but the hydrolysis rate of Mg_2Ge can be significantly promoted by adding the hydrochloric acid.
4. The hydrolysis rates of both Mg_2Ge and Mg_2Si are very slow.

CHAPTER SEVEN: STUDY ON THE HYDROLYSIS BEHAVIOUR OF ALUMINIDES AND SODIDES AND ITS APPLICATION IN PRODUCTION OF NANOPARTICLES

7.1 Introduction

The hydrolysis behavior of magnides has been described in detail in Chapters IV, V and VI. It seemed likely that the aluminides and sodides would have the same hydrolysis behaviour as the magnides. In this chapter, we have extended our investigation from magnides to aluminides and then the sodium intermetallic compounds (sodides). Al_3Ni and Al_3Ni_2 were chosen as representatives of the aluminides. Ag_2Na and PtNa were chosen as representatives of the sodides.

7.2 Hydrolysis of Ni aluminides

Al_3Ni , and Al_3Ni_2 alloys (nominal compositions: $\text{Al}_{3.4}\text{Ni}$, and AlNi_2 , respectively) were prepared by a conventional melting and casting method. 10 grams of the ball-milled Al_3Ni particles were then immersed in 500ml distilled water for 120h. Since Al_3Ni_2 underwent a very slow hydrolysis, the hydrolysis test of the ball-milled Al_3Ni_2 particles was extended to 720h.

7.2.1 Hydrolysis of Al₃Ni

The as-cast Al₃Ni pellets consisted of Al₃Ni (JCPDS file No.02-0416) and Al (see Fig.7.1a). The XRD pattern (Fig.7.1b) indicates that there was some bayerite (Al(OH)₃, (JCPDS file No.20-0011) and un-hydrolyzed Al and Al₃Ni in the hydrolysis product of the ball-milled Al₃Ni particles in water. Although, no significant Ni diffraction peaks were found in Fig.7.1b, the hydrolysis product of Al₃Ni exhibited paramagnetism when examined using a magnet. Only Ni of all the potential hydrolysis products is known to exhibit paramagnetism. These results showed that Al₃Ni can spontaneously hydrolyze at room temperature. When the ball-milled Al₃Ni particles were immersed in distilled water, the pH value of the solution rapidly reached a stable value of 5~6, and thereafter remained at that level.

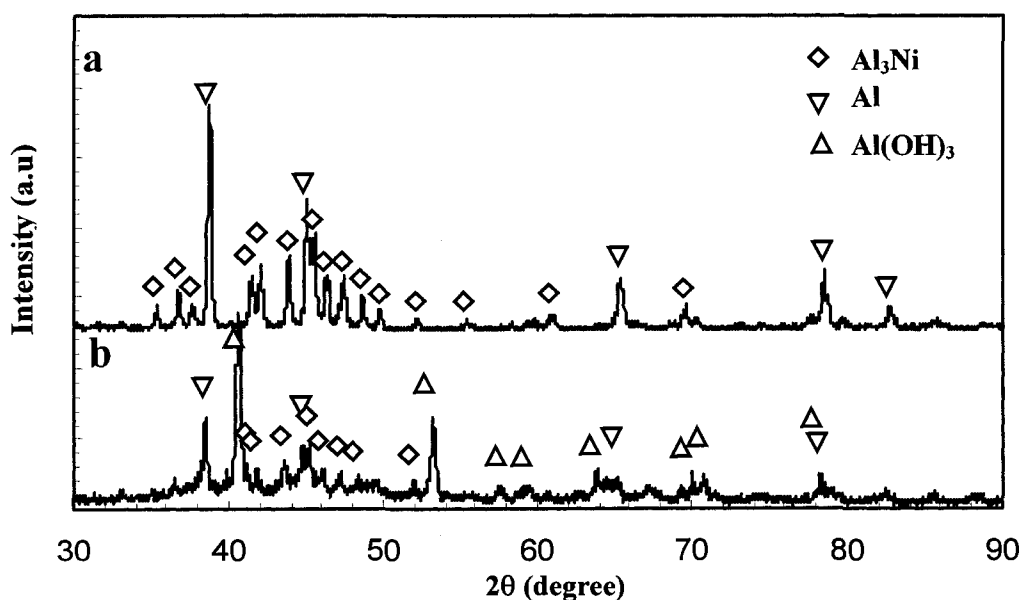
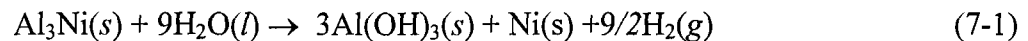


Fig.7.1 XRD powder diffraction patterns for a) as-cast Al₃Ni alloy, b) its hydrolysis product in distilled water for 120h.

Chapter VII: Study on the hydrolysis behaviour of aluminides and sodides and its application in production of nanoparticles

Generally, Al is more active than Al₃Ni. Therefore, Al₃Ni would be protected from water attack by hydrolysis of Al. In other words, Al₃Ni should theoretically not be hydrolyzed before Al was totally converted into Al(OH)₃. In this case, part of the Al₃Ni had been hydrolyzed into Al(OH)₃, Ni and H₂ while some Al was still present.

The hydrolysis reaction for the hydrolysis of Al₃Ni is given as follows:



The standard formation enthalpies and the standard entropies for Al(OH)₃ and Al₃Ni are -1284KJ/mol and 71J/°C•mol, -149.5KJ/mol and 110.64 J/°C•mol, respectively [184,185].

The standard free energy change ΔG_{7-1} is as follows:

$$\Delta G_{7-1} = -1278.17 \text{ KJ/mol} + RT \ln \frac{\alpha_{\text{Al}(\text{OH})_3}^3 \alpha_{\text{Ni}} \rho_{\text{H}_2}^9}{\alpha_{\text{Al}_3\text{Ni}} \alpha_{\text{H}_2\text{O}}^9} \quad (7-2)$$

The negative standard free energy change indicates that Reaction 7-1 is spontaneous.

The standard free energy change for the hydrolysis reaction of Al₃Ni is much smaller than that for Mg₂Ni. Thus, from thermodynamic considerations, the hydrolysis of Al₃Ni should be much easier than that of Mg₂Ni. From a crystal structure point of view, more Al atoms surround a Ni atom in Ni₃Al than Mg atoms surround a Ni atom in Mg₂Ni. However, the hydrolysis rate of Al₃Ni was much slower than that of Mg₂Ni. This might be caused by the fact that the hydrolysis product, Al(OH)₃, covered the whole surface of the Al particles and inhibited their further hydrolysis.

7.2.2 Hydrolysis of Al₃Ni₂

In order to systematically investigate the hydrolysis behavior of aluminides, the hydrolysis behaviour of Al₃Ni₂ was then studied. Al₃Ni₂ has a hexagonal D5₁₉ structure.

Chapter VII: Study on the hydrolysis behaviour of aluminides and sodides and its application in production of nanoparticles

Either 3 Al atoms, or one Al atom and two Ni atoms form a trigonal omega structure, which can be viewed as a five-layer close-packed unit cell with stacking *ABCBCA* [189]. Al_3Ni_2 ((JCPDS file No.65-9699), Ni and some small Al_3Ni diffraction peaks were observed in the XRD pattern of as-cast Al_3Ni_2 (Fig 7.2a). Al_3Ni_2 , Ni and small amount of $\text{Al}(\text{OH})_3$ were found in the hydrolysis product (see Fig.7.2b). The pH value of the solution was in the range of 5 to 6. Comparing the XRD patterns before and after the ball-milled Al_3Ni_2 particles were immersed in water for 720h, the change in intensity of the Al_3Ni_2 diffraction peaks was very small, which suggests that Al_3Ni_2 barely undergoes hydrolysis. The small amount of $\text{Al}(\text{OH})_3$ in the hydrolyzed product could probably result from the hydrolysis of the small amount of Al_3Ni in the initial material.

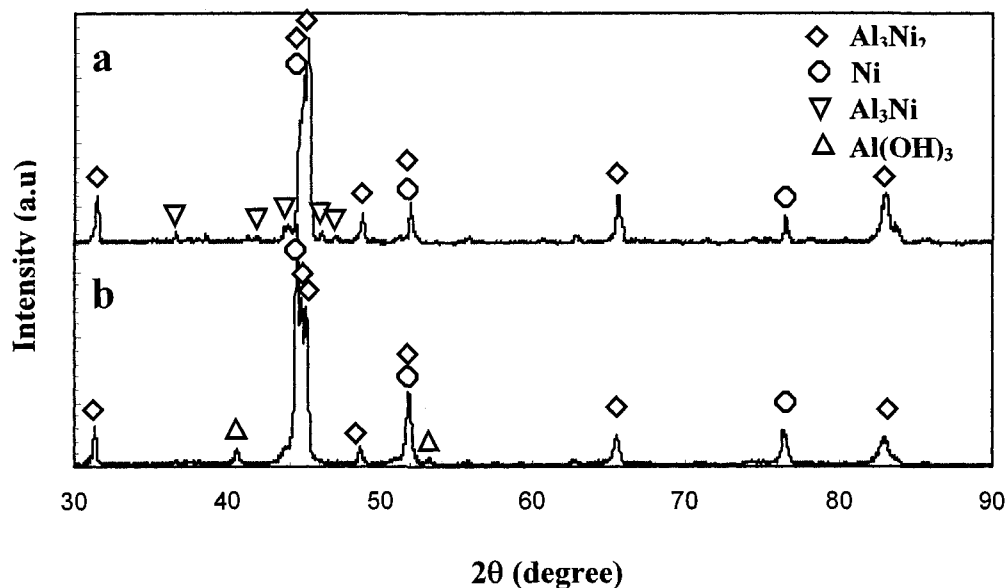
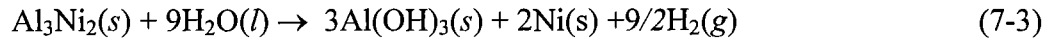


Fig.7.2 XRD powder diffraction patterns for a) as-cast Al_3Ni_2 alloy, b) its hydrolysis product in distilled water for 720h.

Chapter VII: Study on the hydrolysis behaviour of aluminides and sodides
and its application in production of nanoparticles

If Al_3Ni_2 were to undergo hydrolysis, the hydrolysis reaction would probably be as follows:



The standard formation enthalpy and the standard entropy for Al_3Ni_2 is -1284KJ/mol and $71\text{J/}^\circ\text{C}\cdot\text{mol}$. The standard free energy change ΔG_{7-3} is given as follows:

$$\Delta G_{7-3} = -1278.17\text{KJ/mol} + RT \ln \frac{\alpha_{\text{Al}(\text{OH})_3}^3 \alpha_{\text{Ni}}^2 P_{\text{H}_2}^{\frac{9}{2}}}{\alpha_{\text{Al}_3\text{Ni}_2} \alpha_{\text{H}_2\text{O}}^9} \quad (7-4)$$

From a thermodynamics viewpoint, the negative standard free energy change suggests that Reaction 7-3 is spontaneous. However, our experimental results showed that Al_3Ni_2 barely undergoes hydrolysis in distilled water at room temperature. Therefore, the hydrolysis of Al_3Ni_2 was limited by other factors, which may include the reaction kinetics and crystal structure factors. From a thermodynamics viewpoint and crystal structure factor, the hydrolysis of AlNi and AlNi_3 in the Ni-Al binary system would be much slower than for Al_3Ni_2 .

The solubility of product constants of $\text{Al}(\text{OH})_3$ is 1.3×10^{-33} [184]. The corresponding theoretical pH value is 4.3. The experimental pH value that we measured using pH papers was between 4 and 5. Therefore, increasing the pH value of the solution (adding some alkali) will accelerate the hydrolysis of Al_3Ni_2 . Although the hydrolysis of Al_3Ni_2 barely proceeds in water, it can be carried out in a concentrated, hot NaOH solution [185].

There are two means of removing the $\text{Al}(\text{OH})_3$ in the hydrolysis product of aluminide, that is by using acids or alkalis. Due to the low acidity of $\text{Al}(\text{OH})_3$, using dilute hydrochloric acid to remove $\text{Al}(\text{OH})_3$ will lead to a fairly low pH value of solution. As a result, the chemically active transition metals such as Fe, Co, Ni, or even Cu

Chapter VII: Study on the hydrolysis behaviour of aluminides and sodides and its application in production of nanoparticles

nanoparticles cannot survive in the solution, especially when it is exposed to air. Only chemically inert transition metals such as Au could be prepared by this method.

The method which directly uses alkali to promote the hydrolysis of the aluminides and to remove $\text{Al}(\text{OH})_3$, is similar to the Raney method: The Raney method, which uses concentrated hot NaOH solution to dissolve the aluminum in the finely ground aluminides with the evolution of H_2 , will give rise to very finely divided transition metal particles. The method was first described in detail in 1927 in a patent issued to Raney [1].

7.3 Hydrolysis of sodides

Many small Ag-Na and Pt-Na pellets (about 0.05g each) were cut from the two ingots. The Ag-Na or Pt-Na pellets with a total weight of about 0.5g were put into 500ml distilled water in a matrass (having a fine and long neck to avoid splashes resulted from small explosions) one by one.

7.3.1 Hydrolysis of Ag_2Na

Both Ag_2Na and PtNa pellets were synthesized at 600°C for 2 hours under a protection of argon and cooled down to room temperature in furnace. Ag_2Na (JCPDS file No. 29-1146), Na and NaOH (JCPDS file No. 35-1009) diffraction peaks were observed in the XRD patterns for the Ag-Na pellets prepared at 600°C for 2 hours (see Fig.7.3). No Ag peaks were observed, which shows that all the Ag powders in the initial materials were totally converted to Ag_2Na after *in-situ* synthesis. The presence of NaOH suggests that some Na in the pellets was oxidized by either oxygen and/or moisture in the air during testing.

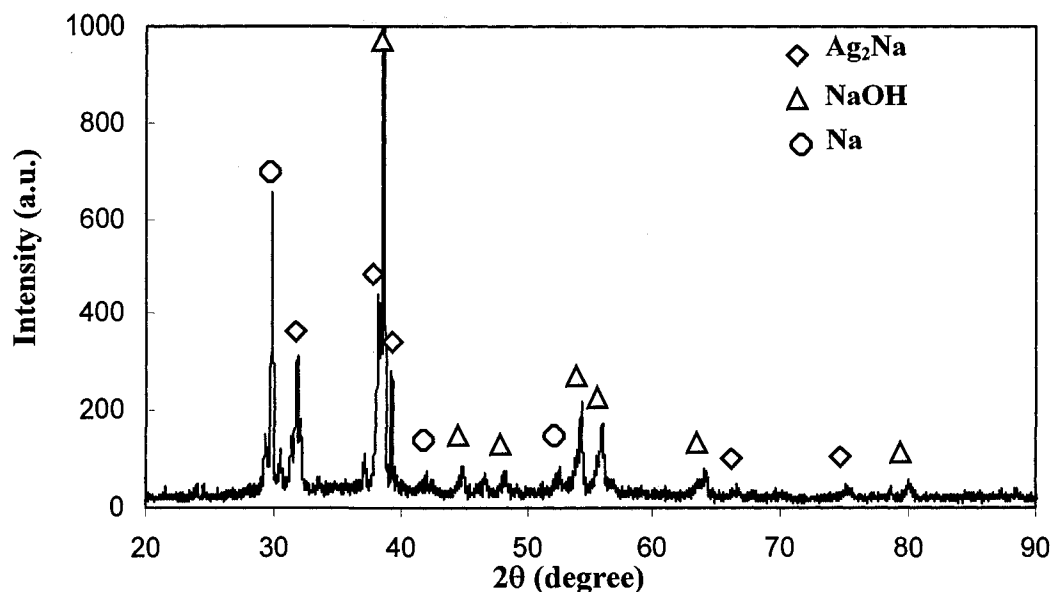
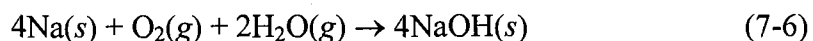
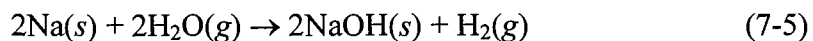


Fig.7.3 XRD powder diffraction pattern of the Ag-Na pellets prepared at 600°C for 2 hours.

The oxidation product of sodium in the Ag-Na pellets was NaOH. The possible oxidation reactions in air are as follows:



When the small Ag-Na pellets were dropped into a matrass, which contained 500ml distilled water, the hydrolysis reactions were very severe, sometimes, accompanied by small explosions or combustion. The solution in the matrass instantaneously became a colloid.

After being rinsed in water and ethanol, and dried in flowing air, Ag nanoparticles were obtained. The XRD result (see Fig.7.4) indicates that the final solid product in the Ag-Na

Chapter VII: Study on the hydrolysis behaviour of aluminides and sodides and its application in production of nanoparticles

sample only consisted of Ag particles (JCPDS file No. 04-0783) after rinsing with distilled water and ethanol.

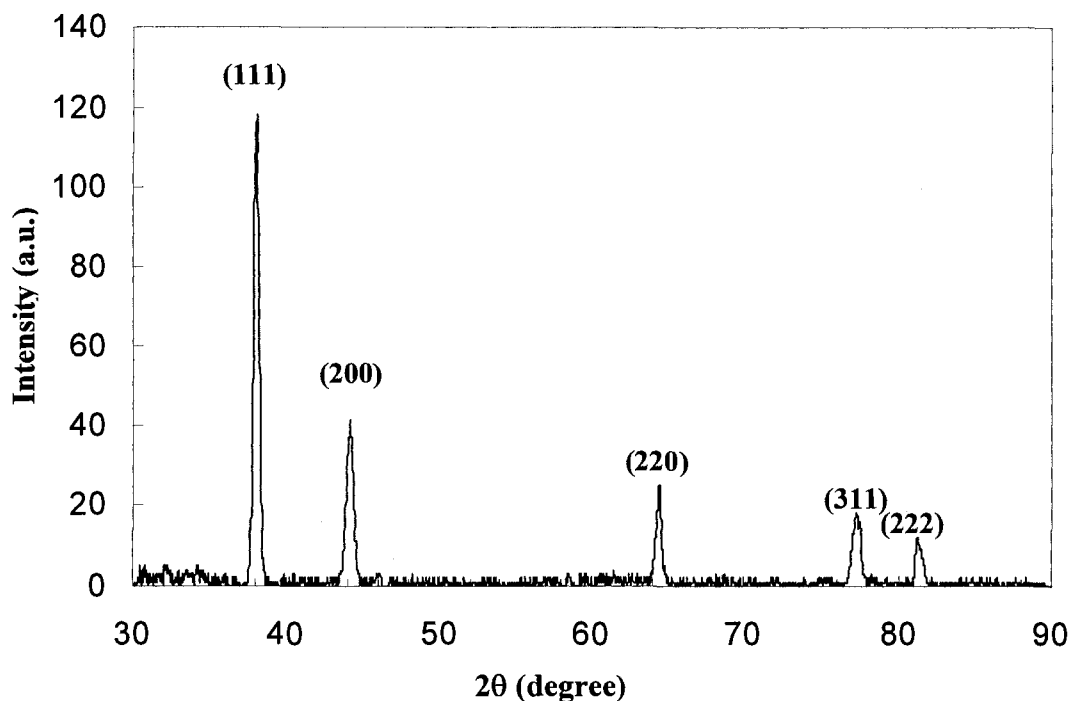


Fig.7.4 XRD powder diffraction pattern of the Ag nanoparticles prepared by hydrolysis of Ag_2Na .

Discrete Ag nanoparticles were observed (see Fig.7.5a). The Ag nanoparticles were predominantly spherical in shape and had a size of around 10 nm, which agrees with the results of the particle size analysis (see Fig.7.6). The size of the Ag nanoparticles ranged from 5.4nm to 17.2nm with a mean size of 8.3nm. The high-resolution TEM image for individual nanoparticles (see Fig.5b) shows that the spacing for the lattice fringes of the indicated nanoparticles is 0.230nm. This is close to the (111) interplanar spacing for Ag

Chapter VII: Study on the hydrolysis behaviour of aluminides and sodides and its application in production of nanoparticles

(0.2259nm). In addition, the fringes for the individual particles indicate that some of the small Ag nanoparticles are single crystals. The EDS spectrum shows that no significant oxygen or Na was present (see Fig.7.7). Their result suggests that the Ag nanoparticles are resistant to oxidation from both the dissolved oxygen in an aqueous solution, and oxygen in flowing air.

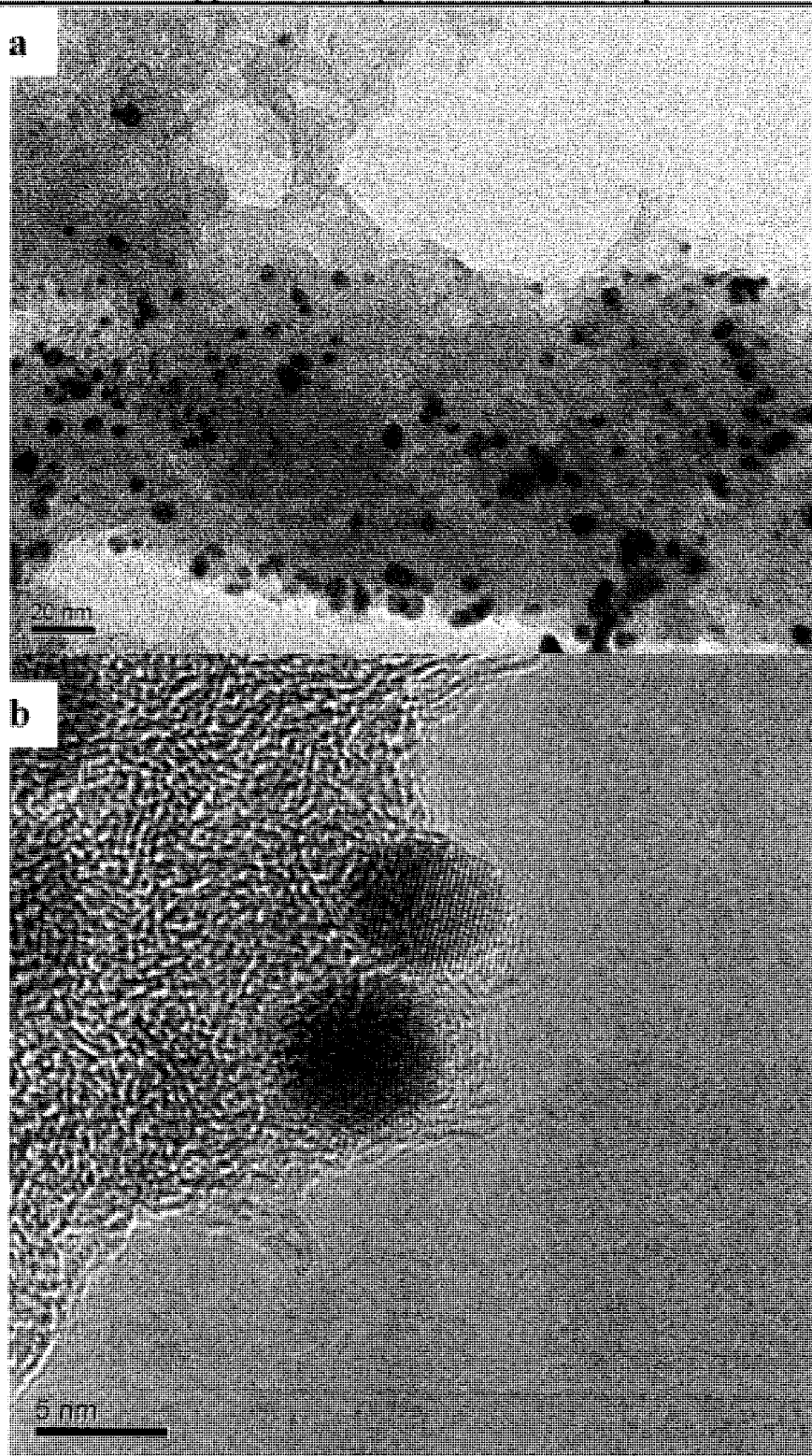


Fig.7.5 Morphology of Ag nanoparticles prepared by hydrolysis of Ag_2Na , a) TEM image, b) HRTEM image.

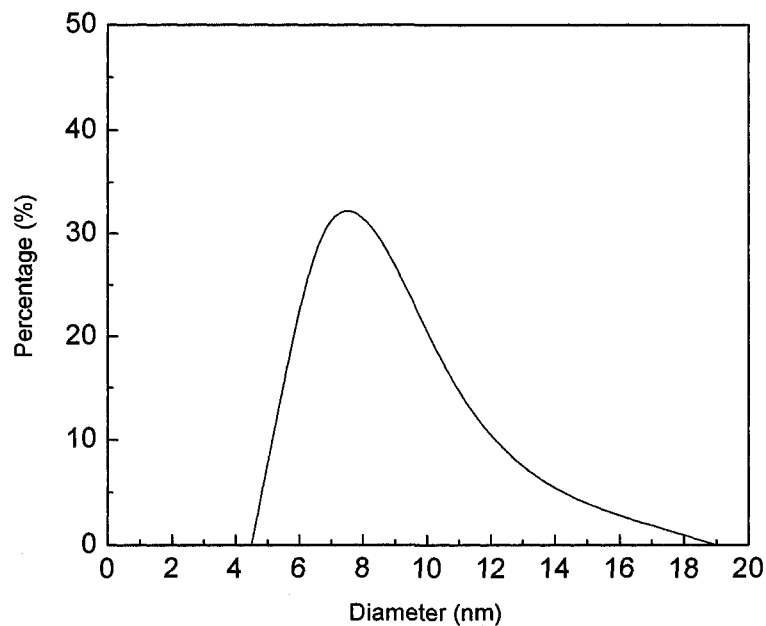


Fig.7.6 Particle size distribution of the Ag nanoparticles prepared by hydrolysis of Ag_2Na .

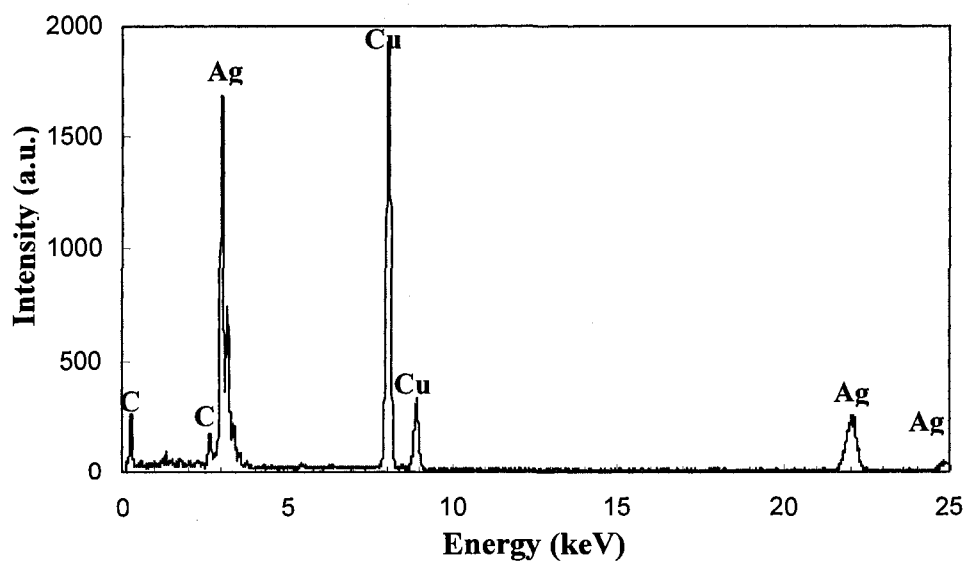


Fig. 7.7 EDS pattern of the Ag nanoparticles prepared by hydrolysis of Ag_2Na .

7.3.2 Hydrolysis of PtNa

Na, PtNa (JCPDS file No. 50-2018), NaOH and Pt (JCPDS file No. 65-2868) diffraction peaks were observed in the XRD patterns for the Pt-Na pellets prepared at 600°C for 2 hours (see Fig.7.8). The Pt peaks in Fig.7.8 were fairly broad, which reflects the fact that the crystallite size of Pt particles was extremely small (much smaller than 500nm for the initial Pt particles).

It has been reported that Pt and Na with a atomic ratio of 1:1 are totally converted into PtNa at 350-400°C, and a lower transformation temperature can be achieved when the Pt concentration was less than 50 atomic percent [192].

According to the compositions of the initial materials in the two samples, a close to homogeneous alloy melt would be generated at 600°C. In other words, Pt should be completely converted into PtNa after cooling down. Therefore, the Pt particles in the Pt-Na pellets do not come from the initial Pt powders. In addition, the Pt diffraction peaks in Fig.7.8 were fairly broad, which reflects the fact that the crystallite size of the Pt particles was extremely small. Hence, the Pt particles in the Pt-Na pellets resulted from the dissociation of PtNa (Further TEM and particle size analysis results presented at this end of this Chapter will further verify this point).

NaOH was observed in the Pt-Na pellets, which suggested that both sodium and PtNa react with moisture rather than with oxygen.

A possible reaction of PtNa is given as follows:



Only a part of the Na was oxidized in the Ag-Na pellets during storage. In comparison with the Ag-Na pellets, all Na in the Pt-Na pellets had oxidized into NaOH, even a part of

Chapter VII: Study on the hydrolysis behaviour of aluminides and sodides and its application in production of nanoparticles

PtNa was converted into Pt. Therefore, the oxidation rate of the Pt-Na pellets in air was much higher than that of the Ag-Na pellets under the same conditions.

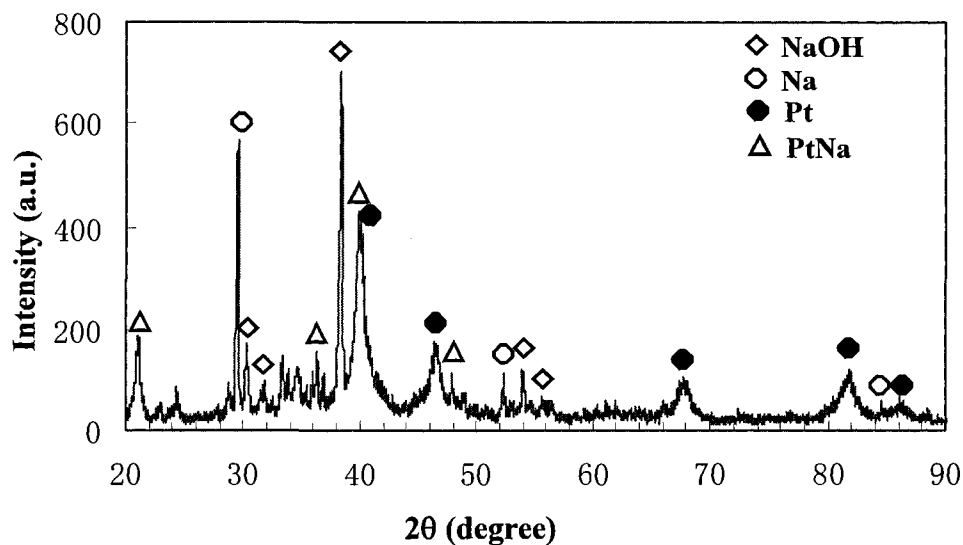


Fig.7.8 XRD powder diffraction pattern of the Pt-Na pellets prepared at 600°C for 2 hours.

Pt is a catalyst for the formation reaction of H_2O from hydrogen and oxygen at room temperature. Sodium and PtNa prefer to react with moisture rather than with oxygen, and spontaneously generate hydrogen. The hydrogen under the existence of the newly formed Pt nanoparticles could react with oxygen and form water again. Thus, Pt is able to accelerate the oxidation of sodium in the Pt-Na pellets.

When the Pt-Na pellets were dropped into a matrass, which contained 500ml distilled water, the reactions were very fast, sometimes, accompanied by small explosions or combustion. Water in the matrass instantaneously became a colloid.

The reactions of Ag_2Na and PtNa in water can be written as follows:

Chapter VII: Study on the hydrolysis behaviour of aluminides and sodides and its application in production of nanoparticles

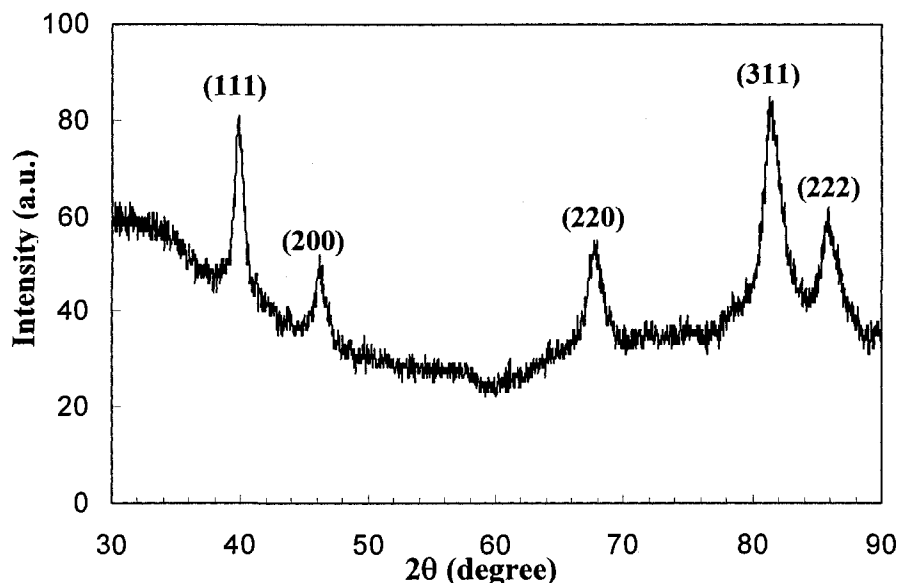
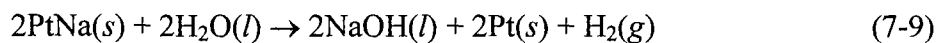
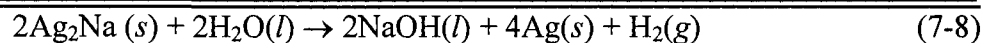


Fig.7.9 XRD diffraction pattern of the Pt nanoparticles prepared by hydrolysis of PtNa.

After rinsing with water and ethanol, and evaporation in flowing air, Pt nanoparticles were obtained. The XRD diffraction pattern, Fig.7.9, shows that the solid final product in the Pt-Na sample consisted only of Pt particles. The morphology of the Pt nanoparticles (see Fig.7.10a) was similar to that of the Ag nanoparticles (close to spherical in shape and a size of around 10 nm). The high-resolution TEM images for individual nanoparticles (see Fig.7.10b) show that the spacings for the lattice fringes of the nanoparticles are 0.235nm. This is close to 0.2265nm, the interplanar spacing for the {111} planes in Pt. The result of particle analysis (see Fig.7.11) shows that the size of the Pt nanoparticles ranged from 5.6nm to 17.9nm with a mean size of 8.7nm. The size of the initial Pt particles used for the preparation of the Pt-Na pellets ranged from 150nm to 500nm,

Chapter VII: Study on the hydrolysis behaviour of aluminides and sodides and its application in production of nanoparticles

which confirmed that these Pt nanoparticles resulted from the hydrolysis of the Pt-Na intermetallic compounds.

No significant oxygen and Na was detected by EDS as shown in Fig.7.12, which indicates that Pt nanoparticles are resistant to oxidation from both the dissolved oxygen in an aqueous solution and oxygen in flowing air.

Compared with the hydrolysis of magnides, the reaction byproduct, NaOH, has a high solubility and is easily removed. This method offers a simpler method for preparing transition metal nanoparticles than the use of magnides or aluminides. The drawback of this method is the difficulty in controlling the reaction rate.

Besides the transition metal (and semiconductor element) – sodium intermetallic compounds, there are many other alkali metal or alkali earth metal intermetallic compounds. Due to their high chemical activity, they could exhibit a similar hydrolysis behavior in water. Hence, they could also have a potential to produce transition metal and semiconductor element nanoparticles.

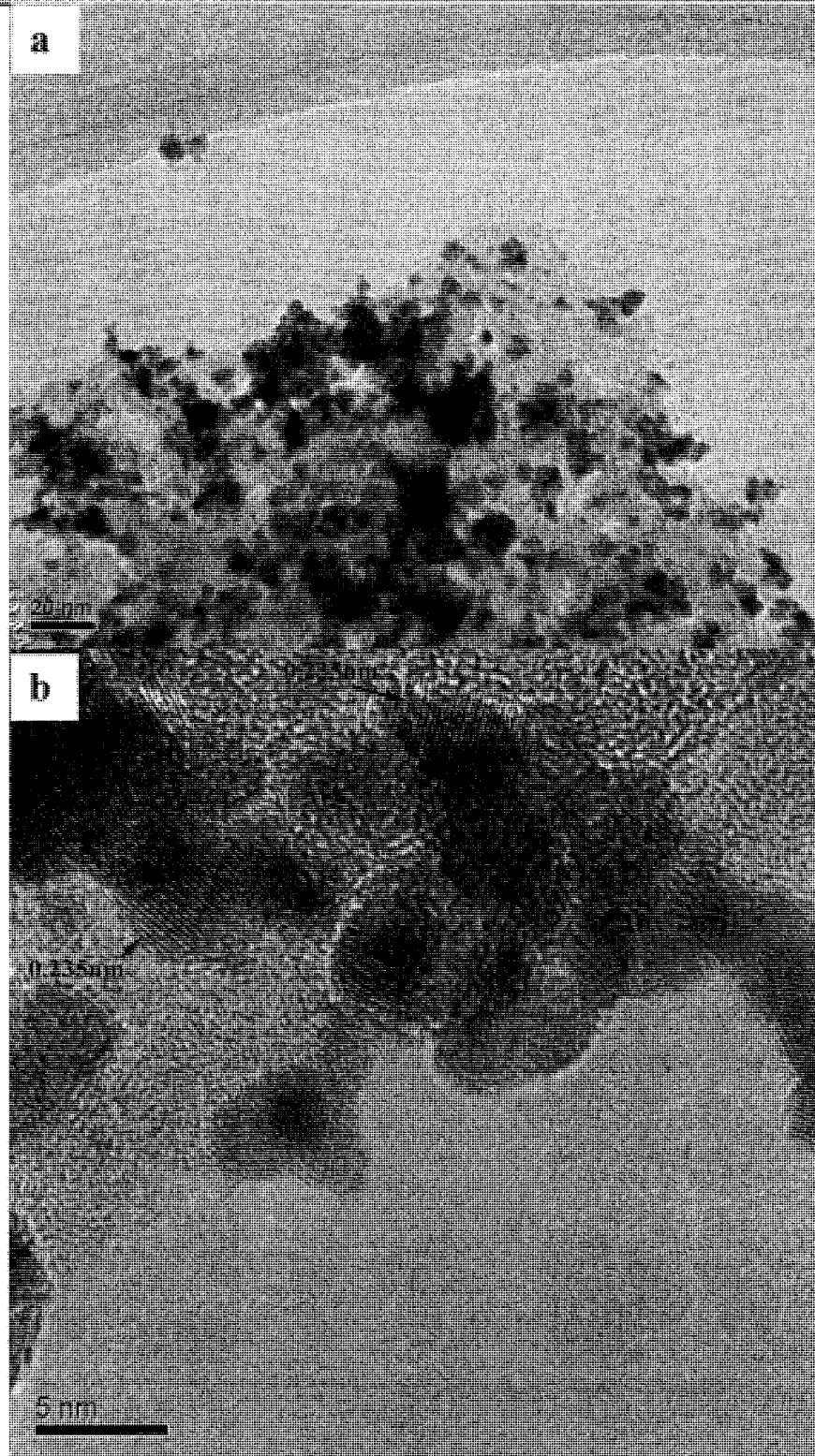


Fig.7.10 Morphology of the Pt nanoparticles prepared by hydrolysis of PtNa ,
a) TEM image, b)HRTEM image.

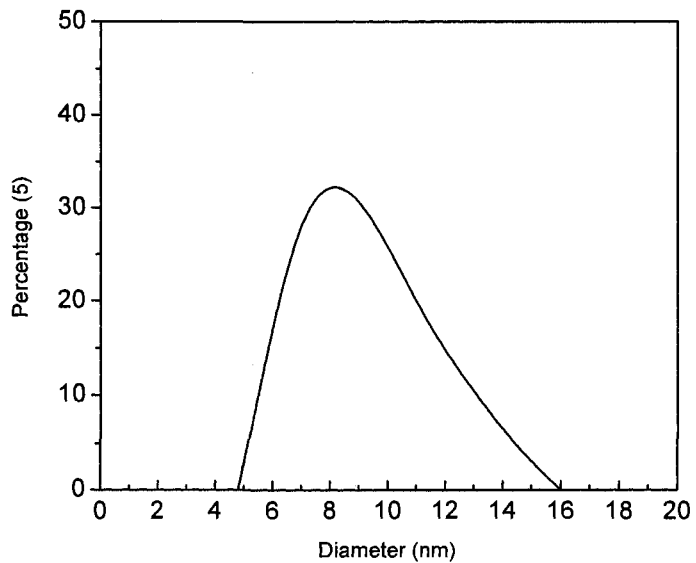


Fig.7.11 Particle size distribution of the Pt nanoparticles prepared by hydrolysis of PtNa.

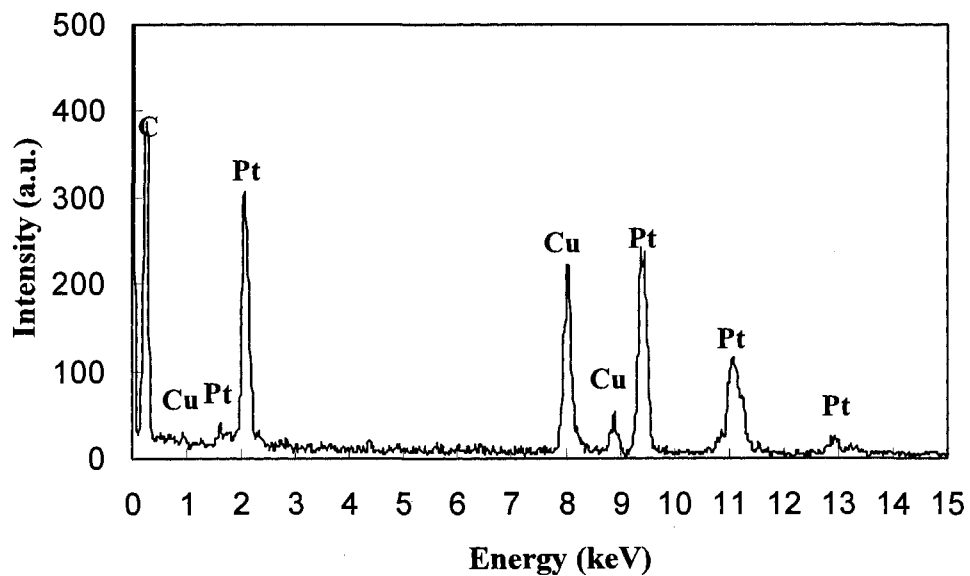


Fig.7.12 EDS pattern of the Pt nanoparticles prepared by hydrolysis of PtNa.

Chapter VII: Study on the hydrolysis behaviour of aluminides and sodides and its application in production of nanoparticles

7.4 Summary

The main conclusions from this study of aluminides and sodides can be summarized as follows:

1. Among the Ni aluminides, Al_3Ni spontaneously undergoes hydrolysis in water at room temperature, and forms $\text{Al}(\text{OH})_3$, Ni and hydrogen in distilled water at room temperature. However, Al_3Ni_2 barely undergoes hydrolysis under the same conditions. The hydrolysis of AlNi and AlNi_3 in the Ni-Al binary system would be much slower than for Al_3Ni_2 due to the thermodynamics and kinetics including crystal structure factors.
2. Although from thermodynamic considerations, the negative standard free energy change for the hydrolysis reaction of Al_3Ni is much larger than that for Mg_2Ni , and from a crystal structure point of view, more Al atoms surround a Ni atom in Ni_3Al than Mg atoms surround a Ni atom in Mg_2Ni , the hydrolysis of Al_3Ni should be much easier than that of Mg_2Ni . In fact, the hydrolysis rate of Al_3Ni was much slower than that of Mg_2Ni , which may result from the relative reaction kinetics.
3. Due to the low acidity of $\text{Al}(\text{OH})_3$, using dilute hydrochloric acid to remove $\text{Al}(\text{OH})_3$ will lead to a fairly low pH value of the solution. As a result, the chemically active transition metals such as Fe, Co, Ni, or even Cu nanoparticles would not survive in the solution, especially when it is exposed to air. Only chemically inert transition metals such as the noble metals could be prepared by this method.
4. The oxidation of sodium in the Pt-Na pellets were much faster than that in the Ag-Na pellets since Pt is able to accelerate the oxidation of sodium in the Pt-Na pellets.

Chapter VII: Study on the hydrolysis behaviour of aluminides and sodides and its application in production of nanoparticles

5. The Ag and Pt nanoparticles prepared by hydrolysis of either Ag_2Na or PtNa were crystalline in nature. The size of the Ag and Pt were spherical in shape with a mean size of around 10nm.
6. The reaction byproduct of sodide hydrolysis, NaOH , has a high solubility and is easier to remove than $\text{Mg}(\text{OH})_2$, the hydrolysis byproduct of magnides. This method thus offers a simpler method for preparing transition metal nanoparticles than hydrolysis of magnides. The drawback of this method is the difficulty in controlling the reaction rate.
7. There are many transition metal (and semiconductor element) - alkali metal or alkali earth metal intermetallic compounds besides sodides. Due to their chemical activity, they could exhibit a similar hydrolysis behavior in water. Hence, they could also have the potential to produce transition metal and semiconductor element nanoparticles.

CHAPTER EIGHT: DISCUSSION AND CONCLUSIONS

The particle size distributions of Ni, Cu, Ag and Au nanoparticles prepared by hydrolysis of Mg_2Ni , $MgNi_2$, Mg_2Cu , $Mg_{45}Ag_{17}$ and Mg_3Au , respectively, are shown in Fig.8.1. The particle size distribution of Ni nanoparticles produced by hydrolysis of Mg_2Ni (Curve Ni(Mg_2Ni) in Fig.8.1) resembles that of Cu nanoparticles prepared by hydrolysis of Mg_2Cu (Curve Cu(Mg_2Cu) in Fig.8.1). The particle size distribution of Au nanoparticles (Curve Au(Mg_3Au) in Fig.8.1) is close to that of Ag nanoparticles prepared by hydrolysis of $Mg_{54}Ag_{17}$ (Curve Ag($Mg_{54}Ag_{17}$) in Fig.8.1). The particle size distributions of the Ni and Cu nanoparticles are larger than that of the Ag and Au nanoparticles, but smaller than that of Ni nanoparticles produced by hydrolysis of $MgNi_2$ (Curve Ni($MgNi_2$) in Fig. 8.1).

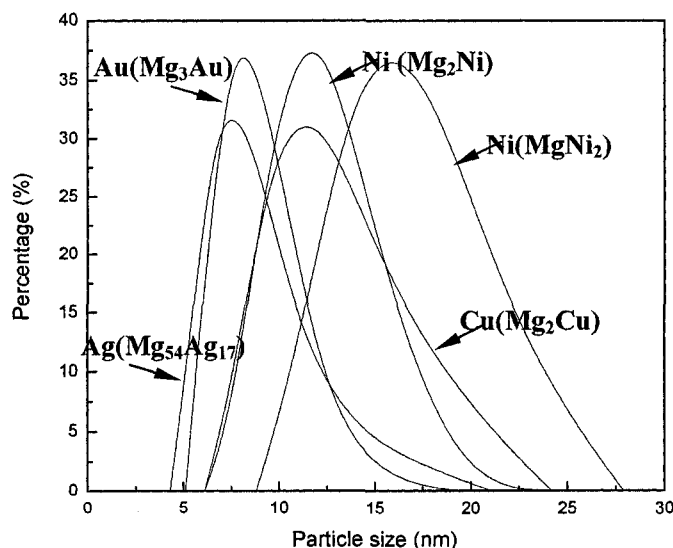


Fig.8.1 A comparison of particle size distribution of Au, Ag, Cu and Ni nanoparticles prepared by hydrolysis of Mg_2Ni , $MgNi_2$, Mg_2Cu , $Mg_{45}Ag_{17}$ and Mg_3Au , respectively.

All above results indicate that the particles size distributions of the transition metal nanoparticles prepared by the magnides with higher atomic ratios of Mg to transition metal are smaller than that of the transition metal nanoparticles prepared by the magnides with lower atomic ratios of Mg to transition metal.

Since the solubility of $\text{Mg}(\text{OH})_2$ in water is very small, the newly-formed $\text{Mg}(\text{OH})_2$ has to precipitate from water in the vicinity of the Mg dissolution sites. The existence of the $\text{Mg}(\text{OH})_2$ particles, and the low mobility of the transition metal atoms at room temperature, could be the reason that the particle size distribution of the transition metal nanoparticles prepared by this method appears not to be sensitive to the concentration of the initial magnides in aqueous solution and the type of transition metal elements.

The atomic ratios of Mg to transition metal in magnides determine the contact opportunities of transition metal atoms derived from hydrolysis of magnides. More contact opportunities mean that transition metal nanoparticles have more chances to grow large. Higher atomic ratios of Mg to transition metal cause less contact opportunities of transition metal atoms derived from hydrolysis of magnides, and smaller sizes of transition metal nanoparticles.

A comparison of transition metal (including semiconductor elements: Ge and Si) nanoparticle synthesis by hydrolysis of magnides, aluminides and sodides is given in Table 8.1. In comparison with hydrolysis of sodides, the hydrolysis reactions of magnides are mild, and suitable for applying to produce transition metal nanoparticles. The disadvantage of the magnide hydrolysis method is the need to remove $\text{Mg}(\text{OH})_2$ by an acid. Si and Ge magnides undergo extremely slow hydrolysis.

Chapter VIII: Discussion and Conclusions

The Ge and Si nanoparticles prepared by hydrolysis of Si and Ge magnides have either poor crystallinity or are amorphous, and are easily oxidized to their oxides. Hence, the hydrolysis method of Si and Ge magnides is not suitable for production of Si and Ge nanoparticles.

There is a large difference in hydrolysis rates between Al_3Ni and Al_3Ni_2 due to the thermodynamic and kinetic, and crystal structure factors. Because of the difficulty in removal of $\text{Al}(\text{OH})_3$, the hydrolysis method of aluminides is also not suitable for production of transition metal nanoparticles.

The sodide hydrolysis method offers a simpler method preparing transition metal nanoparticles than the hydrolysis of magnides. The drawback of this method is the difficulty in controlling the reaction rate.

Chapter VIII: Discussion and Conclusions

Table 8.1 Comparison of nanoparticle synthesis by hydrolysis of magnides, aluminides and sodides

Starting Materials	Hydrogen evolution	pH of solution	Product of hydrolysis	Solid byproduct	Characterization of nanoparticles	Advantages (A) and disadvantages(D)
Mg ₂ Ni	Fast	10-11	Ni+Mg(OH) ₂ +H ₂	Mg(OH) ₂	Around 12nm; close to spherical in shape	A: mild hydrolysis reaction; D: need to remove Mg(OH) ₂ by an acid
Mg ₂ Cu	Fast	10-11	Cu+Mg(OH) ₂ +H ₂			
Mg ₃ Au	Fast	10-11	Au+Mg(OH) ₂ +H ₂		Around 8nm; close to spherical in shape	
Mg ₅₄ Ag ₁₇	Fast	10-11	Ag+Mg(OH) ₂ +H ₂			
MgNi ₂	Slow	10-11	Ni+Mg(OH) ₂ +H ₂		Around 16nm; close to spherical in shape	A: Higher efficiency than Mg ₂ Ni; D: relatively coarse; need to remove Mg(OH) ₂ by an acid;
Mg ₂ Ge	very slow	10-11	Ge+Mg(OH) ₂ +H ₂		Poor crystallinity	D: Amorphous or poor crystallinity
Mg ₂ Si	Extremely slow	10-11	Si+Mg(OH) ₂ +H ₂		amorphous	The newly formed nanoparticles are easily oxidized.
Al ₃ Ni	Slow	5-6	Ni+Al(OH) ₃ +H ₂	Al(OH) ₃	—	D: Difficult to remove Al(OH) ₃
Al ₃ Ni ₂	Extremely slow	5-6	—	—	—	—
Ag ₂ Na	Extremely fast	14	Ag+NaOH+H ₂	NaOH	Around 10nm	A: No need of acid bath; D: severe hydrolysis reaction;
PtNa		14	Pt+NaOH+H ₂		Around 10nm	

The main conclusions from this dissertation are summarized as follows:

1. The in-situ synthesized Mg_2Ni particles can not reach their maximum hydrogen storage capacity (3.6wt%) at the first hydrogenation at 300°C and 320°C due to the limitation of hydrogen diffusion kinetics.
2. Both the in-situ synthesized Mg_2Ni and the as-cast Mg_2Ni exhibited a near zero charge/discharge capacity.
3. When Mg_2Ni or Mg_2NiH_4 were immersed in water or in an alkaline solution, they spontaneously reacted with water to form $\text{Mg}(\text{OH})_2$, Ni and hydrogen. Reducing the pH value of the solution (adding an acid) will accelerate the hydrolysis of Mg_2Ni and Mg_2NiH_4 .
4. The hydrolysis characteristics of Mg_2Ni and Mg_2NiH_4 suggest that they are not suitable for use as electrodes in rechargeable batteries due to their hydrolysis behavior. However, the hydrolysis behavior can be utilized to produce Ni nanoparticles.
5. As well as Mg_2Ni , MgNi_2 , Mg_2Cu , Mg_3Au , Mg_2Cu , $\text{Mg}_{54}\text{Ag}_{17}$, and MgAg were also shown to spontaneously undergo hydrolysis in water at room temperature. The corresponding transition metal nanoparticles can be produced by hydrolysis of these compounds.
6. The hydrolysis byproduct of magnides, $\text{Mg}(\text{OH})_2$, has a very small solubility in water. The newly-formed $\text{Mg}(\text{OH})_2$ precipitates from water in the vicinity of the Mg dissolution sites. The existence of the $\text{Mg}(\text{OH})_2$ particles, and the low mobility of transition metal atoms at room temperature, give rise to the formation of very fine transition metal nanoparticles. In addition, the particles size of these transition metal

Chapter VIII: Discussion and Conclusions

- nanoparticles prepared by this method was not sensitive to the concentration of the initial materials in aqueous solution.
7. Compared with conventional preparation methods for transition metal nanoparticles, the hydrolysis method has the potential to inexpensively produce transition metal nanoparticles on a large scale.
 8. Compared with using the Mg-rich compounds, using the hydrolysis behavior of transition metal-rich magnides to produce transition metal nanoparticles offers a higher output efficiency, saves raw materials and reduces the pollution resulting from the dissolution of the hydrolysis byproduct ($\text{Mg}(\text{OH})_2$) by using an acid.
 9. Before the initial particles of transition metal magnides are totally hydrolyzed, the transition metal nanoparticles will be protected from oxidation by the dissolved oxygen because of the higher chemical affinity of the magnesium atoms in these magnides to oxygen.
 10. The newly formed transition metal (including semiconductor elements Si and Ge) nanoparticles will be readily attacked by the dissolved oxygen in the aqueous solution during hydrolysis and removal of $\text{Mg}(\text{OH})_2$ by using a dilute acid. Au and Ag nanoparticles prepared by this method are able to resist oxidation from the dissolved oxygen in an aqueous solution. Ni, Cu, Si and Ge nanoparticles are oxidized into their hydroxides. The Cu and Ge hydroxides are unstable, and will further dissociate into their corresponding oxides (CuO and GeO_2).
 11. If all preparation procedures were conducted in a zero oxygen environment, transition metal nanoparticles with low oxygen content could be synthesized by hydrolysis of these transition metal magnides.

Chapter VIII: Discussion and Conclusions

12. Transition metal nanoparticles synthesized by hydrolysis of their magnides were close to spherical in shape and had a mean size of around 10nm.
13. Hydrolysis of Mg_2Ge was sluggish at room temperature under one atmosphere. but the hydrolysis rate of Mg_2Ge can be significantly promoted by adding hydrochloric acid. The Ge prepared by the hydrolysis method exhibited poor crystallinity.
14. Mg_2Si barely underwent hydrolysis in water at room temperature. Hydrolysis of the Mg_2Si particles was accelerated by adding hydrochloric acid. The hydrolysis product was amorphous Si.
15. Among the Ni aluminides, Al_3Ni spontaneously undergoes hydrolysis in water at room temperature, and forms $Al(OH)_3$, Ni and hydrogen in distilled water at room temperature. However, Al_3Ni_2 barely undergoes a hydrolysis under the same conditions. The hydrolysis of $AlNi$ and $AlNi_3$ in the Ni-Al binary system would be much slower than for Al_3Ni_2 due to thermodynamic, kinetic and crystal structure factor considerations.
16. Although from thermodynamic considerations, the negative standard free energy change for the hydrolysis reaction of Al_3Ni is much larger than that for Mg_2Ni , and from a crystal structure point of view, more Al atoms surround a Ni atom in Ni_3Al than Mg atoms surround a Ni atom in Mg_2Ni , and therefore the hydrolysis of Al_3Ni should be much easier than that of Mg_2Ni , in fact, the hydrolysis rate of Al_3Ni was much slower than that of Mg_2Ni , This may result from the relative reaction kinetics.
17. Due to the low acidity of $Al(OH)_3$, using dilute hydrochloric acid to remove $Al(OH)_3$ will lead to a fairly low pH value of solution. As a result, the chemically active transition metals such as Fe, Co, Ni, or even Cu nanoparticles would not survive in

Chapter VIII: Discussion and Conclusions

the solution, especially when it is exposed to air. Only chemically inert transition metals such as the noble metals can be prepared by this method.

18. The oxidation of sodium in the Pt-Na pellets were much faster than that in the Ag-Na pellets since Pt is a catalyst for water formation.
19. The Ag and Pt nanoparticles prepared by hydrolysis of either Ag_2Na or PtNa were crystalline in nature. The Ag and Pt nanoparticles were close to spherical in shape with a mean size of around 10nm.
20. The reaction byproduct of sodide hydrolysis, NaOH , has a high solubility and is easier to remove than $\text{Mg}(\text{OH})_2$, the hydrolysis byproduct of magnides. This method offers a simpler method preparing transition metal nanoparticles than the hydrolysis of magnides. The drawback of this method is the difficulty in controlling the reaction rate.

CHAPTER NINE: RECOMMENDATIONS FOR FUTURE WORK

Based on the results of the present investigation, the following areas are suggested for future work:

1. In this study, all our experiments were conducted in air. Hence, the newly formed transition metal nanoparticles (including those of the semiconductor elements: Si and Ge) prepared by hydrolysis of magnides are attacked by the dissolved oxygen in the aqueous solution during hydrolysis and removal of $Mg(OH)_2$ by using dilute acid. Chemically active transition metals (including Si and Ge) nanoparticles were always contaminated by oxygen. In particular, the hydroxides of the semiconductor elements Si and Ge are weak acids, they easily react with the hydrolysis byproduct of magnides, $Mg(OH)_2$ and form some complex oxides, which are difficult to remove from the final product. Thus, further investigation of hydrolysis of magnides under a zero oxygen environment is needed to improve the purity of these nanoparticles.
2. The morphology and the size distribution of transition metal nanoparticles are particularly important to their properties. Modifying their shape and size distribution by solution chemical methods could significantly improve their properties and enhance the stability of these properties.
3. Both silicon and germanium nanocrystals exhibit size dependent photoluminescence resulting from quantum confinement effects. However, preparation of Si and Ge

Chapter IX: Recommendations for future work

nanocrystals at high temperatures is needed to promote crystallization due to their strong covalent bonding. Ge nanoparticles produced by hydrolysis of Mg_2Ge at room temperature have poor crystallization. Most Si nanoparticles produced by hydrolysis of Mg_2Si at room temperature were amorphous. Although we increased the hydrolysis temperature to help improve crystallinity, higher hydrolysis temperatures promoted the oxidation of Ge and Si nanoparticles by the dissolved oxygen since our experiments were conducted in air. More work is needed to improve crystallization of Ge and Si nanoparticles by high temperature hydrolysis under a zero oxygen environment, perhaps through the use of supercritical fluids (high pressure and temperatures higher than 100°C).

4. As well as selenides, many transition metal (and semiconductor element) - alkali metal or alkali earth metal intermetallic compounds are expected to have a similar hydrolysis behavior in water due to their chemical reactivity. Hence, they also have a potential to produce transition metal and semiconductor element nanoparticles through hydrolysis. However, the investigation of their hydrolysis behavior was not conducted in this dissertation due to time limitations.
5. The hydrolysis product of transition metal magnides (transition metal nanoparticles and $\text{Mg}(\text{OH})_2$) has a potential to be directly made into catalysts (a porous composite of transition nanoparticles and magnesia).

CHAPTER TEN: STATEMENT OF ORIGINALITY

Aspects of this study that constitute, in the author's opinion, new and distinct contributions to knowledge, include:

1. The hydrolysis behaviors of Mg_2Ni and Mg_2NiH_4 in water, or in an alkaline solution, were first detailed in this dissertation work. The hydrolysis characteristics of Mg_2Ni and Mg_2NiH_4 determine that they are not suitable for use as electrodes in rechargeable batteries due to their hydrolysis behavior, even though Mg_2Ni exhibits a good hydrogen storage capacity (3.6wt%) and has a theoretical discharge capacity as high as 999mAh/g.
2. Since Mg_2Ni spontaneously reacts with water to form $Mg(OH)_2$, Ni and hydrogen, a simple hydrolysis method has been successfully developed to produce Ni nanoparticles.
3. Further investigation reveals that the hydrolysis behavior is a common phenomenon for both the magnesium-rich and the transition metal-rich magnides. Transition metal and the semiconductor Si and Ge nanoparticles can be produced by this hydrolysis method.
4. The intermetallic compounds between transition metals (and some the semiconductor elements) and alkali metals (or the alkali earth metals) also exhibit hydrolysis behavior, which could also be utilized to produce transition metal and semiconductor nanoparticles (or nanocrystals).

5. Among the aluminides, only Al-rich aluminides such as Al_3Ni undergo hydrolysis in water at room temperature. However, due to the low acidity of $\text{Al}(\text{OH})_3$, using dilute hydrochloric acid to remove $\text{Al}(\text{OH})_3$ will require a lower pH value of the solution. As a result, the chemically active transition metals such as Fe, Co, Ni, or even Cu nanoparticles cannot survive in the solution, especially when exposed to air. Only chemically inert transition metals such as the noble metals can be prepared by this method.

REFERENCES

1. M. S. Spencer, M. V. Twigg, Metal catalyst design and preparation in control of deactivation, *Annu. Rev. Mater. Res.*, 2005, 35: 427–464.
2. E. J. Klabunde, ed. *Nanoscale Materials in Chemistry*, John Wiley & Sons Inc, 2001, New York.
3. S. Han, H. Lee, N. Goo, W. Jeong, K. Lee, Improvement of electrode performance of Mg₂Ni by mechanical alloying, *J. Alloys Comp.*, 2002, 330–332: 841–845.
4. D. L. Feldheim, C. A. Foss, Jr., eds. *Metal Nanoparticles: Synthesis, Characterization, and Applications*, Marcel Dekker, 2002, New York.
5. A. P. Weber, M., Seipenbusch and G. Kasper, Size effects in the catalytic activity of unsupported metallic nanoparticles, *J. Nanopart. Res.*, 2003, 5: 293–298.
6. H. Morisaki, Above-band-gap photoluminescence from Si fine particles, *Nanotechnology* 1992, 3: 196-201.
7. L. T. Canham, Silicon quantum wire array fabricated by electrochemical and chemical dissolution of wafers, *Appl. Phys. Lett.*, 1990, 57: 1046-1048.
8. L. T. Canham, Gaining light from silicon, *Nature* 2000, 408: 411-412.
9. G. Belomoin, J. Therrien, A. Smith, S. Rao, R. Twesten, S. Chaieb, M. H. Nayfeh, L. Wagner and L. Mitas, Observation of a magic discrete family of ultra bright Si nanoparticles, *Appl. Phys. Lett.*, 2002, 80: 841-843.
10. G. Belomoin, E. Rogozhina, J. Therrien, I. P. V. Braun, L. Abuhassan, and M. H. Nayfeh, Effects of surface termination on the band gap of ultra bright Si₂₉ nanoparticles: Experiments and computational models, *Phys. Rev. B*, 2002, 65:193406-193412.

References

11. H. Chen, J. Chiu and T. Perng, On the photoluminescence of Si nanoparticles, *Mater. Phys. Mech.*, 2001, 4: 62-66.
12. B. Voigtlander, B. Meyer, N. M. Amer., Epitaxial growth of thin magnetic cobalt films on Au(111) studied by scanning tunneling microscopy, *Phys. Rev. B*, 1991,44: 10354–10357
13. T. O. Ely, C. Amiens, B. Chaudret, E. Snoeck, M. Verelst, M. Respaud and J. M. Broto, Synthesis of nickel nanoparticles: influence of aggregation induced by modification of poly(vinylpyrrolidone) chain length on their magnetic properties, *Chem. Mater.* 1999, 11,526-529.
14. M. Yoon, Y. Kim, Y. Kim, V.Volkov, H. Song, Y. Park, I. Park, Superparamagnetic properties of nickel nanoparticles in anion exchange polymer film, *Mater. Chem. Phys.*, 2005, 91: 104–107.
15. S. Lin, S. Chang, R. Liu, S. Hu, N. Jan, Fabrication and magnetic properties of nickel nanowires, *J. Magnetism Magnetic Mater.*, 2004, 282: 28–31.
16. C. Liu, L. Guo, R. Wang, Y. Deng, H. Xu and S. Yang, Magnetic nanochains of metal formed by assembly of small nanoparticles, *Chem. Commun.*, 2004, 2726–2727.
17. T. Castro, R. Reifenberger, E. Choi and R. P. Andres, Size-dependent melting temperature of individual nanometer-sized metallic clusters, *Phy. Rev. B.*, 1990, 42: 8548-8556.
18. Radha Narayanan, Shape-dependent nanocatalysis and the effect of catalysis on the shape and size of colloidal metal nanoparticles, Ph.D dissertation, Georgia Institute of Technology, March, 2005.

References

19. R.T. Vang, K. Honkala, S. Dahl, E. K. Vestergaard, J. Schnadt, E. Lagsgaard, B.S. Clausen, J. K. Norskov and F. Besenbacher, Controlling the catalytic bond-breaking selectivity of Ni surfaces by step blocking, *Nature Mater.*, 2005, 4: 160-162.
20. Y. Cui, H. Xu, Q. Ge, Y. Wang, S. Hou, W. Li, Structure sensitive dissociation of CH₄ on Ni/Al₂O₃: Ni nano-scale particles linearly compensate the E_a and lnA_s for the CH₄ pulse kinetics, *J. Molecular Catalysis. A: Chem.*, 2006, 249: 53–59.
21. J. Libera, Y. Gogotsi, Hydrothermal synthesis of graphite tubes using Ni catalyst, *Carbon*, 2001, 39: 1307–1318.
22. Z. Ren, Z. Huang, D. Wang, J. Wen, J. Xu, J. Wan, L. E. Calvet, J. Chen, J. F. Klemic, M. A. Reed, Growth of a single free standing multiwall carbon nanotube on each nanonickel dot, *Appl. Phys. Lett.*, 1999, 75: 1086-1088.
23. H. Cheng, F. Li, G. Su, H. Pan, L. He, X. Sun and M. S. Dresselhaus, Large-scale and low-cost synthesis of single-walled carbon nanotubes by the catalytic pyrolysis of hydrocarbons, *Appl. Phys. Lett.*, 1998, 72: 3822-3824.
24. A. Kukovecz, Z. Konya, N. Nagaraju, I. Willems, A. Tamasi, A. Fonseca, J. B. Nagy, and I. Kiricsi, Catalytic synthesis of carbon nanotubes over Co, Fe and Ni containing conventional and sol gel silica. Aluminas, *Phys. Chem. Chem. Phys.*, 2000, 2: 3071-307.
25. D. P. Curran, Reduction of Δ-isoxazolines. Raney-nickel catalyzed formation of β-hydroxy ketones, *J. Am. Chem. Soc.* 1983, 105: 5826-5833.
26. S. P. Daley, A. L. Utz, T. R. Trautman, and S. T. Ceyer, Ethylene hydrogenation on Ni (111) by bulk hydrogen, *J. Am. Chem. Soc.* 1994, 116: 6001-6002.

References

27. N. Iwasa, S. Masuda and N. Takezawa, Steam reforming of methanol over Ni, Co, Pd and Pt supported on ZnO, *React. Kinet. Catal. Lett.*, 1995, 55: 349-353.
28. A. Sharma, H. Nakagawa, K. Miura, Uniform dispersion of Ni nanoparticles in a carbon based catalyst for increasing catalytic activity for CH₄ and H₂ production by hydrothermal gasification, *Fuel*, 2006, 85: 2396–2401.
29. S. Li and B. Li, Study on non-noble metal catalysts for automotive emission control, *React. Kinet. Catal. Lett.*, 1996: 57: 183-190.
30. Z. Jiang, S. Li, F. Zhao, Z. Liu, C. Yin, Y. Luo, S. Li, Research on the combustion properties of propellants with low content of nano metal powders, *Propellants, Explosives, Pyrotechnics*, 2006, 31: 139-147.
31. A. Y. Rozovskii and G. I. Lin, Fundamentals of methanol synthesis and decomposition, *Topics in Catalysis*, 2003, 22: 137-150.
32. M. V. Twigg, M. S. Spencer, Deactivation of supported copper metal catalysts for hydrogenation reactions, *Appl. Catal.*, 2001, 212A: 161–74
33. M. V. Twigg, M. S. Spencer, Deactivation of copper metal catalysts form ethanol decomposition, methanol steam reforming and methanol synthesis, *Topics Catal.*, 2003, 22: 191–203.
34. X. Ma, Z. Li, B. Wang and G. Xu, Effect of Cu catalyst preparation on the oxidative carbonylation of methanol to dimethyl carbonate, *React. Kinet. Catal. Lett.*, 2002, 76: 179-187.
35. N.A. Dhas, C. P. Raj and A. Gedanken, Synthesis, characterization, and properties of metallic copper nanoparticles, *Chem. Mater.*, 1998, 10: 1446-1452.

References

36. H. Zhang, X. Dong, G. Lin, X. Liang and H. Li, Carbon nanotube promoted Co–Cu catalyst for highly efficient synthesis of higher alcohols from syngas, *Chem. Commun.*, 2005, 5094–5096.
37. S. Galvagno, G. Parravano, Chemical reactivity of supported gold, IV: Reduction of nitric oxide by hydrogen, *J. Catal.*, 1978, 55: 178-190.
38. M.B. Cortiel and E. van der Lingen, Catalytic gold nano-particles, *Mater. Forum*, 2002, 26: 1-14
39. M. Valden, X. Lai, D. W. Goodman, Onset of catalytic activity of gold clusters on titania with the appearance of nonmetallic properties, *science*, 1998, 281: 1647-1650.
40. M. Haruta, T. Kobayashi, H. Sano, N. Yamada, Novel gold catalysts for the oxidation of carbon monoxide at a temperature far below 0°C, *Chem. Lett.*, 1987, 405-406.
41. Y. Yuan, K. Asakura, H. Wan, K.T Sai, Y. I Wasawa, Supported gold catalysts derived from gold complexes and as-precipitated metal hydroxides, highly active for low-temperature CO oxidation, *Chem. Lett.*, 1996, 9: 755-756.
42. M. Haruta, N. Yamada, T. Kobayashi, S. Ijima, Gold catalysts prepared by coprecipitation for low-temperature oxidation of hydrogen and of carbon monoxide, *J. Catal.*, 1989, 115: 301-309.
43. M. M. Maye, Y. Lou, C. Zhong, Core-shell gold nanoparticle assembly as novel electrocatalyst of CO oxidation, *Langmuir* 2000, 16: 7520-7523.
44. Y. Lou, M. M. Maye, L. Han, J. Luo, C. Zhong, Gold-platinum alloy nanoparticle assembly as catalyst for methanol electro-oxidation, *Chem. Commun.*, 2001, 473-474.

References

45. Y. Luo, M. M. Maye, Y. Lou, L. Han, M. Hepel, C. Zhong, Catalytic activation of core-shell assembled gold nanoparticles as catalyst for methanol electrooxidation, *Catal.Today*, 2002, 77: 127-138.
46. M. Haruta, A. Ueda, S. Tsubota, R. M. Torres Sanchez, Low-temperature catalytic combustion of methanol and its decomposed derivatives over supported gold catalysts, *Catal. Today*, 1996, 29: 443-447.
47. T. Hayashi, K. Tanaka, and M. Haruta, Selective vapor-phase epoxidation of propylene over Au/TiO₂ catalysts in the presence of oxygen and hydrogen, *J. Catal.*, 1998, 178: 566-575.
48. D.A.H. Cunningham, W. Vogel, R.M. Torres-Sanchez, K. Tanaka, and M. Haruta, Structural analysis of Au/TiO₂catalysts by Debye function analysis, *J. Catal.*, 1999, 183: 24-31.
49. A. Ueda, T. Oshima, M. Haruta, Reduction of nitrogen monoxide with propene in the presence of oxygen and moisture over gold supported on metal oxides. *Appl. Catal. B*, 1997, 12: 81-93.
50. D. Andreeva, T. Tabakova, V. Idakiev, P. Chistov, R. Giovanoli, Au-Fe₂O₃ catalyst for water-gas shift reaction prepared by deposition-precipitation, *Appl. Catal. A*, 1998, 169: 9-14.
51. H. Sakurai, M. Haruta, Synergism in methanol synthesis from carbon dioxide over gold catalysts supported on metal oxides, *Catal. Today*, 1996, 29: 361-365.
52. R. Yamamoto, Y. Sawayama, H. Shibahara, Y. Ichihashi, Promoted partial oxidation activity of supported Ag catalysts in the gas-phase catalytic oxidation of benzyl alcohol, *J. Catalys.*, 2005, 234: 308-317.

References

53. X. Wang, Y. Xie, Deep oxidation of methane over Cu and Ag modified manganese oxide catalysts, *React. Kinet. Cataly. Lett.*, 2000, 71: 121-128.
54. T. Jacob, W.A. Goddard, Water formation on Pt and Pt-based alloys: a theoretical description of a catalytic reaction, *Chem. Phys. Chem.*, 2006, 7: 992-1005.
55. J. Zeng, F. Su, J. Lee, W. Zhou, X. Zhao, Methanol oxidation activities of Pt nanoparticles supported on microporous carbon with and without a graphitic shell, *Carbon*, 2006, 44: 1713–1717.
56. Liu, Z. Tian, S. Jiang, Synthesis and characterization of Nafion-stabilized Pt nanoparticles for polymer electrolyte fuel cell, *Electrochem. Acta*, 2006, 52: 1213-1220.
57. K. Watanabe, D. Menzel, N. Nilius and H. J. Freund, Photochemistry on metal nanoparticles, *Chem. Rev.*, 2006, 106: 4301-4320
58. T. Vondrak, D. J. Burke, S. R. Meech, The dynamics and origin of NO photodesorbed from NO/Ag(111), *Chem. Phys. Lett.*, 2000, 327: 137-140.
59. Y. Matsumoto, Y. A. Gruzdkov, K. Watanabe, K. J. Sawabe, Study on photochemistry of methane on Pt(111)) and Pd(111) surfaces, *J. Chem. Phys.*, 1996,105: 4775-4782.
60. K. Watanabe, Y. Matsumoto, Comparative study of photochemistry of methane on Pt(111)) and Pd(111) surfaces, *Surf. Sci.*, 1997, 390: 250-256.
61. K. Watanabe, Y. Matsumoto, Photochemistry of methane on Cu(111), *Surf. Sci.*, 2000, 454: 262-267.
62. K. Watanabe, K. Sawabe, Y. Matsumoto, Adsorbate-localized excitation in surface methane on Pt(111) photochemistry, *Phys. Rev. Lett.*, 1996,76: 1751-1757.

References

63. M. Zahn, Magnetic fluid and nanoparticle applications to nanotechnology, J. Nanopart. Res., 2001, 3: 73–78.
64. T. Baron, B. Pelissier, L. Perniola, F. Mazen, J. M. Hartmann, G. Rolland, Chemical vapor deposition of Ge nanocrystals on SiO₂, Appl. Phys. Lett., 2003, 83: 1444-1449.
65. A. Kanjilal, J. L. Hansen, P. Gaiduk, A. N. Larsen, N. Cherkashin, A. Claverie, P. Normand, E. Kapetanakis, D. Skarlatos, D. Tsoukalas, Structural and electrical properties of silicon dioxide layers with embedded germanium nanocrystals grown by molecular beam epitaxy, Appl. Phys. Lett., 2003, 82: 1212-1216.
66. D. Tsoukalas, P. Dimitrakis, S. Kolliopoulou, P. Normand, Recent advances in nanoparticle memories, Mater. Sci. Eng. B, 2005, 124–125: 93–101.
67. S. Tiwari, F. Rana, H. Hanafi, A. Hartstein, E. F. Crabbe, K. Chan, A silicon nanocrystals based memory, Appl. Phys. Lett., 1996, 68: 1377-1380.
68. E. Kapetanakis, P. Normand, D. Tsoukalas, K. Beltsios, J. Stoemenos, S. Zhang, J. van den Berg, Charge storage and interface states effects in Si-nanocrystal memory obtained using low-energy Si implantation and annealing, Appl. Phys. Lett., 2000, 77: 3450-3453.
69. S. J. Baik and K. S. Lim, Characteristics of silicon nanocrystal floating gate memory using a amorphous carbon /SiO₂ tunnel barrier, Appl. Phys., Lett., 2002, 81: 5186-5188
70. S. J. Baik, S. Choi, U. Chung, J. Moon, Engineering on tunnel barrier and dot surface in Si nanocrystal memories, Solid-State Electronics, 2004, 48: 1475–1481

References

71. S. Kolliopoulou, P. Dimitrakis, P. Normand, H. Zhang, N. Cant, S. D. Evans, S. Paul, C. Pearson, A. Molloy, M. C. Petty, D. Tsoukalas, Fabrication and characterization of a metal nanocrystal memory using molecular beam epitaxy, *J. Appl. Phys.*, 2003, 94: 5234-5239.
72. G. Belomoin, J. Therrien, A. Smith, S. Rao, R. Twesten, S. Chaieb, M. H. Nayfeh, L. Wagner and L. Mitas, Observation of a magic discrete family of ultra bright Si nanoparticles, *Appl. Phys. Lett.*, 2002, 80: 841-843.
73. L. Pavesi, L. Dal Negro, C. Franzo and F. Priolo, Optical gain in silicon nanocrystals, *Nature*, 2000, 408: 440-444 .
74. <http://www.technologyreview.com/Nanotech/16830/>
75. C. A. Mirkin, R. L. Letsinger, R. C. Mucic, J. J. Storhoff, DNA-based method for rationally assembling nanoparticles into macroscopic materials. *Nature*, 1996, 382: 607-609.
76. T. A. Taton, R. C. Mucic, C. A. Mirkin, R. L. Letsinger, The DNA-mediated formation of supramolecular mono- and multi- layered nanoparticle structures. *J. Am. Chem. Soc.*, 2000, 122: 6305-6306.
77. L. M. Demers, C. A. Mirkin, R. C. Mucic, R. A. Reynolds, R. L. Letsinger, R. Elghanian, G. A. Viswanadham, Fluorescence- based method for determining the surface coverage and hybridization efficiency of thiol-capped oligonucleotides bound to gold thin films and nanoparticles, *Anal. Chem.*, 2000, 72: 5535-5541.
78. M. J. Natan, L. A. Lyon, Surface plasmon resonance biosensing with colloidal Au amplification, *Metal nanoparticleless synthesis, characterization and applications*, Ed by D. L. Feldheim, A. F. Colby, Marcel Dekker, New York, 2002, 183-205.

References

79. N. T. K Thanh, Z. Rosenzweig, Development of an aggregation-based immunoassay for anti-protein using gold nanoparticles, *Anal. Chem.*, 2002, 74: 1624-1628.
80. C. Zhang, Z. Zhang, B. Yu, J. Shi, X. Zhang, Application of the biological conjugate between antibody and colloid Au nanoparticles as analyte to inductively coupled plasma mass spectrometry, *Anal. Chem.*, 2002, 74: 96-99.
81. X. Luo, A. Morrin, A. J. Killard, M. R. Smyth, Application of nanoparticles in electrochemical sensors and biosensors, *Electroanalysis*, 18 (2006) 319–326.
82. M. Majima, K. Koyama, Y. Tani, H. Toshioka, M. Osoegawa, H. Kashihara And S. Inazawa, Development of conductive material using metal nano particles, *SEI Tech. Review*, 2002, 54: 25-27.
83. I. Okada, K. Shimoda And K. Miyazaki, Development of fine circuit pattern formation process using nano-metal ink, *SEI Tech. Review*, 2006, 62: 55-56.
84. H. Jiang, K. Moon, J. Lu, And C. Wong, Conductivity enhancement of nano silver-filled conductive adhesives by particle surface functionalization, *J. Elect. Mater.*, 2005, 34: 1432-1437.
85. Q.A.Pankhurst, J.Connolly, S. K.Jones and J.Dobson, Applications of magnetic nanoparticles in biomedicine, *J. Phys. D: Appl. Phys.*, 2003, 36: R167–R181.
86. P. Tartaj, M. P. Morales, S. V. Verdaguer, T.G. Carreno and C. J. Serna, The preparation of magnetic nanoparticles for applications in biomedicine, *J. Phys. D: Appl. Phys.*, 2003, 36: R182–R197.
87. S. Son, J. Reichel, B. He, M. Schuchman, and S. Lee, Magnetic nanotubes for magnetic-field-assisted bioseparation, biointeraction, and drug delivery, *J. Am. Chem. Soc.*, 2005, 127: 7316-7317.

References

88. M. Bettge, J. Chatterjee and Y. Haik, Physically synthesized Ni-Cu nanoparticles for magnetic hyperthermia, *Biomagnetic Res. Tech.*, 2004, 2: 4-10.
89. M. Tanase, L.A. Bauer, A. Hultgren, D.M. Silevitch, L. Sun, D. H. Reich, P. C. Searson, and G. J. Meyer, Magnetic alignment of fluorescent nanowires, *Nano Lett.*, 2001, 1: 155-158.
90. J. J. Mock, S. J. Oldenburg, R. Smith, D. A. Schultz, and S. Schultz, Composite plasmon resonant nanowires, *Nano Lett.*, 2002, 2: 465-469.
91. [http://qs.nano.com/new/QSI_Nano%20Silver%20\(AG\).pdf](http://qs.nano.com/new/QSI_Nano%20Silver%20(AG).pdf)
92. T. A. Taton, R. C. Mucic, C. A. Mirkin, R. L. Letsinger, The DNA-mediated formation of supramolecular mono- and multi-layered nanoparticle structures. *J. Am. Chem. Soc.*, 2000, 122: 6305-6306.
93. Y. Sun, B. Gates, B. Mayers and Y. Xia, Crystalline silver nanowires by soft solution processing, *Nano Lett.*, 2002, 2: 165-168.
94. D. Chen, Y. Huang, Spontaneous formation of Ag nanoparticles in dimethylacetamide solution of poly(ethyleneglycol), *J. Colloid Interface Sci.*, 2002, 255: 299-302.
95. S. Chen and J. M. Sommers, Alkanethiolate-protected copper nanoparticles: spectroscopy, electrochemistry, and solid-state morphological evolution, *J. Phys. Chem. B*, 2001, 105: 8816-8820.
96. D. Li, S. Chen, S. Zhao, X. Hou, H. Ma, X. Yang, Simple method for preparation of cubic Ag nanoparticles and their self-assembled films, *Thin Solid Films*, 2004, 460: 78-82.

References

97. D. Xu, K. Zhang, X. Zhu, Preparation of Ag Nanoparticles in the Presence of Low Generational Poly(ester-amine) Dendrimers, *J. Appl. Polym. Sci.*, 2007, 104: 422–426.
98. L. Zhang, X. Sun, Y. Song, X. Jiang, S. Dong and E. Wang, Didodecyldimethylammonium bromide lipid bilayer-protected gold nanoparticles: synthesis, characterization, and self-assembly, *Langmuir*, 2006, 22: 2838-2843.
99. B. D. Busbee, S. O. Obare and C. J. Murphy, An improved synthesis of high aspect ratio gold nanorods, *Adv. Mater.*, 2003, 15: 414-416.
100. T. K. Sau and C. J. Murphy, Room Temperature, High-Yield Synthesis of Multiple Shapes of Gold Nanoparticles in Aqueous Solution, *J. Am. Chem. Soc.*, 2004, 126: 8648-8649
101. S. Wu and D. Chen, Synthesis and characterization of nickel nanoparticles by hydrazine reduction in ethylene glycol, *J. Colloid Interf. Sci.*, 2003, 259: 282–286.
102. D. Chen and C. Hsieh, Synthesis of nickel nanoparticles in aqueous cationic surfactant solutions, *J. Mater. Chem.*, 2002, 12: 2412–2415.
103. Y. Tan, Y. Li, and D. Zhu, Preparation of silver nanocrystals in the presence of aniline, *J. Colloid Interface Sci.*, 2003, 258: 244–251.
104. Z. Jiang, W. Yuan, H. Pan, Luminescence effect of silver nanoparticles in water phase, *Spectrochimica Acta A*, 2005, 61: 2488–2494.
105. Z. Liu, S. Li, Y. Yang, S. Peng, Z. Hu and Y. Qian, Complex-surfactant-assisted hydrothermal route to ferromagnetic Ni nanobelts, *Adv. Mater.*, 2003, 15: 1946~1947.

References

106. Q. Liu, H. Liu, M. Han J. Zhu, Y. Liang, Z. Xu and Y. Song, Nanometer sized nickel hollow spheres, *Adv. Mater.*, 2005, 17: 1995~1999.
107. Y. Tan, X. Dai, Y. Li and D. Zhu, Preparation of gold, platinum, palladium and silver nanoparticles by the reduction of their salts with a weak reductant–potassium bitartrate, *J. Mater. Chem.*, 2003, 13: 1069–1075.
108. P. Raveendran, J. Fu and S. L. Wallen, A simple and “green” method for the synthesis of Au, Ag, and Au–Ag alloy nanoparticles, *Green Chem.*, 2006,8: 34–38
109. S. S. Shankar, A. Rai, A. Ahmad and M. Sastry, Rapid synthesis of Au, Ag, and bimetallic Au core–Ag shell nanoparticles using Neem (*Azadirachta indica*) leaf broth, *J. Colloid and Interf. Sci.*, 2004, 275: 496–502.
110. T. Teranishi, R. Kurita, and M. Miyake, Shape control of Pt nanoparticles, *J. Inorgan. Organometallic Polym.*, 2000,10: 145-156.
111. B. Xue, P. Chen, Q. Hong, J. Lin and K. Tan, Growth of Pd, Pt, Ag and Au nanoparticles on carbon nanotubes, *J. Mater. Chem.*, 2001, 11: 2378–2381.
112. H. Hah and S. Koo, Preparation of silver nanoparticles through alcohol reduction with organoalkoxysilanes, *J. Sol-Gel Sci. Techn.*, 2003, 26: 467–471.
113. S. Eustis, H. Hsu, and M. El-Sayed, Gold nanoparticle formation from photochemical reduction of Au^{3+} by continuous excitation in colloidal solutions. A proposed molecular mechanism, *J. Phys. Chem. B*, 2005, 109: 4811-4815
114. S. Keki, J. Torok, G. Deak, L. Daroczi and M. Zsuga, Silver Nanoparticles by PAMAM-Assisted Photochemical Reduction of Ag^+ , *J. Colloid Interf. Sci.*, 2000, 229: 550–553.

References

115. N. Arul Dhas, C. Paul Raj and A. Gedanken, Synthesis, characterization and properties of metallic copper nanoparticles, *Chem. Mater.*, 1998, 10: 1446-1452.
116. T. Fujimoto, S. Terauchi, H. Umehara, I. Kojima, and W. Henderson, Sonochemical preparation of single-dispersion metal nanoparticles from metal salts, *Chem. Mater.*, 2001, 13: 1057-1060.
117. Y. J. Chou, M. S. El-Aasser and J. W. Vanderhoff, Mechanism of emulsification of styrene using hexadecyltrimethylammonium bromidecetyl alcohol mixtures, *J. Dispers. Sci. Technol.*, 1980, 1: 129-50.
118. K. Landfester, Synthesis of colloidal particles in miniemulsions, *Annu. Rev. Mater. Res.*, 2006, 36: 231-79.
119. D. Chen and C. Chen, Formation and characterization of Au-Ag bimetallic nanoparticles in water-in-oil microemulsions, *J. Mater. Chem.*, 2002, 12: 1557-1562.
120. M. Wu, L. Lai, Synthesis of Pt/Ag bimetallic nanoparticles in water-in-oil microemulsions, *Colloids Surf.A:Physicochem..Eng. Aspects*, 2004, 244: 149-157.
121. Y. Hou, S. Gao. Monodisperse nickel nanoparticles prepared from a monosurfactant system and their magnetic properties, *J. Mater. Chem.*, 2003, 13: 1510-1512
122. N. Wu, L. Fu, M. Su, M. Aslam, K. Wong and V. P. Dravid, Interaction of fatty acid monolayers with cobalt nanoparticles, *Nano Lett.*, 2004, 4: 383-386.
123. C. Petit, M. P. Pileni, Physical properties of self-assembled nanosized cobalt particles, *Appl. Surf. Sci.*, 2000, 162-163: 519-528.
124. W. Wang, J. Huang and Z. Ren, Synthesis of germanium nanocubes by a low-temperature inverse micelle solvothermal technique, *Langmuir*, 2005, 21: 751-754.

References

125. J. Tanori and M. P. Pileni, Control of the shape of copper metallic particles by using a colloidal system as template, *Langmuir*, 1997, 13: 639-646.
126. H. Ohde, F. Hunt and C. Wai, Synthesis of silver and copper nanoparticles in a water-in-supercritical-carbon dioxide microemulsion, *Chem. Mater.*, 2001, 13: 4130-4135
127. J. P. Carson, K. Khambaswadkar, C. B. Roberts, Ligand-induced gold nanocrystal superlattice formation in colloidal solution, *Chem. Mater.*, 1999, 11: 198-202.
128. S. Lin, S. Chang, R. Liu, S. Hu, N. Jan, Fabrication and magnetic properties of nickel nanowires, *J. Magnet. Mater.*, 2004, 282: 28-31.
129. W. Han, J. Choi, G. Hwang, S. Hong, J. Lee, S. Kang, Fabrication of Cu nanoparticles by direct electrochemical reduction from CuO nanoparticles, *Appl. Surf. Sci.*, 2006, 252: 2832-2838.
130. A. Ledo-Suárez, L. Rodríguez-Sánchez, M. C. Blanco and M. A. López-Quintela, Electrochemical synthesis and stabilization of cobalt nanoparticles, *Phys. Stat. Sol.*, 2006, 203A: 1234-1240.
131. Y. Sun, H. W. Rollins and R. Guduru, Preparations of nickel, cobalt, and iron nanoparticles through the rapid expansion of supercritical fluid solutions (RESS) and chemical reduction, *Chem. Mater.* 1999, 11: 7-9.
132. J. Park, E. Kang, S. Son, H. Park, M. Lee, J. Kim, K. Kim, et al. Monodisperse nanoparticles of Ni and NiO: synthesis characterization, self-assemblyd superlattices, and catalytic applications in the Suzuki coupling reaction, *Adv. Mater.*, 2005, 17: 429-434.

References

133. J. Chang, J. Chang, B. Lo, S. Tzing, Y. Ling, Silver nanoparticles spontaneous organize into nanowires and nanobanners in supercritical water, *Chem. Phys. Lett.*, 2003, 379: 261–267.
134. M. J. Meziani, P. Pathak, F. Beacham, L. F. Allard, Y. Sun, Nanoparticle formation in rapid expansion of water-in-supercritical carbon dioxide microemulsion into liquid solution, *J. Supercritical Fluids*, 2005:34 : 91–97.
135. <http://www.kobelco.co.jp/p108/p14/sfe01.htm>
136. J. B. McClain, D. E. Betts, D. A. Canelas, E. T. Samulski, J. M. DeSimone, J. D. Londono, H. D. Cochran, G. D. Wignall, D. Chillura-Martino, R. Triolo, *Science* 1996, 274: 2049
137. G. J. C. Carpenter and Z. S. Wronski, The characterization of nanostructured CVD Ni powders using transmission electron microscopy, *J. Nanoparticle Res.*, 2004, 6: 215–221.
138. J. Choi, X. L. Dong and B. K. Kim, Characterization of Fe and Co nanoparticles synthesized by chemical vapour condensation, *Script. Mater.*, 2001, 44: 2225–2229
139. T. O. Ely, C. Amiens and B. Chaudret, Synthesis of nickel nanoparticles. influence of aggregation induced by modification of poly(vinylpyrrolidone) chain length on their magnetic properties, *Chem. Mater.*, 1999, 11: 526-529.
140. X. L. Dong, C. J. Choi, B. K. Kim, Chemical synthesis of Co nanoparticles by chemical vapour condensation, *Script. Mater.*, 2002, 47: 857–861.
141. N. Cordente, M. Respaud, F. Senocq, M. Casanove, C. Amiens and B. Chaudret, Synthesis and magnetic properties of nickel nanorods, *Nano Lett.*, 2001, 1: 565-568.

References

142. H. Shao, Y. Huang, H. Lee, Y. Su, C. Kim, Cobalt nanoparticles synthesis from $\text{Co}(\text{CH}_3\text{COO})_2$ by thermal decomposition, *J. Magnet. Magnet. Mater.*, 2006, 304: e28–e30.
143. M. L. Ostraata, H. A. Atwater, R. C. Flagan, The feasibility of inert colloidal processing of silicon nanoparticles, *J. Colloid Interf. Sci.*, 2005, 283: 414–421
144. M. Ehbrecht and F. Huisken Gas-phase characterization of silicon nanoclusters produced by laser pyrolysis of silane, *Phys. Rev.*, 1999, B59, 2975 - 2985.
145. F. Huisken, G. Ledoux, O. Guillois and C. Reynaud, Light-emitting silicon nanocrystals from laser pyrolysis, *Adv. Mater.* 2002, 14: 1861-1865.
146. S. Botti, A. Celeste and R. Coppola, Particle size control and optical properties of laser-synthesized silicon nanopowders, *Appl. Organometal. Chem.* 1998: 12,361-365..
147. B. Giesen, H. Wiggers, A. Kowalik and P. Roth, Formation of Si-nanoparticles in a microwave reactor: Comparison between experiments and modelling, *J. Nanoparticle Res.*, 2005, 7: 29–41.
148. Y. Dong, A. Bapat, S. Hilchie, U. Kortshagen, S. A. Campbell, Generation of nano-sized free standing single crystal silicon particles, *J. Vac. Sci. Technol., B*, 2004, 22: 1923-1930.
149. X. Lu, K. J. Ziegler, A. Ghezelbash, K. P. Johnston and B. A. Korge, Synthesis of germanium nanocrystals in high temperature supercritical fluid solvents, *Nano Lett.*, 2004, 4: 969- 974.
150. R. A. Bley and S. M. Kauzlarich, A low-temperature solution phase route for the synthesis of silicon nanoclusters, *J. Am. Chem. Soc.*, 1996, 118: 12461-12462.

References

151. D. Gerion, N. Zaitseva, C. Saw, M. Francesca Casula, S. Fakra, T. Vanbuuren, and G. Galli, Solution synthesis of germanium nanocrystals: success and open challenges, *Nano Lett.*, 2004, 4: 597-602.
152. K. Lee, S. Park, D. Lee, Nanogold synthesis by inert gas condensation for immuno-chemistry probes, *J. Alloy. Comp.*, 2005, 390: 297–300.
153. Z. Liu and Y. Bando, A novel method for preparing copper nanorods and nanowires, *Adv. Mater.*, 2003, 15: 303-305
154. B. Chung, C. Liu. Synthesis of cobalt nanoparticles by DC magnetron sputtering and the effects of electron bombardment, *Mater. Lett.*, 2004, 58: 1437–1440.
155. S. Tripathy, R. K. Soni, S. K. Ghoshal and K. P. Jain, Optical properties of nano-silicon, *Bull. Mater. Sci.*, 2001, 24: 285–289.
156. A. A. Sirenko, J. R. Fox, I. A. Akimov, X. Xi, S. Ruvimov, Z. Liliental-Weber, In situ Raman scattering studies of the amorphous and crystalline Si nanoparticles, *Solid State Comm.*, 2000, 113: 553–558.
157. A. Fojtik, A. Henglein, *Ber.Buns. Gesellsch.*, Studies on the amorphous and crystalline Si nanoparticles, *Phys. Chem. Chem. Phys.*, 1993, 97: 252-258.
158. G. Chen, M. Hong, B.Lan, Z. Wang, Y. Lu, T. Chong, Convenient way to prepare magnetic colloids by direct Nd:YAG laser ablation, *Appl. Surf. Sci.*, 2004, 228: 169–175.
159. T. Tsuji, T. Hamagami, T. Kawamura, J. Yamaki, M. Tsuji, Laser ablation of cobalt and cobalt oxides in liquids: influence of solvent on composition of prepared nanoparticles, *Appl. Surf. Sci.*, 2005, 243: 214–219.

References

160. P. Smejkal, J. Pflieger, K. Siskova, B. Vlckova, O. Dammer, M. Slouf, In-situ study of Ag nanoparticle hydrosol optical spectra evolution during laser ablation/fragmentation, *Appl. Phys.* 2004, A79: 1307–1309.
161. Y. Chen, C. Ye, Laser ablation method: use of surfactants to form the dispersed Ag nanoparticles, *Colloids Surf. A: Physicochem.Eng. Aspects*, 2002, 197: 133–139.
162. D. Poondi, R. Subramanian, M. Otooni and J. Singh, Synthesis of silver nanoparticles by a laser-liquid-solid interaction technique, *J. Mater. Syn. Process.*, 1998, 6: 89-104
163. T. Makimura, T. Mizuta, K. Murakami, Formation process of Si nanoparticles in rare gas observed by a decomposition method, *Appl. Phys. A*, 1999, 69[Suppl.]: S213–S215.
164. M. Seo, D. Kim, H. Kim, D. Choi and S. Jeoung, Formation of photoluminescent germanium nanostructures by femtosecond laser processing on bulk germanium: role of ambient gases, *Optics Express*, 2006, 4908-4914.
165. J. L. Heinrich, C. L. Curtis, G. M. Credo, K. L. Kavanagh, M. J. Sailor. Luminescent colloidal silicon suspensions from porous silicon, *Science*, 1992, 255: 66–68.
166. F. Feng, M. Geng, and D. Northwood, Electrochemical behaviour of intermetallic based hydrides used in Ni/metal hydride batteries: a review, *Inter. J. Hydrogen. Energy*, 2001, 26:725-734.
167. T. Yang, X. Gao, W. Hu, F. Wu and D. Noreus, Studies on rechargeable NiMH batteries, *Inter. J. Hydrogen. Energy*, 2006, 31:525-530.

References

168. N. Cui, B. Luan, H. Zhao, H. Lin and S Dou, Synthesis and electrode characteristics of the new composite alloys $Mg_2Ni-xwt\%Ti_2Ni$. *J. Alloys Comp.*, 1996, 240: 229-234.
169. H. Yuan, Q. Li, H. Song, Y. Wang, J. Liu, Electrochemical characteristics of Mg_2Ni -type alloys prepared by mechanical alloying, *J. Alloys Comp.*, 2003, 353: 322-326
170. C. Iwakura, Hi Inoue, S. Zhang, S. Nohara, Hydriding and electrochemical characteristics of a homogeneous amorphous Mg_2Ni-Ni composite, *J. Alloys Comp.*, 1998, 270: 142-144.
171. D. Sun, Y. Lei, W. Liu, J. Jiang, J. Wu, and D. Wang, The relation between the discharge capacity and the cycling numbers of mechanically alloyed Mg_xNi_{100-x} amorphous electrode alloys, *J. Alloys and Comp.*, 1995, 231: 621-624.
172. M. Abdellaoui, S. Mokbli, F. Cuevas, M. Latroche, A. Percheron-Guegan, H. Zarrouk, Structural and electrochemical properties of amorphous rich Mg_xNi_{100-x} nanomaterial obtained by mechanical alloying, *J. Alloys Comp.*, 2003, 356-357: 557-561
173. T. Ma, Y. Hatano, T. Abe, K. Watanabe, Effects of Pd addition on electrochemical properties of $MgNi$, *J. Alloys Comp.*, 2004, 372: 251-258.
174. T. Kuji, H. Nakano, T. Aizawa, Hydrogen absorption and electrochemical properties of $Mg_{2-x}Ni(x0-0.5)$ alloys prepared by bulk mechanical alloying, *J. Alloys Comp.*, 2002, 330-336: 590-596.
175. L. Li, T. Akiyama, J. Yagi, Reaction mechanism of hydriding combustion synthesis of Mg_2NiH_4 , *Intermetallics*, 1999, 7: 671-677.

References

176. L. Li, T. Akiyama, T.Kabutomori, K.Terao, J. Yagi , Hydriding/dehydriding behaviors of the product in hydriding combustion synthesis of Mg_2NiH_4 , *J. Alloys Comp.*, 1999, 228: 98-103.
177. L. Li, I. Saita, K.Saito, T. Akiyama, Effect of synthesis temperature on the purity of product in hydriding combustion synthesis of Mg_2NiH_4 , *J. Alloys Comp.*, 2002, 345: 189-195.
178. L. Li, I. Saita, K.Saito, T. Akiyama, Hydriding combustion synthesis of hydrogen storage alloys of Mg-Ni-Cu system, *Intermetallics*, 2002, 10: 927-932.
179. L. Li, T. Akiyama, J. Yagi, Activity and capacity of hydrogen storage alloy Mg_2NiH_4 produced by hydriding combustion synthesis, *J. Alloys Comp.*, 2001, 316: 118-123.
180. T.B. Massalski, eds. Binary alloy phase diagrams, American Society for Metals, W. B. Scott Jr., New York, 1986.
181. T. Hirata, T. Matsumoto, M. Amano and Y. Sasaki, In situ x-ray diffractometry study of the hydride in the intermetallic compound MgNi, *J. Phys. F: Metal Phys.*, 1981, 11: 521-9.
182. P. Zolliker, K.Yvon, J. D.Jorgensen and F.J.Rotella, Structural studies of the hydrogen storage material Mg_2NiH_4 . 2. Monoclinic low-temperature structure, *Inorg. Chem.*, 1986, 25, 3590.
183. J. Xue, G. Li, Y. Hu, J. Du, C. Wang and G. Hu, Electrochemical characteristics of Al-substituted Mg_2Ni As negative electrode, *J. Alloys Comp.*, 2000 307, 240-244.
184. A. Dean, eds. Lange's Handbook of Chemistry , 15th edition, McGraw-Hill Inc., 1999.

References

185. O. Kubaschewski, C.B. Alcock, Metallurgical Thermochemistry, 5th Edition, International Series on Mater. Sci. Tech. Volume 24, Pergamon Press, 1979, Toronto.
186. V.P. Perminov, Structure characteristics and crystal chemistry of binary magnides, Poroshkovaya Metallurgiya, 1967, 5: 89-96.
187. G. N. Garcia, J. P. Abriata and J. O. Sofo, Hydrogen movement in cubic Mg₂NiH₄, Phys. Rev. B, 2002, 65: 4306-4312.
188. G. N. Garcia, J. P. Abriata, and J. O. Sofo, Calculation of the electronic and structural properties of cubic Mg₂NiH₄, Phys. Rev. B, 2004, 58: 11746-11754.
189. F. Gingl, P. Selvam and K. Yvon, Structure refinement of Mg₂Cu and a comparison of the Mg₂Cu, Mg₂Ni and Al₂Cu structure types, Acta Crystal., 1993, 49B: 201-205.
190. B. R. Taylor, S. M. Kauzlarich, G. R. Delgado and H. W.H. Lee, Solution synthesis and characterization of quantum confined Ge nanoparticles, Chem. Mater. 1999, 11: 2493-2500
191. H. Chiu, C. N. Chervin, and S. M. Kauzlarich, Phase changes in Ge nanoparticles, Chem. Mater. 2005, 17: 4858-4864.
192. O. Loebich, Jr. and Ch. J. Raub, Reactions between some alkali and platinum group metals, Platinum Metals Rev., 1981, 25: 113-120.

PUBLICATIONS

1. Publications derived from this dissertation

1. **H. Wang**, D. O. Northwood, A novel synthesis method for Ni nanoparticles, *Journal of Materials Science*, 43: 1050—1056 (2008)
2. **H. Wang**, D. O. Northwood, Synthesis of Ag nanoparticles by hydrolysis of the Mg-Ag intermetallic compounds, *Journal of Materials Processing Technology*, in press, doi.org/10.1016/j.jmatprotec.2007.11.043 .
3. **H. Wang**, D. O. Northwood, A novel method of preparing transition metal nanoparticles, *Journal of Nanoscience and Nanotechnology*, (accepted on Nov. 28, 2007).
4. **H. Wang**, D. O. Northwood, Hydrolysis behaviour of magnides and aluminides and its application to the synthesis of nanoparticles, *Intermetallics*, 16:479-484 (2008)
5. **H. Wang**, X. Hu, D. O. Northwood, Synthesis of Cu nanoparticles by hydrolysis of Mg₂Cu, *Materials Letters*, in press, doi:10.1016/j.matlet.2008.02.046.
6. **H. Wang**, L. Han, H. Hu and D. O. Northwood, The hydrolysis behaviour of Mg₂Ni and Mg₂NiH₄ in water or a 6M KOH solution and its application to Ni nanoparticles synthesis, *Journal of Alloys and Compounds*, doi:10.1016/j.jallcom.2008.03.016.
7. **H. Wang**, D. O. Northwood, Synthesis of Ag and Pt nanoparticles by hydrolysis of either Ag₂Na or PtNa, *Research Letters in Materials Science*,

Publications

[doi:10.1155/2008/6190327](https://doi.org/10.1155/2008/6190327).

8. **H. Wang, D. O. Northwood**, Synthesis of Au nanoparticles by hydrolysis of Mg_3Au , *Gold Bulletin*, (submitted on Sept. 28, 2007).
9. **H. Wang, D. O. Northwood**, Synthesis of Ni nanoparticles by hydrolysis of $MgNi_2$, *Advanced Materials and Manufacturing Processes*, (accepted on April 12, 2008)

Publications

2. Other publications during PH.D study

1. **H. Wang**, J. Han S. Du, and D.O.Northwood, Reaction synthesis of nickel /aluminide multilayer composites using Ni and Al foils: Microstructures, tensile properties and deformation behaviour, *Metallurgical and Materials Transactions*, A38:409-419 (2007).
2. **H. Wang**, J. Han S. Du and D.O.Northwood, Effects of Ni foil thickness on the microstructure and tensile properties of reaction synthesized multilayer composites, *Materials Science and Engineering*, A445-446: 517-525 (2007).
3. **H. Wang**, J. Han S. Du and D. O. Northwood, Reaction synthesis of Ni /Ni₃Al multilayer composites using Ni and Al foils: High-temperature tensile properties and deformation behaviour, *Journal of Materials Processing Technology*, 200: 433-440, (2008)
4. **H. Wang**, D. O. Northwood, J. Han and S. Du, Combustion synthesis of AlN-whiskers, *Journal of Materials Science*, 41[6]: 1697-1703 (2006).
5. **H. Wang**, D. O. Northwood, J. Han and S. Du, Growth Mechanisms for SiC-AlN Solid Solution Crystals Prepared by Combustion Synthesis, *Journal of American Ceramic Society*, 89[2]: 501-508 (2006).
6. **H. Wang**, D. O. Northwood, J. Han and S. Du, Combustion synthesis of AlN-SiC solid solutions, *Journal of Australasian Ceramic Society*, 41[1]: 48-57 (2005).
7. **H. Wang**, D.O. Northwood, Low cost preparation of high quality aluminum nitride powders and whiskers, *Ceramic Transactions*, 177: 115-133 (2006).

Publications

3. Presentations

1. **H. Wang**, D. O. Northwood, A novel method of preparing transition metal nanoparticles, International Conference on Nanoscience and Technology: China Nano-2007, June 3-7, 2007. Beijing.
2. **H. Wang**, D.O. Northwood, Low cost preparation of high quality aluminum nitride powders and whiskers, Proceedings of the 107th Annual Meeting of the American Ceramic Society, Baltimore, April 10-13, 2005.
3. **H. Wang**, D. O. Northwood, Hydrogen absorption/desorption behaviour and electrochemical properties of Mg_2Ni , 17th World Hydrogen Energy Conference, Brisbane, Australia, 2008 (Abstract submitted).
4. **H. Wang**, D. O. Northwood, Synthesis of metallic nanoparticles by hydrolysis of magnides, aluminides, and sodides, 3rd International Conference Processing Materials for Properties, Bangkok, Thailand, 2008, (Abstract submitted).

VITA AUCTORIS

NAME: Huabin Wang

PLACE OF BIRTH: Anhui, P. R. China

YEAR OF BIRTH: 1971

EDUCATION: Anhui University of Science and Technology,
Wuhu, Anhui, P. R. China
1988 -1992, B. Eng. in Engineering Materials

Harbin Institute of Technology,
Harbin, Heilongjiang, P. R. China
1992 -1995, M. Eng. in Engineering Materials

University of Windsor,
Windsor, Ontario, Canada
2003 - 2008 Ph.D in Engineering Materials